A SINGULAR PERSPECTIVE ON CHROMOSOMAL REPLICATION:

STUDYING LIVE CELLS BY EMPLOYING A MULTI-DISCIPLINARY APPROACH

A SINGULAR PERSPECTIVE ON CHROMOSOMAL REPLICATION:

STUDYING LIVE CELLS BY EMPLOYING A MULTI-DISCIPLINARY APPROACH

Proefschrift

ter verkrijging van de graad van doctor
aan de Technische Universiteit Delft,
op gezag van de Rector Magnificus prof. ir. K. C. A. M. Luyben,
voorzitter van het College voor Promoties,
in het openbaar te verdedigen op vrijdag 13 maart 2015 om 12:30 uur

door

Martinus Charl MOOLMAN

natuurkundig ingenieur
geboren te Pretoria, Zuid-Afrika.

Dit proefschrift is goedgekeurd door de promotor:

Prof. dr. N.H. Dekker

Samenstelling promotiecommissie:

Rector Magnificus,	voorzitter
Prof. dr. N. H. Dekker,	Technische Universiteit Delft, promotor
Prof. dr. C. Dekker,	Technische Universiteit Delft
Prof. dr. M. C. Leake,	University of York, United Kingdom
Prof. dr. P. L. Graumann,	Universität Marburg, Germany
Dr. C. J. A. Danelon,	Technische Universiteit Delft
Dr. S. Manley,	École polytechnique fédérale de Lausanne, Switzerland
Dr. R. Reyes-Lamothe,	McGill University, Canada
Prof. dr. M. Dogterom,	Technische Universiteit Delft, reservelid

TUDelft Delft University of Technology
Bionanoscience Department
Think big about life at the smallest scale
Casimir research school
NWO
Nederlandse Organisatie voor Wetenschappelijk Onderzoek
MitoSys

Keywords: replication; repair; *E. coli*; microfabrication; nanotechnology; single-molecule; fluorescence microscopy; photoactivatable fluorescence microscopy; microfluidics

Printed by: Gildeprint

Front & Back: Melanie Römer-Moolman

Casimir PhD Series, Delft-Leiden 2015-03

ISBN 978-90-8593-211-6

CONTENTS

1

INTRODUCTION

It has become abundantly clear that much more will be demanded of scientists before we can claim to fully understand a process such as DNA replication or DNA recombination.

- Bruce Alberts, 2003

The information contained in the nucleotide sequences of chromosomal DNA (chromosome) is essential for cell viability and proliferation [1]. All dividing cells must ensure the accurate and timely duplication (replication) of their chromosome to ensure a copy is passed on to the next generation. This is not a trivial endeavor, which the multi-protein complex, known as the replisome [2], has to accomplish. The chromosome is highly compacted inside a cell [3, 4]. For example, *Escherichia coli* (*E. coli*) succeeds to maintain its ~ 1 mm long chromosome [5] inside a cell that is approximately a 1000x shorter (~ 3 μm) in length. Furthermore, this compacted chromosome is continuously accessed throughout the cell cycle by numerous different proteins involved in for example transcription, repair and chromosome segregation. In the midst of all of this chromosome utilization, the chromosome is concurrently being replicated by numerous different proteins working in concert together with an astounding error rate of about one nucleotide in a billion [6]. Even though most of the proteins involved in the process of replication are known, the intricate molecular details enabling the cell to accomplish this daunting feat is still open for investigation.

The ability to probe the precise details of replication in single live cells, have been made possible due to relatively recent technological advances in the fields of genetic engineering, optical microscopy and microfluidics [7–11]. It has become possible, via recombineering techniques, to reliably fuse the gene encoding for a specific fluorescent protein to the protein of interest - ensuring specific labeling [12]. This is of essential importance when doing quantitative fluorescence microscopy. Other methods of *in vivo* protein labeling have some finite chance of aspecific binding, which makes analysis and interpretation of the results even more arduous if not impossible. Due to the advances in detector sensitivity and speed, in combination with higher laser excitation power, one is able to study a single fluorescently labeled molecule inside a cell - effectively using the cell itself as a test tube [13]. Though *in vitro* experiments have proven to be a powerful and important way to probe biological systems, the environment of the cell can be fundamentally different than a test tube. To accurately perform an *in vitro* reaction, one needs to known all the required components and conditions as they occur in the cell. This information is not always available, or sometimes only partially known. For that reason, some events as they would normally occur in the cell, might be obscured or even non-existent during an *in vitro* experiment. Thus, being able to investigate a (single) protein in its natural environment provides one with added insight into the process under investigation that might otherwise have been invisible in an artificial *in vitro* situation. This type of *in vivo* investigation enables one to probe the temporal dynamics, stoichiometry and co-localization of proteins and protein complexes in their natural environment. The advance of microfluidics ('lab-on-a-chip' technology) has provided the means of high spatial control over individual cells and the environment they are in. This has opened a whole new paradigm for investigating cells and their interactions with their environment [10]. One is able to study individual cells over multiple cell cycles, probe cell-to-cell heterogeneity and elucidate aging to name but a few example applications, while having exact control over the growth conditions of the cells.

In this dissertation, I describe experimental methods and measurements aimed at furthering our understanding of chromosomal replication in the context of live *E. coli* cells. The work that I describe in this thesis was conducted by myself in collaboration with other individuals. The contributions of each individual related to the specific project are clearly stated at the end of each chapter. Utilizing a multi-disciplinary approach by employing the above mentioned techniques: microfluidics, quantitative fluorescence microscopy and genetic engineering, allowed us to probe this fundamental process on the single cell level throughout successive cell cycles during active replication. The outline of this thesis is as follows:

In Chapter 2 we provide a review of how genomic processes (transcription, translation and replication) can be investigated with different single-molecule techniques *in vitro* as well as *in vivo*. We provide an overview of the common techniques used and highlight certain key studies over the past years. We conclude with a summary of the current challenges and future directions for exploration.

In Chapter 3 we present a detailed fabrication methodology of a microfluidic device used for immobilization of cells for extended time-lapse microscopy without chemical fixation. We utilize electron beam lithography for precise and accurate patterning, together with dry etching protocols to fabricate the features of the device into silicon. These features are reliably transferred to polydimethylsiloxane, which the final microfluidic device is made. We demonstrate the successful implementation of the device for gram-positive (*Lactococcus lactis*) and gram-negative (*E. coli*) bacteria.

In Chapter 4 we systematically evaluate different analysis algorithms for studying fluorescent foci in bacteria. We employ a novel approach where experimental data is combined with simulation. Diffuse fluorescent molecules are imaged in individual live *E. coli* cells, and used as an exact representation for the cellular background in a bacterial cell. A focus with varying intensity is simulated onto these measured images while keeping the total intensity of the cell constant. The different algorithms (custom written Gaussian fit algorithms and the common 'SpotFinderZ' tool) are evaluated using these images. We demonstrate that there is a clear background dependency on the accuracy of the localization and intensity determination. Furthermore, we demonstrate that the localization error is also dependent on the distance of the focus from the bacterial cell edge. Our results enable use to provide guidelines for designing experiments where a fluorescent focus is studied in the noisy background of the bacterial cell.

In Chapter 5 we present a detailed study of the *in vivo* dynamics of the β_2-sliding clamp (β_2-clamp), a protein that is part of the replisome and essential for replication and repair processes. We quantify the recruitment, binding and turnover of the β_2-clamps on DNA during replication using convention- and photoactivatable fluorescence microscopy in combination with microfluidics. We demonstrate that β_2-clamps are loaded onto DNA shortly after initiation of replication, remain DNA-bound on the order of minutes, and accumulate on the DNA until a steady-state plateau is reached. This accumulated number of β_2-clamps form a binding platform for other proteins necessary for DNA metabolism. Our findings provide further detailed insight into the processes of both replication and repair.

In Chapter 6 we turn our attention to termination of replication. We investigate the fate of an active replication fork when it encounters a natural replication roadblock located in the terminus region of the chromosome. We follow the replisome, together with specific chromosomal loci, in a *E. coli* strain where one of the two replisomes encounters the roadblock prior to the other replisome. Our results suggest that the replisome (as assessed by visualizing the β_2-clamp) remains stability bound after hitting the roadblock, is slowed down but not halted indefinitely, and that the presence and absence of the roadblock affects the organization of the newly replicated sister chromosomes. Our results provide further insight into the robustness of the cell in completing the essential process of chromosomal replication.

REFERENCES

[1] B. Alberts, *DNA replication and recombination,* Nature **421**, 431 (2003).

[2] C. S. McHenry, *DNA replicases from a bacterial perspective.* Annual review of biochemistry **80**, 403 (2011).

[3] X. Wang, P. Montero Llopis, and D. Z. Rudner, *Organization and segregation of bacterial chromosomes.* Nature Reviews Genetics **14**, 191 (2013).

[4] T. B. Le and M. T. Laub, *New approaches to understanding the spatial organization of bacterial genomes.* Current Opinion in Microbiology **22C**, 15 (2014).

[5] D. Skoko, D. Yoo, H. Bai, B. Schnurr, J. Yan, S. M. McLeod, J. F. Marko, and R. C. Johnson, *Mechanism of chromosome compaction and looping by the Escherichia coli nucleoid protein Fis.* Journal of Molecular Biology **364**, 777 (2006).

[6] I. J. Fijalkowska, R. M. Schaaper, and P. Jonczyk, *DNA replication fidelity in Escherichia coli: a multi-DNA polymerase affair.* FEMS microbiology reviews **36**, 1105 (2012).

[7] D. Court and J. Sawitzke, *Genetic Engineering Using Homologous Recombination,* Annual Review of Genetics **36**, 361 (2002).

[8] G. M. Whitesides, *The origins and the future of microfluidics.* Nature **442**, 368 (2006).

[9] A. Gahlmann and W. E. Moerner, *Exploring bacterial cell biology with single-molecule tracking and super-resolution imaging.* Nature Reviews Microbiology **12**, 9 (2014).

[10] F. J. H. Hol and C. Dekker, *Zooming in to see the bigger picture: microfluidic and nanofabrication tools to study bacteria.* Science **346**, 1251821 (2014).

[11] R. Reyes-Lamothe, E. Nicolas, and D. J. Sherratt, *Chromosome Replication and Segregation in Bacteria,* Annual Review Of Genetics **46**, 121 (2012).

[12] T. Xia, N. Li, and X. Fang, *Single-Molecule Fluorescence Imaging in Living Cells,* Annual review of physical chemistry **64**, 459 (2013).

[13] X. S. Xie, J. Yu, and W. Y. Yang, *Living cells as test tubes,* Science **312**, 228 (2006).

2

STUDYING GENOMIC PROCESSES AT THE SINGLE-MOLECULE LEVEL: INTRODUCING THE TOOLS AND APPLICATIONS

To understand genomic processes such as transcription, translation or splicing, we need to be able to study their spatial and temporal organization at the molecular level. Single-molecule approaches provide this opportunity, allowing researchers to monitor molecular conformations, interactions or diffusion quantitatively and in real time in purified systems and in the context of the living cell. This Review introduces the types of application of single-molecule approaches that can enhance our understanding of genome function.

This chapter have been published as: David Dulin, Jan Lipfert, M. Charl Moolman and Nynke H. Dekker. Studying genomic processes at the single-molecule level: introducing the tools and applications. *Nature Reviews Genetics*, **14**, 9-22 (2013)

2.1. INTRODUCTION

Cells rely on the correct readout, maintenance, repair and replication of genomic information. These are processes that involve a stunning variety of carefully coordinated and regulated molecular actors. Although many of the important players were identified decades ago, quantitative and mechanistic insight into their actions and interactions remains a challenge that has attracted scientists from disciplines that neighbour molecular biology and biochemistry, such as biophysics, bioinformatics and nanoscience.

To obtain quantitative insight into genomic processes, probing at the single-molecule level has proved to be very successful. For example, single-molecule methods can detect transient intermediates or rare events that are masked when ensemble techniques that average the behaviour of a large number of molecules are used. Single-molecule measurements require techniques that are capable of probing biological material with nanometre-scale spatial and millisecond temporal resolution. Furthermore, techniques must be compatible with aqueous environments, as genomic processing takes place in the context of the living cell. Single-molecule methods now exist that reach this capability in a range of environments from simple saline solutions used for *in vitro* studies to the densely crowded environment of the living cell.

Using single-molecule approaches, a wealth of quantitative information on the activity of proteins involved in genome processing has been obtained in recent years. For example, experiments have allowed us to distinguish the different stepping motions used by helicases, to witness the progress of RNA polymerase (RNA Pol) base pair by base pair and to follow the activity of the replisome in live cells in real time, to name but a few. Complementing excellent studies using bulk approaches that for reasons of space we cannot detail in this Review, the results of single-molecule studies have provided us with detailed mechanistic insight into the functions and mechanisms of motor proteins and have even found a major commercial application in single-molecule DNA-sequencing approaches (recently reviewed in Ref. [1]). Yet the field is by no means mature. Single-molecule studies are increasingly going ’beyond single molecules’. Experiments are beginning to address multi-component systems and their mutual interactions: for example, they study more than the interaction of a single protein with DNA. This development has gone hand-in-hand with the ability of techniques to detect different molecular components simultaneously and to carry out many single-molecule experiments in parallel, allowing high-throughput data collection while still resolving the fundamental behaviour of individual molecules.

In this Review, we provide an introduction to single-molecule approaches to study genomic processes and highlight examples of insights obtained using these methods. We first focus on transcription and translation, then highlight recent progress in studying RNA export and splicing and conclude by demonstrating the dynamics of protein-protein interactions in replication. Other areas of genome processing that have benefited from the single-molecule approach include DNA repair and recombination, and these have been reviewed elsewhere [2, 3]. As it is possible to monitor the motion of a single biological molecule both *in vitro* as well as inside a living cell, we compare and contrast genome processing in these two different contexts. Throughout, we indicate how specific insights rely on the capabilities afforded by single-molecule methods.

2.2. MEASURING AT THE SINGLE-MOLECULE LIMIT

Although achieving the single-molecule limit is in and of itself fairly straightforward (for example, by sufficient dilution of a molecular sample), the challenge has always been how to observe or to manipulate single molecules. Signals are inevitably weak, and the measurement apparatus is always macroscopic. Techniques such as electron microscopy [4–6] and patch clamp detection [7] were early advances along these lines. In this Review, we focus on the principal single-molecule techniques that are used for the study of genome processing: namely, force spectroscopy (Section 2.2.1) and fluorescence spectroscopy (Section 2.2.2). The developments of atomic force microscopy, video-based tethered particle motion (TPM) and optical and magnetic tweezers have formed the key methodological advances in force spectroscopy. Optical and magnetic tweezers in particular have succeeded in combining great flexibility in terms of molecular manipulation with high spatial and temporal resolution. The development of optical methods to visualize individual molecules [8, 9] the introduction of genetically encodable fluorophores, such as GFP [10], and the introduction of fast detectors and sensitive cameras have been key to the widespread use of fluorescence spectroscopy. Indeed, using this approach it has now become routine to monitor the motion of individual molecules of different types within living cells.

There are many possible reasons for choosing single-molecule methods to study genomic processes. Most obviously, they allow re-examination of known biological processes in real time directly as they occur. In many cases, the high spatial and temporal resolution afforded by single-molecule techniques has made it possible to gain unique insight into enzymatic dynamics. This has particularly been the case for studies of genome processing, in which the ~ 3Å base pair spacing sets a critical length scale. Importantly, single-molecule techniques provide inherent synchronization, in the sense that the starting point of enzymatic activity is always known. Hence, the signals of molecular activities are not affected by averaging asynchronous events. For example, studies of the repetitive cycles of elongation in transcription, translation and replication benefit from this lack of averaging. Additionally, when studying biological systems of considerable compositional complexity (for example, the ribosome and its associated factors), single-molecule techniques can permit the selection, and hence the study, of correctly assembled complexes only. Finally, the sheer diversity of parameters that can be measured by single-molecule techniques - such as enzymatic stall forces [11], backwards motion of an enzyme along a DNA template [12], the presence of friction during enzyme motion [13, 14] and many more - has also played an important part in their wide acceptance.

2.2.1. SINGLE-MOLECULE FORCE-MANIPULATION TECHNIQUES

A range of techniques can be used to apply forces (and, in some cases, torques) to individual molecules or molecular assemblies [15–17]. These single-molecule manipulation techniques rely on specifically attaching the extremities of the molecule (or molecules) of interest between a surface and a force transducer: for example, to a magnetic or dielectric bead or a cantilever used in atomic force microscopy (AFM) [17]. Specific attachment is accomplished by means such as biotin-streptavidin linkage, thiol bonds or antibodies.

In magnetic tweezers (Figure 2.1a), permanent or electrical magnets are used to manipulate surface-tethered magnetic beads by controlling the external fields. The force (shown by the 'F' in the Figure 2.1a) on the magnetic beads depends on the gradient of the magnetic field [18]. In addition to forces, magnetic tweezers can also routinely apply torques by rotating the magnetic fields [19, 20]. In flow-stretch experiments (Figure 2.1b), liquid flow exerts drag forces on tethered beads [21]. The force can be controlled by adjusting the flow rate. In AFM, forces are applied to individual molecules tethered between a functionalized AFM cantilever and a surface [17, 22] (Figure 2.1c). Optical tweezers hold a dielectric particle or bead in the focus of an intense laser beam [17, 23, 24] (Figure 2.1d-f). Common optical tweezers geometries have one end of a nucleic acid tether attached to a bead held in an optical trap while the other end is attached to either the surface (Figure 2.1f) or to another optically trapped bead (Figure 2.1e), a so-called dumb-bell or dual-bead assay, or to a bead held in a micropipette (Figure 2.1d). In flow-stretch and magnetic tweezers set-ups, the tether extension is typically monitored by charge-coupled-device-camera-based tracking of the bead positions. In optical tweezers or AFM, the laser signal is usually read out with a position-sensitive device or quadrant photodiode [22, 23]. Flow-stretch and magnetic tweezers intrinsically operate in constant force mode: that is, for a given setting of the flow speed or magnetic fields, the stretching force exerted on the tether is (nearly) constant. By contrast, optical tweezers and AFM intrinsically control the extension by controlling the position of the optical trap or cantilever. Constant extension techniques can be operated in (approximately) constant force mode by using feedback control or by exploiting trap nonlinearities [25]. All four techniques can apply forces in the pico-Newton (pN) to tens of pN range (Figure 2.1g), which is suitable for studying biological processes at the molecular scale (for example, the stall force for polymerases is in the range of 10 pN). AFM measurements are at the high-force end on this scale, whereas magnetic tweezers are particular well-suited to accurately applying and measuring very low forces [17].

2.2.2. FLUORESCENCE MICROSCOPY TECHNIQUES

Fluorescence microscopy is a versatile, widely used tool for studying biological processes both *in vivo* and *in vitro*. It relies on the fact that molecules can emit light after they have absorbed it at a different (typically shorter) wavelength. The efficiency of this process depends on the type of molecule used. Many different kinds of fluorescent probes are available and each has its own specific set of characteristics [26–28]. They can be divided into two broad classes: fluorescent proteins, which are a common choice for live-cell imaging [27], given their high specificity; and organic dyes, which have a greater brightness but suffer from lower specificity inside living cells.

In addition to the choice of the fluorophore, an important consideration is the excita-

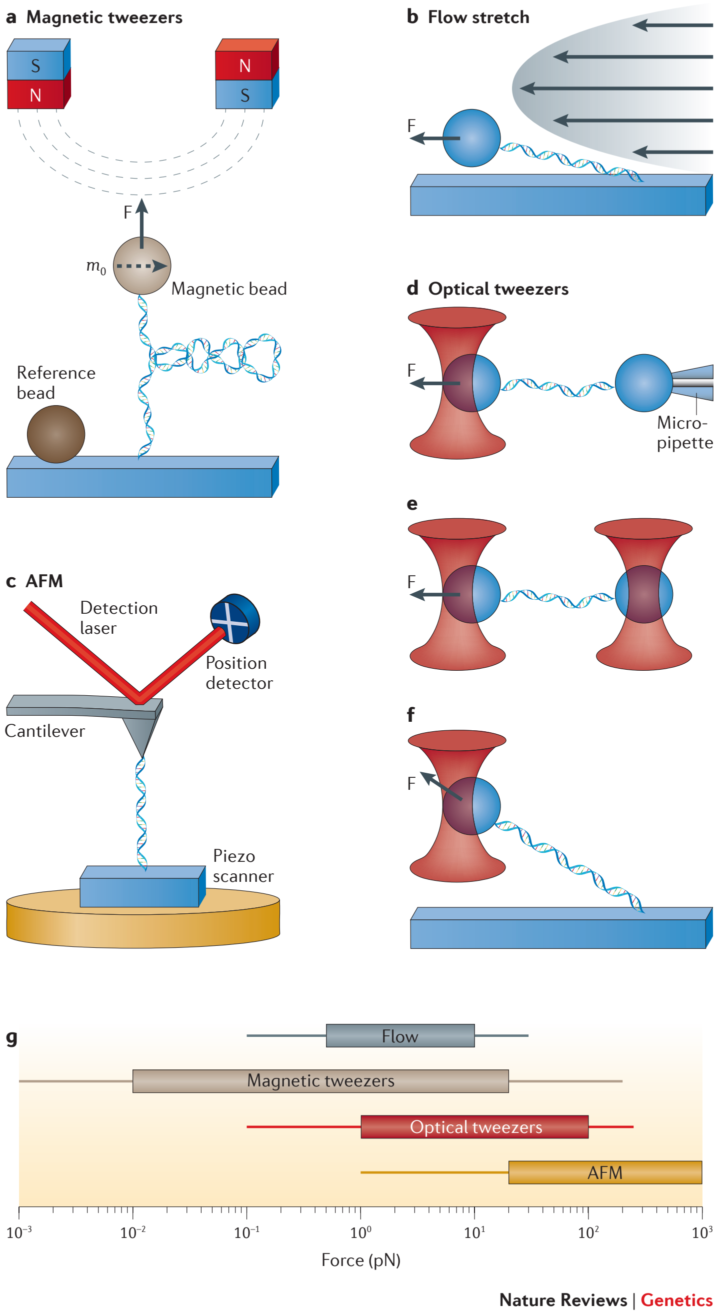

Figure 2.1: Different single-molecule force-manipulation configurations. (a) Magnetic tweezers. (b) Flow-stretching. (c) Atomic force microscopy. (d-f) Optical tweezers. (g) Force range of the different techniques.

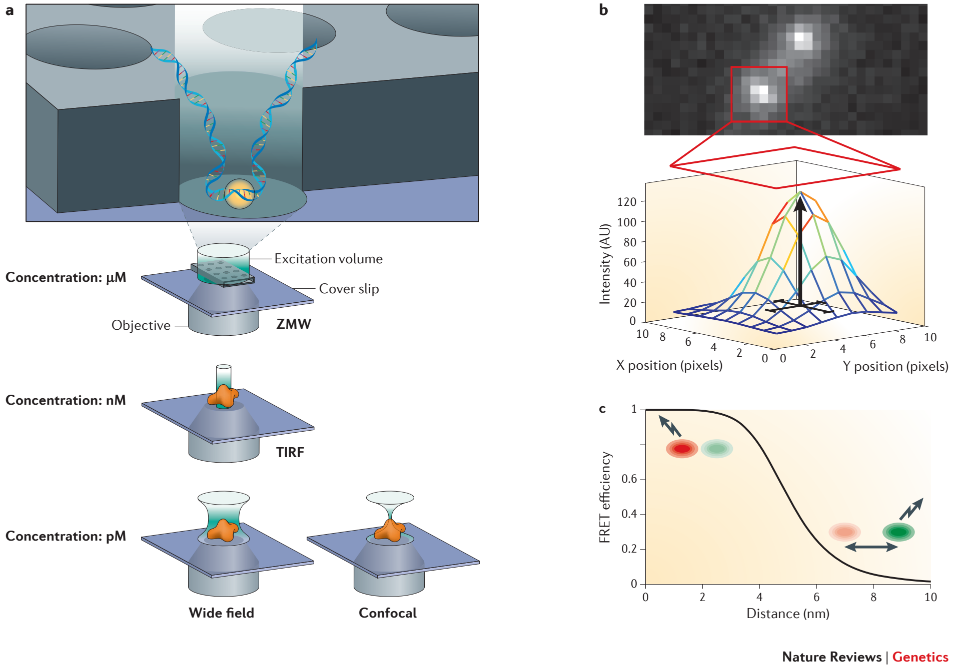

Figure 2.2: Fluorescence microscopy. (a) Commonly used fluorescence excitation methods. Here we depict zero-mode waveguides, total internal reflection fluorescence-, wide field-, and confocal microscopy. (b) Localization of a diffraction-limited focus for sub-pixel position information. (c) The Förster (fluorescence) resonance energy transfer efficiency curve.

tion method used. Figure 2.2a shows four frequently used excitation strategies: wide-field, confocal, total internal reflection fluorescence (TIRF) microscopy and zero-mode waveguides (ZMWs). These methods differ from one another by the excitation volume, shown here in green. In wide-field microscopy, the sample is excited by a nearly collimated light beam. Out-of-focus fluorophores are also excited, increasing the background noise and rendering probe localization more difficult. Confocal microscopy reduces the excitation volume by using a focused laser beam and a spatial filter in front of the detector to eliminate any out-of-focus fluorescence light. Both TIRF microscopy and ZMWs use evanescent waves to reduce the excitation volume, making it possible to excite only molecules that are within ~ 100 nm of the surface and as such substantially reducing the background fluorescence [29]. In ZMWs, the excitation volume in the imaging plane is further restricted compared to TIRF microscopy by making use of nanofabricated structures with typical dimensions of ~ 100 nm (inset). An important parameter in determining the most suitable technique is the required concentration of fluorescently labelled components. For example, physiologically relevant ligand conditions are preferred for studies of enzymatic activity. Higher concentrations of a fluorescently labelled ligand result in higher background fluorescence and, consequentially, an increased need to reduce the excitation and detection volumes. On the left of Figure 2.2a are indicated the typical concentrations of fluorophore-labelled molecules (ranging from pM to μM) that can be investigated with these respective techniques.

Fluorescence excitation of individual fluorophores gives rise to diffraction-limited spots that can be detected with sensitive detectors, typically electron-multiplying charge-coupled-device cameras or photodiodes. The position of these fluorescent foci can be determined using single-molecule localization methods with an uncertainty in the nanometre range (depending on the signal-to-noise ratio of the measurement). Single-molecule localization involves fitting the spatially distributed intensity of the detected fluorescence spot to a mathematical function (typically a Gaussian function) to determine its centre (Figure 2.2b) [30–33] The newly developed super-resolution techniques (which were recently reviewed in [34, 35]) have developed ways of successively localizing neighbouring molecules to build up an image with resolution beyond that permitted by the Rayleigh criterion.

The preferred microscopy method is highly dependent on the type of investigation. Low background techniques, such as TIRF and confocal microscopy, are commonly used to probe three-dimensional conformational changes. This can be done in combination with Förster (fluorescence) resonance energy transfer (FRET). FRET is based on the non-radiative energy transfer between so-called donor (green) and acceptor (red) fluorophores in close proximity [36] (Figure 2.2c). Following excitation, the donor molecule can non-radiatively transfer its energy to a sufficiently close acceptor molecule, resulting in a decrease in the (green) donor fluorescence signal and a concomitant increase in the (red) acceptor fluorescence signal. Monitoring the degree of energy transfer reports on the distance and dynamics of intra- and intermolecular interactions on the sub-10 nm scale [37]. Please note that the diagrams are not drawn to scale and are meant for illustration purposes only. AU, absorbance units.

2.3. TRANSCRIPTION

Our understanding of the key molecular motor that powers transcription, RNA Pol, has been greatly advanced by single-molecule methods. Following the lead of initial single-molecule work on *Escherichia coli* RNA Pol [38], studies have primarily focused on bacterial systems, but more recently eukaryotic RNA Pol II has also been examined.

2.3.1. INITIATION

In bacteria, an important step in transcription initiation is the transition from the so-called closed promoter complex to the open promoter complex, a process in which the RNA polymerase holoenzyme (RNA Pol holoenzyme) locally melts the DNA. The value of *in vitro* multicolour single-molecule total internal reflection fluorescence (TIRF) microscopy based assays (Figure 2.2a) is shown by a study that sheds light on the various substeps of this transition and their dynamics for the case of transcriptional regulation by $\sigma54$ (Ref. [39]). Such an approach is widely applicable and provides large data sets that report on the association and dissociation of multiple, differentially labelled molecules in a single experiment. The low dissociation rates between $\sigma54$, *E. coli* RNA Pol and DNA mean that fairly low concentrations of labelled molecules could be used (because the molecules could 'wait' for the arrival of a labelled component), and thus this facilitated the observation of individual molecules using TIRF microscopy (Figure 2.2). The authors observed that the transition from an unbound *E. coli* RNA Pol to a closed promoter complex can be decomposed into two substeps, each of which is characterized by its own lifetime, and the rate of the second substep is rate-limiting for the overall transition into the open promoter complex. They further determined that in the presence of competing processes, such as dissociation, on average 30 attempts are necessary for *E. coli* RNA Pol to reach the open promoter complex. Interestingly, these studies showed that the dynamics of the $\sigma54$-dependent initiation pathway differ substantially from those of the more common $\sigma70$-dependent pathway but closely resemble eukaryotic pathways.

Single-molecule Förster (fluorescence) resonance energy transfer (smFRET) [36] (Figure 2.2c) and magnetic tweezers [40] (Figure 2.1a) have been used to distinguish between three different models proposed for the transition of the *E. coli* RNA Pol holoenzyme from initiation into elongation: transient excursion (in which *E. coli* RNA Pol diffuses back and forth on the DNA between subsequent abortive initiations); inchworming (in which *E. coli* RNA Pol stretches further along on the DNA template with each successive ribonucleotide incorporation, followed by subsequent release); and scrunching (in which the DNA transcription bubble increases in size with each successive ribonucleotide incorporation, followed by subsequent release). To probe these different possibilities, smFRET was used with several dye-labelling strategies [36] (Figure 2.3A,B). For example, labeling the trailing edge of *E. coli* RNA Pol and the upstream template DNA enabled the authors to monitor the relative distance between these molecules; as this distance did not change, they were able to discard the transient excursion model. Labelling the trailing edge of *E. coli* RNA Pol and the DNA downstream from the promoter revealed that their relative distance was unaltered during the transition into elongation, hence the inchworming model was similarly ruled out. Finally, by labelling the leading edge of *E. coli* RNA Pol and the upstream DNA, the authors showed that 7-9 base pairs are scrunched before elongation. A study that analysed promoter unwinding on supercoiled DNA in magnetic tweezers reached similar conclusions [40]. Eukaryotic RNA Pol II initiation has also been studied using an smFRET-based triangulation approach to observe the transition from the open complex conformation into elongation [41]. By labelling RNA Pol II, the DNA template and several transcription factors, the authors observed a large conformational change of the initiation complex during the transition from initiation into elongation, which is facilitated by the intrinsic flexibility of eukaryotic transcription factor IIB (TFIIB) [41].

2.3.2. ELONGATION

Single-molecule studies of elongation have revealed the rich dynamics of nucleotide incorporation, in particular, the presence of various kinds of pauses, and here we note a few examples to show the types of application of these methods. The first *in vitro* single-molecule studies of RNA Pol (which used TPM) revealed heterogeneities in RNA Pol velocity [38]. Since then, studies of elongation have primarily relied on optical tweezers (Figure 2.3C) and have benefited from the high spatiotemporal resolution that can

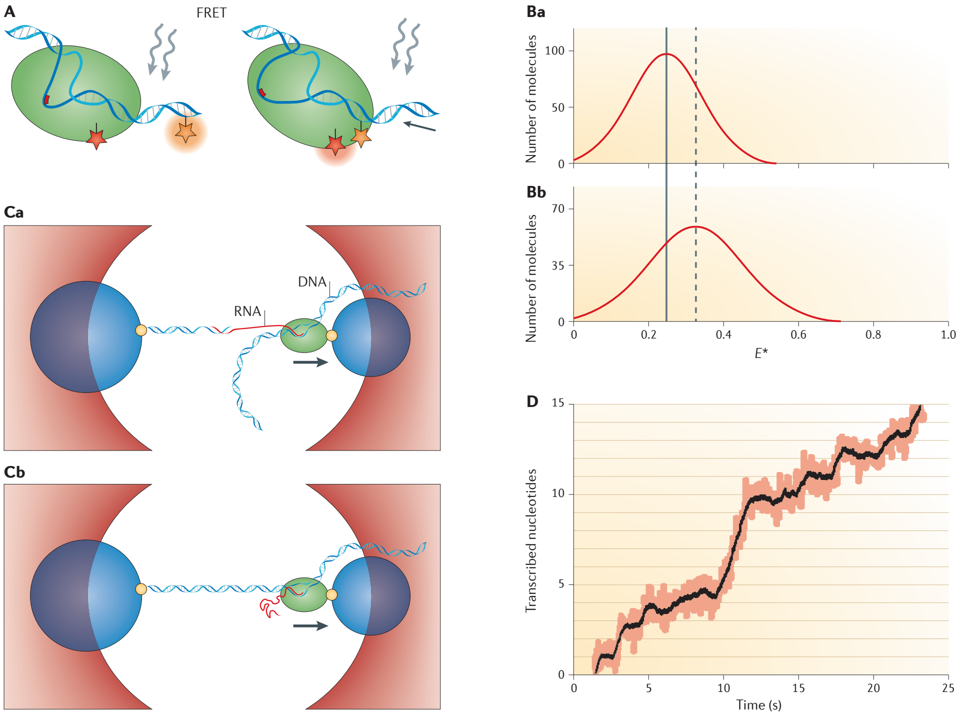

Nature Reviews | Genetics

Figure 2.3: Studies of RNA polymerase at the single-molecule level. (A) A schematic of a small-molecule Förster (fluorescence) resonance energy transfer (smFRET) experiment in which the polymerase and the DNA template strand are labelled by an acceptor and a donor fluorophore, respectively [36]. (B) Representation of the results from this experiment. At the start of the reaction, the FRET signal is weak (a). Subsequent advancement by *Escherichia coli* RNA polymerase (RNA Pol) results in higher FRET efficiency, as shown by the shift in the distribution (b). Even small structural changes in the *E. coli* RNA Pol can be monitored in this way. (C) An example of a force spectroscopy experiment that relies on a dumb-bell assay in an optical trap to monitor transcription. The direction of *E. coli* RNA Pol motion is indicated by the arrows. Note that force can applied in different ways: to the upstream DNA template as an assisting force (a) a force applied to the downstream DNA template (not shown) would provide an opposing force); or to the synthesized mRNA (b). (D) The observation of transcription elongation by a single *E. coli* RNA Pol at base-pair resolution. Raw data are shown in red, and smoothed data are shown in black. The horizontal lines are spaced by the distance between nucleotides. E^*, efficiency of donor-acceptor energy transfer. Data in panels Ba and Bb are taken from Ref. [36]. Panel (C) is modified, with permission, from Ref. [42] © (2008) Elsevier. Panel (D) is modified, with permission, from Ref. [43] © (2005) Macmillan Publishers Ltd. All rights reserved.

now be achieved - single base pairs in a 1-second bandwidth [43] (Figure 2.3D). Such studies of transcription dynamics have highlighted how RNA Pol progression is interrupted by different kinds of pauses [44–49]. For example, studies in which an assisting force was applied to *E. coli* RNA Pol using optical tweezers (Figure 2.3Ca) showed that pauses occur at rates that are sequence- and force-dependent and have durations that are exponentially distributed and independent of the magnitude of the applied force [45, 50]. Such exponentially distributed pauses could be modulated by the presence of co-transcriptional factors, such as NusG (which decreases the pause density [51]) and NusA (which increases the pause density [50]). Conversely, the application of an opposing force on *E. coli* RNA Pol resulted in the observation of long pauses attributed to backtracking [46, 52]. Backtracking involves backwards diffusion of RNA Pol on its template while part of the mRNA is extruded, and it is facilitated by nucleotide misincorporation [46]. However, studies of *E. coli* RNA Pol disagree on the relative contribution of backtracking pauses versus exponentially distributed pauses [46, 47, 49]. To obtain a unified model of *E. coli* RNA Pol elongation, it will be necessary to address the fact that the lifetime of the shortest pauses is comparable to the typical bandwidth of optical tweezers (both are 1 second): either the experimental spatiotemporal resolution must be further increased, or more accurate analysis methods that can reliably distinguish pauses from elongation steps must be implemented. In both cases, increasing the size of data sets collected by single-molecule experiments will permit more stringent tests of different models [48, 53, 54].

Follow-up *in vitro* studies with optical tweezers have further investigated backtracking: for instance, transcription factors GreA and GreB, which cleave the protruding mRNA strand, were found to rescue backtracked RNA Pol [46], suggesting a possible proofreading mechanism. Additionally, the role of backtracking in the dynamics of eukaryotic polymerases has been investigated: work on RNA Pol II showed that its pause dynamics are dominated by backtracking to the extent that RNA Pol II cannot overcome forces beyond 8.5 pN [47]. Interestingly, the addition of TFIIS (a eukaryotic transcription factor that acts similarly to GreA and GreB) rescued backtracked RNA Pol II and permitted it to overcome forces of up to 16.5 pN. Finally, it has been shown that RNA Pol II backtracking becomes more likely in the vicinity of a roadblock such as a nucleosome [55] and that overcoming such a barrier requires the aid of thermal fluctuations. It is expected that the application of these *in vitro* single-molecule techniques will continue to shed light on the mechanistic details of how RNA Pol progresses in conjunction with the other factors involved in transcription.

To see whether similarly rich dynamics of RNA Pol occur *in vivo*, the dynamics of RNA Pol II in mammalian cells were studied by fluorescently labelling RNA Pol II and simultaneously monitoring an mRNA stem-loop that is specifically recognized by a GFP-labelled protein [56]. Using this approach, the authors observed that the rate-limiting step in transcription is the transition between initiation and elongation (RNA Pol II transcribed the complete gene in only one-ninetieth of cases) and that transcription is interrupted by long pauses that are probably related to backtracking. Although these long pauses are rare (only 4.2% of the polymerases are affected), they nonetheless have a substantial impact, as their cumulative duration can be to halve the total elongation time. Curiously, the pause-free elongation speed observed *in vivo* (~ 70 bp/s after the long pauses have been removed) was substantially higher than the corresponding value observed by *in vitro* (~ 15 bp/s). Whether this can be attributed to a lack of assisting transcription factors in *in vitro* assays or to the reduced temporal resolution of the *in vivo* experiments remains to be determined. Nonetheless, the *in vitro* and *in vivo* approaches yield complementary insights that are relevant for our understanding of this complex enzyme.

2.3.3. TERMINATION

Optical tweezers have been useful for studying the different pathways underlying the termination of transcription [42]. By applying a force directly to the mRNA transcript generated by *E. coli* RNA Pol (Figure 2.3Cb), it was possible to investigate the efficiency of termination for various termination sequences that encoded mRNA hairpins. Using this approach, it was determined that destabilization of the mRNA-DNA hybrid may be induced by a shearing mechanism induced by the hairpin. The degree of shearing, and hence the efficiency of termination, could be enhanced by shortening the hybrid, whereas it could be decreased through the presence of additional secondary structures that interfered with proper folding of the hairpin. However, we note that this result contradicts the results of a previous biochemical study [57] that suggested that the elongation complex is destabilized by the melting of 2 or 3 nucleotides upstream of the mRNA-DNA hybrid in the absence of any shearing. Further studies under applied loads may remain necessary to distinguish between these two models.

Thus, we see that optical tweezers can probe the activity of RNA Pol by using an application of force to perturb its local energy landscape, and smFRET studies report on the kinetics of molecular conformational changes. Integration of the two approaches is likely to be able to determine whether pausing is predominantly a template-related process or whether it is a direct consequence of conformational changes in the enzyme. Future efforts to unravel the dynamics of co-transcriptional phenomena such as translation or splicing warrant further application of single-molecule techniques.

2.4. TRANSLATION

Single-molecule approaches are useful for the study of movements within molecular complexes, as demonstrated by studies of structural changes in the *E. coli* ribosome. These structural rearrangements involve motions on a size scale that is perfectly suited to smFRET measurement [58], and this approach adds dynamic information to the structural snapshots deduced by X-ray crystallography or cryoelectron microscopy (cryo-EM). In addition, insights into the interaction of the *E. coli* ribosome with mRNA during elongation have been obtained using optical tweezers.

2.4.1. INITIATION AND ELONGATION

To demonstrate how smFRET has enhanced our understanding of the motion of ribosomal subunits, we consider the results from three separate studies. In the first study [59], the two subunits of the *E. coli* ribosome (namely, 50S and 30S) were labelled with donor and acceptor dyes, respectively, and their interaction with initiation factor IF2 was studied. It was found that the association of the large subunit with the pre-initiation complex could be accelerated by IF2 by a factor of four. The authors determined that IF2 subsequently hydrolyses a single GTP to align the 30S subunit with the 50S subunit by rotating it with respect to the 50S. This rotation brings the ribosome into the elongation state. A related study [60] showed that this anticlockwise rotation did not require the presence of elongation factor G (EF-G), which supplies the necessary energy for ribosome translocation via GTP hydrolysis. The rotation itself is thermally driven, but it is stabilized in a pre-translocation (that is, rotated or ’unlocked’) state by EF-G binding after peptide bond formation. Subsequent GTP hydrolysis by EF-G propels the ribosome into the ’locked’ (non-rotated) state to drive ribosome translocation. A third smFRET experiment then demonstrated multiple cycles of high-to-low FRET efficiency in a single trace [61], reflecting the successive anticlockwise rotations of the 30S subunit with respect to the 50S subunit required to incorporate multiple amino acids (Figure 2.4a). These observations are in accordance with structural information from cryo-EM studies and with additional smFRET studies that used the fluctuations in the positions of labelled tRNA within the ribosome as their readout [62].

The direct observation of translocation by the ribosomal molecular motor during elongation has been a longstanding challenge. It was overcome by using an optical tweezers assay that exploited the ability of the *E. coli* ribosome to unwind mRNA hairpins [63] (Figure 2.4b), and it demonstrated that the elongation velocity is strongly influenced by the stability of the mRNA secondary structure. More recent investigations by the same group using hairpins with a differing GC content showed that the ribosome uses two distinct mechanisms: interaction of ribosomal proteins S3 and S4 with the mRNA backbone opens weak secondary structures, whereas a lever mechanism involving a tRNA-mRNA interaction and GTP hydrolysis (supplied by EF-G) opens strong secondary structures, as previously suggested by cryo-EM studies [64]. Detailed knowledge of the unwinding mechanism of the ribosome is important in the context of ribosomal frame shifting, in which interactions between the ribosome and particular mRNA sequences shift the mRNA reading frame by a single nucleotide. Investigation of frame shifting will thus provide a natural follow-up to these studies.

Recently, it has become possible to observe ribosomal elongation by fluorescence detection, using zero-mode waveguides (ZMWs) (Figure 2.2a) to detect individual labelled tRNAs or individual labelled amino acids above background fluorescence at physiological concentration [65]. Using this approach, the *E. coli* ribosome was tethered at the bottom of the ZMW by an mRNA template [66], and three different tRNAs (namely, lysine-tRNA, phenylalanine-tRNA and N-formylmethionine-tRNA) were labelled with different colours. Because a ribosome must contain the tRNAfMet to enter elongation, detection of its associated colour could identify tethered ribosomes in the ZMW. Subsequent incorporation of the other two labelled amino acids was then monitored by measuring the dwell times of tRNAs in the ribosome for a total of 12 amino acid incorporation events. Interestingly, the authors observed that the ribosomal A and E sites almost never simultaneously contain a tRNA: most frequently, only the A and P sites contain tRNAs, as the exit of a tRNA from the ribosome occurs rapidly after translocation has taken place [67]. Future studies could use the ZMW approach together with labelled tRNA to observe more complex tRNA dynamics: for example, during frame shifting or in the presence of high concentrations of acylated tRNAs.

2.4.2. TERMINATION AND PROTEIN FOLDING

Translation termination is a multi-step process involving numerous factors for which the dynamics have been studied using smFRET. Such experiments have provided detailed

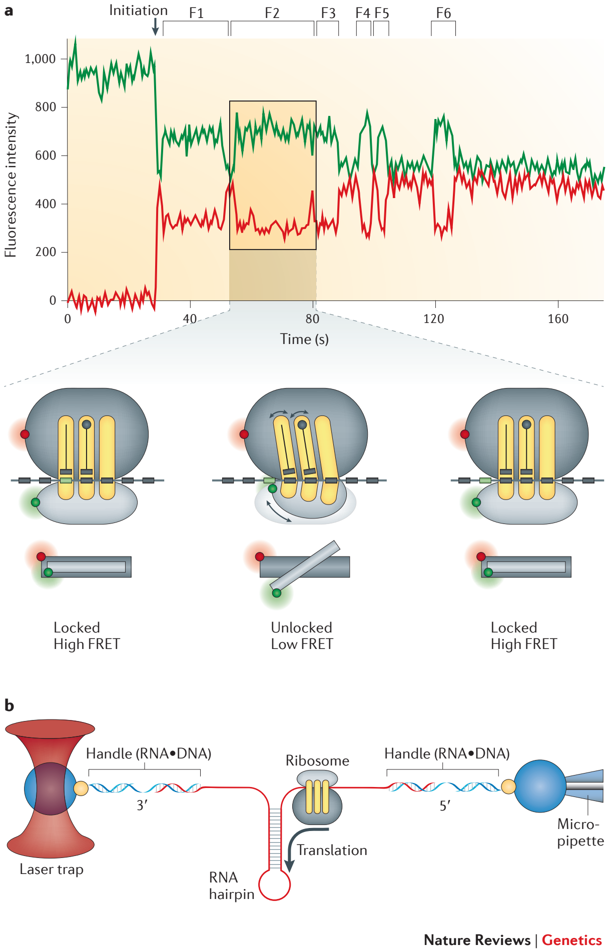

Figure 2.4: Studies of the ribosome and translation at the single-molecule level. (a) Study of the dynamics of the ribosomal subunits over multiple elongation cycles. The two ribosomal subunits are labelled with dyes for single-molecule Förster (fluorescence) resonance energy transfer (smFRET; small subunit labelled with donor, green circle; large subunit labelled with acceptor, red circle), as shown in the inset. A high signal in the green trace implies an increased distance between the dyes, and a high signal in the red trace implies a decreased distance. At the start of the experiment, the labelled 30S subunit is bound to the tethered mRNA, and the labelled 50S subunit is flushed into the flow cell. At t ~ 30 s, initiation is clearly visible by the first appearance of a signal from the acceptor dye (red trace). At each step of the elongation cycle, the rotation of the large subunit with respect to the small subunit was monitored, represented by the signal of the donor (green trace) and the acceptor (red trace). The accompanying mechanical motions within the ribosome are depicted in the inset from two perspectives: a side view showing the tRNA translocation and a bottom view in which subunit rotation is visible. The three yellow slots represent (from right to left) the ribosomal A, P and E sites. (b) A schematic of a force spectroscopy study of ribosome translation dynamics. Here, the ribosome unwinds and translates an mRNA hairpin held at its extremities by two beads, one of which is maintained in an optical trap. Panel (a) is modified, with permission, from Ref. [61] © (2008) Macmillan Publishers Ltd. Panel (b) is modified, with permission, from Ref. [63] ©Macmillan Publishers Ltd. All rights reserved.

mechanistic insights into the association of release factors with the *E. coli* ribosome and into the specific position of the large ribosomal subunit with respect to the small subunit at each step of termination [68]. The influence of the ribosome on protein folding has also been the subject of a recent single-molecule study [69]. To study protein folding in the presence of the *E. coli* ribosome, the authors attached the ribosome to a bead held in a micropipette (Figure 2.1d). In the presence of an *in vitro* translation system, this ribosome synthesized T4 lysozyme, which was then coupled to an optically trapped bead via a DNA handle. By comparing the observed folding pathway to identical experiments carried out in the absence of the ribosome, the influence of the ribosome on the folding pathway was assessed. Interestingly, although the presence of the ribosome reduced both the overall rate (down by more than 100-fold) and the overall yield of folded lysozyme (down nearly fourfold), the lysozymes that did fold assumed a more compact form. Thus, the authors concluded that the ribosome acts as a chaperone that slowly guides the proteins into properly folded structures.

2.4.3. SPLICING AND EXPORT

In eukaryotes, many RNAs need to be exported out of the nucleus: for example, for translation in the cytoplasm. Single-molecule studies have begun to reveal properties of transport through the nuclear pore complex in permeabilized cells [70–72] and of the individual nucleoporins *in vitro* [73, 74]. For example, a two-colour super-registration microscopy approach was used to track mRNA transport *in vivo* [75] (Figure 2.5a). Interesting observations included the finding that individual mRNA molecules often scan multiple pores before being exported and that not all nuclear pore complexes (NPCs) are equally active in mRNA export. The authors were able directly to observe individual mRNAs being exported from the nucleus and to propose a kinetic model for export that suggests that docking to and release from the NPC, rather than transport through the central channel, are the rate-limiting steps [75].

Several single-molecule studies of splicing, including of self-splicing introns, have used purified components and have revealed the dynamics of individual steps in splicing [77, 78]. In a recent study, individual spliceosomal subcomplexes were labelled in yeast whole-cell extract with different organic dyes, and using multicolour TIRF microscopy [76] (Figure 2.2), the authors studied their assembly on fluorescently labelled, surface immobilized precursor mRNA (pre-mRNA) constructs (Figure 2.5b). They were able to deduce the order and kinetics of spliceosome assembly and found that the assembly steps are reversible and that the assembly rates of the different components are similar, such that no particular step is strongly rate-limiting. In the future, single-molecule methods have great potential to reveal further details of the various splicing pathways, including alternative splicing [79, 80].

Nuclear export and splicing both involve very large (>MDa) and complex protein or nucleoprotein assemblies (namely, the NPC and the spliceosome, respectively) that pose substantial challenges to traditional high-resolution structure techniques and bulk biochemical assays. Overcoming these challenges and resolving the dynamics of these complex mechanochemical machines will continue to require new experimental approaches at the single-molecule level.

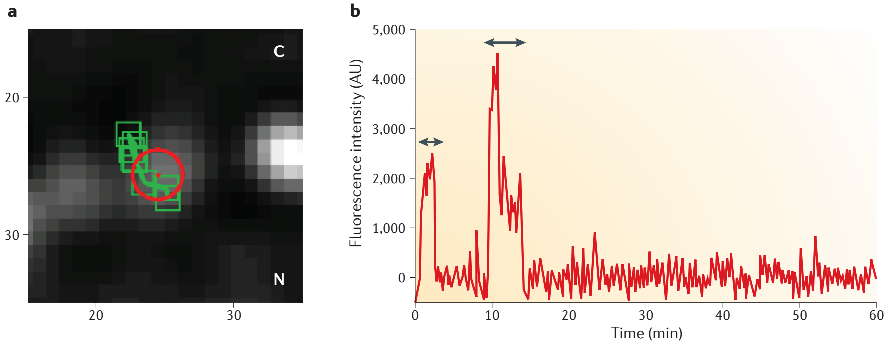

Nature Reviews | Genetics

Figure 2.5: Observations of nuclear export and splicing at the single-molecule level. (a) Following mRNA export from the nucleus by super-registration microscopy. Tracked positions of β-actin mRNA labelled by multiple copies of YFP fused to a MS2 protein tag (in green) overlaid on the position of the nuclear pore complex (NPC) scaffold protein POM121 labelled with tandem Tomato fluorescent protein (in red). 'N' denotes the nucleus, and 'C' denotes the cytoplasm. Axes are in pixel units, and each pixel represents 64 nm. (b) Ordered and dynamic assembly of spliceosomes. Shown here is a single-molecule fluorescence trace of labelled spliceosome subcomplexes U1. The trace reveals multiple binding and dissociation events to precursor mRNA that was colocalized (not shown), suggesting reversible binding. The arrows indicate the duration of binding events that can be analysed to determine the lifetimes. Similar traces were obtained for U2, U5 and the multiprotein Prp19 complex. Panel (a) is modified, with permission, from Ref. [75] © (2010) Macmillan Publishers Ltd. All rights reserved. Panel (b) is modified, with permission, from Ref. [76] © (2011) American Association for the Advancement of Science.

2.5. REPLICATION

The different enzymes that act in concert to carry out DNA synthesis are collectively known as the replisome [81–83]. The architectural complexity of the replisome varies and encompasses four different proteins in bacteriophage T7 (Ref. [84]), eight proteins in bacteriophage T4 (Ref. [84]), twelve in *E. coli* [85] and even more in eukaryotes [85]. Our understanding of replisome dynamics has benefited from studies at the single-molecule level. *In vitro*, it has been possible to investigate the motor activity of individual polymerases [86] or individual helicases [87–89] using magnetic or optical tweezers (Figure 2.1). In a recent study [90], a combination of fluorescence spectroscopy together with optical trapping was used to investigate the polymerization of single-strand binding protein (SSB), which has a key role in lagging strand replication. More recently, it has also become possible to study the activity of complete replisomes *in vitro* at the single-molecule level, relying on either direct reconstitution (for phage T4 (Ref. [91]), phage T7 (Ref. [92]) and *E. coli* [93]) or the use of cell extracts (for eukaryotic systems [94]). Such studies of complete biological complexes should facilitate comparison with *in vivo* experiments.

2.5.1. REPLICATION DYNAMICS

To show how *in vitro* single-molecule assays can be used to probe the dynamics of replication, we briefly describe three recent studies that have focused on the interplay between helicase activity and primase activity. During replication, new primers need to be continuously synthesized to generate Okazaki fragments. The ssDNA template used for priming is formed by the helicase as it unwinds duplex DNA. However, the primase synthesizes RNA primers in the opposite direction to fork progression. Three possible ways to coordinate this process have been suggested: pausing (which would lead to a cessation of unwinding); DNA looping (which would result from continued synthesis by both helicase and primase while they remain associated); and disassembly (in which primase and helicase dissociate from one another). A short DNA hairpin tethered in magnetic tweezers was used to investigate these models for the T4 primosome, in which the helicase and primase are thought to associate. For a given applied force, changes in the length of the DNA molecule provide information about changes in its conformation caused by the primosome complex. It was found that the T4 primosome uses both the disassembly and DNA looping mechanisms and has a preference for the latter in the context of a full replisome (Figure 2.6A). Two other studies, which investigated priming dynamics for the T7 replisome, used a flow-stretching assay [92] and smFRET [95], respectively. These studies revealed partially conflicting results. The flow-stretching assay study indicated that the primase slows down leading-strand synthesis sufficiently to allow lagging-strand synthesis to keep up. However, the smFRET study concluded that the leading strand T7 replisome did not pause (in contrast to the observations in the flow-stretching assay study), that the leading strand synthesis is slower than the lagging strand synthesis, and that priming loops are formed on the lagging strand.

2.5.2. REPLISOME STOICHIOMETRY

Both *in vitro* and *in vivo* single-molecule studies have recently shed new light on replisome stoichiometry. In a study using purified proteins [97], it was proposed that the DNA Pol III holoenzyme contains three DNA Pol III cores - this was in contrast to earlier models that suggested there were only two (bound at the leading and lagging strands, respectively) [98]. Relying on the ability to localize individual DNA-bound fluorescent proteins inside living cells [99] (Figure 2.2), ten different components of the replisome were fluorescently labelled in separate *E. coli* strains [96] (Figure 2.6Ba). Analysis of the number of bleaching events (whereby each event is generated by a single labelled molecule) and their intensities allows determination of the number of molecules that are present within a diffraction-limited spot (Figure 2.6Bb), and this enabled the authors to conclude that the *E. coli* replisome contains three DNA Pol III cores. More recent *in vivo* work has confirmed the observation of three DNA Pol III cores, with the caveat that the binding of the third polymerase appeared to be transient [100]. A potential function for a third polymerase was investigated by using a single-molecule flow-stretching assay (Figure 2.1d) together with a bulk bead-based assay [101]. The authors observed that a tripolymerase (tri-DNA Pol) replisome is more efficient at lagging-strand synthesis than its dipolymerase (di-DNA Pol) counterpart (ssDNA gaps were observed in the di-DNA Pol case) and that it also displays increased processivity. That is, the DNA fragments generated by the tri-DNA Pol were nearly twice as long as those from the di-DNA Pol. From

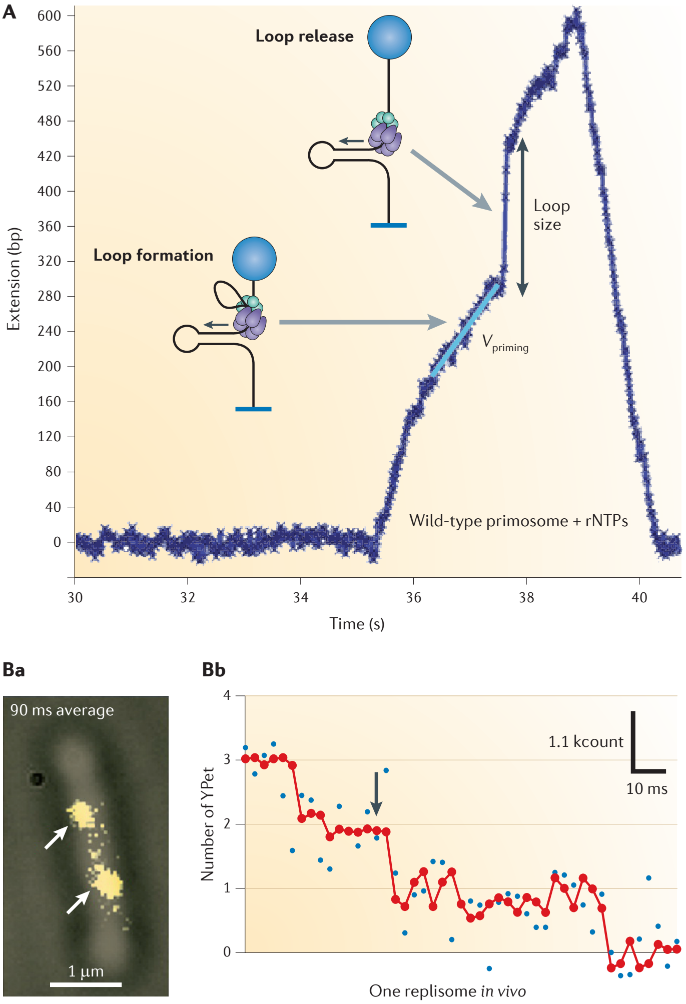

Nature Reviews | Genetics

Figure 2.6: Replisome architecture and dynamics. (A) Looping of DNA during primer synthesis and unwinding. Here, an experimental trace is shown from which the priming velocity and loop size can be inferred. A magnetic tweezer is used, and the changes in DNA length are measured. (B) Stoichiometry of replisome components. (Ba) An overlay of bright-field (grey) and fluorescence images (yellow) of an *E. coli* strain with one of the replisome components fluorescently labelled. (Bb) Photobleaching traces of fluorescent proteins in living *E. coli* indicating the presence of a single replisome. The arrow indicates 45 ms. rNTP, ribonucleotide triphosphate. V priming, unwinding velocity during primer synthesis. Panel (A) is modified, with permission, from ref. [87] © (2009) Macmillan Publishers Ltd. All rights reserved. Panel (A) is modified, with permission, from ref. [96] © (2010) American Association for the Advancement of Science.

these *in vivo* and *in vitro* data, the presence of a third polymerase seems plausible, but further investigations are necessary to exclude other models and to determine the exact role of such a third polymerase *in vivo* [102].

2.6. CHALLENGES AND FUTURE DIRECTIONS

What are the most interesting challenges that remain in our understanding of genomic processes? And how will single-molecule techniques continue to contribute to them? Will some single-molecule techniques become as commonplace as gel electrophoresis?

2.6.1. CHALLENGES IN MOLECULAR MECHANISMS

Many challenges remain in understanding genome processing at the molecular level. For example, although many molecular processes studied using single-molecule force spectroscopy have involved the motion of molecular motors along a linear template, the double-stranded helical nature of DNA also means that there are important roles for rotary motion. For example, the unwinding activity of replisomes or RNA Pol proteins generates torsional stress in the DNA template, and sometimes this may not be dissipated sufficiently rapidly by topoisomerases (reviewed in Ref. [103]). By analogy to the way in which force-velocity relationships have shed light on the mechanochemistry of linear motion, the measurement of torque-angular velocity relations can be used to investigate the mechanochemistry of rotary motion for polymerases, helicases and other genome-processing enzymes. Such investigations will be facilitated by the recent introduction of measurement techniques that report on torque and twist, such as magnetic torque tweezers [19, 104–107].

A separate challenge at the molecular level is to understand how the conformational dynamics of a molecular motor are linked to any physical displacement it executes along a DNA or RNA track. Single-molecule fluorescence techniques such as FRET (Figure 2.2) are ideal for the study of the nanometre-scale conformational changes that proteins undergo. To correlate these (internal) changes with physical displacement along the track of the motor, a feasible approach is the integration of fluorescence spectroscopy with force spectroscopy. Initial efforts along these lines have been published [108–110]. In addition to monitoring the conformational changes of an enzyme during translocation along a DNA track, such approaches could concurrently investigate the coordination of ATP hydrolysis.

2.6.2. INCREASING COMPLEXITY

An ongoing challenge is to apply *in vitro* single-molecule techniques to increasingly complex biological systems. As well as investigating single molecular motors in isolation, motors can be studied as a part of reconstituted protein complexes, as in the case of DNA replication. Alternatively, the interplay between different types of molecular motors could be studied, as in the coordination between transcription and translation. The influence of more complex substrates (such as chromatin) and their influence on genomic processing is another interesting challenge. A possible approach is to examine protein activity in cell extracts, [76, 94, 111], whereby the proteins of interest will have the appropriate post-translational modifications and native binding partners. However, technical challenges, such as unwanted fluorescence background or unwanted adsorption will need to be overcome. An alternative approach towards studying protein assemblies consists of purifying molecular complexes by immunoprecipitation and selectively adsorbing them onto surfaces for *in vitro* analysis [112, 113]. This could improve understanding of molecular assemblies, such as the RNA-induced silencing complex (RISC) and proteins grouped onto telomeres.

Single-molecule techniques could also be harnessed to investigate genome processing over a much wider range of sequences than would typically be considered, potentially up to full genomic coverage. At present, this is the case for single-molecule DNA sequencing, in which genome sequences are determined by single-molecule fluorescence measurements of a large number of genome segments in parallel. Potentially, different parts of the genome could be interrogated at the single-molecule level to ascertain details such as their mechanical properties, transcription efficiency and transcription dynamics through single-molecule force spectroscopy or single-molecule fluorescence, or a combination thereof. These investigations and those of more complex biological systems discussed in the previous paragraph benefit from increased parallelization of single-molecule readouts. In certain approaches, such as TIRF microscopy, parallel readout is already the standard approach, but in other approaches, such as magnetic tweezers, it has only recently become more widely available [114].

2.6.3. STUDIES OF LIVING CELLS

Given that genomic processing in its full complexity occurs in the context of living cells, the ultimate goal is to observe and to manipulate molecular processes *in vivo* at high spatial and temporal resolution. To demonstrate some of the possibilities, Figure 2.7 depicts a range of genomic interactions that take place in and around the nucleus of a eukaryotic cell together with ways in which they might be probed using single-molecule methods. The DNA itself has an overall architecture that depends on the state of the cell cycle; a rapid and detailed series of snapshots of the entire architecture would be of great interest to facilitate understanding of, for example, the influence of architecture on transcriptional patterns. Already, fluorescence spectroscopy has been used for spatial calibration of chromosome capture data to aid mapping of the three-dimensional architecture of the Caulobacter crescentus genome [115]. Super-resolution microscopy has made it possible to resolve the architecture of the bacterial genome in fixed cells to better than 100 nm [116], and there will no doubt be further improvements. It could also be of interest to monitor local stress and strain in DNA intracellularly; a FRET sensor integrated into the DNA could potentially fulfill such a role.

Of similar importance is the monitoring of RNA and proteins *in vivo*. RNA is typically visualized by fluorescence in situ hybridization (FISH), which can be carried out at the single-molecule level [117] or by detection of RNA-bound proteins [118]. However, a recent interesting development is the generation of genetically encodable RNA aptamers that can directly bind fluorescent dyes [119]. Building on the ability to image protein dynamics intracellularly at the single-molecule level, multicolour imaging of different proteins could potentially reveal the dynamics of network interactions. For example, recent work has made it possible to image DNA-binding proteins in the bacterial nucleoid at a high resolution [120, 121]. A similar approach could help to elucidate chromatin structure in live cells: for example, by labelling histone proteins. However, for *in vivo* imaging in particular, an ongoing challenge is to improve the ease and specificity of introducing fluorescent labels and to enhance their photon yield [122].

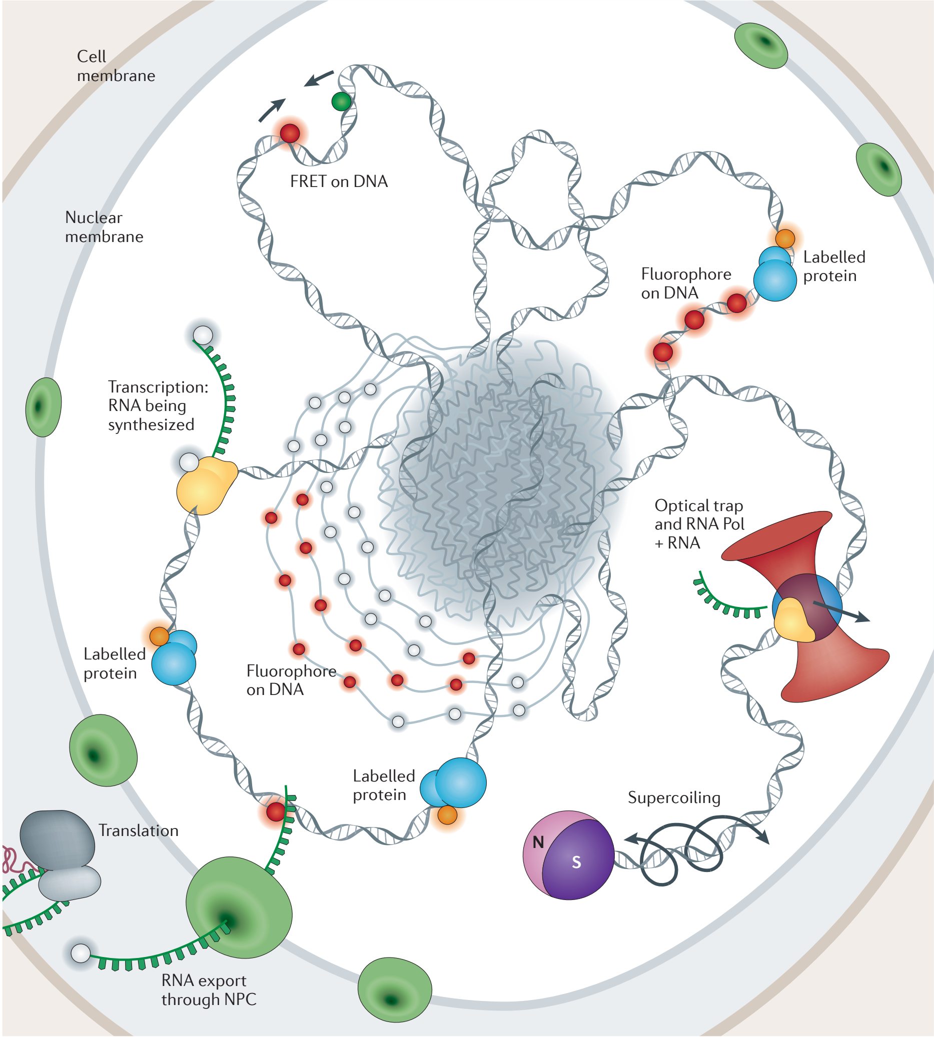

Nature Reviews | Genetics

Figure 2.7: Genome processing taking place inside a cell nucleus and potential ways of monitoring it at the single-molecule level. A schematic view (not to scale) inside the nucleus showing DNA in various stages of condensation being acted on by molecular motors, such as RNA polymerase (RNA Pol) and the replisome, and various potential ways of probing the genome, as well as processing of the genome by single-molecule techniques. FRET, Förster (fluorescence) resonance energy transfer; NPC, nuclear pore complex.

Another area for development is monitoring and applying forces or torques within the cell (Figure 2.7). To date, force measurements on living cells have typically focused on the forces exerted by structures that execute large-scale motion - such as the filopodia involved in cell migration [123] - which allows measurement to be carried out using atomic force microscopy [124] or the deflection of microfabricated pillars[125–127]. Intracellular force measurements are more challenging [128, 129] but can be achieved through the introduction of micron- or submicron-sized particles [130, 131] or careful design of calibrated fluorescent probes [132–134]. In the future, more mature versions of these approaches might be applied to genome-processing events. Finally, it will be very interesting to monitor the extent to which genome processing is sensitive to external mechanical perturbations [135]; this could be examined using a combination of mechanical manipulation through single-molecule force spectroscopy and intra-nuclear readout through fluorescence imaging.

Ultimately, our understanding of the genome and its processing will rely on input from both *in vitro* and *in vivo* techniques and from many fields: biology, bioinformatics, chemistry, physics, engineering, nanoscience and nanotechnology, to name a few. Merging such knowledge into an understanding of cellular function will occupy us for decades to come.

CONTRIBUTIONS

D.D., J.L., M.C.M. and N.H.D. wrote the review. M.C.M. focused on the sections related to fluorescence microscopy and DNA replication.

ACKNOWLEDGMENTS

This work was supported by the European Science Foundation through a European Young Investigators (EURYI) grant to N.H.D. and by the Netherlands Organisation for Scientific Research through grants to N.H.D. and J.L. We thank anonymous referees for useful feedback and D. Grünwald for a critical reading of the manuscript. J. Kerssemakers is thanked for the visual layout of Figure 2.7. We acknowledge the many research efforts by groups in the field of genome processing and regret that owing to space limitations it was not possible to cite a larger number of high-quality works.

REFERENCES

[1] C. S. Pareek, R. Smoczynski, and A. Tretyn, *Sequencing technologies and genome sequencing,* Journal of applied genetics **52**, 413 (2011).

[2] A. L. Forget and S. C. Kowalczykowski, *Single-molecule imaging brings Rad51 nucleoprotein filaments into focus.* Trends in Cell Biology **20**, 269 (2010).

[3] I. J. Finkelstein and E. C. Greene, *Single molecule studies of homologous recombination,* Molecular Biosystems **4**, 1094 (2008).

[4] J. Vinograd, J. Lebowitz, and R. Radloff, *The twisted circular form of polyoma viral DNA.* Proceedings Of The National Academy Of Sciences Of The United States Of America **53**, 1104 (1965).

[5] E. D. Sebring, T. J. Kelly, M. M. Thoren, and N. P. Salzman, *Structure of replicating simian virus 40 deoxyribonucleic acid molecules.* Journal of virology **8**, 478 (1971).

[6] E. A. Ostrander, P. Benedetti, and J. C. Wang, *Template supercoiling by a chimera of yeast GAL4 protein and phage T7 RNA polymerase.* Science (New York, NY) **249**, 1261 (1990).

[7] B. Sakmann and E. Neher, *Patch clamp techniques for studying ionic channels in excitable membranes.* Annual Review of Physiology **46**, 455 (1984).

[8] M. Orrit and J. Bernard, *Single pentacene molecules detected by fluorescence excitation in a p-terphenyl crystal,* Physical review letters **65**, 2716 (1990).

[9] E. Betzig and R. J. Chichester, *Single molecules observed by near-field scanning optical microscopy.* Science (New York, NY) **262**, 1422 (1993).

[10] M. Chalfie, Y. Tu, G. Euskirchen, W. W. Ward, and D. C. Prasher, *Green fluorescent protein as a marker for gene expression,* Science (New York, NY) **263**, 802 (1994).

[11] M. D. Wang, M. J. Schnitzer, H. Yin, R. Landick, J. Gelles, and S. M. Block, *Force and velocity measured for single molecules of RNA polymerase.* Science (New York, NY) **282**, 902 (1998).

[12] D. Dutta, K. Shatalin, V. Epshtein, M. E. Gottesman, and E. Nudler, *Linking RNA polymerase backtracking to genome instability in E. coli.* Cell **146**, 533 (2011).

[13] D. A. Koster, V. Croquette, C. Dekker, S. Shuman, and N. H. Dekker, *Friction and torque govern the relaxation of DNA supercoils by eukaryotic topoisomerase IB.* Nature **434**, 671 (2005).

[14] V. Bormuth, V. Varga, J. Howard, and E. Schäffer, *Protein friction limits diffusive and directed movements of kinesin motors on microtubules.* Science (New York, NY) **325**, 870 (2009).

[15] C. Bustamante, Z. Bryant, and S. B. Smith, *Ten years of tension: single-molecule DNA mechanics.* Nature **421**, 423 (2003).

[16] W. J. Greenleaf, M. T. Woodside, and S. M. Block, *High-resolution, single-molecule measurements of biomolecular motion.* Annual review of biophysics and biomolecular structure **36**, 171 (2007).

[17] K. C. Neuman and A. Nagy, *Single-molecule force spectroscopy: optical tweezers, magnetic tweezers and atomic force microscopy.* Nature Methods **5**, 491 (2008).

[18] J. Lipfert, X. Hao, and N. H. Dekker, *Quantitative modeling and optimization of magnetic tweezers.* Biophysical Journal **96**, 5040 (2009).

[19] J. Lipfert, J. W. J. Kerssemakers, T. Jager, and N. H. Dekker, *Magnetic torque tweez-*

ers: measuring torsional stiffness in DNA and RecA-DNA filaments. Nature Methods **7**, 977 (2010).

[20] T. R. Strick, J. F. Allemand, D. Bensimon, A. Bensimon, and V. Croquette, *The elasticity of a single supercoiled DNA molecule.* Science (New York, NY) **271**, 1835 (1996).

[21] A. M. van Oijen and J. J. Loparo, *Single-molecule studies of the replisome,* Annual Review Of Biophysics **39**, 429 (2010).

[22] H. J. Butt, B. Cappella, and M. Kappl, *Force measurements with the atomic force microscope: Technique, interpretation and applications,* Surface science reports **59**, 1 (2005).

[23] K. Svoboda and S. M. Block, *Biological applications of optical forces,* Annual Review of Biophysics and Biomolecular Structure **23**, 247 (1994).

[24] J. R. Moffitt, Y. R. Chemla, S. B. Smith, and C. Bustamante, *Recent advances in optical tweezers,* Anual Review Biochemistry **77**, 205 (2008).

[25] W. J. Greenleaf, M. T. Woodside, and E. A. Abbondanzieri, *Passive all-optical force clamp for high-resolution laser trapping,* Physical Review Letters **95**, 208102 (2005).

[26] K. van Aelst, J. Tóth, S. P. Ramanathan, F. W. Schwarz, R. Seidel, and M. D. Szczelkun, *Type III restriction enzymes cleave DNA by long-range interaction between sites in both head-to-head and tail-to-tail inverted repeat.* Proceedings Of The National Academy Of Sciences Of The United States Of America **107**, 9123 (2010).

[27] E. L. Snapp, *Fluorescent proteins: a cell biologist's user guide.* Trends in Cell Biology **19**, 649 (2009).

[28] S. P. Ramanathan, K. van Aelst, A. Sears, L. J. Peakman, F. M. Diffin, M. D. Szczelkun, and R. Seidel, *Type III restriction enzymes communicate in 1D without looping between their target sites.* Proceedings Of The National Academy Of Sciences Of The United States Of America **106**, 1748 (2009).

[29] D. Axelrod, *Total internal reflection fluorescence microscopy in cell biology,* Traffic **2**, 764 (2001).

[30] R. E. Thompson, D. R. Larson, and W. W. Webb, *Precise nanometer localization analysis for individual fluorescent probes.* Biophysj **82**, 2775 (2002).

[31] S. Ram, E. S. Ward, and R. J. Ober, *Beyond Rayleigh's criterion: a resolution measure with application to single-molecule microscopy.* Proceedings Of The National Academy Of Sciences Of The United States Of America **103**, 4457 (2006).

[32] C. S. Smith, N. Joseph, B. Rieger, and K. A. Lidke, *Fast, single-molecule localization that achieves theoretically minimum uncertainty.* Nature Methods **7**, 373 (2010).

[33] K. I. Mortensen, L. S. Churchman, J. A. Spudich, and H. Flyvbjerg, *Optimized localization analysis for single-molecule tracking and super-resolution microscopy,* Nature Methods **7**, 377 (2010).

[34] S. W. Hell, *Microscopy and its focal switch,* Nature Methods **6**, 24 (2009).

[35] G. Patterson, M. Davidson, S. Manley, and J. Lippincott-Schwartz, *Superresolution Imaging using Single-Molecule Localization,* Annual review of physical chemistry **61**, 345 (2010).

[36] A. N. Kapanidis, E. Margeat, S. O. Ho, E. Kortkhonjia, S. Weiss, and R. H. Ebright, *Initial transcription by RNA polymerase proceeds through a DNA-scrunching mechanism.* Science (New York, NY) **314**, 1144 (2006).

[37] L.-C. Tu and S. M. Musser, *Single molecule studies of nucleocytoplasmic transport.* Biochimica et biophysica acta **1813**, 1607 (2011).

[38] D. A. Schafer, J. Gelles, M. P. Sheetz, and R. Landick, *Transcription by single molecules of RNA polymerase observed by light microscopy.* Nature **352**, 444 (1991).

[39] L. J. Friedman and J. Gelles, *Mechanism of transcription initiation at an activator-dependent promoter defined by single-molecule observation.* Cell **148**, 679 (2012).

[40] A. Revyakin, C. Liu, R. H. Ebright, and T. R. Strick, *Abortive initiation and productive initiation by RNA polymerase involve DNA scrunching.* Science (New York, NY) **314**, 1139 (2006).

[41] B. Treutlein, A. Muschielok, J. Andrecka, A. Jawhari, C. Buchen, D. Kostrewa, F. Hög, P. Cramer, and J. Michaelis, *Dynamic architecture of a minimal RNA polymerase II open promoter complex.* Molecular Cell **46**, 136 (2012).

[42] M. H. Larson, W. J. Greenleaf, R. Landick, and S. M. Block, *Applied force reveals mechanistic and energetic details of transcription termination,* Cell **132**, 971 (2008).

[43] E. A. Abbondanzieri, W. J. Greenleaf, J. W. Shaevitz, R. Landick, and S. M. Block, *Direct observation of base-pair stepping by RNA polymerase.* Nature **438**, 460 (2005).

[44] K. C. Neuman, E. A. Abbondanzieri, R. Landick, J. Gelles, and S. M. Block, *Ubiquitous transcriptional pausing is independent of RNA polymerase backtracking.* Cell **115**, 437 (2003).

[45] K. M. Herbert, A. La Porta, B. J. Wong, R. A. Mooney, K. C. Neuman, R. Landick, and S. M. Block, *Sequence-resolved detection of pausing by single RNA polymerase molecules.* Cell **125**, 1083 (2006).

[46] J. W. Shaevitz, E. A. Abbondanzieri, R. Landick, and S. M. Block, *Backtracking by single RNA polymerase molecules observed at near-base-pair resolution,* NATURE CELL BIOLOGY **426**, 684 (2003).

[47] E. A. Galburt, S. W. Grill, A. Wiedmann, L. Lubkowska, J. Choy, E. Nogales, M. Kashlev, and C. Bustamante, *Backtracking determines the force sensitivity of RNAP II in a factor-dependent manner.* Nature **446**, 820 (2007).

[48] M. Depken, E. A. Galburt, and S. W. Grill, *The origin of short transcriptional pauses,* Biophysical Journal **96**, 2189 (2009).

[49] Y. X. Mejia, H. Mao, N. R. Forde, and C. Bustamante, *Thermal probing of E. coli RNA polymerase off-pathway mechanisms.* Journal of Molecular Biology **382**, 628 (2008).

[50] J. Zhou, K. S. Ha, A. La Porta, R. Landick, and S. M. Block, *Applied force provides insight into transcriptional pausing and its modulation by transcription factor NusA.* Molecular Cell **44**, 635 (2011).

[51] K. M. Herbert, J. Zhou, R. A. Mooney, and A. L. Porta, *E. coli NusG Inhibits Backtracking and Accelerates Pause-Free Transcription by Promoting Forward Translocation of RNA Polymerase,* Journal of Molecular Biology **28**, 17 (2010).

[52] R. V. Dalal, M. H. Larson, K. C. Neuman, J. Gelles, and R. Landick, *Pulling on the nascent RNA during transcription does not alter kinetics of elongation or ubiquitous*

pausing, Molecular Cell **23**, 231 (2006).

[53] D. O. Maoiléidigh, V. R. Tadigotla, E. Nudler, and A. E. Ruckenstein, *A unified model of transcription elongation: what have we learned from single-molecule experiments?* Biophysical Journal **100**, 1157 (2011).

[54] M. Voliotis, N. Cohen, C. Molina-París, and T. B. Liverpool, *Fluctuations, pauses, and backtracking in DNA transcription.* Biophysical Journal **94**, 334 (2008).

[55] C. Hodges, L. Bintu, L. Lubkowska, M. Kashlev, and C. Bustamante, *Nucleosomal fluctuations govern the transcription dynamics of RNA polymerase II.* Science (New York, NY) **325**, 626 (2009).

[56] X. Darzacq, Y. Shav-Tal, V. de Turris, Y. Brody, S. M. Shenoy, R. D. Phair, and R. H. Singer, *In vivo dynamics of RNA polymerase II transcription,* Nature Structural & Molecular Biology **14**, 796 (2007).

[57] I. Gusarov and E. Nudler, *The mechanism of intrinsic transcription termination,* Molecular Cell **3**, 495 (1999).

[58] A. Petrov, G. Kornberg, S. O'Leary, and A. Tsai, *Dynamics of the translational machinery,* Current opinion in structural biology **21**, 137 (2011).

[59] R. A. Marshall, C. E. Aitken, and J. D. Puglisi, *GTP hydrolysis by IF2 guides progression of the ribosome into elongation.* Molecular Cell **35**, 37 (2009).

[60] P. V. Cornish, D. N. Ermolenko, H. F. Noller, and T. Ha, *Spontaneous intersubunit rotation in single ribosomes.* Molecular Cell **30**, 578 (2008).

[61] C. E. Aitken and J. D. Puglisi, *Following the intersubunit conformation of the ribosome during translation in real time.* Nature Structural & Molecular Biology **17**, 793 (2010).

[62] J. B. Munro, R. B. Altman, N. O'Connor, and S. C. Blanchard, *Identification of two distinct hybrid state intermediates on the ribosome.* Molecular Cell **25**, 505 (2007).

[63] J. D. Wen, L. Lancaster, C. Hodges, and A. C. Zeri, *Following translation by single ribosomes one codon at a time,* Nature **452**, 598 (2008).

[64] O. Namy, S. J. Moran, D. I. Stuart, R. J. C. Gilbert, and I. Brierley, *A mechanical explanation of RNA pseudoknot function in programmed ribosomal frameshifting,* Nature **441**, 244 (2006).

[65] J. Eid, A. Fehr, J. Gray, K. Luong, J. Lyle, G. Otto, and P. Peluso, *Real-time DNA sequencing from single polymerase molecules,* Science (New York, NY) **323**, 133 (2009).

[66] S. Uemura, C. E. Aitken, J. Korlach, and B. A. Flusberg, *Real-time tRNA transit on single translating ribosomes at codon resolution,* Nature **464**, 1012 (2010).

[67] Y.-G. Gao, M. Selmer, C. M. Dunham, A. Weixlbaumer, A. C. Kelley, and V. Ramakrishnan, *The structure of the ribosome with elongation factor G trapped in the posttranslocational state.* Science (New York, NY) **326**, 694 (2009).

[68] S. H. Sternberg, J. Fei, N. Prywes, K. A. McGrath, and R. L. Gonzalez, *Translation factors direct intrinsic ribosome dynamics during translation termination and ribosome recycling.* Nature Structural & Molecular Biology **16**, 861 (2009).

[69] C. M. Kaiser, D. H. Goldman, J. D. Chodera, I. Tinoco, and C. Bustamante, *The ribosome modulates nascent protein folding.* Science (New York, NY) **334**, 1723 (2011).

[70] W. Yang, J. Gelles, and S. M. Musser, *Imaging of single-molecule translocation*

through nuclear pore complexes. Proceedings Of The National Academy Of Sciences Of The United States Of America **101**, 12887 (2004).

[71] U. Kubitscheck, D. Grünwald, A. Hoekstra, D. Rohleder, T. Kues, J. P. Siebrasse, and R. Peters, *Nuclear transport of single molecules: dwell times at the nuclear pore complex.* The Journal of cell biology **168**, 233 (2005).

[72] A. R. Lowe, J. J. Siegel, P. Kalab, M. Siu, K. Weis, and J. T. Liphardt, *Selectivity mechanism of the nuclear pore complex characterized by single cargo tracking.* Nature **467**, 600 (2010).

[73] S. Milles and E. A. Lemke, *Single molecule study of the intrinsically disordered FG-repeat nucleoporin 153.* Biophysical Journal **101**, 1710 (2011).

[74] S. W. Kowalczyk, L. Kapinos, T. R. Blosser, T. Magalhães, P. van Nies, R. Y. H. Lim, and C. Dekker, *Single-molecule transport across an individual biomimetic nuclear pore complex.* Nature nanotechnology **6**, 433 (2011).

[75] D. Grünwald and R. H. Singer, *In vivo imaging of labelled endogenous β-actin mRNA during nucleocytoplasmic transport.* Nature **467**, 604 (2010).

[76] A. A. Hoskins, L. J. Friedman, S. S. Gallagher, D. J. Crawford, E. G. Anderson, R. Wombacher, N. Ramirez, V. W. Cornish, J. Gelles, and M. J. Moore, *Ordered and dynamic assembly of single spliceosomes.* Science (New York, NY) **331**, 1289 (2011).

[77] J. Abelson, M. Blanco, M. A. Ditzler, F. Fuller, P. Aravamudhan, M. Wood, T. Villa, D. E. Ryan, J. A. Pleiss, C. Maeder, C. Guthrie, and N. G. Walter, *Conformational dynamics of single pre-mRNA molecules during in vitro splicing.* Nature Structural & Molecular Biology **17**, 504 (2010).

[78] K. S. Karunatilaka, A. Solem, A. M. Pyle, and D. Rueda, *Single-molecule analysis of Mss116-mediated group II intron folding.* Nature **467**, 935 (2010).

[79] Z. Waks, A. M. Klein, and P. A. Silver, *Cell-to-cell variability of alternative RNA splicing,* Molecular systems biology **7**, 506 (2011).

[80] D. Y. Vargas, K. Shah, M. Batish, M. Levandoski, S. Sinha, S. A. E. Marras, P. Schedl, and S. Tyagi, *Single-molecule imaging of transcriptionally coupled and uncoupled splicing.* Cell **147**, 1054 (2011).

[81] M. O'Donnell, *Replisome architecture and dynamics in Escherichia coli.* The Journal of biological chemistry **281**, 10653 (2006).

[82] D. Bates, *The bacterial replisome: back on track?* Molecular Microbiology **69**, 1341 (2008).

[83] N. Y. Yao and M. O'Donnell, *SnapShot: the replisome,* Cell **141**, 1088 (2010).

[84] S. J. Benkovic and A. M. Valentine, *Replisome-mediated DNA replication,* Annual Review of Biochemistry **70**, 181 (2001).

[85] A. Johnson and M. O'Donnell, *Cellular DNA replicases: components and dynamics at the replication fork.* Annual review of biochemistry **74**, 283 (2005).

[86] B. Maier, D. Bensimon, and V. Croquette, *Replication by a single DNA polymerase of a stretched single-stranded DNA.* Proceedings Of The National Academy Of Sciences Of The United States Of America **97**, 12002 (2000).

[87] M. Manosas, M. M. Spiering, Z. Zhuang, S. J. Benkovic, and V. Croquette, *Coupling DNA unwinding activity with primer synthesis in the bacteriophage T4 primosome.* Nature Chemical Biology **5**, 904 (2009).

[88] N. Ribeck, D. L. Kaplan, I. Bruck, and O. A. Saleh, *DnaB helicase activity is modulated by DNA geometry and force.* Biophysical Journal **99**, 2170 (2010).

[89] D. S. Johnson, L. Bai, B. Y. Smith, S. S. Patel, and M. D. Wang, *Single-molecule studies reveal dynamics of DNA unwinding by the ring-shaped T7 helicase.* Cell **129**, 1299 (2007).

[90] R. Zhou, A. G. Kozlov, R. Roy, J. Zhang, S. Korolev, T. M. Lohman, and T. Ha, *SSB functions as a sliding platform that migrates on DNA via reptation.* Cell **146**, 222 (2011).

[91] M. Manosas, M. M. Spiering, F. Ding, V. Croquette, and S. J. Benkovic, *Collaborative coupling between polymerase and helicase for leading-strand synthesis.* Nucleic Acids Research **40**, 6187 (2012).

[92] J.-B. Lee, R. K. Hite, S. M. Hamdan, X. S. Xie, C. C. Richardson, and A. M. van Oijen, *DNA primase acts as a molecular brake in DNA replication.* Nature **439**, 621 (2006).

[93] N. A. Tanner, S. M. Hamdan, S. Jergic, K. V. Loscha, P. M. Schaeffer, N. E. Dixon, and A. M. van Oijen, *Single-molecule studies of fork dynamics in Escherichia coli DNA replication.* Nature Structural & Molecular Biology **15**, 998 (2008).

[94] H. Yardimci, A. B. Loveland, S. Habuchi, A. M. van Oijen, and J. C. Walter, *Uncoupling of sister replisomes during eukaryotic DNA replication.* Molecular Cell **40**, 834 (2010).

[95] M. Pandey, S. Syed, I. Donmez, G. Patel, T. Ha, and S. S. Patel, *Coordinating DNA replication by means of priming loop and differential synthesis rate.* Nature **462**, 940 (2009).

[96] R. Reyes-Lamothe, D. J. Sherratt, and M. C. Leake, *Stoichiometry and architecture of active DNA replication machinery in Escherichia coli.* Science (New York, NY) **328**, 498 (2010).

[97] P. McInerney, A. Johnson, F. Katz, and M. O'Donnell, *Characterization of a triple DNA polymerase replisome.* Molecular Cell **27**, 527 (2007).

[98] S. T. Lovett, *Polymerase switching in DNA replication,* Molecular Cell **27** (2007).

[99] X. S. Xie, P. J. Choi, G.-W. Li, N. K. Lee, and G. Lia, *Single-Molecule Approach to Molecular Biology in Living Bacterial Cells,* Annual Review Of Biophysics **37**, 417 (2008).

[100] G. Lia, B. Michel, and J.-F. Allemand, *Polymerase exchange during Okazaki fragment synthesis observed in living cells.* Science (New York, NY) **335**, 328 (2012).

[101] R. E. Georgescu, I. Kurth, and M. E. O'Donnell, *Single-molecule studies reveal the function of a third polymerase in the replisome.* Nature Structural & Molecular Biology **19**, 113 (2011).

[102] C. S. McHenry, *DNA replicases from a bacterial perspective.* Annual review of biochemistry **80**, 403 (2011).

[103] D. A. Koster, A. Crut, S. Shuman, M.-A. Bjornsti, and N. H. Dekker, *Cellular strategies for regulating DNA supercoiling: a single-molecule perspective.* Cell **142**, 519 (2010).

[104] J. Lipfert, M. Wiggin, J. W. J. Kerssemakers, F. Pedaci, and N. H. Dekker, *Freely orbiting magnetic tweezers to directly monitor changes in the twist of nucleic acids.* Nature communications **2**, 439 (2011).

[105] J. Gore, Z. Bryant, M. D. Stone, M. Nöllmann, N. R. Cozzarelli, and C. Bustamante, *Mechanochemical analysis of DNA gyrase using rotor bead tracking.* Nature **439**, 100 (2006).

[106] Z. Bryant, M. D. Stone, J. Gore, S. B. Smith, N. R. Cozzarelli, and C. Bustamante, *Structural transitions and elasticity from torque measurements on DNA.* Nature **424**, 338 (2003).

[107] A. La Porta and M. D. Wang, *Optical torque wrench: angular trapping, rotation, and torque detection of quartz microparticles.* Physical review letters **92**, 190801 (2004).

[108] M. J. Comstock, T. Ha, and Y. R. Chemla, *Ultrahigh-resolution optical trap with single-fluorophore sensitivity.* Nature Methods **8**, 335 (2011).

[109] S. Hohng, R. Zhou, M. K. Nahas, J. Yu, K. Schulten, D. M. J. Lilley, and T. Ha, *Fluorescence-force spectroscopy maps two-dimensional reaction landscape of the holliday junction.* Science (New York, NY) **318**, 279 (2007).

[110] R. Liu, S. Garcia-Manyes, A. Sarkar, and C. L. Badilla, *Mechanical Characterization of Protein L in the Low-Force Regime by Electromagnetic Tweezers/Evanescent Nanometry,* Biophysical Journal **96**, 3810 (2009).

[111] J. Yan, T. J. Maresca, D. Skoko, C. D. Adams, B. Xiao, M. O. Christensen, R. Heald, and J. F. Marko, *Micromanipulation studies of chromatin fibers in Xenopus egg extracts reveal ATP-dependent chromatin assembly dynamics.* Molecular biology of the cell **18**, 464 (2007).

[112] K.-H. Yeom, I. Heo, J. Lee, S. Hohng, V. N. Kim, and C. Joo, *Single-molecule approach to immunoprecipitated protein complexes: insights into miRNA uridylation.* EMBO reports **12**, 690 (2011).

[113] A. Jain, R. Liu, B. Ramani, E. Arauz, Y. Ishitsuka, K. Ragunathan, J. Park, J. Chen, Y. K. Xiang, and T. Ha, *Probing cellular protein complexes using single-molecule pull-down.* Nature **473**, 484 (2011).

[114] N. Ribeck and O. A. Saleh, *Multiplexed single-molecule measurements with magnetic tweezers.* The Review of scientific instruments **79**, 094301 (2008).

[115] M. A. Umbarger, E. Toro, M. A. Wright, G. J. Porreca, and D. Bau, *The three-dimensional architecture of a bacterial genome and its alteration by genetic perturbation,* Molecular Cell **44**, 252 (2011).

[116] I. Schoen, J. Ries, E. Klotzsch, H. Ewers, and V. Vogel, *Binding-activated localization microscopy of DNA structures.* Nano Letters **11**, 4008 (2011).

[117] A. Raj, P. van den Bogaard, S. A. Rifkin, A. van Oudenaarden, and S. Tyagi, *Imaging individual mRNA molecules using multiple singly labeled probes.* Nature Methods **5**, 877 (2008).

[118] T. Trcek, J. A. Chao, D. R. Larson, H. Y. Park, D. Zenklusen, S. M. Shenoy, and R. H. Singer, *Single-mRNA counting using fluorescent in situ hybridization in budding yeast.* Nature protocols **7**, 408 (2012).

[119] J. S. Paige, K. Y. Wu, and S. R. Jaffrey, *RNA mimics of green fluorescent protein.* Science (New York, NY) **333**, 642 (2011).

[120] S. F. Lee, M. A. Thompson, M. A. Schwartz, L. Shapiro, and W. E. Moerner, *Super-Resolution Imaging of the Nucleoid-Associated Protein HU in Caulobacter crescen-*

tus, Biophysical Journal **100**, L31 (2011).

[121] W. Wang, G.-W. Li, C. Chen, X. S. Xie, and X. Zhuang, *Chromosome organization by a nucleoid-associated protein in live bacteria.* Science (New York, NY) **333**, 1445 (2011).

[122] M. Fernandez-Suarez and A. Y. Ting, *Fluorescent probes for super-resolution imaging in living cells.* Nature Reviews Molecular Cell Biology **9**, 929 (2008).

[123] J. Eyckmans, T. Boudou, X. Yu, and C. S. Chen, *A Hitchhiker's Guide to Mechanobiology,* Developmental cell **21**, 35 (2011).

[124] Y. F. Dufrêne and A. E. Pelling, *Force nanoscopy of cell mechanics and cell adhesion.* Nanoscale **5**, 4094 (2013).

[125] W. R. Legant, A. Pathak, M. T. Yang, V. S. Deshpande, R. M. McMeeking, and C. S. Chen, *Microfabricated tissue gauges to measure and manipulate forces from 3D microtissues.* Proceedings Of The National Academy Of Sciences Of The United States Of America **106**, 10097 (2009).

[126] C. Xie, L. Hanson, Y. Cui, and B. Cui, *Vertical nanopillars for highly localized fluorescence imaging.* Proceedings Of The National Academy Of Sciences Of The United States Of America **108**, 3894 (2011).

[127] X. R. Zheng and X. Zhang, *Microsystems for cellular force measurement: a review,* Journal of Micromechanics and Microengineering **21**, 054003 (2011).

[128] Y. Dufrêne, E. Evans, A. Engel, and J. Helenius, *Five challenges to bringing single-molecule force spectroscopy into living cells,* Nature Methods **8**, 123 (2011).

[129] Y. Wang, F. Meng, and F. Sachs, *Genetically encoded force sensors for measuring mechanical forces in proteins.* Communicative & integrative biology **4**, 385 (2011).

[130] P. A. Sims and X. S. Xie, *Probing dynein and kinesin stepping with mechanical manipulation in a living cell.* Chemphyschem : a European journal of chemical physics and physical chemistry **10**, 1511 (2009).

[131] A. Celedon, C. M. Hale, and D. Wirtz, *Magnetic manipulation of nanorods in the nucleus of living cells.* Biophysical Journal **101**, 1880 (2011).

[132] S. Hu, J. Chen, B. Fabry, and Y. Numaguchi, *Intracellular stress tomography reveals stress focusing and structural anisotropy in cytoskeleton of living cells,* Am. J. Physiol. Cell Physiol. **285** (2003).

[133] C. Grashoff, B. D. Hoffman, M. D. Brenner, R. Zhou, M. Parsons, M. T. Yang, M. A. McLean, S. G. Sligar, C. S. Chen, T. Ha, and M. A. Schwartz, *Measuring mechanical tension across vinculin reveals regulation of focal adhesion dynamics,* Nature **466**, 263 (2010).

[134] F. Meng and F. Sachs, *Visualizing dynamic cytoplasmic forces with a compliance-matched FRET sensor.* Journal of Cell Science **124**, 261 (2011).

[135] N. Wang, J. D. Tytell, and D. E. Ingber, *Mechanotransduction at a distance: mechanically coupling the extracellular matrix with the nucleus.* Nature Reviews Molecular Cell Biology **10**, 75 (2009).

3

ELECTRON BEAM FABRICATION OF A MICROFLUIDIC DEVICE FOR STUDYING SUBMICRON-SCALE BACTERIA

Controlled restriction of cellular movement using microfluidics allows one to study individual cells to gain insight into aspects of their physiology and behaviour. For example, the use of micron-sized growth channels that confine individual Escherichia coli has yielded novel insights into cell growth and death. To extend this approach to other species of bacteria, many of whom have dimensions in the sub-micron range, or to a larger range of growth conditions, a readily-fabricated device containing sub-micron features is required. Here we detail the fabrication of a versatile device with growth channels whose widths range from $0.3\,\mu m$ *to* $0.8\,\mu m$*. The device is fabricated using electron beam lithography, which provides excellent control over the shape and size of different growth channels and facilitates the rapid-prototyping of new designs. Features are successfully transferred first into silicon, and subsequently into the polydimethylsiloxane that forms the basis of the working microfluidic device. We demonstrate that the growth of sub-micron scale bacteria such as Lactococcus lactis or Escherichia coli cultured in minimal medium can be followed in such a device over several generations. Similar devices could potentially be used to study other submicron-sized organisms under conditions in which the height and shape of the growth channels are crucial to the experimental design.*

This chapter have been published as: M. Charl Moolman[‡], Zhuangxiong Huang[‡], Sriram Tiruvadi Krishnan, Jacob W.J. Kerssemakers and Nynke H. Dekker. Electron beam fabrication of a microfluidic device for studying submicron-scale bacteria. *Journal of Nanobiotechnology*, **11:12**, 1-10 (2013) ([‡]*Equal contribution*)

3.1. INTRODUCTION

The use of microfluidics in biological research has gained much popularity in recent years. Subfields that have been impacted by this technology range from tissue engineering [1], cancer stem cell research [2], gene expression of embryonic stem cells [3], protein interactions [4], diagnostic medicine [5] as well as microbial physiology and behaviour [6–8], to name but a few. A specific contribution to the field of microbiology is the ability to observe and manipulate single cells [9]. Individual cells can significantly differ from one another in terms of their biochemistry and genetics [10]. The ability to observe individual cells under controlled conditions provides one with the ability to investigate the individual functioning of cells as well as their mutual behaviour [11–17]. For example, the use of microfluidics has facilitated the study of molecular behaviour inside individual cells, as demonstrated by e.g. Taniguchi *et al.* [18] in their study of protein and mRNA expression at the single-molecule level inside individual living cells. An additional advantage of microfluidics is that it provides one with the ability to observe many more generations than with conventional agarose pads [9].

Recently Wang *et al.*[19] utilized a microfluidic device to quantitatively study steady-state growth and division of individual *Escherichia coli* (*E. coli*) cells at a defined reproductive age grown in Luria-Bertani (LB) medium. Such a device makes it possible to study a large number of cells that inherit the same cell pole over multiple generations. In their design, cells are confined in growth channels oriented perpendicularly to a trench through which growth medium (LB) is flown. The width and height of the channels are similar to the dimensions of *E. coli*, which has a diameter of *ca.* 1 μm and a length of *ca.* 2.5 μm under these conditions [20, 21]. Cells are immobilized, in the absence of chemical fixation, at the far end of such a growth channel (*ca.* 25 μm in length). The length of the growth channels is chosen so as to ensure sufficient supply of nutrients to the bacteria by diffusion. Such an immobilization scheme allows one to simultaneously study numerous different cells for extensive periods of time.

A microfluidic device that would allow one to probe smaller microorganisms would greatly enhance the applicability of this approach. Notably, many bacterial species have submicron-scale dimensions for which growth channels would require significantly reduced widths. Examples of such species include e.g. *Mycoplasma* (diameter 0.2–0.4 μm [22]), *Prochlorococcus* (diameter 0.5 – 0.7 μm [23]), and *Lactococcus lactis* (diameter of *ca.* 0.75 – 0.95 μm [24]), for which growth channels would require significantly reduced widths. A single device with growth channels of variable widths would furthermore provide maximal flexibility for studying different types of bacteria under a variety of growth conditions. A recent advance along these lines described the fabrication of sub-micron channels in agarose [25]. However, both this approach as well as the device utilized by Wang *et al.* are fabricated using conventional photolithography. While this is a widely available and convenient technique, for the fabrication of devices with smaller dimensions it becomes more cumbersome and alternative approaches such as electron beam lithography (EBL)[26] become more suitable. EBL can readily fabricate smaller features (*ca.* 20 nm in lateral dimensions) compared to conventional photolithography (*ca.* 1 μm) [27], while simultaneously affording greater control of the structure size and shape. An additional advantage of EBL is the reduced time from design to final device, which is convenient in a research environment where it is frequently required to change and improve a device on a relatively short time scale. The structural control and rapid-prototyping needs are thus more easily met by EBL than by conventional photolithography.

Here we present an EBL and poly(dimethylsiloxane) (PDMS) [28] soft-lithography [29] protocol for the fabrication of such a microfluidic device for microbial studies. The device that contains channels of variable widths ranging from 0.3 μm to 0.8 μm (Figure 3.1), designed to accommodate the typical range of sizes of sub-micron scale bacteria. The channels in the microfluidic device are formed out of PDMS, which has a number of attractive features that makes it an excellent material for fabricating microfluidic devices [27]. For example, sub-micron sized structures down to *ca.* 100 nm are possible in PDMS [30]. We demonstrate the use of the final microfluidic device first by injecting fluorescent dye into the channels and imaging the resulting fluorescence, and then by illustrating how sub-micron sized bacteria such as the Gram-positive *Lactococcus lactis* (*L. lactis*) and the Gram-negative bacterium *E. coli* (grown in minimal conditions) can successfully be loaded into the channels and grown for several generations. To illustrate the power of the device using *E. coli* cells, we follow the division occurrence of the mother cell as function of time. In this experiment eight cell cycles are observed.

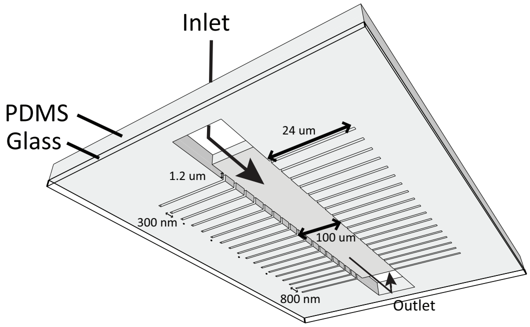

Figure 3.1: Schematic overview of the final PDMS device together with bound cover glass (not to scale). Dimensions are as follows: the main trench has a width of 100 μm and a length of 12.5 mm, growth slits are 24 μm long and 1.2 μm deep, while their widths range from 0.3 μm to 0.8 μm.

3.2. RESULTS AND DISCUSSION

3.2.1. DEVICE FABRICATION

The fabrication of the device contains three principal steps (Figure 3.2). Firstly, we etch the pattern of the device into a 4" silicon (Si) wafer (Figure 3.2, Step 1). We accomplish this by employing EBL together with specific dry etching protocols. Secondly, we use PDMS to create a negative mold of the structure that was fabricated in the Si wafer (Figure 3.2, Step 2). Finally, we make use of this PDMS mold to fabricate the final device in PDMS (Figure 3.2, Step 3). We note that an alternative approach could involve the fabrication of a negative (as opposed to a positive) Si mold, which would reduce the number

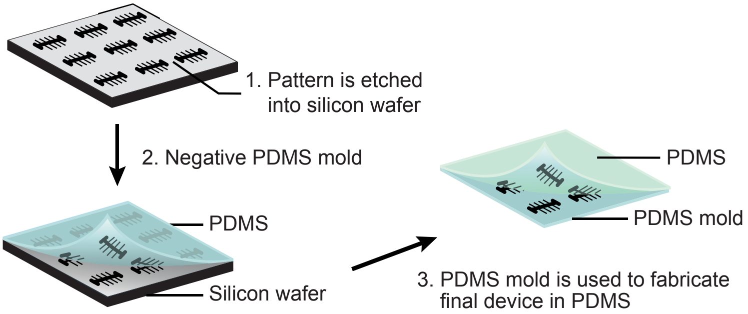

Figure 3.2: Schematic overview of the three principal steps. (Step 1) The patterns are etched into a 4" silicon wafer. (Step 2) The silicon wafer is used as a mold to fabricate the negative structures in PDMS. (Step 3) The PDMS mold is subsequently used to fabricate the final structures in PDMS. For simplicity we depict only 9 structures (whilst typically a wafer contains 24).

of PDMS steps. However, we do not favor such an approach, as it would require one to fabricate the small growth channels *ca.* 25 μm into the Si wafer. To optimize the fabrication yield, we employ a wafer that is much larger than the size of a single device. This allows us fabricate multiple individual devices (in our current protocol 24 in total) in parallel. The only step excepted from the parallel approach is the final bonding step (of glass to PDMS), which is carried out for each device individually. In the following paragraphs we describe the fabrication in Si and PDMS in detail

The main steps in fabricating the structures in Si are depicted in Figure 3.3. We fabricate the structures into a 4" diameter Si wafer (University Wafer, USA). We first fabricate the small growth channels, followed by the main trench. In the first step, we ultrasonically clean the wafer in fuming nitric acid (100% HNO_3) for 15 min (Figure 3.3, Step 1), rinse in deionized (DI) water, and spin dry. We then subsequently prime the wafer surface for resist adhesion using hexamethyldisilazane (HMDS) by spin-coating at 3000 rpm for 1 min (Figure 3.3, Step 2). After this, we spin-coat an approximately 2.2 μm thick layer of poly(methyl methacrylate) (PMMA) 950K A11 positive electron-beam resist onto the wafer at 3000 rpm for 1 min and bake it for 2 min at 100 °C and for 10 min at 175 °C. (Figure 3.3, Step 3).

The first pattern, i.e. the small growth channels, can now be written into the wafer (Figure 3.3, Step 4). We make use of a Leica EBPG 5000+ (acceleration voltage 100 kV, aperture 400 μm) to write the pattern on the wafer. Here we use a spot size of *ca.* 25 nm and a current of *ca.* 46 nA. We choose the beam step size (BSS) to be 20 nm and the dose 1400 $\mu C/cm^2$.

Following electron beam exposure, we develop the exposed PMMA (Figure 3.3, Step 5) by using methyl isobutyl ketone (MIBK) and isopropyl alcohol (IPA). We place the wafer in a beaker containing a 3:1 ratio of IPA and MIBK for 60 s. Directly afterwards, we place the wafer in a beaker containing IPA only for 30 s, and subsequently spin it dry. We then

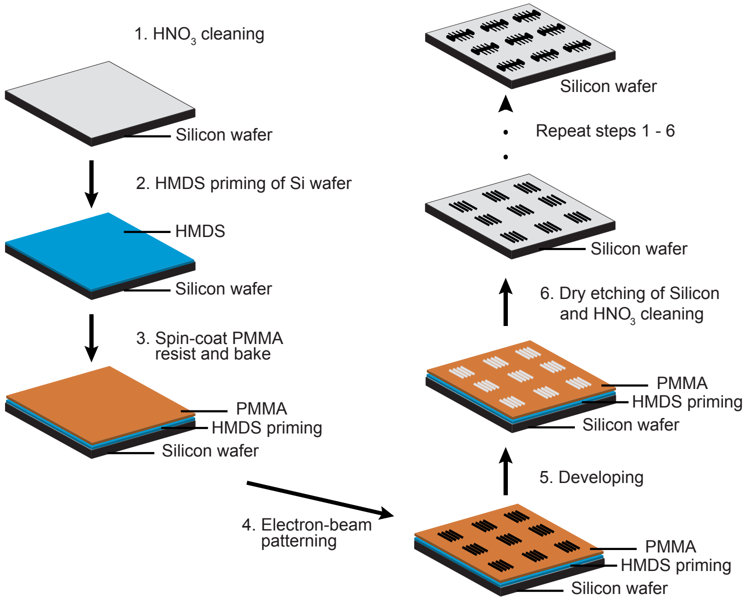

Figure 3.3: Schematic of the fabrication of multiple structures in Si with sub-micron size growth channels using EBL and dry etching. The growth channels are etched first, followed by the main trench. The steps to conduct this are as follows. (Steps 1-3) A 4" silicon wafer is cleaned and prepared for electron beam patterning. (Steps 4-5) Specific regions of the PMMA is exposed to the electron beam and developed. (Step 6) Dry etching of the structures into the wafer is performed. This whole process is then repeated to etch the main trench into the silicon wafer.

clean the wafer by exposing the wafer to an O_2 plasma in a microwave plasma system (Tepla 100) with the power set to 100 W and the pressure maintained at approximately 0.15 mbar).

Following PMMA development, we perform the dry etching of the growth channels (Figure 3.3, Step 6). This is achieved by using an inductive coupled plasma (ICP) reactive-ion etcher (RIE) (Adixen AMS 100 I-speeder) with a mixture of 15 sccm sulfur hexafluoride(SF_6), 20 sccm octafluorocyclobutane(C_4F_8), 10 sccm methane(CH_4) that is diluted in 100 sccm helium (He). We set the ICP power to 2000 W, and the capacitive coupled plasma (CCP) power (biased power) to 250 W. We maintain the sample holder at 0 °C during the entire process. The wall of the main chamber is maintained at 200 °C to inhibit polymer deposition there. We fix the sample holder height at 200 mm and maintain a low pressure of *ca.* 1 Pa. We perform this etching process for 3 min. At an etching rate of *ca.* 390 nm/min, this results in approximately 1.2 μm deep growth channels.

Next we fabricate the main trench together with the inlet and outlet using an identical procedure save for two aspects. Firstly we perform the patterning with a larger spot size, *ca.* 113 nm, at a current of *ca.* 193 nA and an increased BSS of 100 nm. Secondly, we make use of the dry etching process known as Bosch deep reactive ion etching (DRIE) [31]. This type of etching is different than the previous method in the way that the etching process consists of repeating etching (SF_6) and passivation cycles (C_4F_8). The passivation step ensures that the sidewalls of the structure being etched are protected during the etching process (see references [31, 32] for a more thorough description). We maintain the sample holder at 10 °C during the entire etching process. We keep the pressure at approximately 0.04 mbar. We perform the etching step with 200 sccm SF_6 for 7 s with the ICP power 2000 W and the CCP power off. We execute the passivation step with 80 sccm C_4F_8 for 2 s with the ICP power 2000 W and the CCP power set in chopped low frequency (LF) bias mode: 80 W, ON 10 ms, OFF 90 ms. We repeat this etching cycle for 5 min. The etching rate for Si is approximately 5 μm/min, which for these settings results in the *ca.* 25 μm deep trench. After this, we again clean the wafer in 100 % HNO_3 for 15 min, spin it dry and rinse with DI water. A sample wafer following all fabrication steps is depicted in Figure 3.4.

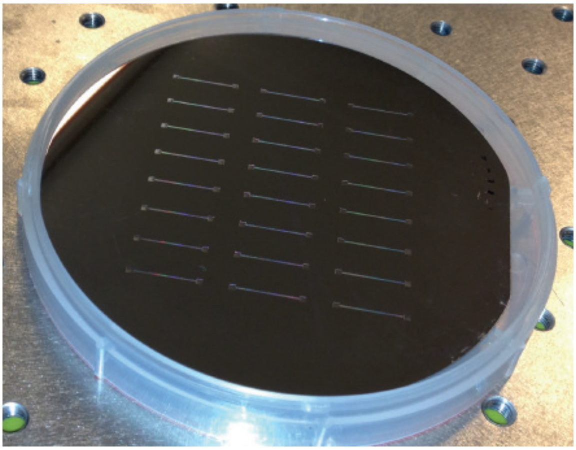

Figure 3.4: Image of the final Si wafer following the fabrication. One can clearly observe the 24 structures etched into the Si wafer. Here the main trench as well as inlet outlet ports are clearly visible. The side growth channels are too narrow to be visualized in this manner.

We validate the fabrication of the structure in Si by SEM using a FEI/Philips XL30S/FEG. Four different SEM images are shown in Figure 3.5. A top and side view of a portion of the main trench together with the smallest growth channels (i.e. 0.3 μm width) are shown in (Figure 3.5a,b). As can be seen from the images, the etching process is successful and we maintain good control of the structures. The scalloping effect that is visible at the side of the trench is a result of the Bosch DRIE etching process. Zooming in on one of the small channels, we observe that the height and depth correspond to the expected values (Figure 3.5 c,d). This implies that the PMMA provides sufficient protection during the etching process. We note that shallower channels could be fabricated simply by reducing the etching time.

The final step we perform before the wafer can be used as a mold is a silanization step.

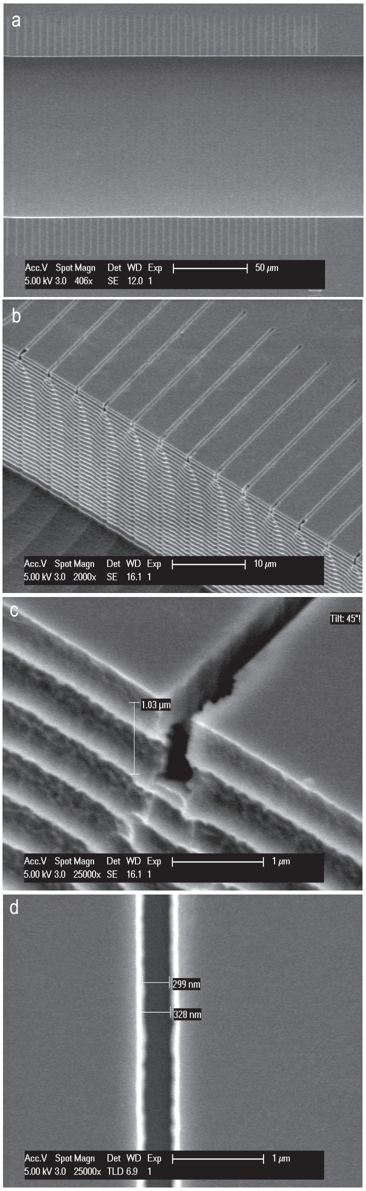

Figure 3.5: SEM images of fabricated sub-micron channels in silicon. (a) Top overview of a part of the main trench and the small growth channels. For illustration purposes we only show the small channels, but obtained similar results for the bigger growth channels. Here one clearly observes the control of the etching process as shown by the sharp boundaries of the structures. (b) Side view of a part of the main trench and the small growth channels. It is evident from this image that the etching resulted in the appropriate structures. (c,d) Zooming in on one of the small channels to illustrate its dimensions. The scalloping effect seen in (b) and (c) has to do with the repeating passivation and etching cycles of the Bosch process.

This is necessary to reduce the adhesion between PDMS and Si in the curing step and is achieved as follows. We expose the wafer to an O_2 plasma for 10 s. We then immediately place the wafer in a desiccator together with 15 μL of silanizing agent (tridecafluoro-1,1,2,2-tetrahydrooctyl trichlorosilane) (TFOCS) [33]. We place the desiccator under a vacuum, which results in evaporation of the silanizing agent and formation of a monolayer on the surface of the Si wafer. This layer renders the Si wafer extremely hydrophobic, preventing the PDMS from adhering to it. After 2 hours under vacuum, the Si wafer is ready to be used as a mold.

To fabricate the final PDMS microfluidic device, we first utilize the Si wafer as a mold to fabricate a PDMS negative of the structures. We then subsequently use the PDMS negative mold to fabricate the final structures in PDMS. A total of eight principal steps yield the final microfluidic device in PDMS (Figure 3.6). In order to fabricate the structures in PDMS we perform the following steps. If the Si wafer is stored for longer than 24 h, we first ultrasonically clean it in 100% HNO_3 for 15 min, rinse with DI water and spin it dry (Figure 3.6, Step 1). Secondly, we prepare PDMS (Mavom Chemical Solutions DC Sylgard 184 elastomer kit) by mixing an elastomer base and curing agent in a ratio of 1:5 to obtain a relatively stiff mold. Afterwards we mix the PDMS thoroughly, we pour it over the clean Si wafer and degas it in a desiccator (Figure 3.6, Step 2). We subsequently bake

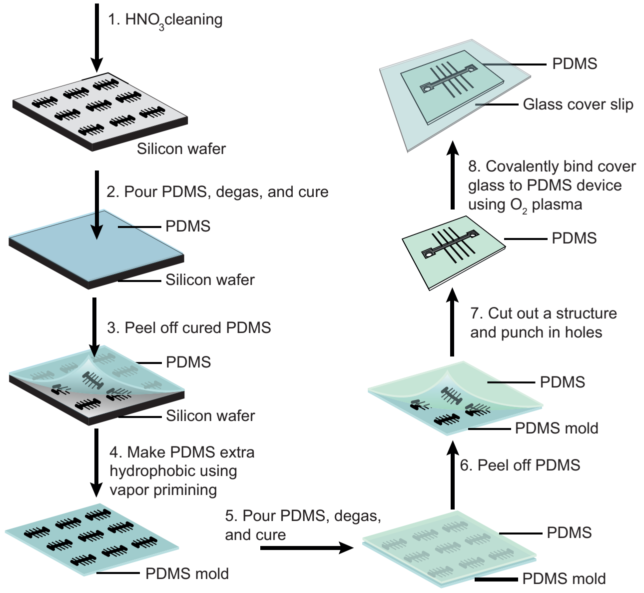

Figure 3.6: Schematic of the fabrication of multiple structures in PDMS with sub-micron sized growth channels. (Step 1) The wafer is cleaned with HNO_3. (Step 2-3) A 1:5 ratio PDMS is poured on the wafer, cured, and carefully peeled off. (Step 4) A silanization step is performed on the resulting PDMS mold. (Step 5) A 1:10 ratio PDMS is poured on the PDMS mold and cured. (Steps 6) The two PDMS layers are carefully separated from one other. (Step 7) A single structure is cut out, and an inlet and outlet port are punched. (Step 8) PDMS and a clean cover glass are bound together using O_2 plasma.

the PDMS and Si wafer for 2 h at 85 °C, and afterwards leave it to cool down for *ca.* 30 min. In the final step, we carefully peel off the PDMS from the Si wafer (Figure 3.6, Step 3).

To verify the successful replica of the structure onto PDMS, we investigate the structure with a SEM. Before we perform the SEM imaging, we first coat the PDMS with a thin layer of gold (Au) to avoid charging during the imaging process. SEM images are made using a FEI/Philips XL30S/FEG (Figure 3.7). One can observe from the top view of the largest growth channels (Figure 3.7a) and a side view of the smallest channels (Figure 3.7b), that the structures are successfully created in PDMS. A small subset of the growth channels suffers from collapse (Figure 3.7b, white arrows), likely the result of the relatively high aspect ratio of the channels (0.3 μm : 1.2 μm) in combination with the relative softness of PDMS. As mentioned above, we can reduce the depth of the growth channels by etching for a shorter time, which could potentially increase the yield. A different approach to circumvent channel collapse would be to utilize a composite two-layer process consisting of a thick "typical" PDMS layer and a thin *h*-PDMS ("hard" PDMS) layer [34]. This

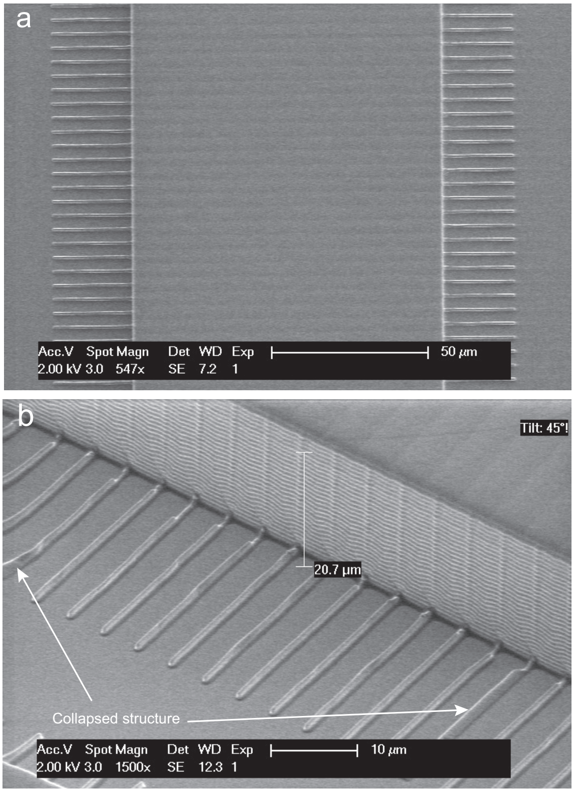

Figure 3.7: SEM image of PDMS mold with a thin layer of gold on its surface. (a) A top view of the biggest channels. (b) A side view of the smallest channels. In both images it is clear that the structures are successfully replicated from silicon into PDMS.

approach has been shown to increase the yield when fabricating sub-100 nm size structures using soft lithography. In our current protocol, however, there are enough upright channels that can serve as a mold for the next step, so we proceed without further alterations. We perform a further silanization process (Figure 3.6, Step 4), to reduce the adhesion between the two PDMS layers after the curing process.

Finally we fabricate the positive structures in PDMS. We mix PDMS in a 1:10 ratio, degas, and pour it onto the previously cured PDMS mold (Figure 3.6, Step 5). We then again degas and allow to cure for 2 h at 85 °C. Once the curing is complete, we leave the PDMS to cool down for at least 30 min. Subsequently we carefully separate the two PDMS layers from each other (Figure 3.6, Step 6). At this point the PDMS mold can be stored for later use.

The cured PDMS layer contains 24 positive structures, each of which can be used in an experiment. To study an organism under the microscope utilizing the device, the PDMS device should have an inlet and outlet port for media exchange, as well as a cover glass that seals the device. To fabricate the inlet and outlet ports we first carefully cut out a single PDMS device and punch holes at the two sides of the main trench using a 0.75 mm Harris Uni-Core puncher (Figure 3.6, Step 7). To bind the cover glass to the PDMS, we simultaneously expose the clean cover glass (ultra-sonicated in acetone and IPA) and the PDMS devices to an O_2 plasma using a microwave plasma system (Plasma-Preen I, Plasmatic Systems Inc.) (Figure 3.6, Step 8). We then bring the two exposed surfaces into contact and press slightly. It is believed that when the surfaces are exposed to plasma, silanol groups (−OH) are developed, which form covalent siloxane bonds (Si−O−Si) when the two surfaces are brought into contact [35, 36]. We then bake the PDMS and attached cover slips for *ca.* 30 min at 85 °C, after which they are ready to be used in an experiment. In the following section we demonstrate the utilization of this device in two types of experiments.

3.2.2. UTILIZING THE PDMS DEVICE

We can now prepare our finished microfluidic device (Figure 3.8a) for studies of bacterial growth. Firstly we verify that the growth channels can indeed be wetted. We accomplish this by injecting a fluorescent dye into the device, and imaging the resulting fluorescence using a fluorescence microscope. In a distinct device, we demonstrate that bacteria can be loaded into the growth channels. We perform two types of experiments, one in which we inject the Gram-positive bacterium, *L. lactis*, into the device, and in the other experiment where we inject the Gram-negative bacterium, *E. coli*. In both the cases, the cells fit well into the respectively sized channels (*ca.* 0.8 μm) and also subsequently grow and divide.

We illustrate the functionality of the microfluidic devices by injecting a fluorescent liquid (Invitrogen Alexa Fluor 514 Goat Anti-Rabbit IgG 2 mg/mL) into the growth channels. First, we attached tubing to the inlet and outlet of the device. We inject phosphate buffered saline (PBS) (Sigma, 0.01 M PBS - NaCl 0.138 M, KCl 0.0027 M, pH 7.4), into the device. After this, we simultaneously autoclave (120 °C for 15 min) the device and tub-

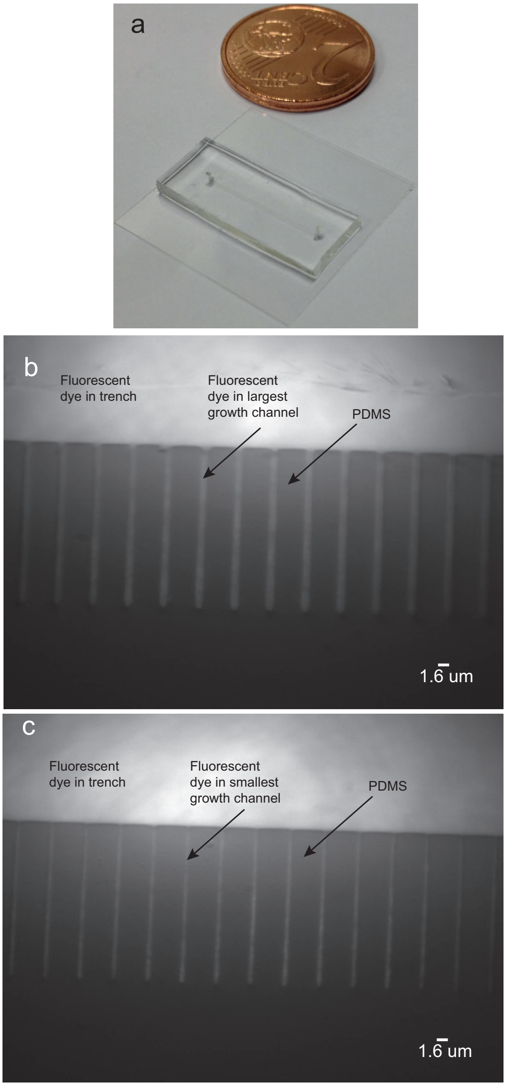

Figure 3.8: An example of the final PDMS device as well as fluorescence images of a fluorescent dye inside the device. (a) The actual final PDMS device as is used in experiments. (b) Presence of fluorescent dye in largest channel, nominally $0.8\,\mu$m, (c) Presence of fluorescent dye in smallest channel, nominally $0.3\,\mu$m. One observes that the dye is able to enter the growth channels. A control experiment where the fluorescent signal was measured in the absence of the fluorescent dye (data not shown here), showed no significant fluorescence in the trench or growth channels. The inhomogeneity of the light intensity observed is due to the Gaussian profile of the laser beam. We performed a control experiment (data not shown here) by measuring the fluorescence signal in the absence of the fluorescent dye. During these conditions no significant fluorescence signal was detected in the trench or growth channels. This observation supports our conclusion that the signal detected as shown in the above images are due to the fluorescent dye in the trench and growth channels.

ing. This is done both to ensure sterile conditions when working with micro-organisms and to remove any air bubbles present inside the device. After the autoclaving process is complete, we flush through 50 μL bovine serum albumin (BSA) (10 mg/mL New England Biolabs) through the device and allow it to incubate for at least 15 min. This surface passivation step is done to reduce unwanted sticking of the specimen being studied to the glass and PDMS surfaces. After this incubation period we injected the dye (diluted 1:50 in PBS) into the device and image on a fluorescence microscope.

We successfully wet the growth channels as shown in Figure 3.8b,c. For illustration purposes we show only the largest growth channels, *ca.* 0.8 μm (Figure 3.8b) and smallest ones *ca.* 0.3 μm (Figure 3.8c). One can clearly observe that dye was successfully injected into both types of channels and can readily visualize their differences in size..

Next we demonstrate that sub-micron size bacteria can successfully be observed in the microfluidic device. For this purpose we use both *L. lactis* and *E. coli*. *L. lactis* has a diameter of *ca.* 0.8 μm [24], as do *E. coli* when cultured in a minimal medium [20]. It is thus possible to immobilize both these species of bacteria in the largest growth channel of this type of microfluidic device.

We verify the successful growth of *L.lactis* in the device as follows. We inject *L. lactis* into the device and load them into the growth channels by means of centrifugation (Figure 3.9). The cells depicted are in the largest size growth channels (*ca.* 0.8 μm), as can be expected given the nominal size of *L. lactis*. During the course of the experiment the cells remain essentially immobilized. Bright field microscopy is used to image the cells.

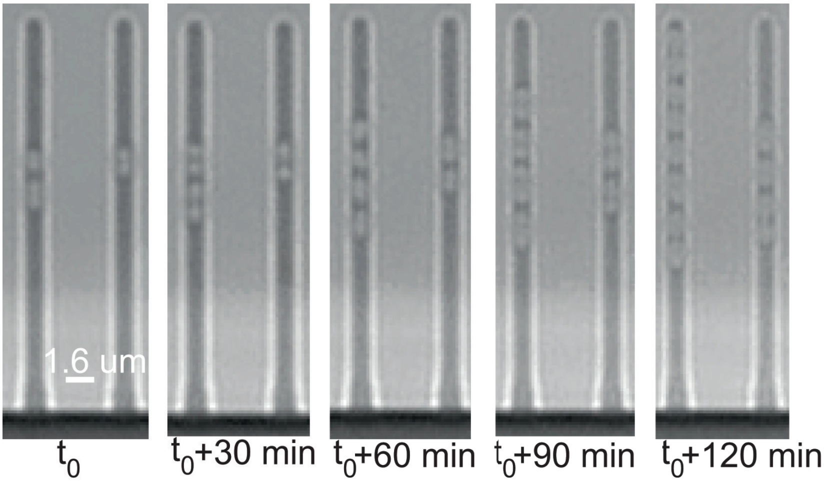

Figure 3.9: Time points (every 30 min starting at t_0) of a 2 h time series measurement of *L. Lactis* in the microfluidic device. Measurements are performed at room temperature (*ca.* 23 °C). One can clearly observe growth and division during these two hours. Looking at the first slit, for example one observes the initial two cells becoming 8 cells in 2 h.

Here we show example time points of approximately 30 min intervals as to demonstrate the growth of *L. lactis* over time. One can clearly observe cell growth in the sample channels shown. As is evident from these time points, the cells grew for approximately two generations during the 2 h measurement duration. The doubling time of these bacteria is estimated from this measurement to be *ca.* 60 min under these conditions.

As with the *L. lactis* cells, we successfully observe *E. coli* growth over multiple generations (Figure 3.10) in the growth channels of the micro-fluidic device. Figure 3.10a depicts a montage (25 min intervals) of a single growth channel, made using the *Make Montage*

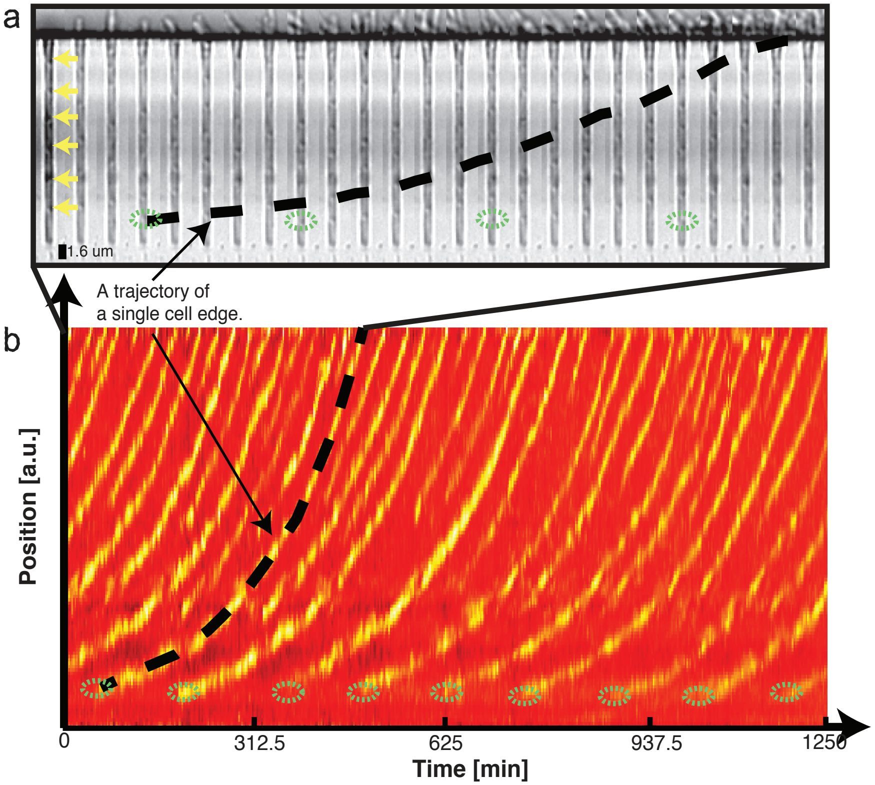

Figure 3.10: A montage (a) and kymograph (b) of *E. coli* growing in the microfluidic device. (a) A montage (interval of 25 minutes) made of a single growth channel using the *ImageJ* software package. The yellow arrows in the montage indicate the edges of the different bacterial cells which corresponds to the yellow traces seen at the beginning of the kymograph. (b) A kymograph (with a duration of *ca.* 21 hrs) of the corresponding growth channel is depicted here. The yellow traces indicate the position of cell edges over time. Custom *Matlab* software was written and used to construct the kymograph from the bright-field images. The dotted black line in both (a) and (b) is drawn by hand and illustrates our ability to follow the spatial movement of a specific bacterium edge as function of time. The division occurrence of the mother cell at the bottom of the growth channel is highlighted by a green ellipse in both the montage as well as the kymograph. From the kymograph it is clear that the growth and division of a single mother cell at the far end of the growth channel can be quantified over multiple cell cycles. In this experiment we observe eight mother cell divisions.

function in the *ImageJ* software package. Cell growth is clearly visible in the 625 min fragment, as well as the division of the mother cell (namely four divisions) at the far end of the growth channel. Despite the relatively low contrast of bright field images, we are able to accurately follow the edges of bacteria, and thus track the division process of single cells over time. This is graphically illustrated by means of the dashed black line in the montage. Figure 3.10b is a kymograph of the same growth channel. The yellow traces in the kymograph indicate the position of cell edges over time. The yellow arrows in the montage highlight the edges of the bacteria which corresponds to the yellow traces seen at the beginning of the kymograph. We graphically emphasize the edge detection and tracking of a single cell pole by means of the dashed black line that corresponds to the dashed line in the montage. It is thus possible to track a cell edge as function of time until it exits the channel. We can follow, highlighted here by means of green ellipses, the division of the mother cell for numerous cell cycles, which is in essence the advantage of using this type of device over conventional agarose pads. In this experiment eight cell cycles of the mother cell are observed. The average doubling times that we observe are found to be independent of a cell's position within the growth channel.

3.3. CONCLUSION

We have presented a detailed protocol based on EBL together with specific dry etching procedures for the fabrication of a microfluidic device suited to study submicron-sized bacteria. In comparison to approaches based on conventional optical lithography, our method provides enhanced versatility and control of the dimensions of the growth channels while satisfying the rapid-prototyping needs in a research environment. The widths of the submicron growth channels allow for the potential immobilization and study of different size bacteria with widths ranging from $0.3\,\mu$m to $0.8\,\mu$m. We verified by means of SEM that these structures are successfully transferred from Si into PDMS as well as from PDMS into PDMS. As a proof-of-principle, we demonstrated that both Gram-positive and Gram-negative bacteria can successfully be loaded and imaged over a number of generations in this device. Similar microfluidic devices could potentially be used to study other submicron-sized organisms under conditions in which the height and shape of the growth channels are crucial to the experimental design.

3.4. METHODS

3.4.1. MICROSCOPY

The microscope setup used during the experiments consists of a commercial Nikon Ti, a customized laser illumination path, and a personal computer (PC) running Nikon NIS elements. Different illumination schemes were used for the different measurements. A Cobolt Fandango 515 nm continuous wave (CW) diode-pumped solid-state (DPSS) laser is used to excite the fluorescent dye to verify device wettability. The experiments with *L.lactis* and *E. coli* are performed using with standard brightfield illumination. In all the experiments a Nikon CFI Apo TIRF 100x oil (NA 1.49) objective is used for imaging. Bright field images are acquired every 5 minutes

3.4.2. CELL CULTURE PREPARATION FOR MICROSCOPY

The *L.lactis* cultures are grown directly from plate in Luria-Bertani medium (LB) at 30 °C until an $OD_{600} \approx 0.2$ is reached. The cell culture is then concentrated by centrifugation and injected into the PDMS device. A syringe pump is used to inject fresh LB medium.

E. coli are grown in M9 medium supplemented with 0.3 % glycerol at 37 °C overnight with shaking, and sub-cultured in the morning until an $OD_{600} \approx 0.2$ is reached. The cell culture is then concentrated by centrifugation and injected into the PDMS device. A syringe pump is used to inject fresh M9-glycerol medium.

CONTRIBUTIONS

M.C.M., Z.H. and N.H.D. designed the research. Z.H. and M.C.M. developed and performed the fabrication procedures. M.C.M. and S.T.K. performed the microscopy experiments. J.W.J. and M.C.M. wrote the software and analyzed the data.

ACKNOWLEDGMENTS

The authors thank Felix Hol, Fabai Wu, Peter Galajda, Jaan Männik, Simon van Vliet, Mats Walldén and Johan Elf for initial help with the fabrication process, Luping Xu and Peipei Chen for initial help with loading of the cells, Arnold van Run, Hozanna Miro, and Marc Zuiddam for technical assistance with the fabrication instruments, Francesco Pedaci for his help with the acquisition of the SEM images, Greg Schneider for initial help with the silanization procedure, Serge Donkers for initial help with *L. lactis*, and Jelle van der Does, Dimitri de Roos and Jaap Beekman for help with instrumentation, Melanie Römer for her help with the illustrations. We also thank the anonymous reviewers for their insightful comments and suggestions to improve the manuscript. This work was supported by the Netherlands Organization for Scientific Research (NWO), Delft University of Technology and the European Community's Seventh Framework Programme FP7/2007-2013 under grant agreements n° 241548 (MitoSys).

REFERENCES

[1] S. M. Kim, S. H. Lee, and K. Y. Suh, *Cell research with physically modified microfluidic channels: a review,* Lab on a chip **8**, 1015 (2008).

[2] Y. Huang, B. Agrawal, D. Sun, J. S. Kuo, and J. C. Williams, *Microfluidics-based devices: New tools for studying cancer and cancer stem cell migration,* Biomicrofluidics **5**, 013412 (2011).

[3] J. F. Zhong, Y. Chen, J. S. Marcus, A. Scherer, S. R. Quake, C. R. Taylor, and L. P. Weiner, *A microfluidic processor for gene expression profiling of single human embryonic stem cells,* Lab on a chip **8**, 68 (2008).

[4] S. J. Maerkl and S. R. Quake, *A systems approach to measuring the binding energy landscapes of transcription factors,* Science **315**, 233 (2007).

[5] P. Yager, T. Edwards, E. Fu, K. Helton, K. Nelson, M. R. Tam, and B. H. Weigl, *Microfluidic diagnostic technologies for global public health,* Nature **442**, 412 (2006).

[6] T. Danino, O. Mondragón-Palomino, L. Tsimring, and J. Hasty, *A synchronized quorum of genetic clocks,* Nature **463**, 326 (2010).

[7] J. Männik, R. Driessen, P. Galajda, J. E. Keymer, and C. Dekker, *Bacterial growth and motility in sub-micron constrictions,* PNAS **106**, 14861 (2009).

[8] M. Gan, J. Su, J. Wang, H. Wu, and L. Chen, *A scalable microfluidic chip for bacterial suspension culture,* Lab on a chip **11**, 4087 (2011).

[9] J. C. W. Locke and M. B. Elowitz, *Using movies to analyse gene circuit dynamics in single cells.* Nature Reviews Microbiology **7**, 383 (2009).

[10] D. B. Weibel, W. R. Diluzio, and G. M. Whitesides, *Microfabrication meets microbiology,* Nature Reviews Microbiology **5**, 209 (2007).

[11] H. Yin and D. Marshall, *Microfluidics for single cell analysis,* Current opinion in biotechnology **23**, 1 (2011).

[12] M. E. Lidstrom and D. R. Meldrum, *Life-on-a-chip,* Nature Reviews Microbiology **1**, 158 (2003).

[13] M. R. Bennett and J. Hasty, *Microfluidic devices for measuring gene network dynamics in single cells,* Nature Reviews Genetics **10**, 628 (2009).

[14] Y. Wang and Z. Chen, *Microfluidic techniques for dynamic single-cell analysis,* Microchimica Acta **168**, 177 (2010).

[15] R. N. Zare and S. Kim, *Microfluidic platforms for single-cell analysis,* Annu. Rev. Biomed. Eng. **12**, 187 (2010).

[16] S. Cookson, N. Ostroff, W. L. Pang, D. Volfson, and J. Hasty, *Monitoring dynamics of single-cell gene expression over multiple cell cycles,* Molecular systems biology **1**, 2005.0024 (2005).

[17] P. Guo, E. W. Hall, R. Schirhagl, H. Mukaibo, C. R. Martin, and R. N. Zare, *Microfluidic capture and release of bacteria in a conical nanopore array,* Lab on a chip **12**, 558 (2012).

[18] Y. Taniguchi, P. J. Choi, G. W. Li, H. Chen, M. Babu, J. Hearn, A. Emili, and X. S. Xie, *Quantifying e. coli proteome and transcriptome with single-molecule sensitivity in single cells,* Science **329**, 533 (2010).

[19] P. Wang, L. Robert, J. Pelletier, W. L. Dang, F. Taddei, A. Wright, and S. Jun, *Robust growth of escherichia coli,* Current biology : CB **20**, 1099 (2010).

[20] N. Grossman, E. Z. Ron, and C. L. Woldringh, *Changes in cell dimensions during amino acid starvation of escherichia coli,* Journal Of Bacteriology **152**, 35 (1982).

[21] D. Nelson and K. Young, *Penicillin binding protein 5 affects cell diameter, contour, and morphology of escherichia coli,* Journal Of Bacteriology **182**, 1714 (2000).

[22] H. Zhao, U. Dreses-Werringloer, P. Davies, and P. Marambaud, *Amyloid-beta peptide degradation in cell cultures by mycoplasma contaminants.* BMC research notes **1**, 38 (2008).

[23] F. Partensky, W. R. Hess, and D. Vaulot, *Prochlorococcus, a marine photosynthetic prokaryote of global significance,* Microbiology And Molecular Biology Reviews **63**, 106 (1999).

[24] A. Kokkinosa, C. Fasseas, E. Eliopoulos, and G. Kalantzopoulos, *Cell size of various lactic acid bacteria as determined by scanning electron microscope and image analysis,* Le Lait **78**, 491 (1998).

[25] J. R. Moffitt, J. B. Lee, and P. Cluzel, *The single-cell chemostat: an agarose-based, microfluidic device for high-throughput, single-cell studies of bacteria and bacterial communities,* Lab on a chip **12**, 1487 (2012).

[26] M. Altissimo, *E-beam lithography for micro-/nanofabrication,* Biomicrofluidics **4**, 026503 (2010).

[27] D. Qin, Y. Xia, and G. M. Whitesides, *Soft lithography for micro- and nanoscale patterning,* Nature protocols **5**, 491 (2010).

[28] J. McDonald, D. Duffy, J. Anderson, D. Chiu, H. Wu, O. Schueller, and G. Whitesides, *Fabrication of microfluidic systems in poly (dimethylsiloxane),* Electrophoresis **21**, 27 (2000).

[29] G. Whitesides and E. Ostuni, *Soft lithography in biology and biochemistry,* Annu. Rev. Mater. Sci. **28**, 153 (2001).

[30] M. Bender, U. Plachetka, J. Ran, A. Fuchs, B. Vratzov, H. Kurz, T. Glinsner, and F. Lindner, *High resolution lithography with pdms molds,* Journal of Vacuum Science & Technology B: Microelectronics and Nanometer Structures **22**, 3229 (2004).

[31] H. V. Jansen, M. J. de Boer, S. Unnikrishnan, M. C. Louwerse, and M. C. Elwenspoek, *Black silicon method x: a review on high speed and selective plasma etching of silicon with profile control: an in-depth comparison between bosch and cryostat drie processes as a roadmap to next generation equipment,* Journal of Micromechanics and Microengineering **19**, 033001 (2009).

[32] J. Wei, *Silicon MEMS for Detection of Liquid and Solid Fronts*, Ph.D. thesis, Delft University of Technology, Micro-elektronica & Computer Engineering (2010).

[33] D. C. Duffy, J. C. McDonald, O. J. Schueller, and G. M. Whitesides, *Rapid prototyping of microfluidic systems in poly(dimethylsiloxane),* Analytical chemistry **70**, 4974 (1998).

[34] T. Odom, J. Love, D. Wolfe, and K. Paul, *Improved pattern transfer in soft lithography using composite stamps,* Langmuir **18**, 5314 (2002).

[35] M. Eddings and M. Johnson, *Determining the optimal pdms–pdms bonding technique for microfluidic devices,* Journal of Micromechanics **18**, 067001 (2008).

[36] S. Bhattacharya, A. Datta, and J. Berg, *Studies on surface wettability of poly (dimethyl) siloxane (pdms) and glass under oxygen-plasma treatment and correla-

tion with bond strength, J. MEMS **14**, 590 (2005).

4

QUANTITATIVE ANALYSIS OF SUB-CELLULAR FLUORESCENT FOCI IN LIVE BACTERIA

Fluorescence microscopy has revolutionized in vivo cellular biology. Through the specific in vivo labeling of a protein of interest with a fluorescent protein, one is able to study movement, co-localization and even count individual proteins in a live cell. Different algorithms exist to quantify the total intensity and position of a fluorescent focus. While these algorithms have been rigorously studied for in vitro conditions, which are very different than the in-homogenous and variable cellular environment, their exact limits and applicability in the context of a live cell have not been thoroughly and systematically evaluated. Here we quantitatively compare different algorithms for analyzing a focus inside a cell: the 'median excess' algorithm, a range of algorithms based on Gaussian fitting, and the popular 'SpotFinderZ' tool. We use a novel approach in which simulated and experimental data are combined to give an exact view of the cellular background fluorescence, while maintaining full control over of the intensity of the focus. This enables us to evaluate the sensitivity of the different algorithms for different focus and background intensity levels. We show that the median excess is by far the best algorithm for determining the focus intensity, as it is the only algorithm that can evaluate a focus relatively well at high cellular background levels. However, the median excess algorithm does not provide position (localization) information. The 1D Gaussian fit together with 'SpotFinderZ', provides the best option when position information is required. Interestingly we also show that the localization error is dependent on the distance of the focus from the bacterial edge. Based on these insights, we conclude with guidelines to be kept in mind in the designing of measurements.

This chapter has been be submitted for publication as: M. Charl Moolman‡, Jacob W.J. Kerssemakers‡ and Nynke H. Dekker. Quantitative analysis of sub-cellular fluorescent foci in live bacteria. (‡ *Equal contribution*)

4.1. INTRODUCTION

Fluorescence microscopy has demonstrated to be an indispensable tool for studying the behavior of proteins and protein complexes. The exact labeling of the protein of interest by means of an *in vivo* fluorescent protein (FP) fusion, enables scientists to address a plethora of questions in the natural environment of the cell see reviews in [1–5]. Due to the technical advances during the last years, it has become possible to localize, track and even count molecules in live cells [1, 6–8]. This is accomplished by studying the position and intensity behavior of the sub-cellular focus detected when the FP-fusion is excited (Figure 4.1).

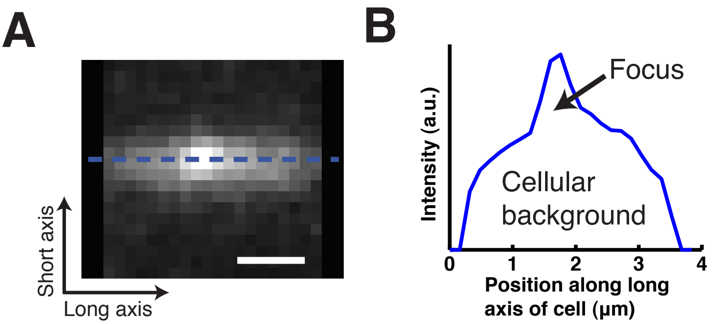

Figure 4.1: Studying a fluorescent focus in the inhomogeneous background of a bacterial cell. (A) Sample fluorescence signal of a focus and cellular background as measured in a single *E. coli* cell. Here the dashed blue line indicates where the line profile in (A) was taken. (B) The corresponding line profile of the sample image in (A). Here we indicate the focus and the cellular background to illustrate the non-negligibility of the background signal when analyzing foci in this context. Scale bar, 1 μm.

A sub-cellular focus is indicative of either immobile FP-fusions within a diffraction limited focus being for example DNA-bound [1], or a single FP-fusion moving throughout the cell [9–11]. The latter detection is only possible if the excitation and image acquisitions are fast enough (requiring typically ~ms frame rate, but somewhat dependent on the biological process being studied).

It has become common practice to fit a model function to a sub-cellular focus in order to determine its position and intensity value [12–15]. One common algorithm of analyzing a diffraction-limited focus is by direct fitting of a Gaussian function to a focus. In doing so, one can determine the position (localization) of the focus with sub-pixel resolution, and also determine the amount of fluorescence that originates from it by direct integration. While this type of analysis has been described and evaluated in detail for ideal *in vitro* and theoretical conditions [14–19], its applicability and reliability in the context of the living cell has not been sufficiently and quantitatively characterized, for reasons that the fluorescent background inside a cell is uneven, in-homogenous and highly variable (Figure 4.1B).

The crowded environment of the cell is significantly different than that of a cleaned flow-cell, where molecules are immobilized in an environment optimized for very limited autofluorescence from the sample. In contrast to this, the cellular environment is not stable. For example within a cell cycle, the protein of interest may be regularly expressed, become mature and degraded. All of this leads to a background fluorescence level that is uneven and constantly fluctuating. Also, the compact and crowded environment of the cell [20] can add to the inhomogeneity of the background fluorescence. Substantial errors can arise when one does not accurately address the influence of the background signal prior to fitting of the FP-fusion focus under investigation.

Here, we systematically characterize the influence of the background fluorescence on the analysis of a diffraction-limited focus in a bacterial cell. In our study we strived to make as few assumptions as possible concerning the background signal, and utilize a novel approach to combine simulations and experiments. As emphasized previously, the cellular background in a live cell is in homogenous and variable. Modeling this background and assuming it is an exact representation of the true cellular context may result in erroneous conclusions. For that reason, we rather simulate a diffraction-limited focus, with varying known signal content at a defined position, inside an experimentally measured background. This allows us to have an exact representation of the cellular background signal. These generated images are subsequently used as input to the different analysis algorithms. Employing the above-described approach allows us to investigate the performance of the different algorithms in a context with a more realistic signal to noise ratio than *in vitro* studies. We determine the position and signal content using our own custom written algorithms, and also the commonly used tool known as ‘SpotFinderZ’ [21] that is part of the ‘MicrobeTracker’ package [21–23]. The resulting localization and fluorescence intensity content from these algorithms are then compared to the known input values. We show that all the algorithms evaluated are sensitive to low focus intensity levels, both in terms of the focus intensity estimation error and as the localization error. The median excess algorithm is the superior choice when only focus intensity is of interest, while the 1D Gaussian with a fixed width together with SpotFinderZ is the algorithm of choice when both position and intensity information are required. Furthermore, we show that the localization error is dependent on the distance a focus is from the bacterial edge. Our results allow us to establish a set of guidelines for what signals can be analyzed to a certain set of spatial and intensity accuracy within a bacterial cell.

4.2. MATERIALS AND METHODS

4.2.1. THE MICROSCOPE SETUP, DATA ACQUISITION AND THE STRAIN USED FOR IMAGING

The microscope setup used for data acquisition is a commercial Nikon Ti equipped with an Andor U897 Electron Multiplying Charge Coupled Device (EMCCD), a Nikon CFI Apo TIRF 100x oil (NA 1.49) objective, and a personal computer running Nikon NIS elements. A Cobolt Fandango 515 nm continuous wave (CW) diode-pumped solid-state (DPSS) laser was used to excite YPet. Images were acquired with an exposure time of 80 ms and the EMCCD camera gain set to 100.

The bacterial strain used for imaging is derived from *E. coli* K12 AB1157, and has a chromosomal *YPet-dnaN* fusion that is fully described in *Moolman et al.* [24].

4.2.2. CELLULAR BACKGROUND ESTIMATION

For background correction, we proceed as follows. First, the sample autofluorescence ('dark level') is determined from a region outside the bacterium. All fluorescence signal counts in the bacterium that exceeds the dark level by one standard deviation (SD) is analyzed further. These counts are summed along the short axis of the bacterium (summed line-profile). The median of this summed-profile is taken as to be representative of the cytoplasmic content in the bacterium (cellular background) in 1D. The advantage using this algorithm of determining the cellular background is that it is not sensitive to the influence of fluctuations.

The median of the summed profile is further utilized to build up a 2D representative background image ('Bacteroidal' image) is constructed as follows. First the 'backbone' of the original bacterial image (Figure 4.2A) is determined. The backbone of the bacterium is defined as the maxima of the fluorescence signal along the short axis of cell for each of the x-positions along the long axis of the cell. Subsequently we convoluted a spike of width 1 pixel with as amplitude the summed median value at that position, with a normalized Gaussian focus having a Full width half maximum (FWHM) comparable to the width of a 'typical' bacterium ($\sim 1\,\mu$m) at each backbone position along the long axis of cell. This results in the counts to 'spread out' and obtain in a noise-free, non-fluctuating 2D 'bacteroidal' shape that contains exactly the same number of counts as the median cellular value, and follows the slightly curved shape of the original bacterium (Figure 4.2B). This image is defined as the 'bacteroidal image' and is seen to be representative of the cellular background signal of the cell. This bacteroidal background is subtracted from the original bacterial image (Figure 4.2C), which is further processed by the respective algorithms for focus analysis.

4.2.3. IMAGE DATABASE GENERATION

We created artificial phase contrast (PH) images from the experimentally measured 'diffuse' cellular background fluorescence images to use as input for MicrobeTracker. Since it is customary to use the mesh-based analysis of the MicrobeTracker/SpotfinderZ package with phase contrast images, and no phase images were acquired, we constructed ar-

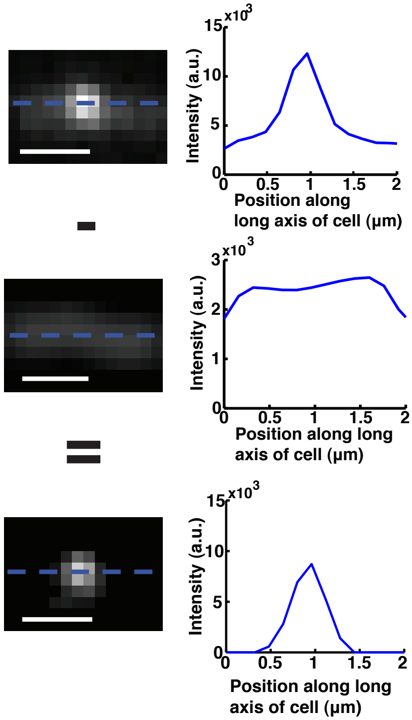

Figure 4.2: ‘Bacteroidal’ background subtraction algorithm. Here we depict a sample result of subtracting the background using our ’Bacteroidal’ background subtraction algorithm. (A) (left) The original image. (right) The corresponding line profile. (B) (left) ’Bacteroidal’ background generated using the steps described in the Materials and Methods section. (right) The corresponding line profile. (C) (left) The result of subtracting (B) from (A). (right) The corresponding line profile. One can appreciate that the background has been substantially eliminated. In all the images the dashed blue line indicates where the line profile was taken. Scale bars, 1 μm.

tificial PH images. These images were built as follows. The afore mentioned ‘bacteroidal’ image was inverted and added to its own, positive blurred variant. This resulted in a smooth, dark, white-rimmed cell picture on a grey background that is easily compatible with the MicrobeTracker phase signal detection software.

4.2.4. FOCUS ANALYSIS ALGORITHMS

We evaluate a series of custom written routines, as well as the commonly used MicrobeTracker SpotfinderZ tool with its own built-in ’ridge’ filter [21], to determine how well a focus is localized and its total intensity is deduced. Here we briefly list the different routines that have been evaluated:

1) A conventional 1D Gaussian fit with a pre-determined fixed width (1D Fixed-width Gaussian) on the summed line-profile of the image from which the ’bacteroidal background’ has been subtracted (see Section 4.2.2). The width was chosen to equal the FWHM of the point spread function of the imaging system. The result provides one with

focus signal content and the position along the long axis of the cell. This algorithm yields sub-pixel position information with a minimum of free parameters.

2) The ’Median Excess’ signal above ’bacteroidal background’. This routine determines the median of the image from which the ’bacteroidal background’ has been subtracted. We define all counts above this median level as focus content. While being a good estimator of focus signal content, this algorithm yields no information on focus position.

3) A conventional 1D Gaussian fit with no constraints on its width (1D Free-width Gaussian) on the summed line-profile of the image from which the ’bacteroidal background’ has been subtracted (see Section 4.2.2) The output information is the same as for the 1D Fixed-width Gaussian.

4) A conventional 2D Gaussian fit with a fixed-width is fitted to the focus of the image where the ’bacteroidal background’ has been subtracted (2D Fixed-width Gaussian). As a pre-estimate (initial guess), the results of the 1D Fixed-width Gaussian are used.

5) ‘SpotFinderZ’. This freely available foci analysis tool was utilized in analyzing the focus position and total intensity in combination with the ’artificial PH images’. The tool utilizes a multi-focus, 2D Gaussian fit with the width being a free parameter, in combination with a ’ridge filter’ background correction [21]. Before analysis, we systematically varied the available parameters to find the best settings to use under these conditions. These settings were determined for 45 % of the total signal being situated in the focus. This resulted in utilizing the ’default’ settings with the upper limit of the ’high cutoff’ parameter set to 2. For the present single-focus analysis, we put focus threshold levels low such as to always obtain multiple foci. The brightest focus is subsequently selected for comparison with the simulation input.

4.3. RESULTS AND DISCUSSION

4.3.1. APPROACH OF USING SIMULATED AND EXPERIMENTALLY OBTAINED DATA TO EVALUATE THE ALGORITHMS USED TO STUDY SUB-CELLULAR FOCI.

We quantify the effect that cellular background fluorescence has on the accuracy with which the total intensity and position localization of a diffraction limited focus may be estimated inside a bacterial cell. An *E. coli* cell is small, having a length, width and height of approximately 3 μm x 1 μm x 1 μm depending on growth conditions and its stage in the cell cycle. A typical Point Spread Function (PSF) having a Full Width Half Maximum (FWHM) of $0.25\,\mu m$ comprises thus 1/10 of the total length of the cell. The contribution of the fluorescence originating from diffusing molecules nearby the focus, together with the background due to the height of the cell, is thus non-negligible when determining the total intensity of a focus situated in a cell.

To study the influence of background fluorescence on focus analysis, we simulate a diffraction limited focus, of known total intensity, inside the experimentally measured fluorescence background in the cell. In doing so, we keep the total fluorescence in the cell constant (Materials and Methods; Figure 4.3A). The position of the focus was chosen to be

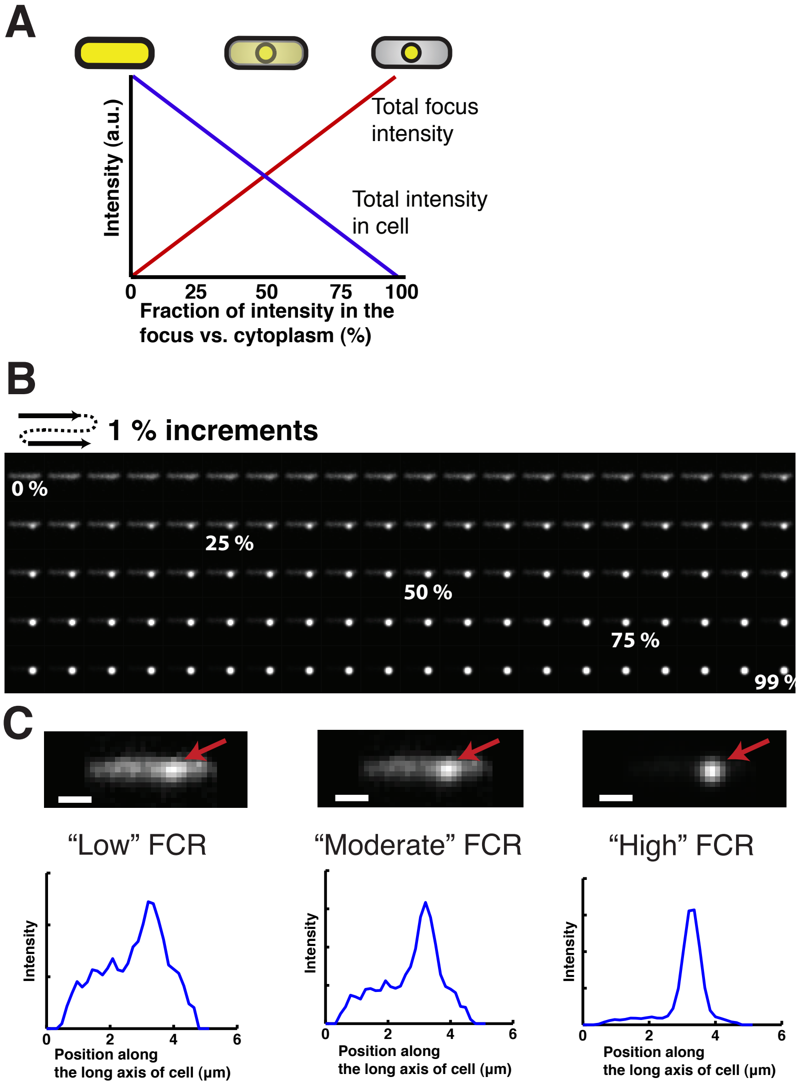

Figure 4.3: The approach taken to systematically evaluate the different algorithms of analyzing a focus. (A) Illustration of our approach of increasing the amount of signal in a focus, while simultaneously maintaining a constant total fluorescence value in the cell. For each increment we simulate a diffraction limited focus with more fluorescence content (red line), while also subtracting that amount of fluorescence from the cellular signal (blue line). We schematically illustrate the effect on the focus and cytoplasmic signal. (B) A sample temporal montage of a complete simulation from no signal in a focus (far left side of (A)) until the signal consists only of a focus (far right side of (A)). (C) Three sample simulations of different focus fluorescence content together with their corresponding line profile plots. Scale bars, 1 μm. Note that the cellular background is measured and not simulated.

at ~ 1/3 position from the center of the cell, except for evaluating the edge sensitivity of the different algorithms. In the latter case we move the focus randomly throughout the cell. The experimental images used to construct the cellular background, results from diffusion of the YPet-DnaN (the β_2 sliding clamp) protein fusion in *Escherichia coli* (*E. coli*) (Material and Methods Section 4.2.1). It has been shown previously that the fluorescence detected from this fusion corresponds to 60 - 120 YPet-DnaN dimer molecules depending on the cell cycle [24]. A substantial number of proteins in *E. coli* have this copy number [25], which makes this expression level representative for a wide range of different proteins. We vary the focus versus total cell intensity ratio (FCR) incrementally, from 0% fluorescence in the focus to 99% fluorescence in the focus (Figure 4.3B). The three sample images together with the respective line profile plots (Figure 4.3C) illustrate the setup of our approach. We perform this operation for different individual cells ($n = 42$) to include cell to cell variability. This database of cells with varying FCRs is subsequently used as input for the different algorithms tested (Materials and Methods Section 4.2.4). Remark that for all the analysis algorithms (except for the SpotfinderZ algorithm), we utilize the bacteroidal background subtraction algorithm (Figure 4.2; Material and Methods Section 4.2.2) prior to focus analysis of images such as depicted in Figure 4.3C.

4.3.2. ESTIMATING THE AMOUNT OF FLUORESCENCE CONTAINED IN A SUB-CELLULAR FOCUS

We investigate the accuracy of different algorithms in estimating the amount of fluorescence contained in a focus at different FCRs (Figure 4.4). We simulate a focus of varying FCR in the cell and input the resulting images to the focus analysis algorithms. The amount of signal in the focus versus input value is compared (Figure 4.4A). One can clearly observe that all the algorithms display overestimates at low focus intensity levels, but converge to the correct value as the FCR is increased (Figure 4.4A). This overestimate is mostly due to incorrect evaluation of 'what a focus is' under these low intensity conditions, and thus incorrectly including too much of the signal from the cytoplasm when determining the intensity of the focus.

From these results it appears that the Median Excess algorithm is significantly less prone in over estimating the focus intensity at low focus signal levels (Figure 4.4B, blue curve). The error in estimating the total intensity in a focus using the Median Excess algorithm is < 10% at a FCR of a few percent, and converges very rapidly (at ~ 15% FCR) to the correct value (Figure 4.4B, blue curve). In contrast with this, all the other algorithms fail for FCRs < 10% (Figure 4.4B). At higher FCRs (> 30%) all the algorithms converge to the correct value. The favorable characteristic of Median Excess algorithm, for not over estimating the focus intensity at low FCRs, was recently exploited to reliably quantify the number of DNA-bound sliding clamps in live *E. coli* cells [24], where the FCR valued between 30% and 60% depending on the point in the cell cycle.

4.3.3. LOCALIZATION OF A SUB-CELLULAR FOCUS

Having established the reliability in determining the total focus intensity for varying FCR, we investigate the accuracy of the different algorithms in estimating the position of a focus at different FCRs (Figure 4.5). Here we simulate a focus at varying FCRs at a

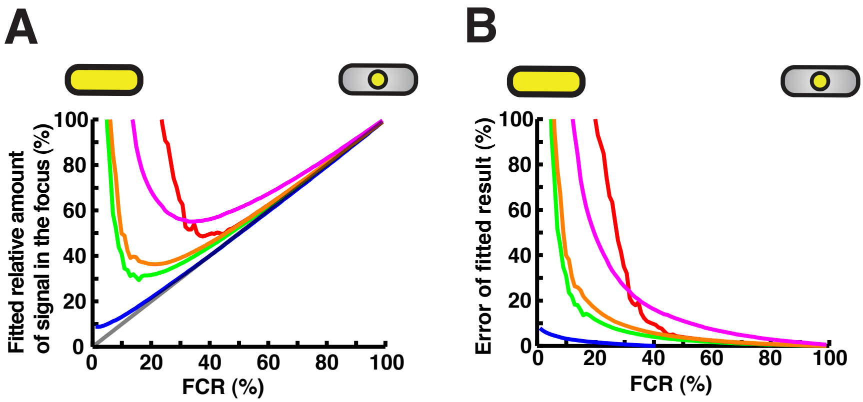

Figure 4.4: Comparison of the different algorithms for determining the total intensity of a focus. (A) The ratio of the amount of signal in the focus as estimated utilizing the different algorithms versus the known total cellular signal. Here we plot the estimated focus content divided by the known total signal. (B) The resulting error in determining the ratio of total intensity of a focus versus total intensity in the cell. Here the relative error is defined as the mean difference between the input value and the fit value for each specific FCR value ($n = 42$ cells). In both panels the colors are (blue) Median Excess, (green) 1D Fixed-width Gaussian, (red) 1D Free-width Gaussian, (orange) 2D Fixed-width Gaussian, (magenta) SpotFinderZ, and (grey) ideal. We only show the fitted results and error up and until 100 %.

fixed position in the cell (~ 1/3 from the center). The resulting images are input to all the algorithms except for the Median Excess algorithm since it does not provide one with position information (Materials and Methods). The error in localizing a focus at different FCRs is only slightly different for all the algorithms evaluated. As can be expected, the localization error is dependent on the signal to noise, one observes a decrease in error with increased FCR (Figure 4.5A). Interestingly, the error in estimating the position of a focus is not dramatically effected by the type of algorithm employed. SpotFinderZ and the 1D Fixed-width Gaussian algorithms are only better by ~ 0.5 pixel compared to the other two algorithms. Even though this may not appear as a huge difference, this localization error does become critical when one wishes to measure positions in the range of tens of nanometers.

All algorithms display a significant number (50 % – 90 %) of incorrect fits at FCRs $< 20\%$, with SpotfinderZ performing the best and the 1D Free-width Gaussian performing the worst (Figure 4.5B). Here an incorrect fit is defined as a fit position that results in being > 2 pixels different than the known (input) value. At FCRs of ~ 25 %, the number of incorrect fits drops to essentially zero.

The localization error is dependent on the position in the cell for low FCRs. Since numerous different proteins localize at disparate positions in the cell [26], we investigate whether the localization error is affected by where the focus is positioned in the cell. This is accomplished by displacing the position of a focus randomly throughout the cell and calculating the distance of the spot, as determined from the simulated position, to the nearest cell edge. Subsequently, each of the focus analysis methods (except for the Me-

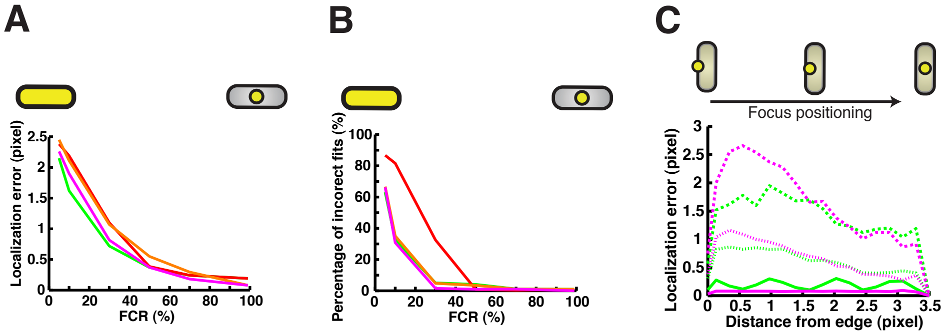

Figure 4.5: Comparison of the performance of different algorithms in localizing a focus. (A) The error in localization of a focus utilizing the different algorithms. Here the error is taken as 2xS.D. (95 % confidence internal) of the distribution of the values resulting by subtracting the fit from the input value for each of the cells at a specific ratio value. (B) The percentage of incorrect fit positions for the different algorithms. An incorrect fit is defined here as a fit position that differs by > 2 pixels from the input value. For (A) and (B) the position of the a focus was taken at a fixed position in the cell (~ 1/3 from the center), and we only simulated FCRs at 5 %, 10 %, 30 %, 50 %, 70 %, and 99 %, due to the time consuming nature of these simulations ($n = 42$ cells). The colors are (blue) Median Excess, (green) 1D Fixed-width Gaussian, (red) 1D Free-width Gaussian, (orange) 2D Fixed-width Gaussian, (magenta) SpotFinderZ. (C) Assessing the dependency of the localization error on the position of a focus in the cell. Here we depict the error in localization for the (green) 1D Fixed-width Gaussian and (magenta) SpotFinderZ algorithms for three different FCRs, namely 10 % (dashed), 30 % (striped) and 99 % (solid).

dian excess algorithm) is used to determine the position of the focus, and compared to the 'known' value. This is performed for 100 positions at three differentness FCRs: 10 %, 30 % and 99 %. For clarity we only show the two best localization algorithms, namely SpotfinderZ and the 1D Fixed-width Gaussian, when analyzing the foci. But, the result is similar for the other algorithms. It is evident that for low FCRs the localization error is a function of the distance of the focus to the edge of the cell (Figure 4.5C). This is an interesting and important result, since many biological processes occur in the vicinity of the cell wall. Examples are proteins involved in cell wall synthesis [27] and proteins that make up the flagella motor [28]. The increased error when the focus is positioned at the edge of the cell is most likely due to the large background intensity gradient. It is thus crucial when calculating the localization error to take this uncertainty component into account when nanometer-range movement or distances are reported.

4.3.4. ANALYSIS GUIDELINES WHEN STUDYING SUB-CELLULAR FOCI.

Our evaluation of the different algorithms on analyzing a focus within the natural inhomogenous cellular environment enables us to provide quantitative guidelines when investigating foci in the cell. We have shown that, independent of the choice of analysis algorithms, one should be extremely careful when investigating a focus that has a low FCR (< 10 %). For these cases we recommend two options to increase the FCR. Firstly, if conventional wide-field microscopy is used one could bleach a big fraction of the cellular fluorescence not contained in the focus. This would lower the cellular background without affecting the focus intensity. Secondly, if possible one could us photactivatable fluorescent proteins [29]. Using a low activation laser would allow one to activate only a small subset of these FPs in the cell. If optimized, one could in principle obtain a higher FCR due to low cellular background while still having a clear focus and having a "high" copy number of the protein under investigation in the cell.

To obtain more insight into the trade-off between the error in determining the total focus intensity and the error in localization, we plot both these quantities simultaneously for different FCRs (Figure 4.6). While it is evident from Figure 4.4 that the Median Excess

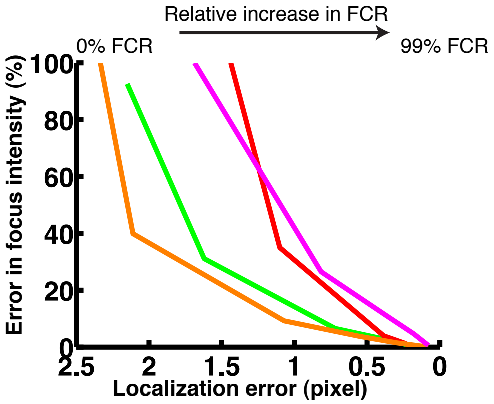

Figure 4.6: Summary of localization vs. total intensity error. A Comparison of the position and intensity errors for different FCR, namely 5 %, 10 %, 30 %, 50 %, 70 %, and 99 %. Here we combine Figure 4.4B and Figure 4.5A at the specified FCRs. The results are shown for 1D Fixed-width Gaussian (green), 1D Free-width Gaussian (red), 2D Fixed-width Gaussian (orange) and SpotFinderZ (magenta). $n = 42$ cells.

is the superior algorithm for quantifying the total intensity of a focus (Section 4.3.2), it is essential to determine if both position and intensity information are required, what the best algorithm would be. Under our evaluation conditions, it appears that the 1D Fixed-width Gaussian together with SpotFinderZ are the algorithms of choice when both total intensity of the focus as well as localization accuracy is required (Figure 4.6). Its error in both intensity and localization drops of the fastest. Our results indicate that for a FCR of 50 % and a "typical" pixel size of 160 nm utilizing the 1D Fixed-width Gaussian algorithm one could expect an error in the focus intensity of ~ 2.5 % and a localization error of ~ 60 nm.

CONTRIBUTIONS

M.C.M., J.W.J.K. and N.H.D. designed the research. J.W.J.K. and M.C.M. wrote software to analyze the data, and performed the analysis.

ACKNOWLEDGMENTS

We thank Sriram Tiruvadi Krishnan for assistance with experiments. This work was supported by a Vici grant by the Netherlands Organisation for Scientific Research (NWO) and the European Community's Seventh Framework Programme FP7/2007-2013 under grant agreements n° 241548 (MitoSys) both to N.H.D.

REFERENCES

[1] X. S. Xie, P. J. Choi, G.-W. Li, N. K. Lee, and G. Lia, *Single-molecule approach to molecular biology in living bacterial cells.* Annual Review Of Biophysics **37**, 417 (2008).

[2] X. Darzacq, J. Yao, D. R. Larson, and S. Z. Causse, *Imaging transcription in living cells,* Annual Review of Biophysics (2009).

[3] B. Wu, K. D. Piatkevich, T. Lionnet, R. H. Singer, and V. V. Verkhusha, *Modern fluorescent proteins and imaging technologies to study gene expression, nuclear localization, and dynamics.* Current opinion in cell biology **23**, 310 (2011).

[4] J. S. Biteen and W. E. Moerner, *Single-molecule and superresolution imaging in live bacteria cells.* Cold Spring Harbor perspectives in biology **2**, a000448 (2010).

[5] H. H. Tuson and J. S. Biteen, *Unveiling the Inner Workings of Live Bacteria Using Super-Resolution Microscopy.* Analytical chemistry (2014).

[6] V. C. Coffman and J. Wu, *Counting protein molecules using quantitative fluorescence microscopy.* Trends in biochemical sciences **37**, 499 (2012).

[7] T. Xia, N. Li, and X. Fang, *Single-molecule fluorescence imaging in living cells,* Annual review of physical chemistry **64**, 459 (2013).

[8] M. Stracy, S. Uphoff, F. Garza de Leon, and A. N. Kapanidis, *In vivo single-molecule imaging of bacterial DNA replication, transcription, and repair.* FEBS letters **588**, 3585 (2014).

[9] B. P. English, V. Hauryliuk, A. Sanamrad, S. Tankov, N. H. Dekker, and J. Elf, *Single-molecule investigations of the stringent response machinery in living bacterial cells.* Proceedings Of The National Academy Of Sciences Of The United States Of America **108**, E365 (2011).

[10] A. Badrinarayanan, R. Reyes-Lamothe, S. Uphoff, M. C. Leake, and D. J. Sherratt, *In vivo architecture and action of bacterial structural maintenance of chromosome proteins,* Science **338**, 528 (2012).

[11] S. Uphoff, R. Reyes-Lamothe, F. Garza de Leon, D. J. Sherratt, and A. N. Kapanidis, *Single-molecule DNA repair in live bacteria.* Proceedings Of The National Academy Of Sciences Of The United States Of America **110**, 8063 (2013).

[12] R. E. Thompson, D. R. Larson, and W. W. Webb, *Precise nanometer localization analysis for individual fluorescent probes.* Biophysical Journal **82**, 2775 (2002).

[13] K. Jaqaman, D. Loerke, M. Mettlen, H. Kuwata, S. Grinstein, S. L. Schmid, and G. Danuser, *Robust single-particle tracking in live-cell time-lapse sequences,* Nature Methods **5**, 695 (2008).

[14] C. S. Smith, N. Joseph, B. Rieger, and K. A. Lidke, *Fast, single-molecule localization that achieves theoretically minimum uncertainty.* Nature Methods **7**, 373 (2010).

[15] K. I. Mortensen, L. S. Churchman, J. A. Spudich, and H. Flyvbjerg, *Optimized localization analysis for single-molecule tracking and super-resolution microscopy,* Nature Methods **7**, 377 (2010).

[16] M. K. Cheezum, W. F. Walker, and W. H. Guilford, *Quantitative comparison of algorithms for tracking single fluorescent particles.* Biophysj **81**, 2378 (2001).

[17] R. J. Ober, S. Ram, and E. S. Ward, *Localization accuracy in single-molecule microscopy,* Biophysical Journal **86**, 1185 (2004).

[18] A. V. Abraham, S. Ram, J. Chao, E. S. Ward, and R. J. Ober, *Quantitative study of single molecule location estimation techniques.* Optics Express **17**, 23352 (2009).

[19] S. Stallinga and B. Rieger, *The effect of background on localization uncertainty in single emitter imaging,* IEEE International Symposium on Biomedical Imaging **9**, 988 (2012).

[20] Morigen, I. Odsbu, and K. Skarstad, *Growth rate dependent numbers of SeqA structures organize the multiple replication forks in rapidly growing Escherichia coli.* Genes to cells : devoted to molecular & cellular mechanisms **14**, 643 (2009).

[21] O. Sliusarenko, J. Heinritz, T. Emonet, and C. Jacobs-Wagner, *High-throughput, subpixel precision analysis of bacterial morphogenesis and intracellular spatio-temporal dynamics ,* Molecular Microbiology **80**, 612 (2011).

[22] W. B. Schofield, H. C. Lim, and C. Jacobs-Wagner, *Cell cycle coordination and regulation of bacterial chromosome segregation dynamics by polarly localized proteins.* The EMBO Journal **29**, 3068 (2010).

[23] E. C. Garner, *MicrobeTracker: quantitative image analysis designed for the smallest organisms.* Molecular Microbiology **80**, 577 (2011).

[24] M. C. Moolman, S. T. Krishnan, J. W. J. Kerssemakers, A. van den Berg, P. Tulinski, M. Depken, R. Reyes-Lamothe, D. J. Sherratt, and N. H. Dekker, *Slow unloading leads to DNA-bound β2-sliding clamp accumulation in live Escherichia coli cells.* Nature communications **5**, 5820 (2014).

[25] Y. Taniguchi, P. J. Choi, G. W. Li, H. Chen, M. Babu, J. Hearn, A. Emili, and X. S. Xie, *Quantifying E. coli Proteome and Transcriptome with Single-Molecule Sensitivity in Single Cells,* Science (New York, NY) **329**, 533 (2010).

[26] D. Z. Rudner and R. Losick, *Protein Subcellular Localization in Bacteria,* Cold Spring Harbor perspectives in biology **2**, a000307 (2010).

[27] D.-J. Scheffers and M. G. Pinho, *Bacterial cell wall synthesis: new insights from localization studies.* Microbiology And Molecular Biology Reviews **69**, 585 (2005).

[28] Y. Sowa and R. M. Berry, *Bacterial flagellar motor,* Quarterly Reviews Of Biophysics (2008).

[29] K. A. Lukyanov, D. M. Chudakov, S. Lukyanov, and V. V. Verkhusha, *Innovation: Photoactivatable fluorescent proteins,* Nature Reviews Molecular Cell Biology **6**, 885 (2005).

5

SLOW UNLOADING LEADS TO DNA-BOUND β_2 SLIDING CLAMP ACCUMULATION IN LIVE *Escherichia coli* CELLS

The ubiquitous sliding clamp facilitates processivity of the replicative polymerase and acts as a platform to recruit proteins involved in replication, recombination, and repair. While the dynamics of the E. coli β_2 sliding clamp have been characterized in vitro, its in vivo stoichiometry and dynamics remain unclear. To probe both β_2 clamp dynamics and stoichiometry in live E. coli cells, we use custom-built microfluidics in combination with single-molecule fluorescence microscopy and photoactivated fluorescence microscopy. We quantify the recruitment, binding, and turnover of β_2 sliding clamps on DNA during replication. These quantitative in vivo results demonstrate that numerous β_2 clamps in E. coli remain on the DNA behind the replication fork for a protracted period of time, allowing them to form a docking platform for other enzymes involved in DNA metabolism.

This chapter have been published as: M. Charl Moolman, Sriram Tiruvadi Krishnan, Jacob W.J. Kerssemakers, Aafke van den Berg, Pawel Tulinski, Martin Depken, Rodrigo Reyes-Lamothe, David J. Sherratt and Nynke H. Dekker. Slow unloading leads to DNA-bound β_2 sliding clamp accumulation in live *Escherichia coli* cells. *Nature Communications*, **5**, 5820 (2014)

5.1. INTRODUCTION

The multi-protein replisome complex (replisome, Figure 5.1a) is responsible for the accurate and timely duplication of the genome prior to cell division. The sliding clamp protein complex is a key subunit of the replisome and is vital for protein-DNA interactions related to DNA metabolism in all three domains of life [1–3]. Through their interaction with polymerases, DNA ligase, replication initiation protein DnaA, the dynamin-like protein CrfC, as well as different mismatch-repair proteins, sliding clamps play important roles in replication, and repair [4–6, 6–15]. In *E. coli*, the β_2 sliding clamp (β_2 clamp) is a homo-dimer [16] (Figure 5.1a (inset)) that encircles double-stranded DNA (dsDNA) and tethers DNA Polymerase III (DNA Pol III) to the template, thereby ensuring sufficiently high processivity during synthesis [17, 18].

The β_2 sliding clamp is actively assembled and disassembled onto DNA during synthesis of the two complementary DNA strands (Figure 5.1b). The loading reaction of a β_2 clamp onto each new primer-template junction [22] is catalyzed by an ATP-dependent heteropentameric clamp-loader complex (clamp-loader), also know as the γ-complex [23]. The clamp-loader pries open the β_2 clamp, recognizes the primer-template junction [24], and closes the β_2 clamp around the dsDNA prior to release [20]. The clamp-loader is also thought to chaperone DNA Pol III onto a newly loaded β_2 clamp [25] and to unload inactive DNA-bound β_2 clamps via the δ-subunit [26]. During all of these reactions, the loader complex and the various clamp binding proteins compete for the C-terminal face of the clamp. In accordance with the proposed model in which the replisome includes three core DNA polymerase III's [27–29], three β_2 clamps can be active at the replication fork, one for each of the three polymerases (Figure 5.1 1a). While leading-strand replication is thought to be continuous, utilizing only a single β_2 clamp, the lagging-stand template is copied in discrete $1-2$ kb Okazaki fragments [30], each utilizing a separate β_2 clamp. These fragments are initiated by the continuous formation of $10-12$ nt RNA primers by the primase (DnaG) which, together with the helicase (DnaB), sets the replication fork clock [31]. Since the number of Okazaki fragments ($2000-4000$) for the 4.6 Mbp genome is roughly an order of magnitude greater than the average number of β_2 clamps per cell in a nutrient-rich culture [26, 32], continuous recycling of β_2 clamps is necessary for total genome replication to occur.

Despite numerous *in vitro* and *in vivo* studies, it still remains unclear whether recycling of the *E. coli* β_2 clamps takes place immediately following the completion of an Okazaki fragment, or at a later time. A slow recycling could permit a β_2 clamp to fulfill additional functions, while remaining bound to the newly synthesized DNA. Quantitative *in vitro* unloading assays [26, 33] indicate that in the absence of the clamp-loader, a loaded β_2 clamp has a long half-life of $t_{\text{unload}} > 1\,\text{hr}$ on the DNA. While this is decreased by more than an order of magnitude to $t_{\text{unload}} \sim 127\,\text{s}/\beta_2$ in the presence of clamp-loader, this unloading time still remains long compared with the typical time required to complete an Okazaki fragment (on the order of seconds). Such a slow unloading time suggests that many β_2 clamps are left behind in the wake of the replication fork [34]. However, a recent *in vitro* single-molecule study indicates that lagging-strand synthesis can persist *in vitro* in the absence of excess β_2 clamps in solution, implying that a β_2 clamp can be directly

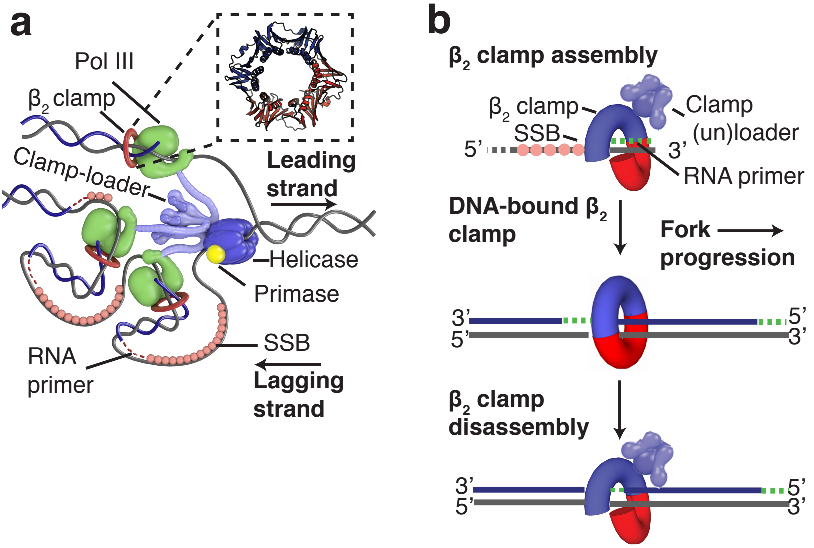

Figure 5.1: The *E. coli* replisome and β_2 clamp assembly during replication. (a) The position of the β_2 sliding clamp within the *E. coli* replisome complex. The helicase (DnaB) unwinds dsDNA ahead of the replicative polymerase (DNA Pol III) which subsequently duplicates the template strands. Different configurations of Pol IIII are potentially possible. Primase (DnaG) synthesizes short RNA primers on the lagging strand for Okazaki fragment initiation. Single-stranded binding proteins (SSB) remove the secondary structure of ssDNA and protect it from digestion. To ensure sufficient processivity during replication, Pol III is tethered to the DNA by the β_2 sliding clamp. β_2 is assembled onto primer-template junctions by the multi-protein($(\tau/\gamma)_3\delta\delta'\psi\chi$) clamp-loader complex. (Inset) A ribbon representation of the DNA-bound β_2 sliding clamp (generated using the Protein Data Bank (PDB) file, 2POL[16]). The β_2 sliding clamp is a homo-dimer that consists of six globular domains [16]. The monomers are arranged in a ring that encircles the DNA [19] and can slide freely along it. Different proteins can bind to the two hydrophobic pockets of the β_2 clamp via a conserved sequence motif [10]. (b) The life cycle of the β_2 clamp during replication. (top) The β_2 clamp is actively loaded by the clamp-loader, which opens the closed clamp and places it onto dsDNA prior to release [20]. (middle) The β_2 clamp remains DNA-bound as long as an Okazaki fragment is being synthesized. (bottom) After the β_2 clamp has reached the end of an Okazaki fragment, DNA Pol III is signaled to release [21]. The β_2 clamp is believed to be disassembled by the clamp-loader.

reused at a successive primer-template junction [35]. Two *in vivo* studies, one in *Bacillus subtilis* (*B. subtilis*) [36] and the other in *E. coli* [28], provided contrasting results. Hence, to understand the regulatory mechanism that underlies the recycling of β_2 clamps in *E. coli*, further insights into their *in vivo* dynamics are required.

To gain detailed insight into the *in vivo* recruitment and turnover of the β_2 clamp, we investigate its dynamics in individual live cells with single-molecule sensitivity. We employ both conventional fluorescence microscopy and Photoactivated Localization Microscopy (PALM) [37, 38], in combination with custom-built microfluidics. Single-molecule techniques have provided us with insights into the dynamics of processes – such as replication, transcription, and translation – that are not readily accessible with conventional ensemble-averaging techniques [39, 40] *In vivo* single-molecule fluorescence imaging in particular has provided detailed insights into the behavior of individual molecules in live cells [41–43]. Combining single-molecule fluorescence microscopy with microfluidics allows us to image individual molecules in live cells over multiple cell cycles, without chemical fixation that could potentially perturb the dynamic behavior of the protein under investigation [44].

By employing this experimental approach, we have measured the number of DNA-bound β_2 clamps during chromosomal replication over the entire course of the cell cycle. Additionally, we have determined the time required to unload an individual DNA-bound β_2 clamp during replication, as well as the effective time required to load a new β_2 clamp during replication. Our data reveal that the number of DNA-bound β_2 clamps accumulates on the DNA after initiation, and then levels off to a constant steady state number of DNA-bound β_2 clamps on the order of minutes. This steady state is maintained throughout the rest of the replication process, until termination occurs and a concomitant decrease of DNA-bound β_2 clamps is observed. The number of DNA-bound β_2 clamps in steady state exceeds the estimates of a previously published *in vivo* study [28] by an order of magnitude. The measured values for the effective loading time and unloading time during replication, in the context of the live cell, are in good agreement with previous biochemical *in vitro* experiments [26]. Taken together, our data indicate a β_2 clamp remains on the DNA for a protracted period of time following the completion of an Okazaki fragment. DNA-bound β_2 clamps that are left behind during fork progression may facilitate the recruitment of additional proteins active during the cell cycle for different processes such as DNA repair.

5.2. RESULTS

5.2.1. THE *in vivo* DYNAMICS OF β_2 CLAMPS MEASURED IN SINGLE CELLS.

To study the dynamics of β_2 clamps by wide-field fluorescence microscopy, we perform long time-lapse imaging of labeled β_2 clamps over multiple replication cycles. During such experiments, we ensure healthy cell physiology by implementing a custom-built microfluidic device (Figure 5.2a; See Methods) [45, 46] in which cells growing in steady state are immobilized in micron-sized growth channels. Through a neighboring central trench, growth medium is continuously supplied throughout an experiment (See Methods). In such a microfluidic device, cells experience minimal perturbation over the course of the time-lapse experiment, as stable growth conditions remain continuously present. This contrasts with long time-lapse experiments performed on agarose pads in which nutrients and water may become depleted, leading to non-steady state cell populations as result. Additional benefits of such a device are that daughter cells ultimately grow out of the growth channels, preventing accumulation of cells, and that the cells are always aligned, which facilitates data analysis.

Labeling of the β_2 clamp was accomplished by using a functional N-terminal YPet [47] fusion [28] (Supplementary Figure 5.1; Supplementary Table 1; See Methods) expressed from (and replacing) the endogenous *E. coli dnaN* gene locus. Fluorescence images are acquired under shuttered 515 nm laser excitation (See Methods; Figure 5.2a (inset)). Fluorescence images of YPet$-\beta_2$ within individual cells either yielded no (Figure 5.2b, left),

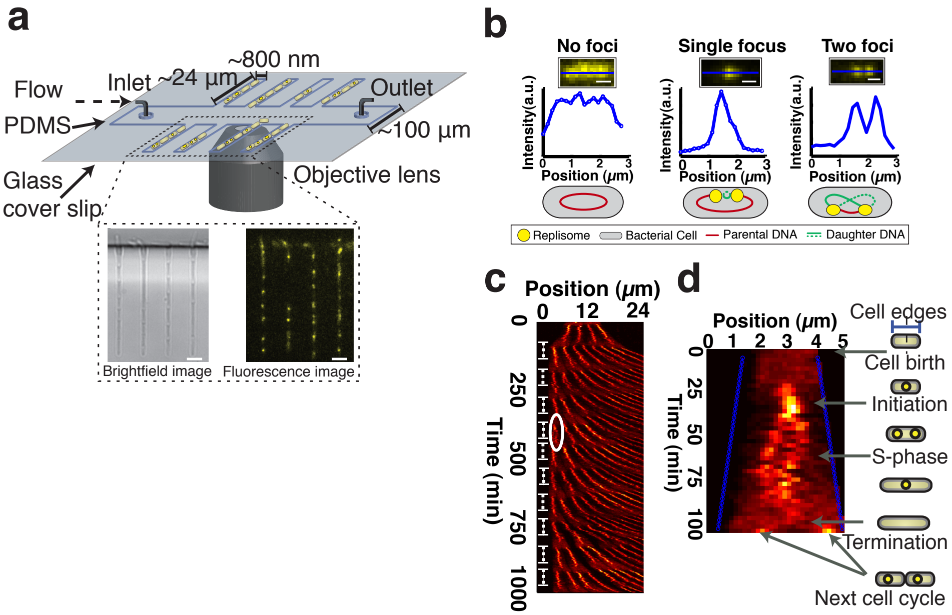

Figure 5.2: Long time-lapse fluorescence microscopy of the β_2 sliding clamp at the single-cell level utilizing microfluidics. (a) The microfluidic device used for performing long-time lapse fluorescence microscopy. *E. coli* cells are immobilized in growth channels perpendicular to a main trench through which growth medium is actively pumped. (inset) A brightfield image and corresponding YPet–β_2 fluorescence image (80 ms laser light exposure) are acquired every 2.5 min for the duration of the time-lapse experiment. Scale bars, 3 μm. (b) YPet–β_2 molecules that are either DNA-bound or freely diffusing are studied using wide-field fluorescence microscopy. (left) Freely diffusing YPet–β_2 molecules in the cytoplasm of a cell. This signal is representative to YPet–β_2 dynamics prior to and after replication. (middle) A clear focus is observed due to DNA-bound YPet–β_2 molecules. The observation of a single focus, instead of two distinct foci, shortly after initiation results from the overlap of diffraction limited spots. (right) Two distinct foci are visible, indicative of two individual replisomes. Scale bars, 800 nm. (c) Kymograph of a single growth channel during an overnight time-lapse experiment. The cells first grow the growth channel full, and maintain a steady state growth rate as can be observed from the curved shape of the fluorescence signal. The shape of the fluorescence signal is due to the individual cells growing and pushing each other in the direction of the main trench. Clear observable diffuse patterns occur at regular intervals, indicative of no DNA-bound β_2 clamps prior to initiation or after termination. This repeating pattern is due to the multiple cycles of replication (indicated with repeating white dashed lines). (d) A kymograph of an individual replication cycle indicated in panel (c). The blue lines are the cell boundaries detected from the brightfield images. The illustrations on the right-hand side indicate the different stages of replication that can be observed during the cell cycle.

a single (Figure 5.2b, middle), or two cellular foci (Figure 5.2b, right), depending on the stage of replication, in agreement with previous reports of fluorescently labeled replisome components [48]. Prior to each fluorescence image, a brightfield image is acquired to provide details of the cell periphery (Figure 5.2a (inset)). This alternating imaging sequence has a sufficiently long period to avoid giving rise to any notable deleterious growth effects, as assessed by comparing the doubling time of cell growth in a shake flask with cells grown in the micro-fluidic device (Supplementary Figure 5.1, 5.2).

Using this approach, we are able to observe numerous consecutive replication (and corresponding division) cycles of cells in the different growth channels. We examine the global replication dynamics of multiple cells within a growth channel by converting the time-lapse images into a kymograph (Figure 5.2c; See Methods). A distinct reoccurring pattern indicative of multiple replication cycles in generations of cells is clearly noticeable (indicated in repeating dashed lines in Figure 5.2c). Under these experimental conditions (See Methods), the analysis of individual cells (n = 137) in our microfluidic system yields an average replication time (C-period) of $t_{\text{rep}} = 68 \pm 10\,\text{min}$, and a doubling time of $t_{\text{double}} = 84 \pm 17\,\text{min}$ (Supplementary Figure 5.2). In both cases the error is ± s.d. We further analyze these kymographs to investigate the sub-cellular dynamics of the YPet−β_2 molecules within individual cells from cell birth till cell division (Figure 5.2d). One can clearly observe the dynamic of the two β_2 clamp foci associated with the two independent replisomes.

5.2.2. THE ASSEMBLY AND ACCUMULATION OF β_2 CLAMPS ON DNA.

We use the fluorescence intensity from the YPet−β_2 fusion to determine the number of β_2 clamps that are DNA-bound as well as in the total number in the cell during the life cycle of a cell. A sample montage of the YPet−β_2 fluorescence signal from cell birth till after cell division (Figure 5.3a) illustrates that there is a distinct increase in the foci following the B-period[49] of the cell cycle (represented by a diffuse signal after birth) (5.3a (inset)) and a similar decrease prior to cell division. The fraction of fluorescence that originates from DNA-bound YPet−β_2 (foci) provides clear evidence that > 50 % of β_2 clamps are DNA-bound shortly after initiation of replication (5.3b). The steady decline in the fraction of DNA-bound β_2 clamps that commences roughly 10 min after initiation, results from the increase of total number of β_2 clamps in the cell as the cell grows. In assessing this intensity fraction, we verified that very little out-of-focus fluorescence escapes detection (Supplementary Section S5.1; Supplementary Figure 5.3).

5.2.3. A CONSTANT NUMBER OF DNA-BOUND β_2 CLAMPS IS MAINTAINED.

To precisely quantify the number of DNA-bound β_2 clamps as function of the replication cycle, we exploited a single-molecule *in vitro* calibration method [28] that allows us to reliably convert the detected YPet−β_2 signal into an absolute number of molecules (Supplementary Section S5.2). We immobilize single purified YPet molecules on a cover glass and determine the average intensity of a single YPet fluorescent protein under these conditions (Supplementary Figure 5.4). Using this calibration, we perform control stoichiometry experiments of previously studied DNA-bound replisome components [28], specifically the ϵ-subunit of Pol III and the τ-subunit of the clamp-loader to verify that our *in vitro* single-molecule calibration remains reliable *in vivo* [50] (Supplementary Figure 5.5). For both the proteins, we reproduced the stoichiometry for the pair of sister replisomes as previously published [28], namely 5.74 ± 0.04 molecules in total for the ϵ-subunit (n = 64) and 6.12 ± 0.03 molecules in total for the τ-subunit (n = 66). Here the error is ± s.e.m. We also verified that a YPet-β intensity standard provides the same mean intensity value under our experimental conditions (Supplementary Figure 5.4g). Therefore, we subsequently use this average intensity value to estimate the number of β_2 clamps in our experiments. In calculating the number of YPet−β_2 molecules, we correct

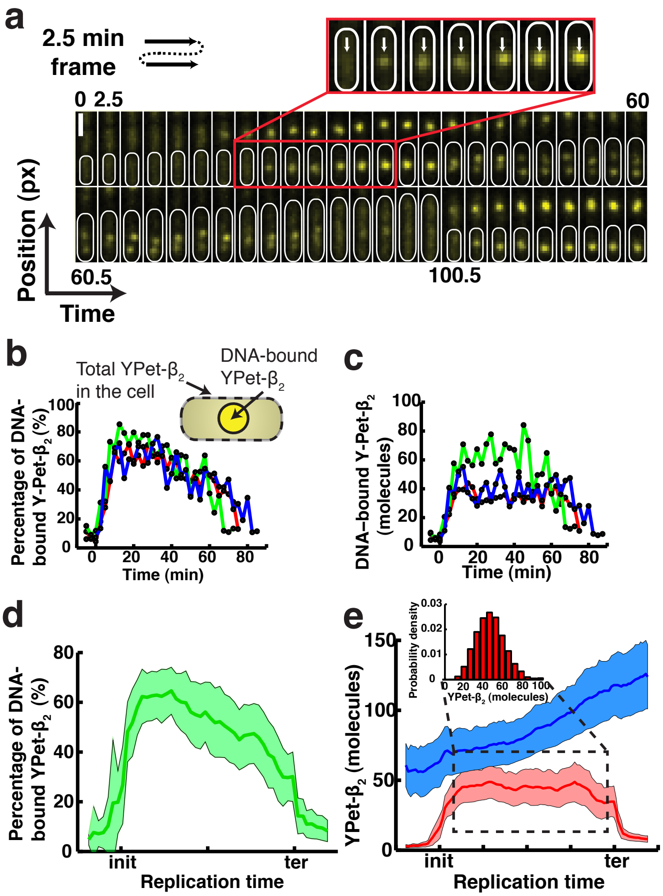

Figure 5.3: Quantification of the *in vivo* β_2 sliding clamp stoichiometry during replication. (a) A representative temporal montage of the YPet-β_2 fluorescence signal from prior to initiation until after cell division. A clear intensity increase is observed at the focus formation following initiation (indicated with white arrows in inset) Scale bar, 1.6 μm. (b-c) Traces of focus formation in individual cells. In (b) we plot the fraction of YPet-β_2 molecules that are DNA-bound compared to the total number in the cell. More than than 50 % of the total YPet-β_2 molecules are DNA-bound. The gradual decline in this fraction results from the increase of β_2 during the cell cycle. The inset indicates how the DNA-bound YPet-β_2 molecules and the total YPet-β_2 in the cell are defined. In (c) we plot the absolute number of DNA-bound YPet-β_2 molecules. Here the gradual increase, steady state and gradual decrease of the DNA-bound YPet-β_2 molecules can clearly be seen. In both (b) and (c) the traces have been aligned with respect to initiation. (d-e) The average behavior of individual YPet-β_2 molecules measured in individual cells. (d) The fraction of DNA-bound YPet-β_2 molecules is on average > 50 % half way through the replication cycle. (e) The YPet-β_2 molecules in the whole cell (blue curve) approximately doubles during the cell cycle, from 60 to 120 YPet-β_2 molecules. The DNA-bound YPet-β_2 molecules (red curve) remarkably increases to a mean steady state value of 46 YPet-β_2 molecules (s.d. = 12, s.e.m. = 1) following initiation. This value is maintained throughout the replication process until a concomitant decreases is observed after or during termination. Individual traces have been normalized with respect to initiation and termination to make averaging possible. (inset) A histogram of the distribution of number of DNA-bound YPet-β_2 molecules during steady state. (n=137).

for photo-bleaching (Supplementary Section S5.3; Supplementary Figure 5.3) and verify that the fraction of immature, dark YPet proteins is negligible (Supplementary Section S5.4, Supplementary Figure 5.3). In our conversion from intensity to molecules, we also take into account that β_2 clamps are dimers by dividing the measured YPet signal by two. This is a realistic assumption since it is believed that β_2 clamps are in closed conformation even when they are not DNA-bound [20].

Using this calibration standard, we quantify the absolute number of DNA-bound YPet$-\beta_2$ molecules for individual traces of DNA replication. Representative individual time-traces of single cells clearly demonstrate that following initiation of replication, a gradual increase of the number of DNA-bound β_2 occurs until a steady state plateau is reached (Figure 3c). This plateau is maintained until decrease is observed shortly after or during termination (Figure 3c). From the individual traces, one can observe that there is significant cell-to-cell variability in the absolute number of DNA-bound β_2 clamps, but that the overall trend in which the number of DNA-bound β_2 clamps is constant for a significant fraction of the cell cycle is the same for all cells. We compared this temporal behavior to that of a different replisome component, the $\tau-$subunit of the clamp-loader in a strain in which both the β_2 clamp and the τ-subunit are fluorescently labelled. (Supplementary Section S5.5). The τ-YPet fluorescence signal fluctuates strongly and does not yield a stable plateau, in contrast to the mCherry-β_2 fluorescent signal (Supplementary Figure 5.6).

To obtain a statistically significant values for both the total number of β_2 clamps in the cell and the number of DNA-bound β_2 clamps, we extracted the average behavior from analysis over numerous cells (n=137) (Figure 5.3d,e). Figure 5.3d clearly depicts that for an average cell the fraction of DNA-bound β_2 clamps is more than half of the total content in the cell, which decreases to roughly zero after termination. During the cell cycle, an average cell doubles its YPet$-\beta_2$ content from approximately 60 to 120 molecules. This number of β_2 clamps in the cell is in good agreement with ensemble Western estimates we performed under the same growth conditions (Supplementary Section S5.6; Supplementary Figure 5.7). Remarkably, the number of DNA-bound YPet$-\beta_2$ is held at a stable value of $N_{\beta_2} = 46$ (s.d. = 12, s.e.m. = 1) (Figure 5.3e (inset)). We also observe that the number of DNA-bound β_2 clamps are close to zero prior to initiation and after termination. We ruled out the presence of an ectopic *dnaN* gene, by verifying that only a single copy of the *dnaN* gene is present in the strain that we used for these experiments (Supplementary Section S5.7; Supplementary Figure 5.7). The experiment was successfully reproduced with a different fluorescent protein fusion (mCherry-β_2), which strengthens the argument that accumulation is unlikely the result of fluorophore aggregation [51, 52], but rather due to physiological build-up of DNA-bound clamps (Supplementary Section S5.8; Supplementary Figure 5.8). The slightly lower mean number of DNA-bound clamps ($N_{\beta_2} = 34$, s.d. = 12, s.e.m. = 1.5) as measured using the mCherry-β_2 protein fusion, in combination with the mCherry intensity calibration , possibly results from the less ideal photophysical properties of mCherry, which make it less suitable than YPet for rigorous quantitative fluorescence microscopy.

5.2.4. SINGLE β_2 CLAMPS ARE NOT RAPIDLY UNLOADED *in vivo*.

To study the *in vivo* unloading time of an individual β_2 clamp, we utilized single-molecule PALM (Figure 5.4a). The endogenous *dnaN* gene was replaced with a functional N-terminal PAmCherry [53] fusion (See Methods). Fluorescence images are acquired under shuttered 561 nm excitation (See Methods), while activation is performed once with low 405 nm laser illumination, such that on average less than one DNA-bound PAmCherry-β per cell is activated. Prior to fluorescence activation, a PH image is acquired to determine the cell's position and its periphery. Sample pre- and post-activation images (Figure 5.4b), together with the corresponding line-profile intensity plots (Figure 5.4c), demonstrate successful activation of individual DNA-bound PAmCherry-β molecules in our strain. The advantage of PALM over more conventional techniques like Fluorescence Recovery After Photobleaching (FRAP) and Fluorescence Loss In Photobleaching (FLIP) for measuring protein turnover is that it allows one to directly image a single unloading event, as shown in the sample temporal montage and the corresponding integrated intensity trace (Figure 5.4d). We image a different field of view of cells for each complete PALM measurement sequence (Figure 5.4a) to ensure that the cell physiology and β_2 clamp behavior are not influenced by excessive 405 nm light exposure. Using the individual analyzed traces from different cells, we are able to build up a distribution for the on-time events of single PAmCherry$-\beta$ molecules (Figure 5.4d). In order to visualize a single unloading event, we only image one out of the two PAmCherry$-\beta_2$ dimer subunits. After correcting for photo-bleaching (Supplementary Section S5.9; Supplementary Figure 5.9), we estimate the *in vivo* unloading time to be $t_{\text{unload}} = 195 \pm 58\,\text{s}/\beta_2$ (Figure 5.4e) . This result is in good agreement with previous *in vitro* experiments ($127\,\text{s}/\beta_2$) [26].

5.2.5. THE EFFECTIVE *in vivo* LOADING RATE OF β_2 CLAMPS.

The *in vivo* loading time of a β_2 clamp during chromosomal replication provides us with insight into how frequently a new clamp β_2 is needed for processive genome duplication. We utilize both the long-time lapse and the single-molecule PALM data to compute the effective loading time *in vivo* of a new β_2 clamp ($t^{\text{eff}}_{\text{load}}$). The designation 'effective' is added since we do not directly measure the loading of an individual β_2 clamp, but rather the total loading rate of β_2 clamps onto DNA. We have shown in the preceding section that the number of DNA-bound β_2 clamps remains essentially constant ($\text{N}_{\beta_2} = 46$) during ~ 2/3 of the replication process. We independently determined the *in vivo* unloading time via PALM to be $t_{\text{unload}} = 195\,\text{s}/\beta_2$ during replication. In the steady state regime, the total unloading rate of β_2 clamps is balanced by the effective loading rate of β_2 clamps ($t^{\text{eff}}_{\text{load}}$) onto newly formed primer for Okazaki fragment synthesis:

$$\frac{1}{t^{\text{eff}}_{\text{load}}} = N_{\beta_2} \cdot \frac{1}{t_{\text{unload}}}. \tag{5.1}$$

Using Equation (5.1), we compute the *in vivo* effective loading time for a β_2 clamp during replication to be $t^{\text{eff}}_{\text{load}} = 4 \pm 1\,\text{s}/\beta_2$. The reader is referred to Supplementary Section S5.10 and Supplementary Figure 5.10 for a more detailed discussion of Equation (5.1).

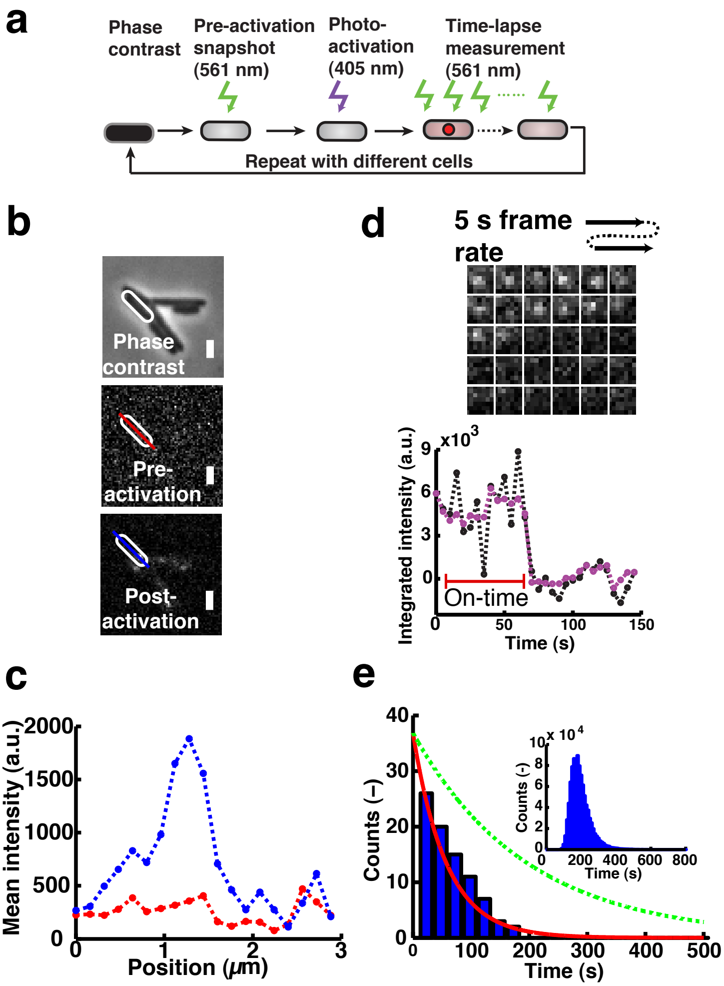

Figure 5.4: Direct measurement of the *in vivo* unloading time of the β_2 sliding clamp during replication. (a) Illustration of the measurement sequence to image a single β_2 clamp unloading event. First a phase contrast (PH) and pre-activation snapshot are taken, after which molecules are activated only once, and subsequently imaged until foci are no longer visible (b-c) Single PAmCherry$-\beta$ molecules are visualized by PALM. The sample PH image together with the respective pre-activation and post-activation fluorescence images illustrate that a single PAmCherry$-\beta$ molecule can successfully be photo-activated. The corresponding pre-activation (red) and post-activation (blue) line profile plots of the single DNA-bound PAmCherry$-\beta$ molecule. Scale bars, 1.6 μm. (d) A representative example of a montage showing the fluorescence intensity of a PAmCherry-β molecule over time and the corresponding intensity trace of the signal. The single-step disappearance is indicative of a single molecule. (e) On-time distribution for individual PAmCherry-β molecules (n=84) fitted with an exponential (red line), and the distribution for the unloading times corrected for photobleaching (dashed green line). The inset shows the distribution of the fitted unloading time constants over the 10^6 bootstrapped data sets from which the confidence interval for the unloading time is determined.

5.3. DISCUSSION

DNA replication, orchestrated by the multi-protein replisome-complex, is a process essential to cell viability. By using *in vivo* single-molecule fluorescence microscopy in combination with microfluidics, we were able to investigate the detailed dynamics of an essential component of the replisome, the β_2 clamp, during DNA replication in live *E. coli* cells. Lagging-strand synthesis is a complex and highly dynamic process, and the sliding clamp is one of the key proteins involved. Each new primer-template junction requires a loaded β_2 clamp to ensure processive replication by DNA Pol III, which is signaled to cycle from one Okazaki fragment to the next [21] as the replication fork progresses at approximately 600 bp/s. Given the average replication fork speed and the typical size of an Okazaki fragments (1-2 kb), one would expect a β_2 clamp to be necessary $\sim 1.5 - 3$ s. Leading-strand synthesis might be less processive than commonly believed, which would imply that a new β_2 clamp would also need to be loaded on the leading-strand. In what follows however, we have assumed that during normal replication the exchange of β_2 clamps on the leading-strand is a much less frequent occurrence than β_2 clamp exchange for the lagging-strand. It was until now not demonstrated *in vivo* whether these loaded β_2 clamps are predominantly recycled (i.e., immediately unloaded and reloaded) between successive Okazaki fragments, or whether β_2 clamps remain bound to a completed fragment for a prolonged period of time.

Our results indicate that the number of DNA-bound β_2 sliding clamps increases during the course of the cell cycle, peaking at more than twenty behind an individual fork. Following initiation of replication, we observe that the number of DNA-bound β_2 clamps gradually increases until a steady state plateau is reached. This plateau, whose magnitude is such that about 50 % of the total β_2 clamps in the cell are DNA-bound, is maintained throughout the remainder of the cell cycle. We determined the number of β_2 clamps in the cell $(60 - 120)$ during replication, as well as the total number of DNA-bound β_2 clamps $(N_{\beta_2} = 46)$. After termination, β_2 clamps are presumably no longer being loaded, and the fraction of DNA-bound β_2 clamps decays accordingly.

Notably, our measurements for the number of DNA-bound β_2 clamps differ from the value measured previously by some of us in a comprehensive *in vivo* study of the whole *E. coli* replisome complex [28]. In this study, the number of β_2 clamps was estimated to be 3 for each of the two independent replisomes [48], for a total of 6 DNA-bound β_2 clamps present during replication. We note that stoichiometries for most other proteins have been duplicated independently, and therefore the difference of the number of DNA-bound β_2 clamps appears an isolated case [29]. While we cannot fully explain the difference in the number of DNA-bound β_2 clamps, we can nonetheless delineate some possible contributions. The difference may result from the cell physiology due to the immobilization method, lower statistics due to the challenging nature of the 'slim-field' experiments at the time, or due to inadvertent changes of the imaging system since measurements spanned across months in the earlier study. It is thus crucial to maintain healthy cell physiology and cell cycle synchronization during experiments, which highlights the utility of microfluidics in live cell single-molecule fluorescence measurements.

The substantial number of DNA-bound β_2 clamps behind each replication fork suggests that β_2 clamps are not rapidly recycled during replication. To corroborate this view, we have utilized PALM to directly measure the *in vivo* unloading rate of a single β_2 clamp ($t_{\text{unload}} = 195\,\text{s}/\beta_2$). Together with the number of DNA-bound β_2 clamps in steady state this allows us to calculate the effective time of loading (Equation (5.1)) a β_2 clamp during replication as $t^{\text{eff}}_{\text{load}} = 4\,\text{s}/\beta_2$. This result is in good agreement with our previous calculated average estimate of the primer formation time using the Okazaki fragment size range and the typical size of the *E. coli* genome. Also, this effective loading rate is in accordance with the model that DnaG sets the fork speed [31]. DnaG is thought to synthesizes RNA primers at a rate of approximately one primer every one to two seconds [54], which is in good agreement with our calculated *in vivo* effective loading time. We suggest that an individual β_2 clamp remains on the DNA for a protracted period of time during chromosomal replication, as has been proposed on this basis of *in vitro* experiments [26, 55] and plasmid replication [56]. Our results are in agreement with the behavior of the sliding clamp for the Gram-positive bacterium *B. subtilis* [36]. In this bacterium, the number of DNA-bound β_2 clamps was estimated at ~ 200 during replication, indicative of clamps being left behind during fork progression. There is a slight possibility that the loading and unloading reaction could be sterically hampered by the fusion protein. However, we have no reason to believe that this is the case since our results are in very good agreement with previous *in vitro* [26] and *in vivo* work [36]. Our study shows that rapid recycling of β_2 clamps for subsequent lagging-strand synthesis [35], though observed in *in vitro* experiments in the absence of excess β_2 clamps in solution, is not the predominant mode *in vivo*. While our data does not exclude that β_2 clamps are rapidly recycled at the replication fork, the fact that the loading rate from solution matches the estimated primer formation rate strongly suggests that direct recycling is not the dominant mode of clamp loading.

To illustrate the overall β_2 clamp dynamics during replication, we perform a Monte Carlo simulation (See Methods) that takes our experimentally determined values for N_{β_2}, t_{unload}, $t^{\text{eff}}_{\text{load}}$ and t_{rep} as input parameters (Figure 5.5a). Since the approximate rate of clamp removal during termination (Figure 5.3e) agrees with the value measured by PALM during steady-state replication ($\sim 195\,\text{s}/\beta_2$), we simply input the latter (likely more accurate) value into the simulations. The simulation starts at $t = 0$ with no DNA-bound β_2 clamps, after which it takes $< 10\,\text{min}$ to reach a stable steady state number of β_2 bound to DNA (Figure 5.5b, left). This value is maintained for $\sim 60\,\text{min}$ (Figure 5.5b, middle), after which termination occurs and clamps are unloaded in $< 5\,\text{min}$ (Figure 5.5b, right). The number of β_2 clamps in steady state as well as the rise and fall times underline our measured results, and are depicted schematically in Figure 5.5c.

The steady state build-up of DNA-bound β_2 sliding clamps forms a β_2-landing pad [36] for different proteins to dock themselves to DNA during the life cycle of the cell. Numerous different proteins utilize the β_2 clamp via the same binding pocket [57] to perform their respective biological function. These other β_2 clamp-binding proteins range from DNA ligase for Okazaki fragment maturation, inactivation of DnaA through the β_2–Hda$_2$ interaction [11–13, 58, 59], potential screening of DNA damage due to sliding capability

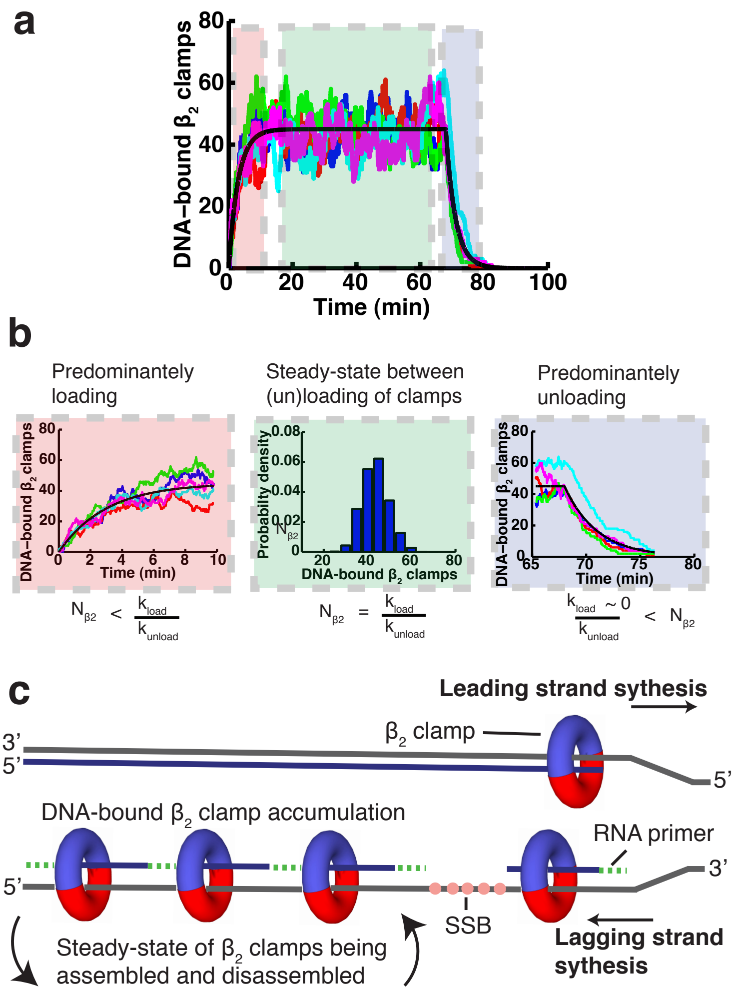

Figure 5.5: Describing the β_2 sliding clamp recycling process during replication. (a) A Monte Carlo simulation of the β_2 clamp assembly and disassembly reaction. For illustrative purposes we perform a Monte Carlo simulation of the proposed model, utilizing the experimentally determined primer formation and unloading rate, as well as the replication time, and under the assumption that primer formation is rate limiting. We show the simulation results for 5 individual traces (coloured lines). The black curve is the analytical solution for the average number of loaded β_2 clamps. Here we divide the total trace into three time regions, namely initiation (red), steady state (green) and termination (blue). (b) A zoom of the different sections from (a). (left) A build-up of loaded β_2 clamps on the DNA proceeds for ~ 10 min. (middle) After the gradual accumulation of loaded β_2 clamps, a steady state plateau of 46 DNA-bound β_2 clamps is maintained for approximately 2/3 of the replication process. (right) After termination, all DNA-bound β_2 clamps are unloaded in ~ 5 min. (c) A cartoon illustrating the DNA-bound β_2 clamp build up during replication. As the rate at which β_2 clamps are loaded (one every 4 s) is much faster than the unloading rate of individual β_2 clamps (once every 195 s) during replication, there will be a dynamic reservoir of β_2 clamps that have not yet been unloaded left on the lagging strand.

of the β_2 clamps [57], the tethering of the necessary polymerases for repair [4–8], overcoming replication barriers [60], as well as coupling mismatch-detection and replication by positioning MutS at newly replicated DNA [61]. It is still unclear which of the above mentioned(or other) proteins are the main users of the DNA-bound clamps that are not directly situated at the replication fork. Since Okazaki fragment maturation seems to be relatively fast as assessed via Ligase and Pol I dynamics [62], it is likely not these proteins that predominantly occupy the DNA-bound clamps. The extent to which DNA-bound β_2 clamps are utilized while being docked to the Okazaki fragment will most likely be dependent on the physiological state of the cell at a particular time in its cell cycle. In the case of stress conditions, for example, MutS and the different repair polymerases might predominantly make use of DNA-bound β_2 clamps, while under minimal stress conditions ligase, CrfC and Hda_2 are the likely candidates. A thorough *in vivo* investigation of the stoichiometry and dynamic of different β_2 associated proteins over the course of the cell cycle would provide the quantitative underpinning required to provide further insight into these biological processes.

5.4. METHODS

5.4.1. STRAINS AND STRAIN CONSTRUCTION.

All strains are derivatives of *E. coli* K12 AB1157 Strains were constructed either by P1-transduction [63] or by λ-red recombination [64].

The *Ypet-dnaN*:*tetR-mCerulean* was constructed using P1 transduction by transducing the *YPet-dnaN* fusion [28] together with the adjacent *kanR* gene into a strain that contains a *tetO* array (50 kb clockwise from the dif-site) as well as the chromosomal integrated chimeric gene *tetR-mCerulean* [48]. The presence of the *YPet-dnaN* gene fusion was verified using the oligonucleotides: 5' – CGT TGG CAC CTA CCA GAA AG – 3' and 5' – ATG CCT GCC GTA AGA TCG AG – 3'. The sequence of the *YPet-dnaN* fusion was confirmed by DNA sequencing.

A chromosomal fusion of the gene encoding for the photoactivatable fluorescent protein (PAmCherry1) [53] to the N-terminus of the *dnaN* gene was created using λ-red recombination [64]. The gene encoding for PAmCherry1 was amplified by PCR. The forward primer used contains an *XmaI* restriction site (5' – GCG GGC CCC GGG ATG GTG AGC AAG GGC GAG GAG – 3'). The reverse primer used contains a sequence coding for a 11 amino acid linker and a *SacI* site (5' – CGA TCG GAG CTC CGC GCT GCC AGA ACC AGC GGC GGA GCC TGC CGA CTT GTA CAG CTC GTC CAT GCC – 3'). The PCR product was cloned into the backbone of pROD44 [28] containing a kanamycin resistance cassette, flanked by *frt* sites, resulting in the template plasmid PAmCherry1.

This plasmid was then used as a template plasmid for generating the insert sequence used during λ-red recombination to create the *PAmCherry-dnaN* strain. The primer sequences used were: Forward 5' – ACG ATA TCA AAG AAG ATT TTT CAA ATT TAA TCA GAA CAT TGT CAT CGT AAC TGT AGG CTG GAG CTG CTT C – 3'; Reverse 5' – ACC TGT TGT AGC GGT TTT AAT AAA TGC TCA CGT TCT ACG GTA AAT TTC ATC GCG CTG CCA

GAA CCA GCG G – 3’. The DNA fragment was gel purified and ~ 700 ng of the linear DNA was used for electroporation of AB1157 cells over expressing λ-Red proteins from pKD46 [64]. The correct insertion of the fragment into the chromosome of the resulting strain was assayed by PCR. The oligonucleotides used were 5’ – CGT TGG CAC CTA CCA GAA AG – 3’ and 5’ – ATG CCT GCC GTA AGA TCG AG – 3’. The sequence of the fusion gene in this strain was confirmed by DNA sequencing.

Construction of the *mCherry-dnaN* strain. The *mCherry* gene was amplified by PCR. The forward primer used for this contains an *XmaI* restriction site (5’ – TAG GCT CCC GGG ATG AGC AAG GGC GAG GAG GAT AAC – 3’). The reverse primer used contains a *SacI* site and sequence coding for an 11 amino acid linker (5’ – AAG GAG CTC GCG CTG CCA GAA CCA GCG GCG GAG CCT GCC GAC TTG TAC AGC TCG TCC ATG CC – 3’). The *Frt* flanked kanamycin resistance gene was amplified using the following primers: Forward 5’ –TTA CCC GGG CAT ATG AAT ATC CTC CTT AG-3’; Reverse 5’-TTA GGA TCC TGT AGG CTG GAG CTG CTT CG – 3’. The resulting fragment was digested with *XmaI* and *BamHI*. The *mCherry* fragment and the kanamycin fragment were cloned into pUC18 between *SacI* and *BamHI* sites.

The λ-red recombination was performed as mentioned in the previous section using the primers: Forward 5’ – TAT CAA AGA AGA TTT TTC AAA TTT AAT CAG AAC ATT GTC ATC GTA AAC CTG TAG GCT GGA GCT GCT TCG – 3’; Reverse 5’ – ACC TGT TGT AGC GGT TTT AAT AAA TGC TCA CGT TCT ACG GTA AAT TTC ATC GCG CTG CCA GAA CCA GC – 3’. The presence of the gene fusion was verified using oligonucleotides 5’ – CGT TGG CAC CTA CCA GAA AG – 3’ and 5’ – ATG CCT GCC GTA AGA TCG AG – 3’. The sequence of the fusion gene in this strain was confirmed by DNA sequencing.

The *dnaX(τ)-YPet*:*mCherry-dnaN* strain was constructed using P1 transduction by transducing the *dnaX-YPet* fusion [28] together with the adjacent *kanR* gene into a strain that contains the *mCherry-dnaN* gene fusion. The presence of the *dnaX-YPet* gene fusion after transduction was verified using the oligonucleotides: 5’ – GAG CCT GCC AAT GAG TTA TC – 3’ and 5’ – GGC TTG CTT CAT CAG GTT AC – 3’ and similarly the *mCherry-dnaN* fusion using, 5’ – CGT TGG CAC CTA CCA GAA AG – 3’ and 5’ – ATG CCT GCC GTA AGA TCG AG – 3’. The sequences of the fusions in this strain were confirmed by DNA sequencing.

Supplementary Tables 2 and 3 provide an overview of the plasmids used, as well as a summary of the different strains. The cell morphology and the doubling times of the fusion strains in LB and M9-glycerol growth medium were compared to AB1157 wild type (WT). No significant differences were observed (Supplementary Table 1 and Supplementary Figure 5.1a). The doubling times of the cells in the microfluidic device were similar (slightly faster) compared to cells grown in a shake flask (Supplementary Figure 5.2). We also confirmed that in the the absence of IPTG (the experimental condition used during long-time lapse microscopy) no DNA-bound foci were detected for the *YPet-dnaN*:*tetR-mCerulean* strain. (Supplementary Figure 5.1b).

5.4.2. M9 GROWTH MEDIUM USED IN EXPERIMENTS.

The M9 growth medium used in experiments is as follows. 1 L of M9 growth medium contains 10.5 g/L of autoclaved M9 broth (Sigma-Aldrich); 0.1 mM of autoclaved $CaCl_2$ (Sigma-Aldrich); 0.1 mM of autoclaved $MgSO_4$ (J.T.Baker); 0.3 % of filter-sterilized glycerol (Sigma-Aldrich) as carbon source; 0.1 g/L of filter-sterilized 5 amino acids, namely L-threonine, L-leucine, L-proline, L-histidine and L-arginine (all from Sigma-Aldrich) and 10 μL of 0.5 % filter-sterilized Thiamine (Sigma-Aldrich).

5.4.3. MICROFLUIDICS FOR EXTENDED TIME LAPSE MICROSCOPY.

We use our own design [45] of the previously published microfluidic device known as the *mother machine* [46] for cell immobilization during long time-lapse experiments. The reader is referred to Moolman *et al.* [45] for a detailed description of the complete fabrication process. Here we only briefly outline the main steps involved. First, we use electron-beam lithography in combination with dry etching techniques to create the structure in silicon. Next, we make a negative mold of this structure in polydimethylsiloxane (PDMS). The PDMS mold is then used to fabricate the positive structure in PDMS which is subsequently used for experiments.

5.4.4. PREPARATION OF CELLS FOR MICROSCOPY.

Cells were streaked on Luria-Bertani (LB)-plates containing the appropriate antibiotic. Single colonies from these plates where inoculated overnight at 37 °C with shaking in M9 medium supplemented with 0.3 % glycerol (Gly), essential nutrients together with the appropriate antibiotics. The subsequent day the overnight culture was sub-cultured into the same medium and grown at 37 °C with shaking until an $OD_{600} \sim 0.2$ was reached. Cells were concentrated by centrifugation for 2 min at 16 100 g. The subsequent steps are dependent on the type of microscopy experiment performed as outlined next.

For agarose pad experiments, the supernatant was decanted and the pellet was resuspended in 100 μL M9-Gly supplemented with essential nutrients. The resuspended cells were subsequently vortexed for 2 s and immobilized on an M9-Gly 1.5 % agarose pad between two coverslips. (The coverslips were ultra-sonically cleaned in Acetone and Isopropyl alcohol and burned by a flame to minimize the fluorescent background prior to use).

For microfluidic device experiments, the supernatant was decanted and the pellet was resuspended in 50 μL M9-Gly with essential nutrients and injected into the microfluidic device. After injection into the device, the device was centrifuged for 10 min at 2500 g (Eppendorf 5810R) as to load the cells into the growth channels. Following centrifugation the device was mounted on the microscope with tubing attached and incubated for ~ 45 min at 37 °C. After incubation, fresh M9-Gly with essential nutrients and the appropriate antibiotics are flushed through the device. The syringe containing the medium is then attached to an automated syringe pump to continuously infuse fresh M9-Gly, essential nutrients and 0.2 mg/mL bovine serum albumin (BSA) through the device at a rate of 0.5 mL/hr.

5.4.5. MICROSCOPE SETUP.

All images were acquired on a commercial Nikon Ti microscope equipped with a Nikon CFI Apo TIRF 100x, 1.49 NA oil immersion objective and an Andor iXon 897 Electron Multiplying Charge Coupled Device (EMCCD) camera operated by a personal computer (PC) running Nikon NIS elements software. Cell outlines were imaged using the standard Nikon brightfield halogen lamp and condenser components. The fluorescence excitation was performed using custom-built laser illumination. A Cobolt Fandango 515 nm continuous wave (CW) diode-pumped solid-state (DPSS) laser was used to excite YPet, Cobolt Jive 561 nm CW DPSS laser was used to excited mCherry and PAmCherry respectively. PAmCherry was activated by a Votran Stradus 405 nm. All three laser beams were combined using dichroic mirrors (Chroma ZT405sp-xxr, 575dcspxr) and subsequently coupled into a single-mode optical fiber (KineFLEX). The output of the fiber was expanded and focused onto the back focal plane of the objective mounted on the microscope. Notch filters (Semrock NF03-405E, NF03-514E, NF03-561E) were used to eliminate any laser light leaking onto the camera. The emission of the different fluorescent proteins was projected onto the central part of the EMCCD camera using custom filter sets: Chroma z561, ET605/52m, zt561rdc (mCherry), Chroma z514, ET540/30m, zt514rd (YPet), Chroma zet405, ET480/40m, zt405rdc (CFP). A custom design commercial temperature control housing (Okolabs) enclosing the microscope body maintained the temperature at 37 °C. Sample position was controlled with a Nikon stage (TI-S-ER Motorized Stage Encoded, MEC56100) together with the Nikon Perfect Focus System (PFS) to eliminate Z-drift during image acquisition.

5.4.6. CELL LYSATE PREPARATION FOR INTENSITY CALIBRATION.

The cell lysate used for single-molecule intensity calibration was prepared as follows. Cells were grown overnight at 37 °C with shaking in M9 medium supplemented with 0.3 % glycerol (Gly), essential nutrients together with the appropriate antibiotics. The subsequent day the overnight culture was sub-cultured into the same medium and grown at 37 °C with shaking until an $OD_{600} \sim 0.5$ was reached. The cells were harvested by centrifugation at 6000x g (Beckman JLA 9.1000 rotor) for 15 min. Cells were subsequently resuspended in 5 mL M9-Gly and essential nutrients. The cell suspension was French pressed (Constant Systems) twice at 20000 psi. The cell lysate was then spun down at 30000x g (Beckman JA-17 rotor) for 35 min. The supernatant was shock frozen using liquid nitrogen and kept at −80 °C until needed.

5.4.7. DATA ACQUISITION.

All data acquisition was performed on the same microscope setup. Image acquisition was performed with Nikon NIS-elements software. The acquisition protocol was dependent on the type of experiment performed as outlined next.

Long time-lapse experiments were conducted as follows. The cell outlines were imaged using standard brightfield illumination. Subsequently, the sample was excited by laser excitation (515 nm) with an intensity of approximately $5\,\mathrm{W \cdot cm^{-2}}$ as calculated according to [65]. The exposure time was set to 80 ms. The camera gain was set to 100. Brightfield and fluorescence images were acquired every 2.5 min. Data spanning ~ 10 hrs of measurement were acquired overnight.

We conducted two types of PALM experiments. First, we determined the bleaching characteristic of PAmCherry under our experimental conditions, and secondly we measured the unloading time of a single β_2 clamp. PALM images where acquired as follows. First the cell outlines where imaged by taking a single phase-contrast (PH) image using a commercial Nikon external phase ring configuration. The sample was then excited for a single frame (400 ms exposure time) by a 561 nm laser with an intensity of approximately $5\,\mathrm{W}\cdot\mathrm{cm}^{-2}$, calculated according to Grünwald *et al.* [65]. This image was used to determine the auto-fluorescence level due to the sample prior to activation. Photoactivation of PAmCherry was done with a single pulse (5 s) of 405 nm with an intensity of approximately $2.5\,\mathrm{W}\cdot\mathrm{cm}^{-2}$, calculated according to Grünwald *et al.* [65]. Subsequently a post-activation time-lapse of images were acquired using the 561 nm laser at the same intensity at a frame rate of either ~ 700 ms (bleaching experiments) or 5 s (unloading experiments) with an exposure time of 400 ms per frame. Camera gain was set to 100.

5.4.8. IMAGE ANALYSIS OF LONG TIME-LAPSE EXPERIMENTS.

Images were analyzed with custom-written MATLAB software (MathWorks). Prior to any analysis, we subtract the uneven background using a rolling-ball filter [66] and subsequently corrected for illumination heterogeneity by using the previously measured laser beam profile [67]. We also align the brightfield and fluorescence signals with respect to each other with 1 pixel accuracy. X-Y drift is corrected in both the fluorescence and brightfield images by tracking a fiducial marker in the PDMS to within 1 pixel.

Each drift-corrected region of interest, consisting out of a single growth channel, is analyzed individually. The brightfield images are used to determine the cell poles of all the cells in a given frame. For the fluorescence signal, a kymograph of the fluorescence signal is constructed by summation of the pixel intensities per image perpendicular to the channel direction for each frame. This results in summed intensity information as function of time per growth channel (Figure 5.2c). We make use of the generated kymographs to determine individual replication and division cycles per cell (Figure 5.2d). A post-processing step is subsequently performed to eliminate cells that did not match the following selection criteria: correct cell length, sufficient growth characteristics, observation of a complete cell cycle, clear fluorescence signal that both starts and ends in a diffuse state (Figure 5.2d).

The fluorescence images of the detected individual cells that pass the above selection criteria are analyzed further. We base our fluorescence analysis on an image of an individual bacterium with its long axis aligned with the horizontal direction of the image. The width of the image is equal to the length of the bacterium. We fix the height of the image such that a sufficient area above and below the bacterium is included that is indicative of the auto-fluorescence of the sample. We analyze the fluorescent intensity counts of a single bacterium using the individual fluorescence kymographs of each cell (summed line-profiles) by calculating three types of image content for a specific bacterium, namely ’background’, ’foci’ and ’cytoplasm’ (Supplementary Figure 3a). In brief, we first estimate the background fluorescence from the sample using the signal outside of the bacterium. We did not have to take into account auto-fluorescence from the bacterium itself, since we conducted our experiments using minimal medium which results in negligible levels of cellular auto-fluorescence (Supplementary Figure 3b). The intensity outside the bacterium is used for a threshold with the remaining pixels intensities being representative of the total bacterium fluorescent counts. We subsequently separate ’cytoplasm’ and ’foci’ signals by determining the median of the summed line-profiles. The signal significantly above this value is attributed to foci, while the remainder (lower values) are treated as the fluorescence signal from the cytoplasm (Supplementary Figure 3a). This results in an integrated intensity value for the foci and also for the cytoplasm.

5.4.9. IMAGE ANALYSIS OF PALM EXPERIMENTS.

PALM data was analyzed using custom-written MATLAB software (MathWorks) in combination with the freely available MicrobeTracker software [68]. Prior to any spot analysis, the fluorescence images are subjected to illumination correction and to alignment with respect to the phase-contrast (PH) images. The resulting corrected and aligned fluorescence images are then used during further analysis.

Using the PH image, the different cells are detected in the field of view and their respective outlines are determined using MicrobeTracker. Subsequently, using the spot detection algorithm as described in Olivo-Marin *et al.* [69], the spots in each individual image of the fluorescence time-lapse series are detected, and the integrated intensity determined by summing the pixel values of each spot [70] . The integrated intensities of the spots as followed as function of time. This results in individual time-lapse integrated intensity traces of single molecules (Figure 5.3c). The cell outlines as determined previously are over layed with the fluorescence images. Any foci that are not situated in a bacterial cell (false positives) are rejected from further analysis. Only cells that had a clear fluorescence intensity focus where analyzed. This focus is indicative of DNA-bound clamps and thus DNA replication. Foci that exhibit multiple steps in fluorescence intensity are also rejected. For the remainder of the foci, the time it takes from the start of the data acquisition until spot disappearance is recorded (Figure 5.3c). These calculated time differences are indicative of molecule unloading (or bleaching, depending on the time of acquisition) and analyzed further as described in the following section.

5.4.10. MONTE CARLO SIMULATION OF β_2 LOADING AND UNLOADING DYNAMICS.

For illustrative purposes, we perform Monte-Carlo simulations (Figure 5.5) starting with no clamps loaded and no primers formed ($N_{\beta_2} = 0$), and assuming the loading rate to be much faster than the rate of primer formation ($N_{\mathrm{p}} \approx 0$). In each small time-step dt we let $N_{\beta_2} \to N_{\beta_2} + 1$ with probability $dt\, t_{\mathrm{p}}^{-1}$ and $N_{\beta_2} \to N_{\beta_2} - 1$ with probability $N_{\beta_2}\, dt\, t_{\mathrm{unload}}^{-1}$. This is repeated until the replication time is reached, upon which the primer formation rate t_{p}^{-1} is set to zero.

CONTRIBUTIONS

M.C.M. and N.H.D. designed the research and the experiments. M.C.M. and S.T.K. undertook the experiments. S.T.K. constructed the strains. P.T. performed the western blot. S.T.K. performed the Southern blot. M.C.M. and J.W.J.K. wrote the software to analyse all the microscopy data. M.C.M., A.v.d.B. and M.D. analysed the data. A.v.d.B. performed the Monte Carlo simulation. R.R.-L. and D.J.S. provided strains and contributed to the planning and discussion of the work.

ACKNOWLEDGMENTS

We thank Ilja Westerlaken for her assistance with the French Press for cell lysate preparation, Hugo Snippert for initial help with the Southern blotting, and Bronwen Cross for initial help with the Western blot, as well as Jasper van Veen, Kasper de Leeuw, and Liliane Jimenez van Hoorn for initial help with constructing the *PAmCherry-DnaN* strain. We thank Anjana Badrinarayanan for providing the *mCherry-DnaN* strain. We thank Jan Lipfert, Anne Meyer, Tim Blosser, Yaron Caspi, Antoine van Oijen, and Theo van Laar for stimulating discussions. We thank Francesco Perdaci, David Dulin, David Gruenwald, Chirlmin Joo, and Stanley Dinesh Chandradoss for initial help with microscopy. We thank Bernd Rieger for initial help with image analysis. We acknowledge contributions from Jelle van der Does, Dimitri de Roos, and Jaap Beekman for instrumentation and infrastructure. This work was supported by the European Community's Seventh Framework Programme FP7/2007-2013 under grant agreement n° 241548 (MitoSys) and a Vici grant by Netherlands Organization for Scientific Research (NWO), both to NHD, a Wellcome Trust Program Grant WT083469 to D.J.S., a TU Delft startup grant to M.D., and the Natural Sciences & Engineering Research Council of Canada (#435521-13) for R.R.L.

REFERENCES

[1] C. Indiani, P. McInerney, R. Georgescu, M. F. Goodman, and M. O'Donnell, *A sliding-clamp toolbelt binds high- and low-fidelity dna polymerases simultaneously.* Molecular Cell **19**, 805 (2005).

[2] F. J. López de Saro, *Regulation of interactions with sliding clamps during DNA replication and repair.* Current genomics **10**, 206 (2009).

[3] J. B. Vivona and Z. Kelman, *The diverse spectrum of sliding clamp interacting proteins.* FEBS letters **546**, 167 (2003).

[4] R. Napolitano, R. Janel-Bintz, J. Wagner, and R. P. Fuchs, *All three SOS-inducible DNA polymerases (Pol II, Pol IV and Pol V) are involved in induced mutagenesis.* The EMBO Journal **19**, 6259 (2000).

[5] J. Wagner, S. Fujii, P. Gruz, T. Nohmi, and R. P. Fuchs, *The beta clamp targets DNA polymerase IV to DNA and strongly increases its processivity.* EMBO reports **1**, 484 (2000).

[6] F. J. López de Saro and M. O'Donnell, *Interaction of the beta sliding clamp with MutS, ligase, and DNA polymerase I.* Proceedings Of The National Academy Of Sciences Of The United States Of America **98**, 8376 (2001).

[7] S. Kobayashi, M. R. Valentine, P. Pham, M. O'Donnell, and M. F. Goodman, *Fidelity of Escherichia coli DNA polymerase IV. Preferential generation of small deletion mutations by dNTP-stabilized misalignment.* The Journal of biological chemistry **277**, 34198 (2002).

[8] M. Tang, P. Pham, X. Shen, J. S. Taylor, M. O'Donnell, R. Woodgate, and M. F. Goodman, *Roles of E. coli DNA polymerases IV and V in lesion-targeted and untargeted SOS mutagenesis.* Nature **404**, 1014 (2000).

[9] S. Jergic, N. P. Horan, M. M. Elshenawy, C. E. Mason, T. Urathamakul, K. Ozawa, A. Robinson, J. M. H. Goudsmits, Y. Wang, X. Pan, J. L. Beck, A. M. van Oijen, T. Huber, S. M. Hamdan, and N. E. Dixon, *A direct proofreader–clamp interaction stabilizes the pol iii replicase in the polymerization mode,* EMBO Journal **32** (2013).

[10] B. P. Dalrymple, K. Kongsuwan, G. Wijffels, N. E. Dixon, and P. A. Jennings, *A universal protein-protein interaction motif in the eubacterial DNA replication and repair systems.* Proceedings Of The National Academy Of Sciences Of The United States Of America **98**, 11627 (2001).

[11] T. Katayama, T. Kubota, K. Kurokawa, E. Crooke, and K. Sekimizu, *The initiator function of DnaA protein is negatively regulated by the sliding clamp of the E. coli chromosomal replicase.* Cell **94**, 61 (1998).

[12] J. Kato and T. Katayama, *Hda, a novel DnaA-related protein, regulates the replication cycle in Escherichia coli.* The EMBO Journal **20**, 4253 (2001).

[13] M. Kurz, B. Dalrymple, G. Wijffels, and K. Kongsuwan, *Interaction of the sliding clamp beta-subunit and Hda, a DnaA-related protein.* Journal of Bacteriology **186**, 3508 (2004).

[14] S. Ozaki, Y. Matsuda, K. Keyamura, H. Kawakami, Y. Noguchi, K. Kasho, K. Nagata, T. Masuda, Y. Sakiyama, and T. Katayama, *A replicase clamp-binding dynamin-like protein promotes colocalization of nascent dna strands and equipartitioning of chromosomes in e. coli.* Cell reports **4**, 985 (2013).

[15] L. A. Simmons, B. W. Davies, A. D. Grossman, and G. C. Walker, *Beta clamp directs localization of mismatch repair in Bacillus subtilis.* Molecular Cell **29**, 291 (2008).

[16] X. Kong, R. Onrust, M. O'Donnell, and J. Kuriyan, *Three-dimensional structure of the β subunit of E. coli DNA polymerase III holoenzyme: A sliding DNA clamp,* Cell **69**, 425 (1992).

[17] A. Johnson and M. O'Donnell, *Cellular DNA replicases: components and dynamics at the replication fork.* Annual review of biochemistry **74**, 283 (2005).

[18] C. S. McHenry, *Dna replicases from a bacterial perspective.* Annual review of biochemistry **80**, 403 (2011).

[19] R. E. Georgescu, S.-S. Kim, O. Yurieva, J. Kuriyan, X.-P. Kong, and M. O'Donnell, *Structure of a sliding clamp on dna,* Cell **132**, 43 (2008).

[20] J. N. Hayner and L. B. Bloom, *The β sliding clamp closes around dna prior to release by the escherichia coli clamp loader γ complex.* The Journal of biological chemistry **288**, 1162 (2013).

[21] Q. Yuan and C. S. McHenry, *Cycling of the E. coli lagging strand polymerase is triggered exclusively by the availability of a new primer at the replication fork.* Nucleic Acids Research **42**, 1747 (2014).

[22] J. Turner, M. M. Hingorani, Z. Kelman, and M. O'Donnell, *The internal workings of a dna polymerase clamp-loading machine,* The EMBO Journal **18** (1999).

[23] M. Hedglin, R. Kumar, and S. J. Benkovic, *Replication clamps and clamp loaders.* Cold Spring Harbor perspectives in biology **5**, a010165 (2013).

[24] K. R. Simonetta, S. L. Kazmirski, E. R. Goedken, A. J. Cantor, B. A. Kelch, R. McNally, S. N. Seyedin, D. L. Makino, M. O'Donnell, and J. Kuriyan, *The mechanism of ATP-dependent primer-template recognition by a clamp loader complex.* Cell **137**, 659 (2009).

[25] C. D. Downey and C. S. McHenry, *Chaperoning of a replicative polymerase onto a newly assembled DNA-bound sliding clamp by the clamp loader.* Molecular Cell **37**, 481 (2010).

[26] F. P. Leu, M. M. Hingorani, J. Turner, and M. O'Donnell, *The delta subunit of dna polymerase iii holoenzyme serves as a sliding clamp unloader in escherichia coli.* The Journal of biological chemistry **275**, 34609 (2000).

[27] P. McInerney, A. Johnson, F. Katz, and M. O'Donnell, *Characterization of a triple dna polymerase replisome.* Molecular Cell **27**, 527 (2007).

[28] R. Reyes-Lamothe, D. J. Sherratt, and M. C. Leake, *Stoichiometry and architecture of active dna replication machinery in escherichia coli.* Science **328**, 498 (2010).

[29] G. Lia, B. Michel, and J. Allemand, *Polymerase exchange during Okazaki fragment synthesis observed in living cells.* Science **335**, 328 (2012).

[30] T. Ogawa and T. Okazaki, *Discontinuous DNA replication,* Annual review of biochemistry **49**, 421 (1980).

[31] K. Tougu and K. J. Marians, *The interaction between helicase and primase sets the replication fork clock.* The Journal of biological chemistry **271**, 21398 (1996).

[32] P. M. Burgers, A. Kornberg, and Y. Sakakibara, *The dnaN gene codes for the beta subunit of DNA polymerase III holoenzyme of escherichia coli.* Proceedings Of The National Academy Of Sciences Of The United States Of America **78**, 5391 (1981).

[33] N. Yao, J. Turner, Z. Kelman, P. T. Stukenberg, F. Dean, D. Shechter, Z. Q. Pan, J. Hurwitz, and M. O'Donnell, *Clamp loading, unloading and intrinsic stability of the pcna, β and gp45 sliding clamps of human, e. coli and t4 replicases.* Genes Cells **1**, 101 (1996).

[34] A. Yuzhakov, J. Turner, and M. O'Donnell, *Replisome assembly reveals the basis for asymmetric function in leading and lagging strand replication,* Cell **86**, 877 (1996).

[35] N. A. Tanner, G. Tolun, J. J. Loparo, S. Jergic, J. D. Griffith, N. E. Dixon, and A. M. van Oijen, *E. coli dna replication in the absence of free β clamps.* The EMBO Journal **30**, 1830 (2011).

[36] M. Su'etsugu and J. Errington, *The replicase sliding clamp dynamically accumulates behind progressing replication forks in bacillus subtilis cells.* Molecular Cell **41**, 720 (2011).

[37] S. T. Hess, T. P. K. Girirajan, and M. D. Mason, *Ultra-high resolution imaging by fluorescence photoactivation localization microscopy.* Biophysj **91**, 4258 (2006).

[38] E. Betzig, G. H. Patterson, R. Sougrat, O. W. Lindwasser, S. Olenych, J. S. Bonifacino, M. W. Davidson, J. Lippincott-Schwartz, and H. F. Hess, *Imaging intracellular fluorescent proteins at nanometer resolution,* Science **313**, 1642 (2006).

[39] D. Dulin, J. Lipfert, M. C. Moolman, and N. H. Dekker, *Studying genomic processes at the single-molecule level: introducing the tools and applications,* Nature Reviews Genetics **14**, 19 (2013).

[40] K. E. Duderstadt, R. Reyes-Lamothe, A. M. van Oijen, and D. J. Sherratt, *Replication-Fork Dynamics.* Cold Spring Harbor perspectives in biology **6** (2013).

[41] T. Xia, N. Li, and X. Fang, *Single-molecule fluorescence imaging in living cells,* Annual review of physical chemistry **64**, 459 (2013).

[42] F. Persson, I. Barkefors, and J. Elf, *Single molecule methods with applications in living cells.* Current opinion in biotechnology **24**, 737 (2013).

[43] A. Gahlmann and W. E. Moerner, *Exploring bacterial cell biology with single-molecule tracking and super-resolution imaging.* Nature Reviews Microbiology **12**, 9 (2014).

[44] X. Wang, R. Reyes-Lamothe, and D. J. Sherratt, *Visualizing genetic loci and molecular machines in living bacteria,* Biochemical Society Transactions **36**, 749 (2008).

[45] M. C. Moolman, Z. Huang, S. T. Krishnan, J. W. J. Kerssemakers, and N. H. Dekker, *Electron beam fabrication of a microfluidic device for studying submicron-scale bacteria.* Journal of nanobiotechnology **11**, 12 (2013).

[46] P. Wang, L. Robert, J. Pelletier, W. L. Dang, F. Taddei, A. Wright, and S. Jun, *Robust growth of escherichia coli,* Current biology **20**, 1099 (2010).

[47] A. W. Nguyen and P. S. Daugherty, *Evolutionary optimization of fluorescent proteins for intracellular fret,* Nature biotechnology **23**, 355 (2005).

[48] R. Reyes-Lamothe, C. Possoz, O. Danilova, and D. J. Sherratt, *Independent positioning and action of escherichia coli replisomes in live cells,* Cell **133**, 90 (2008).

[49] O. Michelsen, M. J. Teixeira de Mattos, P. R. Jensen, and F. G. Hansen, *Precise determinations of C and D periods by flow cytometry in Escherichia coli K-12 and B/r.* Microbiology (Reading, England) **149**, 1001 (2003).

[50] V. C. Coffman and J. Wu, *Counting protein molecules using quantitative fluorescence*

microscopy. Trends in biochemical sciences **37**, 499 (2012).

[51] M. T. Swulius and G. J. Jensen, *The helical mreb cytoskeleton in escherichia coli mc1000/ple7 is an artifact of the n-terminal yellow fluorescent protein tag,* Journal of Bacteriology **194**, 6382 (2012).

[52] D. Landgraf, B. Okumus, P. Chien, T. A. Baker, and J. Paulsson, *Segregation of molecules at cell division reveals native protein localization.* Nature Methods **9**, 480 (2012).

[53] F. V. Subach, G. H. Patterson, S. Manley, J. M. Gillette, J. Lippincott-Schwartz, and V. V. Verkhusha, *Photoactivatable mcherry for high-resolution two-color fluorescence microscopy.* Nature Methods **6**, 153 (2009).

[54] K. J. Marians, *Prokaryotic DNA replication.* Annual review of biochemistry **61**, 673 (1992).

[55] P. T. Stukenberg, J. Turner, and M. O'Donnell, *An explanation for lagging strand replication: Polymerase hopping among DNA sliding clamps,* Cell **78**, 877 (1994).

[56] R. Reyes-Lamothe, T. Tran, D. Meas, L. Lee, A. M. Li, D. J. Sherratt, and M. E. Tolmasky, *High-copy bacterial plasmids diffuse in the nucleoid-free space, replicate stochastically and are randomly partitioned at cell division.* Nucleic Acids Research **42**, 1042 (2014).

[57] G. Wijffels, B. Dalrymple, K. Kongsuwan, and N. E. Dixon, *Conservation of eubacterial replicases,* IUBMB life **57** (2005).

[58] M. Su'etsugu, T.-R. Shimuta, T. Ishida, H. Kawakami, and T. Katayama, *Protein associations in DnaA-ATP hydrolysis mediated by the Hda-replicase clamp complex.* The Journal of biological chemistry **280**, 6528 (2005).

[59] M. L. Mott and J. M. Berger, *DNA replication initiation: mechanisms and regulation in bacteria,* Nature Reviews Microbiology **5**, 343 (2007).

[60] R. E. Georgescu, Yao, N. Y, and M. O'Donnell, *Single-molecule analysis of the escherichia coli replisome and use of clamps to bypass replication barriers.* FEBS letters **584**, 2596 (2010).

[61] J. S. Lenhart, A. Sharma, M. M. Hingorani, and L. A. Simmons, *Dnan clamp zones provide a platform for spatiotemporal coupling of mismatch detection to dna replication.* Molecular Microbiology **87**, 553 (2013).

[62] S. Uphoff, R. Reyes-Lamothe, F. Garza de Leon, D. J. Sherratt, and A. N. Kapanidis, *Single-molecule DNA repair in live bacteria.* Proceedings Of The National Academy Of Sciences Of The United States Of America **110**, 8063 (2013).

[63] L. C. Thomason, N. Costantino, and D. L. Court, *E. coli genome manipulation by p1 transduction.* Current protocols in molecular biology **Chapter 1**, Unit 1.17 (2007).

[64] K. A. Datsenko and B. L. Wanner, *One-step inactivation of chromosomal genes in escherichia coli k-12 using pcr products.* Proceedings Of The National Academy Of Sciences Of The United States Of America **97**, 6640 (2000).

[65] D. Grünwald, S. M. Shenoy, S. Burke, and R. H. Singer, *Calibrating excitation light fluxes for quantitative light microscopy in cell biology,* Nature protocols **3**, 1809 (2008).

[66] Sternberg, *Biomedical Image Processing,* IEEE Computer **16**, 22 (1983).

[67] Y. Taniguchi, P. J. Choi, G. W. Li, H. Chen, M. Babu, J. Hearn, A. Emili, and X. S. Xie,

Quantifying E. coli Proteome and Transcriptome with Single-Molecule Sensitivity in Single Cells, Science **329**, 533 (2010).

[68] O. Sliusarenko, J. Heinritz, and T. Emonet, *High-throughput, subpixel precision analysis of bacterial morphogenesis and intracellular spatio-temporal dynamics ,* Molecular Microbiology **80**, 612 (2011).

[69] J. C. Olivo-Marin, *Extraction of spots in biological images using multiscale products,* Pattern Recognition **35** (2002).

[70] M. H. Ulbrich and E. Y. Isacoff, *Subunit counting in membrane-bound proteins.* Nature Methods **4**, 319 (2007).

SUPPLEMENTARY INFORMATION

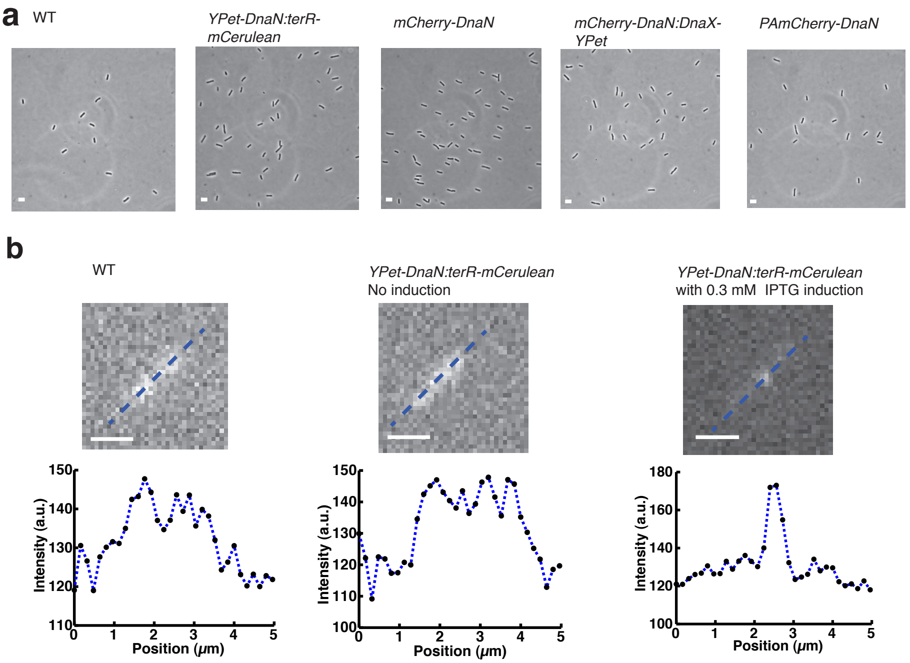

Supplementary Figure 5.1: Verification of the different *E. coli* variant used in this study. (a) Sample phase contrast images of the cells used in this study, which indicate that the physical appearance of these strains is essentially indistinguishable from that of WT. Scale bars: 3 μm. (b) Verification that in the absence of IPTG, terR-mCerulean is hardly expressed. Here we show the sample fluorescence images and the corresponding line-profile plots. There is essentially no difference between WT and *YPet-dnaN*:*tetR-mCerulean* in the absence of IPTG. Conversely, in the presence of IPTG a clear focus can be observed in *YPet-dnaN*:*tetR-mCerulean*. Scale bars: 1.6 μm

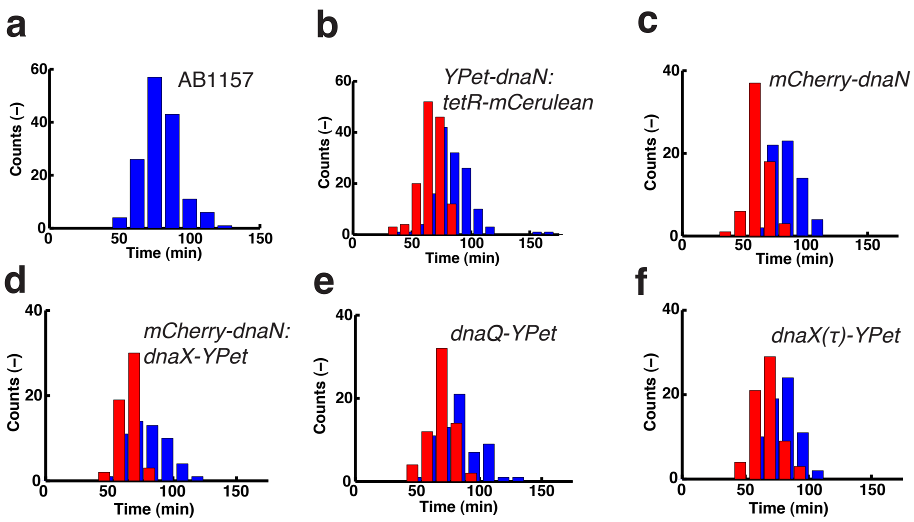

Supplementary Figure 5.2: Cell doubling and replication times of the different *E. coli* variants measured in the microfluidic device. (a) The doubling distribution of the AB1157 parental strain in the microfluidic device during a long time-lapse experiment. The doubling time is $t_{\text{double}} = 80 \pm 13$ min, n = 148 (mean and ±s.d.). (b-f) The doubling (blue) and replication (red) distributions of the different *E. coli* strains in the microfluidic device during a long time-lapse experiment. The average replication time (t_{rep}) and doubling time (t_{double}) are presented with the error being ± s.d.. (b) *YPet-dnaN*:*tetR-mCerulean*. $t_{\text{rep}} = 68 \pm 10$ min and $t_{\text{double}} = 84 \pm 17$ min (n = 137). (c) *mCherry-dnaN*. $t_{\text{rep}} = 63 \pm 9$ min and $t_{\text{double}} = 84 \pm 12$ min (n = 65) (d) *dnaX(τ)-YPet*:*mCherry-dnaN*. $t_{\text{rep}} = 67 \pm 8$ min and $t_{\text{double}} = 79 \pm 15$ min (n = 54). (e) *dnaQ-YPet*. $t_{\text{rep}} = 70 \pm 10$ min and $t_{\text{double}} = 82 \pm 17$ min (n = 64). (f) *dnaX(τ)-YPet*. $t_{\text{rep}} = 67 \pm 12$ min and $t_{\text{double}} = 79 \pm 12$ min (n = 66)

.

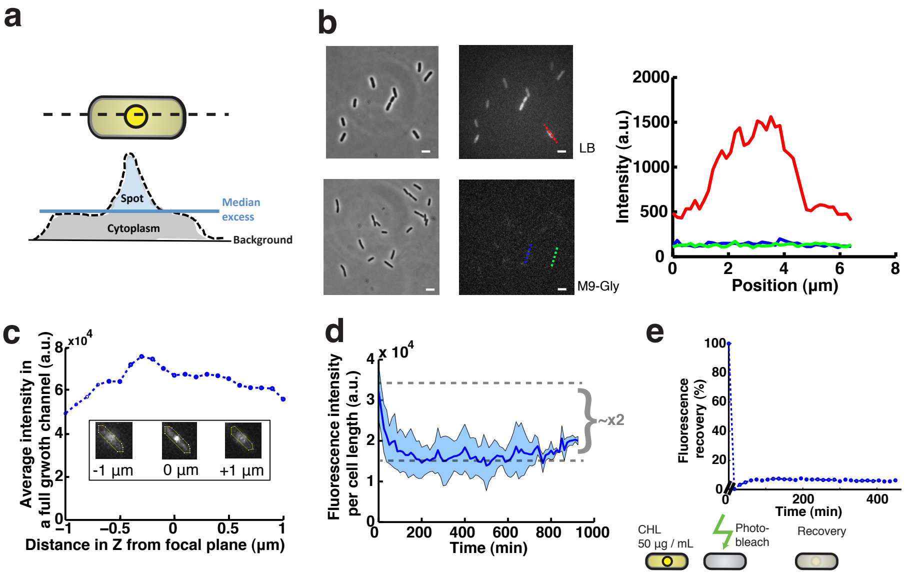

Supplementary Figure 5.3: The fluorescence signal definition and the different microscopy control experiments performed. a) Illustration of how the integrated line-profile is used to define sample background intensity, foci intensity, and total intensity in the cell. (b) Comparison of the degree of auto-fluorescence of *E.coli* AB1157 in LB and M9-Gly growth medium. (left) Example phase contrast and corresponding fluorescence images of cells grown in LB or M9-Gly. Scale bars: $3\,\mu m$. (right) Example line-profile plots of a cell in LB (red curve), M9-Gly (blue curve) and an arbitrary position in the M9-Gly fluorescence image (green curve). (c) A sample fluorescence signal of a z-stack of cells in a full growth channel (range: $-1\,\mu m$ to $+1\,\mu m$ with respect to the focus). (d) The bleaching behaviour of the YPet-β_2 fluorescence signal during a long-time lapse experiment. The relative change in the intensity as function of time is used to correct for YPet-β_2 bleaching. (e) Fluorescence recovery after photobleaching of cells in the presence of chloramphenicol.

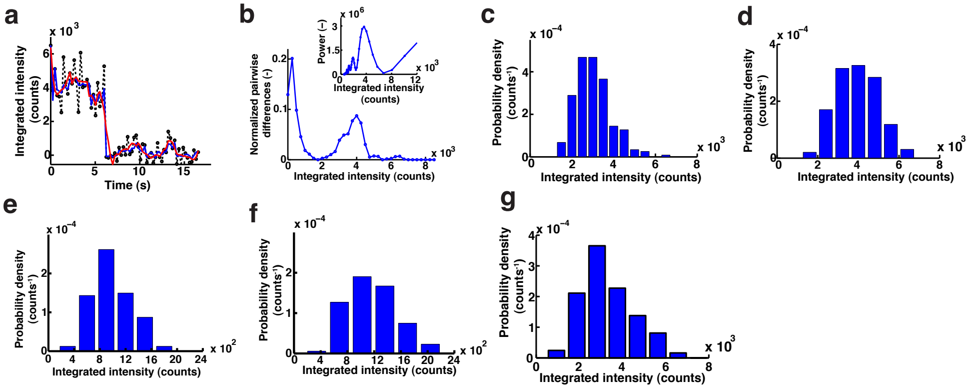

Supplementary Figure 5.4: Single YPet fluorescence intensity calibration. (a) A sample integrated intensity trace of a single immobilized YPet molecule as function of time. Here we show the data points (black line), the Chung-Kennedy (CK) filtered result of the data (blue line) and the Savitsky-Golay (SK) filtered trace (red). In the further analysis steps the CK-filtered data result was used. (b) The pairwise difference distribution function (PDDF) of the CK-filtered trace in (a) and its corresponding power spectrum (inset). (c) The integrated intensity distribution of single YPet molecules imaged in M9 growth medium supplemented with 0.3 % glycerol and essential nutrients (n = 235, $\mu = 3070$, $\sigma = 856$). (d) The integrated intensity distribution of single YPet molecules imaged in french-pressed cell lysate ($n = 245$, $\mu = 3884, \sigma = 1108$). (e) The integrated intensity distribution of single mCherry molecules imaged in M9 growth medium supplemented with 0.3 % glycerol and essential nutrients ($n = 107$, $\mu = 990, \sigma = 318$). (f) The integrated intensity distribution of single mCherry molecules imaged in french-pressed cell lysate ($n = 102$, $\mu = 1158, \sigma = 380$). Images where acquired, for both (e) and (f), at an exposure time of 400 ms. The resulting intensity values where subsequently converted to values equivalent to an exposure time of 80 ms by dividing them by 5. (g) The integrated intensity distribution of single YPet-β molecules imaged in M9 growth medium supplemented with 0.3 % glycerol and essential nutrients (n = 131, $\mu = 3305$, $\sigma = 856$).

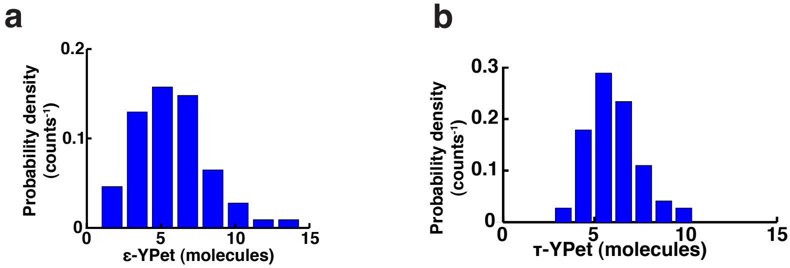

Supplementary Figure 5.5: Stoichiometry of DnaQ and DnaX. (a-b) The distributions of the stoichiometry of the DnaQ (ϵ-YPet) (n = 64) and DnaX (τ-YPet) (n = 66) molecules within the replisome.

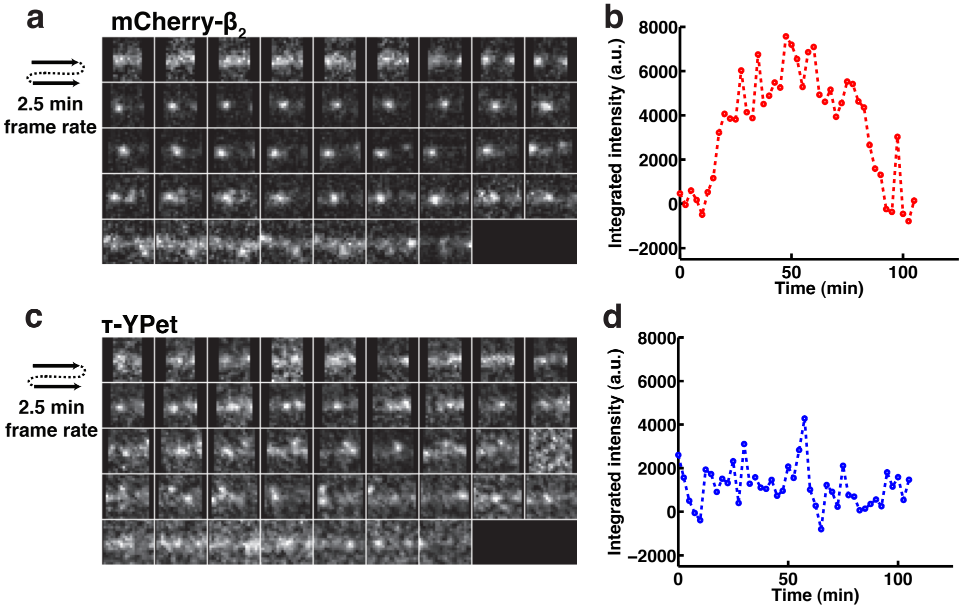

Supplementary Figure 5.6: The dual-color experiment that simultaneously monitors the temporal dynamics the β_2 clamp and the clamp loader (τ). (a) A sample temporal montage of the mCherry-β_2 clamp behaviour for one replication cycle. (b) The integrated intensity of the foci from the mCherry-β_2 signal shown in (a). (c) A sample temporal montage of the τ-YPet behaviour for one replication cycle. (b) The integrated intensity of the foci from the τ-YPet signal shown in (c).

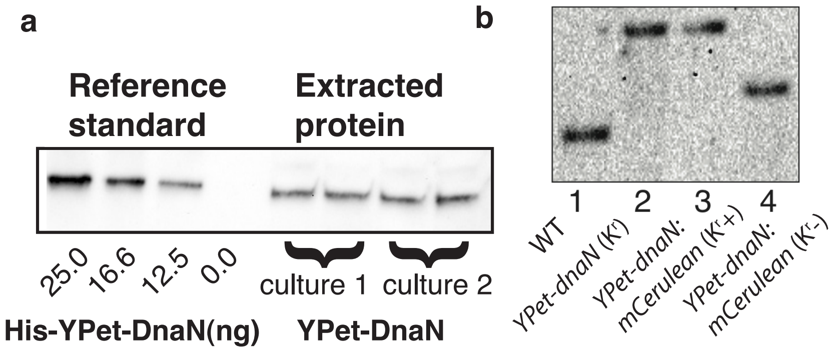

Supplementary Figure 5.7: Western blot and Southern blot control experiments. (a) The Western blot result, indicating the average number of clamps in the cell. Using the purified His-YPet-DnaN (Lanes 1-4 from left to right) as the quantitative standard we determined the average amount for two independent cultures (Lanes 5-8 from left to right) (b) The Southern blot result, indicating that there is only a single gene copy of *dnaN*. Here we compare WT cells (lane 1) to three different *E. coli* variant (lane 2-4) we have created. We used the strain in lane 3 (described in Methods) in this study.

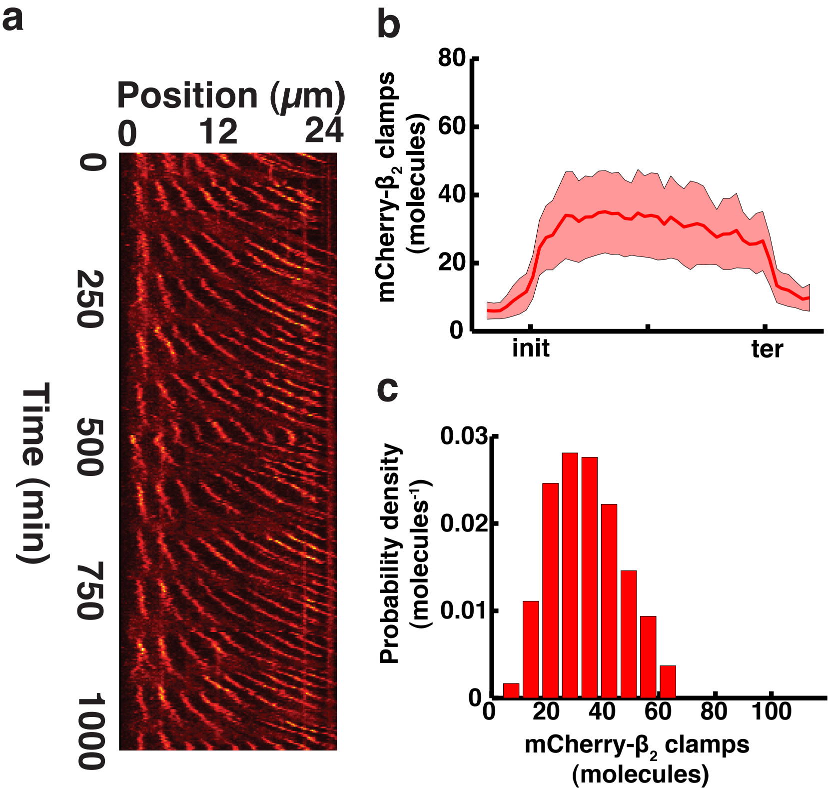

Supplementary Figure 5.8: The temporal dynamics of the YPet-β_2 are reproduced with a mCherry-β_2 fusion. (a) A sample kymograph of a single growth channel during an overnight experiment. (b) The behaviour of DNA-bound mCherry-β_2 clamps in both the replisomes during replication. Here we have normalized the time to make averaging of different cells, possible (n=65). The error bars represent ±s.d., from the mean. (c) The distribution of DNA-bound mCherry-β_2 clamps in both replisomes during steady-state replication. The mean number of DNA-bound clamps is $N_{\beta_2} = 34$ with s.d. = 12, s.e.m. = 1.5.

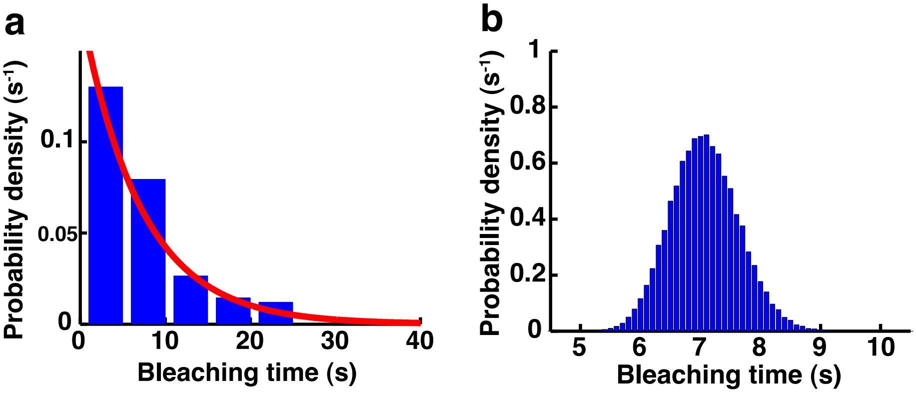

Supplementary Figure 5.9: The PAmCherry bleaching curve together with the bootstrapped values for uncertainty estimation. (a) The distribution of the bleaching time measured under our experimental conditions. The red curve is a single exponential MLE fit to the data. (b) The distribution of the fitted bleaching time constants over 10^6 bootstrapped data sets, from which the standard deviation for the bleaching time was determined.

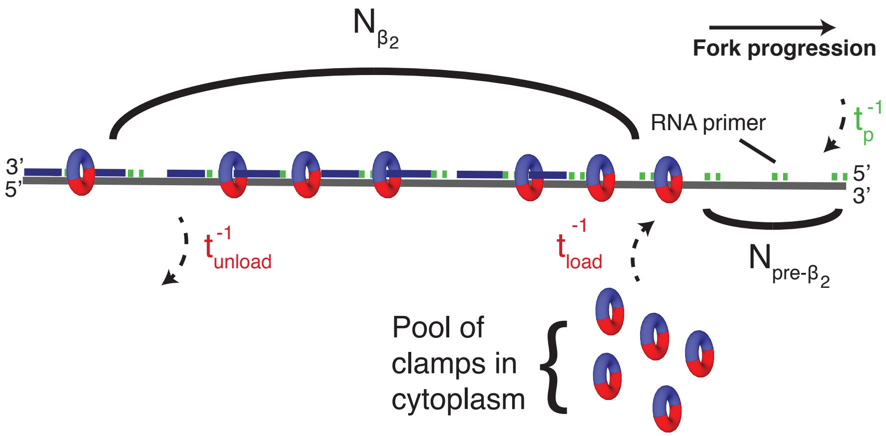

Supplementary Figure 5.10: A schematic illustrating the recycling model used. In our model we have five different variables. They are the number of primers having a loaded β_2 clamp (N_{β_2}), the number of primers that do not have a loaded β_2 clamp ($N_{p,unocc}$), the rate of loading a β_2 clamp (k_{load}), the rate of unloading a clamp (k_{unload}), and the rate at which primers are being formed (k_p).

E. coli **strain**	**Generation time (min)**	
	M9-Gly	LB
AB1157	103 ± 4	37 ± 2
YPet-dnaN:tetR-mCerulean	103 ± 1	37 ± 2
PAmCherry-dnaN	102 ± 3	38 ± 2
mCherry-dnaN	105 ± 3	38 ± 1
mCherry-dnaN:dnaX-YPet	103 ± 1	39 ± 1

Supplementary Table 5.1: Bulk generation times of the different strains in LB and M9-Gly growth mediumThe numbers specified indicate the mean ± s.d. The generation times where determined from three independent cultures for all the strains.

Plasmids	**Relevant genotype**	Construction
pKD46	Plasmid with λ-Red recombinase genes expressed under arabinose promoter	Created by standard cloning [64]
pROD44	*Ypet* template plasmid for N-terminus fusion	Cloning *Ypet* and *frt-kanR-frt* in pUC18 backbone [28]
mCherry-N	*mCherry* template plasmid for N-terminus fusion	Cloning *mCherry* and *frt-kanR-frt* in pUC18 backbone
PAmCherry1	*PAmCherry1* template plasmid	Cloning *PAmCherry1* in place of *Ypet* in pROD44 backbone

Supplementary Table 5.2: Summary of different plasmids used in this study.

Strains	**Relevant genotype**	**Construction**
BN1110	AB1157 strain containing pKD46 plasmid	*E. coli* K-12 derivative [48]
BN1108	*tetO* array (50 kb clockwise from the *dif*-site) and *PlacI-tetR-mCerulean* in place of *galK*	Phage transduction [48]
BN1109	*Ypet* fused to *dnaN*	λ-red recombination: *Ypet-kanR* from pROD44 → BN1107
BN1219	*YPet-dnaN* and *tetR-mCerulean*	Phage transduction: BN1109→BN1108
BN1682	*mCherry* fused to *dnaN* with *kanR*	λ-red recombination: *mCherry-kanR* from mCherry-N→BN1107
BN1683	*mCherry* fused to *dnaN*	*Flp-frt* recombination: *kanR* flipped out from BN1682
BN1684	*dnaX*(τ) fused to *Ypet* with *kanR*	λ-red recombination [48]
BN1864	*dnaX*(τ)-*Ypet* and *mCherry-dnaN*	Phage transduction: BN1684→BN1683
BN1867	*PAmCherry1* fused to *dnaN* with *kanR*	λ-red recombination: *PAmCherry1-kanR* from *PAmCherry1*→BN1107

Supplementary Table 5.3: Summary of different strains used in this study.

S5.1. DETERMINING THE ERROR OF ESTIMATING THE TOTAL YPET-β_2 CONTENT IN THE CELL FROM THE DETECTED OUT OF FOCUS FLUORESCENCE

Using the detected fluorescence to estimate the total amount of clamps in the whole cell, we had to verify that we do not miss a significant amount of out of focus fluorescence. We verified this by determining the total intensity measured in a growth channel at different focal positions. A z-stack ($\pm 1\,\mu$m out of focus) was measured on the same growth channel. We determined the total intensity of these cells at the different Z-positions (Supplementary Figure 5.3c). As can be seen, the difference is < 10%.

S5.2. SINGLE-MOLECULE FLUORESCENCE CALIBRATION

We use a similar approach as in [1, 28] to determine the average intensity of a single YPet molecule under our experimental conditions. In brief, purified single YPet molecules were immobilized on a clean cover glass through conjugation via the anti-YPet antibody (Clonetech) [2] either in M9-Gly or cell lysate. Using these two different buffer conditions, we were enable to estimate whether cytoplasm of the cell could potential influence the YPet brightness. These YPet proteins were subsequently imaged until they irreversibly photobleached using the same imaging conditions used for the long-timelapse experiments apart from a higher frame rate (~ 300 ms).

The acquired images were analyzed with custom-written MATLAB software (MathWorks). Prior to spot analyses, we subtracted the uneven background using a rolling ball filter [3, 66] and subsequently corrected for illumination heterogeneity by using a known measured laser beam profile [67]. Spot detection is performed in each individual frame for the whole time-lapse series taken using the algorithms as defined in [69]. For each of the detected spots, we calculate the integrated intensity by pixel summation [70] in each individual frame. The integrated intensity of each respective spot in each frame is subsequently linked, which results in individual time-lapse integrated intensity traces (Supplementary Figure 5.4a) of single molecule bleaching.

Each individual trace is subsequently processed as follows. First we perform an edge-preserving Chung-Kennedy (C-K) filter [4] on the trace, using code adapted from [5]. We then calculated the pair-wise difference distribution function (PDDF) of the C-K filtered trace (Supplementary Figure 5.4b). The single-sided power spectrum is subsequently calculated for the PDDF, which provided us with the intensity of that respective single YPet molecule (Supplementary Figure 5.4b (inset)). Performing this analysis for subsequent YPet molecules resulted in a distribution for the intensity of a single YPet molecule in M9-Gly or cell lysate (Supplementary Figure 5.4c,d) for our imaging conditions. A similar approach was utilized to calibrate the intensity of a single mCherry molecule in M9-Gly (Supplementary Figure 5.4e) or cell lysate (Supplementary Figure 5.4f). In both the YPet and mCherry cases, the intensity value used to convert counts to molecules is the average between the means of the M9-Gly and cell lysate measurements. We experimentally confirmed that a YPet-β fluorescence standard and a YPet standard provide the same mean fluorescent intensity in our experimental conditions (Supplementary Figure 5.4g). In other words, the YPet intensity is thus unaffected by the fusion to the clamp.

As a control to verify our calibration, we determined the stoichiometry of both the ϵ-subunit (DnaQ) of DNA Polymerase III as well as the τ-subunit (DnaX) of the clamp loader complex using YPet fusions to the respective proteins. In both the cases we determined the combined stoichiometry of the proteins in both the replisomes. We reproduced the numbers as previously published [28] for these replisome components (Supplementary Figure 5.5a,b). This established that our *in vitro* single-molecule calibration is applicable *in vivo*.

S5.3. ESTIMATION OF β_2 CLAMP STOICHIOMETRY FROM FLUORESCENCE TIME-LAPSE DATA

We determine the number of sliding clamps in the cell from the integrated intensity detected using the single-molecule calibration, while correcting for photo-bleaching and converting from monomers to dimers.

To correct for photo-bleaching, we use the following approach. We assume that cell growth and protein copy number in the cell increases linearly from cell birth until cell division. The ratio of these two numbers, as function of time, should thus remain constant throughout the cell cycle of a cell if there were no photo-bleaching. However, due to photobleaching, this ratio will decrease as function of time (Supplementary Figure 5.3d). We fit this curve with a single exponential and multiply the detected fluorescent signal with the appropriate factor as function of time in order to correct for this decline in fluorescence due to photobleaching.

This intensity corrected for photo-bleaching is subsequently converted into clamp dimers by dividing the fluorescence signal by the single-molecule calibration integrated intensity value as subsequently dividing by a factor of two to convert from monomers to dimers.

S5.4. ESTIMATION OF THE IMMATURE FRACTION OF YPET MOLECULES

We estimated the immature fraction of YPet (dark fraction) using a similar fluorescence recovery after photobleaching (FRAP) protocol as was previously published by *Badrinarayanan et al.* [6], with slight variation due to our experimental approach. An experiment was prepared as described in Methods, and the cells were allowed to incubate for ~ 2 hrs without any measurement. A reference fluorescence and brightfield image were acquired after which, M9 growth medium supplemented with 50 μg/mL of chloramphenicol (CHL) was flushed through the microfluidic system. The fluorescence was subsequently bleached until roughly background level. This growth medium supplemented with CHL was continuously injected at a rate of 500 μL/hr while fluorescence and brightfield images were acquired at a frame rate of 15 min with an exposure time of 80 ms for ~ 2 hrs. The CHL treated cells do not express further proteins, and thus the fluorescence recovery is indicative of the maturation of previously (at the start of the experiment) immature YPet (Supplementary Figure 5.3e). This measured value was estimated to be less than 15 % of the starting value. We estimate the maturation time of YPet in *E. coli* under our experimental conditions using the method as describe in *Wang et al*

[7] to be $t_{\text{mature}} < 12.5\,\text{min}$.

S5.5. DUAL-COLOR MEASUREMENT OF DNAX-YPET AND MCHERRY-DNAN

In order to compare the dynamics of the clamp (mCherry–β_2) and the clamp loader complex (τ–YPet) we performed a dual-color experiment. Images were acquired in the same way as for the YPet–β_2 experiment, with the only difference being measuring both the mCherry and YPet signals sequentially. As is evident from Supplementary Figure 5.6, the temporal behavior of the τ-subunit is significantly different than that oft he β_2 clamp. In contrast to reaching a steady-state plateau, the τ-subunit seems to be highly dynamic and might even be exchanged during replication.

S5.6. DETERMINATION OF CELLULAR YPET-DNAN MOLECULES BY WESTERN BLOTTING

HIS-YPET-DNAN REFERENCE STANDARD

The cloning was conducted as follows. The *Ypet-dnaN* gene from the AB1157 cells was amplified using primers 5' – CTC CAG GGA TCC GAT GTC TAA AGG TGA AGA A – 3' and 5' – GAT CAA CAA GCT TGT GAG GGA CAT TAC AGT CTC ATT GGC ATG ACA ACA TAA GCC – 3'. The PCR amplicon was digested with *HindIII* and *BamHI*, and ligated into expression vector pRSETb (Invitrogen), resulting in construct pRSETb-dnaN. The cloning was confirmed by plasmid sequencing using the T7 promotor and terminator flanking regions. BL21pLysS cells (Promega) were transformed with the pRSETb-dnaN construct to allow inducible protein expression of YPet-DnaN-His. Bacterial cells were grown in LB broth supplemented with ampicillin (100 μg/mL) and chloramphenicol (34 μg/mL) at 37 °C with shaking until an $OD_{600} \sim 0.6$. The protein induction was performed using 1 mM Isopropyl-β-D-thio-galactoside (IPTG). After 4 hr of induction, bacterial cells were collected by centrifugation at 4000 g for 5 min. A 10 % SDS-PAGE system was used to analyze the resulting proteins.

The protein purification was performed as follows. The bacterial pellets were thawed on ice, re-suspended in buffer (50 mM Na_2HPO_4 pH 8.0, 0.3 M NaCl, 8 M urea, 10 mM imidazole) and lysed by sonication. The supernatant was cleared by ultracentrifugation at 20000 g (Beckman JA-17 rotor) for 30 min and subsequently incubated with Ni-NTA beads (Thermo) for 1 h at room temperature (RT). The beads were washed twice with 10 volumes of washing buffer (8 M Urea, 50 mM Na_2HPO_4 pH 8.0, 0.3 M NaCl 20 mM imidazole). The beads were subsequently washed with refolding buffer (50 mM Na_2HPO_4 pH 8.0, 0.3 M NaCl 20 mM imidazole) to refold the His-Tagged protein. Finally, the N-terminally His6-tagged protein was eluted from the beads using elution buffer 50 mM Na_2HPO_4 pH 8.0, 0.3 M NaCl and 250 mM imidazole). Proteins were subsequently stored in 50 % glycerol at −80 °C until used.

CULTURE PREPARATION FOR WESTERN BLOT

The *Ypet-dnaN* cells were grown overnight at 37 °C with shaking in M9 medium supplemented with 0.3 % glycerol (Gly), essential nutrients together with the appropriate antibiotics. The subsequent day the overnight culture was sub-cultured (~ 2 %) into 50 mL of the same medium and grown at 37 °C with shaking until an $OD_{600} \sim 0.35$ was reached.

The bacterial culture was serially diluted in Phosphate Buffered Saline (PBS) and subsequently plated on LB Agar medium. The plates were incubated overnight at 37 °C and colony forming units (CFU) were enumerated after 24 hrs. Bacteria were harvested by centrifugation at 4000 g (Eppendorf 5810R) for 5 min. The bacterial pellet was resuspended in 2 mL of B-PER Protein Extraction Reagents (Thermo Scientific) to isolate the total amount of protein using the instructions provided by the manufacturer. Isolated proteins were subsequently stored at −80 °C until used.

CONDUCTING THE WESTERN BLOT

The protein standard (25 ng, 16.6 ng, 12.5 ng of His-Ypet-DnaN) and total cell lysed were separated on 10 % SDS-PAGE gel under 100 V for 1 hr (Biorad). A Western blot assay was conducted using the above mentioned purified recombinant His-YPet-DnaN protein and total cell lysed. The gel were blotted onto a nitrocellulose membrane using a transfer buffer containing 25 mM Tris (pH = 8.3), 192 mM glycine and 10 % methanol at 200 mA for 1 hr at 4 °C. The blotted membrane was blocked with 5 % (w/v) skim milk in PBS with 0.05 % tween 20 (T-PBS) for 1 hr at room temperature. The blot was incubated for 1 hr at room temperature (RT) with the primary antibody (Clonetech). After diluting 1:10000, the blots were washed three times with T-PBS and incubated with the secondary antibodies peroxidase conjugated goat anti-mouse IgG at a 1:7500 dilution in T-PBS. The blots were then washed three times with T-PBS and reactions were developed by SuperSignal Western Blot Enhancer (ThermoScientific) according to the manufacturer's instructions.

QUANTIFICATION OF BANDS

The bands corresponding to the protein standards, as well as bands of appropriate DnaN protein in the crude extract (Supplementary Figure 5.7e) were quantified using Image Lab (Biorad). The intensities of the bands were plotted versus protein concentration (ng) and fitted to a straight line, which yielded a function to related intensity and protein concentration. This linear equation was subsequently used to calculate the amount of that protein present in the crude cell extract. Finally, the number of protein molecules per cell (C) was calculated using the following equation:

$$C = \frac{MA}{LN}. \tag{5.2}$$

Here M is the amount of protein in the crude cell extract (grams), A is Avogadro's number (molecules/mol), L is the molecular mass of the fusion protein (~ 69 kDa) and N is the number of cells (in the volume of crude cell extract used for Western analysis). The two independent experiments (Supplementary Figure 5.7a) resulted in a combined average of 198 ± 12 YPet-DnaN monomer molecules per cell.

S5.7. VERIFICATION OF THE *dnaN* GENE COPY NUMBER BY SOUTHERN BLOTTING

The genomic copy number of *dnaN* in WT and YPet-DnaN:tetR-mCerulean strains was verified by Southern blotting as follows. Genomic DNA was extracted from the strains. The respective DNA was digested by restriction enzymes *BamHI* and *SacI* overnight. The digested DNA samples were separated by gel electrophoresis on an 0.8% agarose gel at 30V for 3hr. The digested DNA in the gel of the strains was depurinated, denaturated, neutralized and subsequently transferred to a Hybond-N+ nylon membrane (GE Healthcare) using capillary blotting. The probe (870 bp) for southern blotting was obtained from the wildtype AB1157 chromosome by PCR amplifying the region in the *dnaN* gene using the primers 5' – GCA CCG CTA TAG GTA ACG TC – 3' and 5' – TCG TCC TAC GCT ACC GAT TC – 3'. Subsequently the PCR product was labelled with thermostable alkaline phosphatase using the Amersham AlkPhos Direct kit (GE Healthcare) according to the instructions of the manufacturer. The labeled DNA probe was then added to the membrane and incubated at 55 °C overnight. After adding the luminescent substrate, imaging was performed using Gel-Doc. The resulting number of bands obtained is indicative of the copy number of the probed region in the chromosome (Supplementary Figure 5.7b). As is evident from the blot, there is only a single band, and thus only a single copy of the *dnaN* gene, in the chromosome of the WT (lane 1) and the strain (lane 3) used in the experiments.

S5.8. REPRODUCIBILITY OF THE β_2 CLAMP DYNAMICS WITH A *mCherry-dnaN* FUSION

Fluorescent proteins have been show to potentially aggregate in cells. This aggregation could lead to imaging artifacts [51, 52]. We conducted the same long-time lapse experiment with an mCherry-DnaN fusion in order to strengthen the argument that the stoichiometry and accumulation of clamps are reproducible with a different fluorescent protein and less likely due to any aggregation artifact. As is clearly visible the result agree within experimental error with what we have measured for the YPet-DnaN fusion strain (Supplementary Figure 5.8). In determining the mCherry-DnaN stoichiometry we used the single-molecule intensity calibration done for mCherry (Supplementary Information Section S5.2).

S5.9. DETERMINING THE UNLOADING TIME OF THE β_2 CLAMP FROM THE PALM EXPERIMENTS

The distribution of dwell-times of bound clamps is approximated with a single-exponential and has the following form:

$$p(t) = e^{-t/t_\mathrm{m}}\, t_\mathrm{m}^{-1},\ \ t_m^{-1} = t_\mathrm{unload}^{-1} + \tilde{t}_\mathrm{bl}^{-1}. \tag{5.3}$$

Here t_m^{-1} is the total decay rate of fluorescence, expressed as the sum of bleaching rate ($\tilde{t}_\mathrm{bl}^{-1}$) and the unloading rate (t_unload^{-1}). As we are ultimately interested in extracting the unloading time from Equation (5.3), we first determined the total decay rate and the bleaching rate.

To determine the decay rate of fluorescence for our experiments, the distribution in Equation (5.3) was fitted to the unloading data through maximum likelihood (ML) estimation, and errors were estimated over 10^6 bootstrapped data sets (Figure 5.4e (inset)). This resulted in $t_\mathrm{m} = 57 \pm 4$ s. Here the error is ± s.d. from the bootstrapped data.

To determine the bleaching rate, we first note that in the unloading experiments the proteins are only exposed to light during a fraction of the time they stay bound. Thus, the bleaching time ($\tilde{t}_{\text{bl}}$) in Equation (5.3) is related to the constant-exposure bleaching time (t_{bl}) through:

$$\tilde{t}_{\text{bl}} = \frac{T}{t_{\text{ex}}}\, t_{\text{bl}}. \tag{5.4}$$

Here T is the experimental time between frame start times, and t_{ex} is the experimental exposure time. The constant-exposure (no shuttering, thus t_{ex} is the camera exposure in this case) bleaching time was independently determined from the unloading experiments (Figure 5.9). Using ML estimation of the bootstrapped data sets, we arrive at $t_{\text{bl}} = 7 \pm 0.6\,\text{s}$, giving $\tilde{t}_{\text{bl}} = 80.5 \pm 6.9\,\text{s}$ by Equation (5.4). Using Equation (5.3), we now extract $t_{\text{unload}} = 195 \pm 58\,\text{s}$, where the confidence intervals were estimated through bootstrapping 10^6 datasets (under the assumption that we can ignore the error in our estimate of the bleaching time).

S5.10. ESTIMATING THE EFFECTIVE LOADING RATE

During chromosomal replication, the number of DNA-bound β_2 clamps (N_{β_2}) fluctuates around an average in the steady state. We assume here that primers are formed at the rate t_p^{-1}, and that individual β_2 clamps are loaded at a rate of t_{load}^{-1} (Supplementary Figure 5.10). The number of primers that have not been loaded with a β_2 clamp is denoted as $N_{\text{pre}-\beta_2}$ and the number of DNA-bound clamps is denoted as N_{β_2}. For each cell in the steady-state regime of replication, the rate of primer formation (t_{p}^{-1}) and the total rate that β_2 clamps are loaded ($t_{\text{load}}^{\text{eff}-1} = N_{\text{pre}-\beta_2}\, t_{\text{load}}^{-1}$) must balance,

$$t_{\text{p}}^{-1} = t_{\text{load}}^{\text{eff}-1} = N_{\text{pre}-\beta_2}\, t_{\text{load}}^{-1}. \tag{5.5}$$

This shows that the rate of primer formation sets the effective loading rate within our model in the steady state regime. According to Equation (5.5), a change in primer formation rate will always be compensated by a change in the steady state value of primers that have not had a β_2 clamp loaded. Our data does not allow us to directly extract either $N_{\text{pre}-\beta_2}$, or t_{load}. Similarly, if a β_2 clamp unloads at a rate, (t_{unload}^{-1}), the total effective rate at which β_2 clamps load ($N_{\text{pre}-\beta_2}\, t_{\text{load}}^{-1}$) must equal the total rate they unload ($N_{\beta_2}\, t_{\text{unload}}^{-1}$), giving:

$$N_{\beta_2}\, t_{\text{unload}}^{-1} = N_{\text{pre}-\beta_2}\, t_{\text{load}}^{-1}. \tag{5.6}$$

Together, Equations (5.5) and (5.6) give:

$$t_{\text{p}}^{-1} = t_{\text{load}}^{\text{eff}^{-1}} = N_{\beta_2}\, t_{\text{unload}}^{-1}. \tag{5.7}$$

Using Equation (5.7) the effective loading time is $t_{\text{load}}^{\text{eff}} = 4 \pm 1\,\text{s}$. Here the error was derived via propagation from the errors in t_{load} and N_{β_2} and calculated from Equation (5.7):

$$\frac{< \Delta t_{\text{p}}^2 >}{t_{\text{p}}^2} = \frac{< \Delta t_{\text{unload}}^2 >}{t_{\text{unload}}^2} + \frac{< \Delta N_{\beta_2}^2 >}{N_{\beta_2}^2}, \tag{5.8}$$

where we have assumed the errors in t_{unload} and N_{β_2} to be uncorrelated as they originate from different experiments.

SUPPLEMENTARY REFERENCES

[1] M. C. Leake, J. H. Chandler, G. H. Wadhams, F. Bai, R. M. Berry, and J. P. Armitage, *Stoichiometry and turnover in single, functioning membrane protein complexes.* Nature **443**, 355 (2006).

[2] G. I. Mashanov, D. Tacon, A. E. Knight, M. Peckham, and J. E. Molloy, *Visualizing single molecules inside living cells using total internal reflection fluorescence microscopy,* Methods (San Diego, Calif) **29**, 142 (2003).

[3] A. B. Loveland, S. Habuchi, J. C. Walter, and A. M. van Oijen, *A general approach to break the concentration barrier in single-molecule imaging.* Nature Methods **9**, 987 (2012).

[4] S. H. Chung and R. A. Kennedy, *Forward-backward non-linear filtering technique for extracting small biological signals from noise.* Journal of Neuroscience Methods **40**, 71 (1991).

[5] N. F. Reuel, P. Bojo, J. Zhang, A. A. Boghossian, J. Ahn, J. Kim, and M. S. Strano, *Norse: noise reduction and state evaluator for high-frequency single event traces.* Bioinformatics **28**, 296 (2012).

[6] A. Badrinarayanan, R. Reyes-Lamothe, S. Uphoff, M. C. Leake, and D. J. Sherratt, *In vivo architecture and action of bacterial structural maintenance of chromosome proteins,* Science **338**, 528 (2012).

[7] S. Wang, J. R. Moffitt, G. T. Dempsey, X. S. Xie, and X. Zhuang, *Characterization and development of photoactivatable fluorescent proteins for single-molecule-based superresolution imaging.* Proceedings Of The National Academy Of Sciences Of The United States Of America **111**, 8452 (2014) .

6

THE PROGRESSION OF REPLICATION FORKS AT NATURAL REPLICATION BARRIERS IN LIVE BACTERIA

Protein-DNA complexes are one of the principal roadblocks the replisome encounters during fork progression. Replisome impediments can lead to genomic instability and form a risk for cell viability. One such barrier is the Tus-ter complex, which is a direction dependent barrier for replication fork progression. The details concerning the dynamics of the replisome when encountering these natural Tus-ter barriers in the cell are poorly understood. By performing quantitative fluorescence microscopy in combination with microfluidics, we investigate the effect on the replisome when encountering a Tus-ter roadblock in live Escherichia coli (E. coli) cells. We make use of an E. coli variant that includes only an ectopic origin of replication that is positioned such that one of the two replisomes encounters a Tus-ter barrier substantially before the other replisome. This enables us to single out the effect of encountering a Tus-ter roadblock on an individual replisome. We demonstrate that the replisome remains stably bound after encountering a Tus-ter complex from the non-permissive direction. Furthermore, the replisome is only transiently blocked, and continues replication beyond the barrier. Additionally, we demonstrate that these barriers affect sister chromosome segregation by visualizing specific chromosomal loci in the presence and absence of the Tus protein. These observations demonstrate the resilience of the replication fork to natural barriers, the sensitivity of chromosome alignment to fork progression, and the robustness of the cell in completing the fundamental process of replication.

This chapter has been be submitted for publication as: M. Charl Moolman‡, Sriram Tiruvadi Krishnan‡, Jacob W.J. Kerssemakers, Vincent Lorent, David J. Sherratt and Nynke H. Dekker. The progression of replication forks at natural replication barriers in live bacteria. (‡ *Equal contribution*)

6.1. INTRODUCTION

All dividing cells must ensure the accurate and timely replication of their genome. The replication of DNA is an intricate process undertaken by the ubiquitous multi-protein complex known as the replisome [1–3]. In *Escherichia coli* (*E. coli*), the two independent replisomes [4] assemble at a single origin of replication (*oriC*) and subsequently advance in opposite directions at equal rates to synthesize the 4.6 Mbp genome, while the newly replicated DNA is sequentially segregated [5–9] prior to cell division. During fork progression, the replisomes encounter a substantial number of impediments preceding their fusion in the terminus region [10]. Stalled replication forks are a potential source of genome instability, and thus a risk of cell viability in general [11]. The major source of hindrance for a replisome during replication is believed to be protein-DNA complexes [12]. A specific natural protein-DNA complex that is particularly involved in the termination of replication is the 36 kDa monomeric Tus protein bound to one of the ~ 10 specific 23 bp DNA sequences (*ter*-sites) [13–16]. The majority of these *ter* sequences are spread across the terminus region of the chromosome, spanning ~ 2 Mbp across the two replichores (chromosome halves) [17] (Figure 6.1A). Replication forks are believed to be stalled when approaching such a Tus-*ter* complex from one direction (non-permissive side) but not from the other direction (permissive side) [18–22] (Figure 6.1 B, top), creating a replication fork barrier (RFB). The dominant mechanism of forming such a RFB is thought to be the binding of a conserved G-C(6) base pair residue (Figure 6.1B, left) to Tus. Lock formation is formed through the separation of the parental DNA strand in the non-permissive direction by the replicative helicase (DnaB) until the conserved residue is free and subsequently binds to the binding pocket of Tus (Figure 6.1B, right) [23]. Other lock formation mechanisms, for example protein-Tus interactions, have also been proposed [24]. The binding of Tus to a *ter* site is strongly dependent on ionic strength [25]. For example, Tus has a dissociation constant of K_d ~ pM and a half-life of $t_{1/2}$ ~ 500 min in 0.15 M potassium glutamate, while in 0.25 M potassium chloride (KCl), it exhibits a K_d ~ nM and a $t_{1/2}$ ~ 2min [26]. In physiological ionic strength (150 mM KCl), the half-life for a Tus-*ter* locked complex was found to be $t_{1/2}$ ~ 500 min [23]. The RFB system is conserved in *B. subtilis* [27–29], and has also been demonstrated to be capable of artificially pausing a replication fork in yeast and mammalian cells [30, 31].

The biological significance of the Tus-*ter* RFB and the fate of a replisome when encountering such a barrier remains poorly understood [21]. The ’replication fork trap’ (RFT) model suggests that the Tus-*ter* complexes act as a safeguard, ensuring that forks can enter but not exit the inner termination zone, thereby restraining fork fusion to the zone roughly opposite the origin of replication [32]. However, it is not clear why this would be necessary. It might assist fork fusion by ensuring that one of the two replisomes ’waits’ for the other oppositely progressing replisome to complete replication, or reduce the incidence of head-on collisions between the replication and transcription machineries [10]. It might also be related to the presence of the specific locus important for segregation (*dif*), situated between the innermost *ter*-sites (Figure 6.1A). The multiplicity of *ter*-sites on each of the two chromosome arms suggests that a replication fork may, despite the strong DNA binding of Tus, frequently overcome a non-permissive Tus-*ter* roadblock. A bulk *in vivo* study of plasmid fork arrests [35] suggests that the different

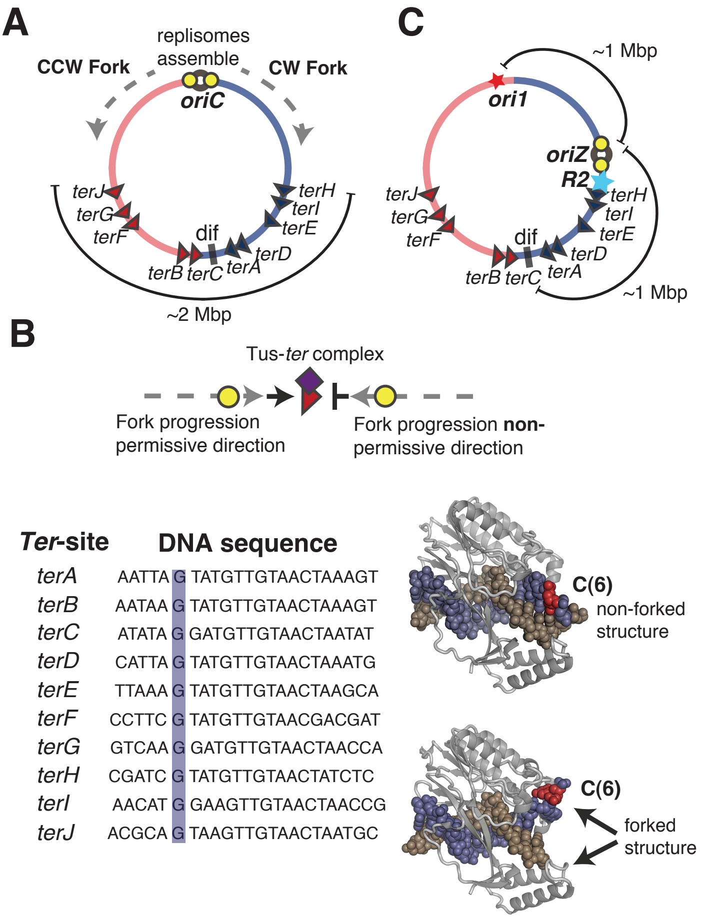

Ter-site	DNA sequence
terA	AATTA G TATGTTGTAACTAAAGT
terB	AATAA G TATGTTGTAACTAAAGT
terC	ATATA G GATGTTGTAACTAATAT
terD	CATTA G TATGTTGTAACTAAATG
terE	TTAAA G TATGTTGTAACTAAGCA
terF	CCTTC G TATGTTGTAACGACGAT
terG	GTCAA G GATGTTGTAACTAACCA
terH	CGATC G TATGTTGTAACTATCTC
terI	AACAT G GAAGTTGTAACTAACCG
terJ	ACGCA G TAAGTTGTAACTAATGC

Figure 6.1: Investigating the Tus-*ter* replication block efficacy in an *E. coli* strain with an ectopic origin. (A-B) The different *E. coli* chromosome arrangements. The left (red) and right replichore (blue), together with their respective *ter*-sites (triangles) are shown. The dashed grey lines indicate the directionality of the two independent replisome (yellow circles) movement. (A) The parental WT strain (oriC-strain) which has roughly equal genomic distance from *oriC* till the innermost *ter*-sites for both replisomes. (B) Polar-fork arrest by the Tus-*ter* complex. (top) A schematic representation illustrating two replisomes approaching the permissive and non-permissive faces of a Tus-*ter* complex. The purple square represents the Tus protein. The replisome approaching from the non-permissive side is believed to be blocked by the Tus-*ter* complex indicated here with a flat arrowhead. (left, right) The dominant mechanism of polar fork arrest by a Tus-*ter* complex. (left) The DNA sequences of the different *ter*-sites. Here the conserved G is highlighted by a light blue rectangle. (right) The crystal structures of a non-forked Tus-bound *ter*-site and a forked Tus-bound *ter*-site approached from the non-permissive direction. Here the Tus protein is depicted in light grey. Images where generated using the Protein Data Bank (PDB) files, 1ECR and 2EWJ [23, 33]. DNA molecules are represented in purple and brown, while the C(6) residue is highlighted in red. (C) The strain with an ectopic origin (oriZ-strain) [34]. Here the origin of replication (*oriZ*) is positioned at 344 kb on the *E. coli* genetic map. The insertion position of a *lacO* operator array at 3908 kb (*ori1*), and a *tetO* operator array at 336 kb (*R2*) are indicated with a red and blue star respectively.

ter-sites have distinct fork arrest efficiencies, with the innermost sites (*terA-E*) being the most effective (20 - 35 %). This is in line with an *in vitro* study that demonstrated that Tus binds strongly to *terA-E* and less strongly to other *ter*-sites [36]. It remains unclear what happens to a replisome when it encounters such a block. Given the relatively low efficiencies of the RFBs and the *in vitro* robustness of the replisome encountering head-on collisions [37, 38], it could be the case that the replisome remains intact after encountering a Tus-*ter* block and proceeds with replication.

To gain insight into the response of a replisome as it encounters a Tus-*ter* roadblock under *in vivo* conditions, we study single live *E. coli* cells that contain only an ectopic origin (*oriZ*) in either the presence or absence of Tus (Supplementary Section S6.1; Figure 6.1C). The *oriZ* position is such that the CW replisome encounters a non-permissive Tus-*ter* complex earlier on in replication than the CCW replisome. Utilizing custom microfluidics [39] to ensure healthy cell physiology in combination with time-lapse widefield fluorescence microscopy, we quantitatively investigate chromosomal replication and segregation during successive cell cycles. We track the replisome as well as specific chromosomal loci on the left (L) and right (R) replichore arms of the chromosome (Figure 6.1C). This enables us to investigate the effect of the Tus roadblock on both replication and segregation. Our data indicate that while the Tus-*ter* roadblock impedes replisome progression, the replisome is sufficiently resilient to avoid disassembly at the barrier, proceeding to overcome it and finish the replication process in an overall time that only exceeds that of cells with the native origin of replication *oriC* by 15 %. The replication time in the absence of Tus (*oriZ:*Δ*Tus* cells) is in excellent agreement with that of *oriC* cells, confirming that the Tus-*ter* complex is indeed the barrier responsible for the increased replication time in *oriZ* cells. We found that the generation time of all ΔTus mutants with an ectopic or native origin of replication exceeded that of *oriC* cells. We investigated the effect of the Tus-*ter* block on the chromosomal segregation organization, since this pattern is sensitive to fork progression [40, 41]. The sister chromosome alignment (SCA) patterns after replication for the *oriZ* and *oriZ:*Δ*Tus* cells were found to differ: SCA patterns changed from a predominant LRLR (*oriZ* cells) configuration to a RLLR configuration (*oriZ:*Δ*Tus* cells). This suggests that the RFB caused by the Tus-*ter* complex can influence the manner in which the sister chromosomes are segregated and positioned following replication. Collectively, our results show that the replisome is stable after encountering a natural impediment in the cell. It does not collapse, but rather remains DNA-bound and overcomes this barrier, possibly with assistance from other proteins.

6.2. RESULTS

6.2.1. DELINEATING THE TIME WHEN THE CW REPLISOME ENCOUNTERS A TUS-*ter* COMPLEX FROM THE NON-PERMISSIVE SIDE.

We utilize time-lapse fluorescence microscopy in combination with a custom-built microfluidic device [39] to track the independent replisomes and chromosomal loci during chromosomal replication. The individual replisomes are visualized via a functional YPet-DnaN chromosomal fusion [34], and the left- and right replichore arms are imaged using a fluorescent-repressor-operator system (FROS) [42]. The *lacO* (*ori1*) is positioned on the left arm, 15 kb CCW from the former position of *oriC*, and the *tetO* (*R2*) array is positioned on the right arm, 21 kb CW of *oriZ* [34] (Figure 6.1C). Fusions of LacI-mCherry and TetR-mCerulean are expressed at low levels to keep any perturbation to the generation and replication times [43] to a minimum [34, 44, 45]. Kymographs of sample individual cells illustrate the YPet-DnaN and *ori1*-mCherry movements during replication (Figure 6.2A-B, left). The respective temporal montages of the individual images are shown in the Supplementary Figure 6.1A-B. We determine the positions of the respective foci for each individual image of a time-lapse measurement by fitting a 1D-Gaussian function across the long axis to the profile summed across the short axis of the bacterium (Supplementary Section S6.2). Figure 6.2A-B (centre) depict sample fluorescence images and their corresponding Gaussian fits. The calculated positions per individual image are used to track the YPet-DnaN and *ori1*-mCherry foci over a complete replication cycle in each individual cell (Figure 6.2C). We perform an equivalent analysis to detect and track the *R2*-mCerulean loci (Supplementary Figure 6.2).

The temporal information of *ori1*-mCherry enables us to establish the precise moment during replication at which the CW replisome encounters the Tus-*terC* roadblock. This is because the distances of *ori1* from *oriZ* (~ 1050 kbp) and of *terC* from *oriZ* (~ 1100 kbp) can be seen as equivalent (~ 1 Mbp) (Figure 6.1C). We determine the time-point at which the *ori1*-mCherry focus doubles (Figure 6.2C). Since the two replisomes are believed to progress at the same rate on average (v_{rep} ~ 550 bp/s) (Supplementary Section S6.3), this time-point is indicative of when the CW replisome encounters the Tus-*terC* roadblock from the non-permissive direction (Figure 6.2C (inset)). The average time following initiation required for the CCW replisome to replicate *ori1* is $t_{ori1} = 26 \pm 6$ min (Error is ± SD; n = 282; Figure 6.2D). This measured time is in agreement with previous measurements [34], as well as with the expected value ($t_{ori1,\text{expected}} = 32$ min) calculated using the distance of *ori1* from *oriZ* and the average replication speed (v_{rep}).

6.2.2. A REPLISOME REMAINS DNA-BOUND AFTER ENCOUNTERING A TUS-*ter* ROADBLOCK.

Since it is conceivable that the replisome disassembles when encountering a Tus-*ter* complex, we examine the dynamics of the replisome in single cells from initiation till termination, with specific attention given to the time point when the replisome reaches the Tus-*terC* roadblock. The DNA-bound YPet-DnaN foci are detected and tracked during the whole replication process (Figure 6.3A, left). The size of the markers in the average time-resolved trace (Supplementary Section S6.2) presented is indicative of the percentage of cells at that time point having either a single focus (black dots) or two foci (black circles). The majority of the cells exhibits a single focus at initiation and just prior to termination, while during elongation cells display single and double foci at equal frequencies (Figure 6.3A, right).

To rule out that the single focus observed in roughly 50 % of the cells during elongation results from the CW replisome disassembly at the Tus-*terC* site, we quantify and compare the DNA-bound YPet-DnaN intensity for two conditions. First, we compare the

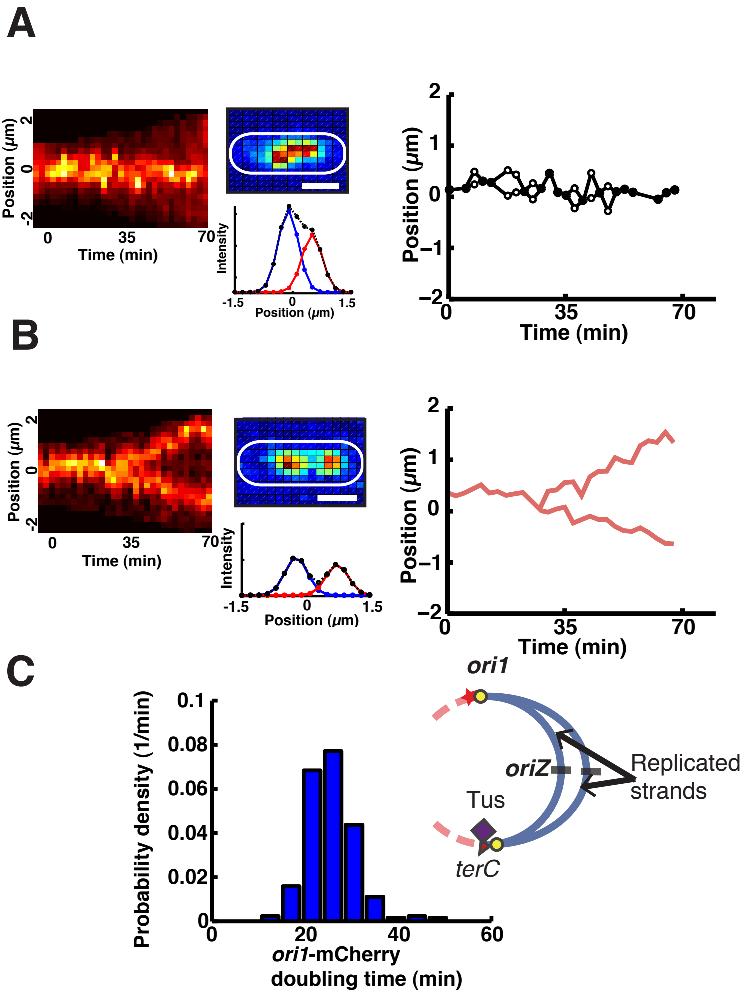

Figure 6.2: An example individual replication cycle of *oriZ* cells. (A-B) Representative DnaN-YPet and *ori1*-mCherry fluorescent signals. (A-B, left) Individual kymographs of the replisome (Ypet-DnaN) and *ori1*-mCherry locus for one complete replication cycle constructed by summation of the pixel intensities along the short axis of the cell. The replisomes remain relatively close together, while the *ori1*-mCherry loci segregate and move to opposite cell poles. (A-B, centre) Sample fluorescent foci of Ypet-DnaN and *ori1*-mCherry imaged (represented here in pseudo-colour) together with the their respective Gaussian fits. Scale bars, 1.3 μm. (A-B, right) The complete YPet-DnaN (A, right) and *ori1*-mCherry (B, right) traces shown in (A, left) and (B, left) determined from the Gaussian fitted positions from individual images for each time point. Here a single YPet-DnaN focus is indicated in a filled circle and two individual foci are indicated as open circles. The lines between data points are included to aid the reader. *ori1*-mCherry positions over time are indicated with solid red lines. (C) The distribution of the time point during replication when the *ori1*-mCherry focus doubles. The mean doubling time of *ori1*-mCherry is $t_{ori1} = 26 \pm 6$ min (Error is ± SD, n = 282). (Inset) We schematically show that when *ori1*-mCherry focus is reached it is indicative of the time point when the CW replisome reaches the Tus-*terC* complex.

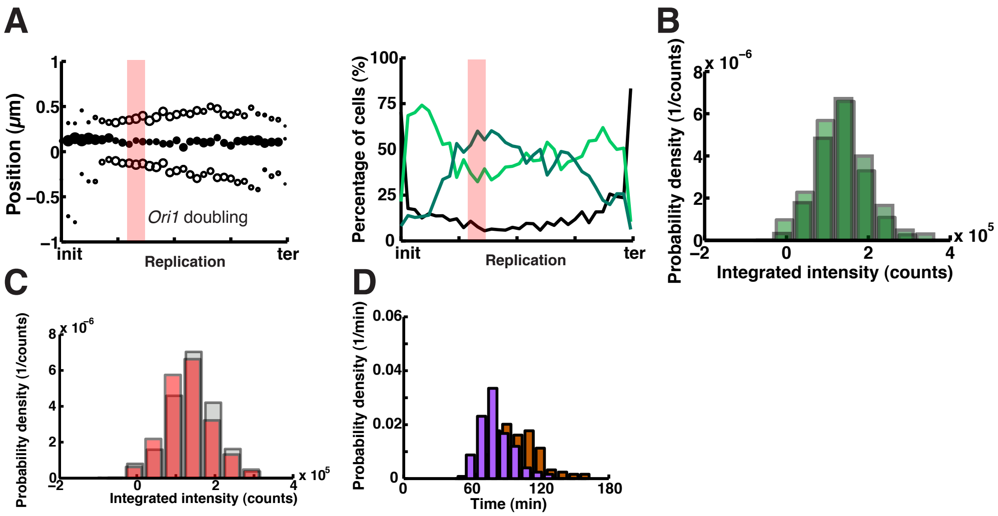

Figure 6.3: The replisome is slowed down at a Tus-*ter* roadblock, but not halted indefinitely. (A) Average replisome behaviour during replication in the oriZ-strain. (left) An average time resolved trace of the two replisomes (YPet-DnaN) from individual cells during complete replication cycles (n = 128). Here we plot the single DnaN-YPet focus (filled circles) and double DnaN-YPet foci (open circles). The size of an individual element at each time point is representative of the percentage of cells having that particular distribution of foci. The traces have been aligned with respect to initiation and termination, and binned. The transparent red rectangle indicates the time when *ori1*-mCherry replicates, as determined from the distribution in Figure 6.2D. The width of the rectangle is ± SD. (right) The percentage of cells that have a single focus (light green line), double foci (dark green line) and no foci (black line) as function of replication time. It is evident that the percentage of cells having a single focus or double foci is roughly equally distributed. (B) The integrated intensity when only a single YPet-DnaN focus (light green) is visible ($I_{\text{single}} = 1.28 \cdot 10^5 \pm 6.11 \cdot 10^4$), (n = 2123), is essential the same as the sum of two individual YPet-DnaN foci (dark green) ($I_{\text{double}} = 1.41 \cdot 10^5 \pm 6.72 \cdot 10^4$), (n = 1647). The difference between the two means of the individual distributions is < 10%. This intensity similarity implies that the same number of YPet-DnaN molecules are DNA-bound when a single focus or two foci are detected. (C) The intensity distributions of DNA-bound YPet-DnaN prior (grey) and post (red) doubling of *ori1*-mCherry. $I_{\text{prior},ori1-\text{mCherry}} = 1.43 \cdot 10^5 \pm 6.58 \cdot 10^4$ counts (n = 1304), $I_{\text{post},ori1-\text{mCherry}} = 1.31 \cdot 10^5 \pm 6.28 \cdot 10^4$ counts (mean ± SD, n = 3157). The difference between the means of the two distributions is < 9%. The number of DNA-bound YPet-DnaN is thus practically unchanged after *ori1*-mCherry has been replicated, i.e. after the CW replisome has encountered the Tus-*terC* roadblock. This unchanged intensity value is indicative of replisomes not being disassembled after encountering a Tus-*ter* roadblock but rather remaining DNA-bound. (D) The distribution of the replication times (purple) and division time (brown) of individual oriZ cells. The average replication time is $t_{\text{rep},oriZ} = 81 \pm 15$ min and the average division time is $t_{\text{div},oriZ} = 97 \pm 21$ min (Error is ± SD).

intensity of a single focus (light green) and double foci (dark green) during replication (Figure 6.3B). We observe only a small difference between the means (< 10%), which suggests that there is no change in the number of DNA-bound YPet-DnaN molecules regardless of whether one or two foci are detected. Thus, the differing number of foci detected does not reflect replisome disassembly, but likely results from DNA conformational changes that result in sufficiently close proximity (below the resolution limit imposed by diffraction) of the two replisomes to preclude their separate identification. Secondly, we compare the intensity of DNA-bound YPet-DnaN prior (grey) and post (red) *ori1*-mCherry doubling (Figure 6.3C). Here also, we only detect slight differences ($< 10\%$). This implies that there is no significant decrease in the number of DNA-bound YPet-DnaN before and after the replisome has encountered the Tus-*terC*. This suggests that the replisome, or at least DnaN, remains DNA-bound after encountering a Tus-*ter* roadblock and is not directly disassembled.

6.2.3. A REPLISOME IS IMPEDED BY A TUS-*ter* COMPLEX, BUT NOT HALTED INDEFINTELY.

We demonstrate that the replisome does not only remain DNA bound, but is capable of progressing past the Tus-*ter* block and continue replication. While the replisome does not disassemble following the encounter with Tus-*terC*, it could potentially stall there without further replication; in other words, it is plausible that the CCW replisome synthesizes the remainder of the chromosome while the CW replisome is halted. To test whether the CW replisome can continue replication after having reached the Tus-*terC* block, we compare the replication and division times of *oriZ* cells with those of *oriC* cells (Table 1). The *oriC* cells have a division time of $t_{\mathrm{div},oriC} = 85 \pm 15\,\mathrm{min}$, and *oriZ* cells have a $t_{\mathrm{div},oriZ} = 97 \pm 21\,\mathrm{min}$ (Errors are ± SD; Figure 6.3D). Thus the division time for *oriZ* cells to that of *oriC* cells increases by $\sim 13\%$. The *oriC* cells have a replication time of $t_{\mathrm{rep},oriC} = 70 \pm 7\,\mathrm{min}$ (The errors are ± SD; Supplementary Figure 6.3A-B). The measured replication time in *oriZ* cells is $t_{\mathrm{rep},oriZ} = 81 \pm 15\,\mathrm{min}$ (mean ± SD; Figure 6.3D). If the CW replisome was halted indefinitely, one would expect the CCW replisome to copy $\sim 1/4$ more of the chromosome. This should cause the replication time in *oriZ* cells to increase by a factor of 1.5, thus to $\sim 105\,\mathrm{min}$, a value that notably exceeds the observed increase of ~ 1.15x. Even though we cannot fully exclude from our data that the CCW replisome might speed up during replication due to an increase availability of deoxyribonucleotide triphosphates(dNTPs) [46] by the stalling of the CW fork, we deem this to not be the dominant factor. Since the sliding clamp (DnaN) is actively unloaded at a rate of one clamp per $\sim 3\,\mathrm{min}$ [47], and the fact that we do not see a decrease in number of DNA-bound clamps after encountering Tus-*terC* suggests that the replisome does not disassemble, and that any contribution from excess dNTP due to collapsed CW replisomes would be small. Thus, the only marginal increase of the replication time suggests that the CW fork is, at least in a large fraction of the cases, capable of passing the Tus-*terC* block.

6.2.4. REPLISOME PROGRESSION IS INFLUENCED BY THE ABSENCE OF TUS IN *oriZ* CELLS.

To verify that the longer replication time observed in *oriZ* cells can be attributed to hampering of the CW replisome by the Tus-*ter* complex, we investigate the replisome dynamics and replication time in *oriZ* cells that do not express Tus (*oriZ:*Δ*Tus*) [48] (Supplementary Section S6.1). This strain is incapable of forming the Tus-*ter* complex, and hence the replisome should be able to progress unimpeded beyond the innermost terminus region.

Double foci are more frequently observed during elongation in *oriZ*Δ*:Tus* cells compared to *oriZ* cells. A sample trace (Figure 6.4A) and its corresponding temporal montage (Supplementary Figure 6.1C-D) illustrate this effect that foci appear to overlap less frequently in *oriZΔ:Tus* cells compared to *oriZ* cells. The average time-resolved trace (Figure 6.4B, top) clearly shows that the fraction of cells displaying a single focus during elongation has decreased by a factor of ~ 2 (Figure 6.4B, bottom). This is most likely due to the influence of the absence of the Tus-*ter* roadblock on the replication-dependent chromosome dynamics and organization [40, 41].

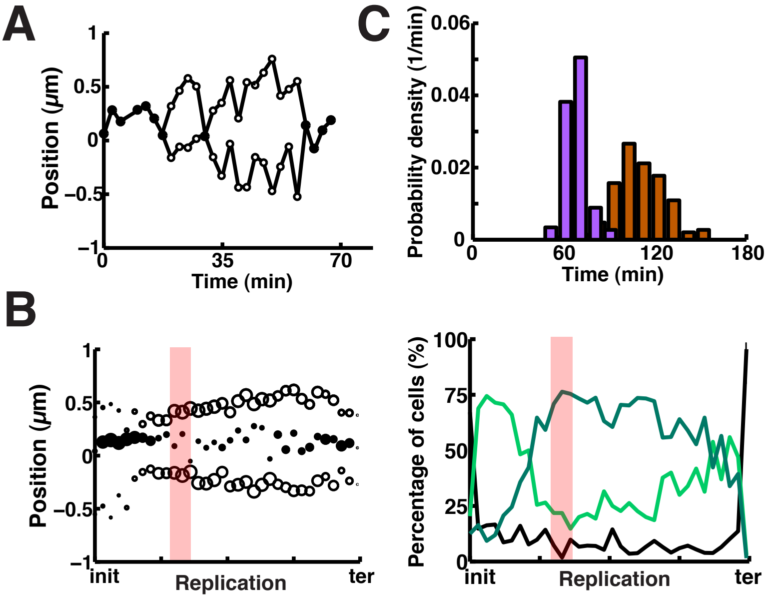

Figure 6.4: Removing the Tus-*ter* roadblock directly affects replication in oriZ:ΔTus cells. (A) A representative complete single replication cycle in a single *oriZ:ΔTus* cell. A single YPet-DnaN focus is indicated with a solid black dot and two individual foci are indicated as circles. The lines between data points are included to aid the reader. (B) (left) An average time resolved trace of the two replisomes (YPet-DnaN) from individual cells during complete replication cycles (n = 152). Single DnaN-YPet focus are represented as filled cicrcls and double DnaN-YPet foci with open circles. The size of an individual element at each time point is again representative of the percentage of cells having that particular foci distribution. The traces have been aligned with respect to initiation and termination and binned. (right) The percentage of cells that have a single focus (light green line), double foci (dark green line) and no foci (black line) as function of replication time. It is evident that the majority of the cells have two foci for the largest part of the replication process. The transparent red rectangle indicates the time when *ori1*-mCherry replicates, as determined from the distribution in Figure 6.2D. The width of the rectangle is ± SD. (C) The distribution of the replication time (purple) and division time (brown) of individual oriZ:Δ*Tus* cells. The average replication time is $t_{\text{rep},oriZ:\Delta\text{Tus}} = 68 \pm 7\,\text{min}$, and the average division time is $t_{\text{div},oriZ:\Delta\text{Tus}} = 109 \pm 18\,\text{min}$ (Error is ± SD).

OriZ:ΔTus cells exhibit very similar replication times to *oriC* cells. The replication time for *oriZ:ΔTus* cells is $t_{\text{rep},oriZ\Delta Tus} = 68 \pm 7\,\text{min}$ (Figure 6.4C), which is consistent with the above argument that the longer replication time in *oriZ* cells compared to *oriC* cells is due to the Tus-*ter* block. The replication time of *OriZ:ΔTus* cells is in close similarity with the replication time for *oriC* cells ($t_{\text{rep},oriC} = 70 \pm 7\,\text{min}$) (Supplementary Figure 6.3B). While the replication time for *oriZ:ΔTus* cells is decreased compared to that of *oriZ* cells where we found $t_{\mathrm{rep},oriZ} \sim 81\,\mathrm{min}$, the division time is slightly longer $t_{\mathrm{div},oriZ\Delta Tus} = 109 \pm 18\,\mathrm{min}$ (Figure 6.4C) compared to $t_{\mathrm{div},oriZ} \sim 97\,\mathrm{min}$.

To gain further insight into the effect on the replication and division times in the absence of Tus, we investigated these times in *oriC* cells that did not express Tus (*oriC:*Δ*Tus*) (Supplementary Section S6.1; Figure S3). We observed a slight increase in both the division time ($t_{\mathrm{div},oriC:\Delta Tus} = 96 \pm 19\,\mathrm{min}$) and replication time ($t_{\mathrm{rep},oriC:\Delta Tus} = 80 \pm 11\,\mathrm{min}$) compared to *oriC* cells where we found $t_{\mathrm{rep},oriC} \sim 70\,\mathrm{min}$ and $t_{\mathrm{div},oriC} \sim 85\,\mathrm{min}$ (Supplementary Figure 6.3C). This increase might be due to the more collision-prone fork fusion in the absence of Tus. No visible difference was observed in the replisome dynamics in terms of single or doubling foci as function of replication time (Supplementary Figure 6.3D-E). The division- and replication times of the four different strains have been summarized in Table 6.1.

***E. coli* strain**	**Division time (min)**	**Replication time (min)**	**D-period (min)**
oriC	85 ± 15	70 ± 7	23 ± 9
*oriC:*Δ*Tus*	96 ± 19	80 ± 11	30 ± 13
oriZ	97 ± 21	81 ± 15	19 ± 13
*oriZ:*Δ*Tus*	109 ± 18	68 ± 7	31 ± 10

Table 6.1: The division- and replication times together with the respective D-periods for the different *E. coli* strains investigated. The numbers specified indicate the mean ± SD. Here replication time is defined as the time interval between YPet-DnaN focus appearance and disappearance. D-period is defined as the time interval between YPet-DnaN focus disappearance and cell division.

6.2.5. THE PRESENCE AND ABSENCE OF TUS INFLUENCES THE SISTER CHROMOSOME ALIGNMENT PATTERN IN *oriZ* CELLS

To gain more insight into the discernibility of the individual replisomes during replication we investigate the chromosome organization in *oriZ* and *oriZ:*Δ*Tus* cells. Utilizing the labeled chromosomal loci on the left (*ori1*-mCherry) and right (*R2*-mCerulean) replichores, we visualize their movement during replication (Figure 6.5A-B). It is evident from the time-resolved traces that the *ori1*-mCherry and *R2*-mCerulean loci segregate and move to opposite cell halves in both cases. The times when the *ori1*-mCherry focus and *R2*-mCerulean focus double are indicated. Since we did not observe a significant difference in the doubling times of the respective loci in the two strains we grouped the *oriZ* and *oriZ:*Δ*Tus* data for better statistics. As stated previously, the time measured for *ori1* foci doubling ($t_{ori1} = 26 \pm 6\,\mathrm{min}$) is in excellent agreement with the expected value. In the case of *R2*, one would expect this region to be replicated ~ 1 min after initiation given its position and the average speed of a replisome, but we measure $t_{R2} = 17 \pm 5\,\mathrm{min}$ (Error is ± SD, n = 167) (Supplementary Figure 6.2B), in agreement with previous measurements [34]. However, this discrepancy between the measured and expected time

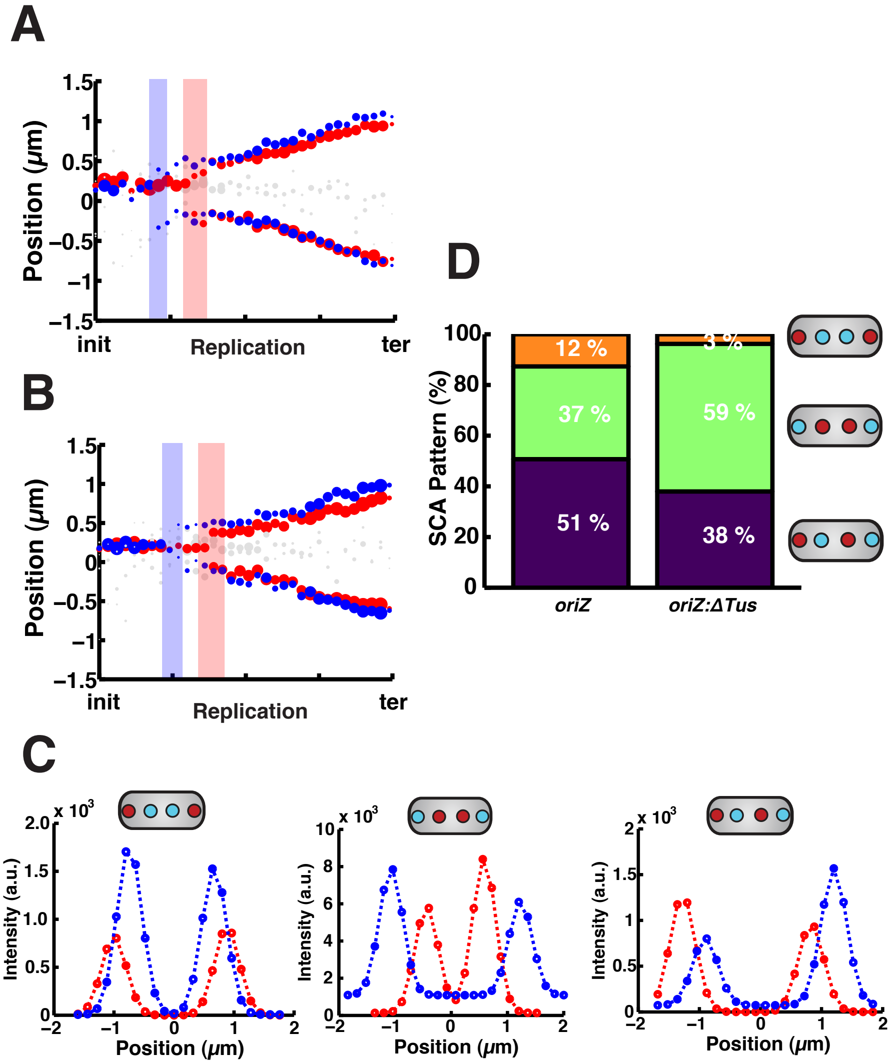

Figure 6.5: Sister chromosome alignment patterns are different for *oriZ* and *oriZ:*Δ*Tus* cells. (A-B) Average time resolved traces of the *ori1*-mCherry (Red) and *R2*-mCerulean (blue) loci. The blue and red rectangles indicates the time when the respective loci replicate as determined from the distributions in Figure 6.2D and Supplementary Figure 6.2B. The shaded white dots are when only a single focus was detected, which was in the minority of cases. As with the previous figures, the size of the dots are representative of the percentage of cells having that particular foci distribution. The width of the shaded region is the SD. (A) *oriZ*-strain (n = 71). (B) *oriZ:*Δ*Tus*-strain (n = 79). (C) Example sister chromosome alignment (SCA) patterns of the left (L) and right (R) replichores after replication. Here we plot the fitted spatial intensity distributions. (left) LRRL, (centre) RLLR and (right) RLRL. (Insets) Schematic depiction of the different chromosomal loci patterns. (D) The distributions of the different SCA patterns for the *oriZ*-, and *oriZ:*Δ*Tus*-cells after replication. The predominant pattern for *oriZ* (51 %) is the LRLR organization, while for *oriZ:*Δ*Tus* cells this is the RLLR organization (59 %).

when *R2* separates, can be attributed to the region of the chromosome that remains juxtaposed for ~ 10 min and not yet segregated fully [4, 49, 50]. One can appreciate that the pattern at the end of replication between the two strains appears to be different (Figure 6.5A-B).

The sister chromosome alignment (SCA) patterns formed illustrate a change in chromosome organization in the absence of Tus. Since the movement or stagnation of the replication fork influences chromosome segregation organization [41, 51], we investigated the resulting arrangement of the left (L) and right (R) replichore loci after termination in both the *oriZ* and *oriZ*:Δ*Tus* cells (Figure 6.5C). The three segregation patterns observed are LRRL (Figure 6.5C, left), RLLR (Figure 6.5C, centre), and LRLR (Figure 6.5C, right). In a minority of the cells (< 9%), the loci of the LR replichore arms spatially overlap (Supplementary Figure 6.4A), preventing their proper classification. Such cells are discarded from further analysis. The small number of cells displaying a RLRL pattern (Supplementary Figure 6.4B) are grouped with the LRLR (conform convention, since it is a symmetric configuration [52]). The majority of the *oriZ* cells displayed a LRLR pattern, consistent with what has been measured previously [34], while the predominant pattern in *oriZ*:Δ*Tus* cells is RLLR. There is thus a switch in the predominant SCA pattern in the absence of Tus. This predominate RLLR pattern is already observed half way through replication (Supplementary Figure 6.4C). The fraction of *oriZ*:Δ*Tus* cells displaying RLLR is larger when determined half way through replication compared to at termination, while for *oriZ* cells it is essentially unaffected. Through some mechanism the cell is able to revert back, but not fully, to the 'normal' LRLR pattern.

6.2.6. FORK FUSION IN *oriZ* CELLS OCCURS MOST LIKELY CLOSE TO *terF*

The time point at which the CW replisome reaches *terC* and the total replication time provide us with insight into the position where termination occurs in *oriZ* cells. Since we demonstrated that the CW replisome is not disassembled at Tus-*terC*, and that it most likely continues synthesis, albeit being slowed down, it is possible to determine the most likely termination site. Calculating from the time when the CW replisome encounters *terC* (~ 26 min) there remain ~ 55 min for the two replisomes to copy the remainder (~ 2300 kbp) of the genome (Figure 6.6A). The CCW replisome is not hampered as it synthesizes in the natural direction and would thus progress ~ 1800 kbp, assuming a constant velocity of $v \sim 550$ bp/s. This implies that the CW replisome is effectively delayed by the Tus-*ter* barriers for ~ 30 min, and replicates only 500 kbp. This suggests that termination, i.e. fork fusion, occurs between *terB*-*terF* but closer to *terF* (Figure 6.6B). This is consistent with *terB* and *terC* being strong roadblocks and slowing down CW replisome progression.

6.3. DISCUSSION

To ensure the accurate inheritance of genetic material one needs faithful completion of replication and chromosome segregation. Our work provides insight into the replisome's robustness *in vivo* and into its ability to circumvent the natural Tus-*ter* replication barriers. We characterize the effect of the Tus-*ter* complex on the stability and progres-

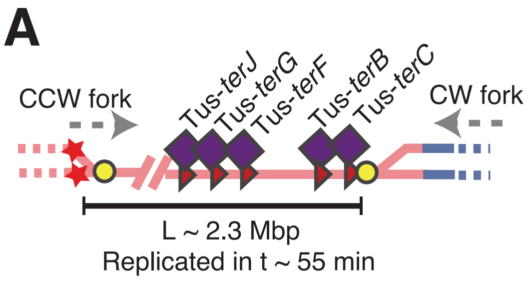

Figure 6.6: The CW replisome crosses *terB* and *terC*. (A) Schematic illustration of the remaining chromosome that needs to be replicated after the CW replisome has encountered the Tus-*terC* roadblock. (B) A graphic representation of the position where termination occurs in *oriZ* cells. Here the transparent yellow circles are representative of the uncertainty on the exact position of fork fusion, i.e. termination, somewhere inbetween *terF* and *terB*.

sion of the replisome when it encounters the barrier from the non-permissive side. Our data suggest that the CW replisome (as assessed by studying YPet-DnaN foci) does not disassemble after having encountered the Tus-*terC* complex from the non-permissive direction, but rather remains stably bound to the DNA. This result is consistent with what has been observed *in vitro* during a head-on collision of the *E. coli* replisome and an RNA polymerase (RNAP) [37]. We observed that the progression of the CW fork is impeded, but that it is capable of overcoming this barrier, as deduced from the unaffected number of DNA-bound YPet-DnaN before and after encountering the roadblock (Figure 6.3C), together with the fact that the overall replication time only increased by 15%(Figure 6.3D).

We demonstrate that the presence and absence of Tus affects the replication- and cell generation-times in both *oriC* and *oriZ* cells. For both *oriZ:ΔTus* and *oriC:ΔTus*, an increase in the mean cell doubling time was observed when compared to *oriC* and *oriZ* cells respectively (~ 11% and ~ 12%, respectively). In both cases this increase could result from processing events required to complete replication when the converging forks fuse at sites other that Tus-bound *ter* sites. This hypothesis is supported by our observation that there is an increase in the D-period for these strains (Table 1). We note that the replication time for *oriZ:ΔTus* was in very good agreement with *oriC* cells, strengthening the view that the Tus-*ter* complexes caused the measured replication fork delay in *oriZ* cells. We observed a slightly longer replication time for *oriC:ΔTus* cells compared to *oriC* cells (~ 14% increase). This observation of longer replication times in *oriC* is in accordance with the RFT model [21, 35] that fork fusion and completion of replication is most effective at Tus-bound *ter* sites [53], rather than at the *dif*-site as has been proposed by bioinformatics analysis [54]. The *dif* locus, located between *terA* and *terC*, is where the XerCD recombinase decatenates newly replicated sister chromosomes and resolves chromosome dimers of nascent daughter chromosomes to allow successful chromosome segregation [55]. If fork fusion occurred at the *dif*-site most frequently, the absence of Tus should have had negligible effect on the replication and cell division. We propose that Tus-*ter* sites around the *dif*-site facilitate the localization of the proteins necessary for proper dimer resolution by ensuring that only one of the two replisomes replicate the *dif* sequence, as postulated by *Duggin et al* [21]. Possibly, fork fusion and attendant collision processes in the direct vicinity of the *dif*-site might influence for example decatenation or dimer resolution, and hence increase the overall duration of replication and cell division.

We observed a switch in the predominant SCA patterns after replication when the *tus* gene was deleted from *oriZ* cells. The predominant SCA pattern in *oriC* and *oriZ* cells has been shown to be LRLR [34]. We indeed observed this pattern for *oriZ* cells, while interestingly the predominant pattern switched to RLLR in the absence of Tus (*oriZ*:Δ*Tus* cells), an organization pattern that is associated with fork stalling [41]. One would rather have anticipated that the proportion of cells displaying LRLR pattern should increase when Tus is absent from the cells; since no replication fork stalling is occurring due to Tus-*ter* complexes. Our different observation may imply that the collision of the CW replisome with different proteins after passing the *dif*-site plays a role in the final SCA in *oriZ* cells.

A future topic of study would be to investigate the mechanistic details by which the replication fork can progress beyond a RFB caused by the Tus-*ter* complex. The β_2 sliding clamps have been shown to facilitate in bypassing of replication barriers [56]. This might be a strategy by which the replisome bridges such an RFB when encountering the Tus-*ter* complex from the permissive side. SSB for example might facilitate repair at these collisions [57] and in that way assist the replisome. It might be other non-replicative helicases that dispose of these roadblocks [58]. For example the *E. coli* helicase II (UvrD) is a 3’ to 5’ helicase that has been shown to be able to remove Tus *in vitro* [59]. It is plausible that it could remove Tus from a *ter* site *in vivo* as well. The FtsK translocase involved in chromosome segregation [60, 61] is another potential candidate for Tus removal, though a recent single-molecule *in vitro* study has shown that FtsK changes direction when encountering Tus and does not seem to dislodge it from the DNA [62]. Independently of which proteins assist the replisome in encountering a roadblock, our work demonstrates that the replisome is robust in continuing replication despite this hurdle.

6.4. EXPERIMENTAL PROCEDURES

The details regarding the experimental procedures can be found in the Supplementary Information. Here we briefly highlight the different strains and techniques used in this study.

6.4.1. STRAINS, STRAIN CONSTRUCTION AND GROWTH FOR MICROSCOPY

All endogenous chromosomal integration of the *lacO* and *tetO* arrays, and fusions of either YPet-DnaN, LacI-mCherry and TetR-mCerulean where constructed in previous work and described in detail [34]. All chromosomal deletions of *tus* in the different strains were realized by λ-red recombination.

Cells used for microscopy were grown in M9-Gly supplemented with the necessary nutrients (Supplementary Section S6.4 and S6.5) until an OD$\sim$ 0.2 was reached. The cells were immobilized for imaging using a custom microfluidic system made from polydimethylsiloxane (PDMS) (Supplementary Section S6.6). Fresh growth medium was continuously injected automatically into the device during an experiment at 0.5 mL/hr via a syringe pump.

6.4.2. MICROSCOPY AND IMAGE ANALYSIS

All microscopy experiments where conducted on a commercial Nikon Ti microscope with custom laser excitation (Supplementary Section S6.7). YPet was imaged using a 515 nm (Cobolt Fandango) laser, mCherry was imaged using a 561 nm (Cobolt Jive) laser and mCerulean was imaged using a 457 nm (Cobolt Twist) laser. Image acquisition was performed with an EMCCD (Andor) using commercial Nikon NIS elements software (Supplementary Section S6.8). The whole microscope body, including sample, was kept at ~ 37 °C using a temperature controller (Okolabs). Image analysis was performed using ImageJ and custom written Matlab code (Supplementary Section S6.2).

CONTRIBUTIONS

M.C.M. and N.H.D. designed the research. M.C.M., S.T.K. and N.H.D. designed the experiments. S.T.K. undertook the experiments. V.L assisted during experiments and contributed to discussions. S.T.K. constructed strains. M.C.M. and J.W.J.K. wrote software to analyze the microscopy data. M.C.M. and J.W.J.K. analyzed the data. D.J.S. provided strains and contributed to the discussion of the work.

ACKNOWLEDGMENTS

We thank Christian Lesterlin for support with the *oriZ*-strain, Roy de Leeuw for help during initial experiments and Theo van Laar for stimulating discussions. We thank Jelle van der Does, Dimitri de Roos, and Jaap Beekman for their contribution towards instrumentation and infrastructure. This work was supported by a Wellcome Trust Program Grant WT083469 to D.J.S., and the European Community's Seventh Framework Programme FP7/2007-2013 under grant agreement n° 241548 (MitoSys) and a Vici grant by Netherlands Organization for Scientific Research (NWO) both to N.H.D.

REFERENCES

[1] A. Johnson and M. O'Donnell, *Cellular DNA replicases: components and dynamics at the replication fork*. Annual review of biochemistry **74**, 283 (2005).

[2] C. S. McHenry, *Dna replicases from a bacterial perspective.* Annual review of biochemistry **80**, 403 (2011).

[3] K. E. Duderstadt, R. Reyes-Lamothe, A. M. van Oijen, and D. J. Sherratt, *Replication-Fork Dynamics.* Cold Spring Harbor perspectives in biology **6** (2013).

[4] R. Reyes-Lamothe, C. Possoz, O. Danilova, and D. J. Sherratt, *Independent positioning and action of escherichia coli replisomes in live cells,* Cell **133**, 90 (2008).

[5] S. Jun and A. Wright, *Entropy as the driver of chromosome segregation,* Nature Reviews Microbiology **8**, 600 (2010).

[6] N. J. Kuwada, K. C. Cheveralls, B. Traxler, and P. A. Wiggins, *Mapping the driving forces of chromosome structure and segregation in Escherichia coli.* Nucleic Acids Research **41**, 7370 (2013).

[7] B. Di Ventura, B. Knecht, H. Andreas, W. J. Godinez, M. Fritsche, K. Rohr, W. Nickel, D. W. Heermann, and V. Sourjik, *Chromosome segregation by the Escherichia coli Min system.* Molecular systems biology **9**, 686 (2013).

[8] J. K. Fisher, A. Bourniquel, G. Witz, B. Weiner, M. Prentiss, and N. Kleckner, *Four-dimensional imaging of E. coli nucleoid organization and dynamics in living cells.* Cell **153**, 882 (2013).

[9] B. Youngren, H. J. Nielsen, S. Jun, and S. Austin, *The multifork Escherichia coli chromosome is a self-duplicating and self-segregating thermodynamic ring polymer.* Genes & Development **28**, 71 (2014).

[10] H. Merrikh, Y. Zhang, A. D. Grossman, and J. D. Wang, *Replication-transcription conflicts in bacteria.* Nature Reviews Microbiology **10**, 449 (2012).

[11] B. Michel, G. Grompone, M.-J. Florès, and V. Bidnenko, *Multiple pathways process stalled replication forks,* Proceedings Of The National Academy Of Sciences Of The United States Of America **101**, 12783 (2004).

[12] M. K. Gupta, C. P. Guy, J. T. P. Yeeles, J. Atkinson, H. Bell, R. G. Lloyd, K. J. Marians, and P. McGlynn, *Protein-DNA complexes are the primary sources of replication fork pausing in Escherichia coli.* Proceedings Of The National Academy Of Sciences Of The United States Of America **110**, 7252 (2013).

[13] T. M. Hill, M. L. Tecklenburg, A. J. Pelletier, and P. L. Kuempel, *tus, the trans-acting gene required for termination of DNA replication in Escherichia coli, encodes a DNA-binding protein.* Proceedings Of The National Academy Of Sciences Of The United States Of America **86**, 1593 (1989).

[14] M. Hidaka, T. Kobayashi, S. Takenaka, H. Takeya, and T. Horiuchi, *Purification of a DNA replication terminus (ter) site-binding protein in Escherichia coli and identification of the structural gene.* The Journal of biological chemistry **264**, 21031 (1989).

[15] T. M. Hill, *Arrest of Bacterial DNA Replication,* Annual review of microbiology **46**, 603 (1992).

[16] F. F. Coskun-Ari, A. Skokotas, G. R. Moe, and T. M. Hill, *Biophysical characteristics of Tus, the replication arrest protein of Escherichia coli.* The Journal of biological chemistry **269**, 4027 (1994).

[17] C. J. Rudolph, A. L. Upton, G. S. Briggs, and R. G. Lloyd, *Is RecG a general guardian of the bacterial genome?* DNA repair **9**, 210 (2010).

[18] T. M. Hill and K. J. Marians, *Escherichia coli Tus protein acts to arrest the progression of DNA replication forks in vitro.* Proceedings Of The National Academy Of Sciences Of The United States Of America **87**, 2481 (1990).

[19] V. Bidnenko, S. D. Ehrlich, and B. Michel, *Replication fork collapse at replication terminator sequences.* The EMBO Journal **21**, 3898 (2002).

[20] C. Neylon, A. V. Kralicek, T. M. HILL, and N. E. Dixon, *Replication termination in Escherichia coli: structure and antihelicase activity of the Tus-Ter complex.* Microbiology And Molecular Biology Reviews **69**, 501 (2005).

[21] I. G. Duggin, R. G. Wake, S. D. Bell, and T. M. Hill, *The replication fork trap and termination of chromosome replication.* Molecular Microbiology **70**, 1323 (2008).

[22] D. L. Kaplan and D. Bastia, *Mechanisms of polar arrest of a replication fork,* Molecular Microbiology **72**, 279 (2009).

[23] M. D. Mulcair, P. M. Schaeffer, A. J. Oakley, H. F. Cross, C. Neylon, T. M. Hill, and N. E. Dixon, *A Molecular Mousetrap Determines Polarity of Termination of DNA Replication in E. coli,* Cell **125**, 1309 (2006).

[24] D. Bastia, S. Zzaman, G. Krings, M. Saxena, X. Peng, and M. M. Greenberg, *Replication termination mechanism as revealed by Tus-mediated polar arrest of a sliding helicase,* Proceedings Of The National Academy Of Sciences Of The United States Of America **105**, 12831 (2008).

[25] P. A. Gottlieb, S. WU, X. Zhang, M. Tecklenburg, P. Kuempel, and T. M. Hill, *Equilibrium, kinetic, and footprinting studies of the Tus-Ter protein-DNA interaction.* The Journal of biological chemistry **267**, 7434 (1992).

[26] C. Neylon, S. E. Brown, A. V. Kralicek, C. S. Miles, C. A. Love, and N. E. Dixon, *Interaction of the Escherichia coli replication terminator protein (Tus) with DNA: a model derived from DNA-binding studies of mutant proteins by surface plasmon resonance.* Biochemistry **39**, 11989 (2000).

[27] P. J. Lewis, G. B. Ralston, R. I. Christopherson, and R. G. Wake, *Identification of the replication terminator protein binding sites in the terminus region of the Bacillus subtilis chromosome and stoichiometry of the binding.* Journal of Molecular Biology **214**, 73 (1990).

[28] D. E. Bussiere, D. Bastia, and S. W. White, *Crystal structure of the replication terminator protein from B. subtilis at 2.6 A.* Cell **80**, 651 (1995).

[29] K. P. Lemon, I. Kurtser, and A. D. Grossman, *Effects of replication termination mutants on chromosome partitioning in Bacillus subtilis.* Proceedings Of The National Academy Of Sciences Of The United States Of America **98**, 212 (2001).

[30] N. A. Willis, G. Chandramouly, B. Huang, A. Kwok, C. Follonier, C. Deng, and R. Scully, *BRCA1 controls homologous recombination at Tus/Ter-stalled mammalian replication forks,* Nature **510**, 556 (2014).

[31] N. B. Larsen, E. Sass, C. Suski, H. W. Mankouri, and I. D. Hickson, *The Escherichia coli Tus-Ter replication fork barrier causes site-specific DNA replication perturbation in yeast.* Nature communications **5**, 3574 (2014).

[32] T. M. Hill, J. M. Henson, and P. L. Kuempel, *The terminus region of the Escherichia*

coli chromosome contains two separate loci that exhibit polar inhibition of replication, PNAS , 1 (1987).

[33] K. Kamada, T. Horiuchi, K. Ohsumi, N. Shimamoto, and K. Morikawa, *Structure of a replication-terminator protein complexed with DNA.* Nature **383**, 598 (1996).

[34] X. Wang, C. Lesterlin, R. Reyes-Lamothe, G. Ball, and D. J. Sherratt, *Replication and segregation of an Escherichia coli chromosome with two replication origins.* Proceedings Of The National Academy Of Sciences Of The United States Of America **108**, E243 (2011).

[35] I. G. Duggin and S. D. Bell, *Termination structures in the Escherichia coli chromosome replication fork trap,* Journal of Molecular Biology **387**, 532 (2009).

[36] M. J. J. Moreau and P. M. Schaeffer, *Differential Tus-Ter binding and lock formation: implications for DNA replication termination in Escherichia coli.* Molecular Biosystems **8**, 2783 (2012).

[37] R. T. Pomerantz and M. O'Donnell, *Direct restart of a replication fork stalled by a head-on RNA polymerase.* Science (New York, NY) **327**, 590 (2010).

[38] J. T. P. Yeeles and K. J. Marians, *The Escherichia coli Replisome Is Inherently DNA Damage Tolerant,* Science (New York, NY) **334**, 235 (2011).

[39] M. C. Moolman, Z. Huang, S. T. Krishnan, J. W. J. Kerssemakers, and N. H. Dekker, *Electron beam fabrication of a microfluidic device for studying submicron-scale bacteria.* Journal of nanobiotechnology **11**, 12 (2013).

[40] E. Rocha, *The replication-related organization of bacterial genomes,* Microbiology-Sgm **150**, 1609 (2004).

[41] X. Liu, X. Wang, R. Reyes-Lamothe, and D. J. Sherratt, *Replication-directed sister chromosome alignment in Escherichia coli,* Molecular Microbiology **75**, 1090 (2010).

[42] X. Wang, R. Reyes-Lamothe, and D. J. Sherratt, *Visualizing genetic loci and molecular machines in living bacteria,* Biochemical Society Transactions **36**, 749 (2008).

[43] C. Possoz, S. R. Filipe, I. Grainge, and D. J. Sherratt, *Tracking of controlled Escherichia coli replication fork stalling and restart at repressor-bound DNA in vivo,* The EMBO Journal **25**, 2596 (2006).

[44] X. Wang, C. Possoz, and D. J. Sherratt, *Dancing around the divisome: asymmetric chromosome segregation in Escherichia coli.* Genes & Development **19**, 2367 (2005).

[45] X. Wang, X. Liu, C. Possoz, and D. J. Sherratt, *The two Escherichia coli chromosome arms locate to separate cell halves.* Genes & Development **20**, 1727 (2006).

[46] Morigen, I. Odsbu, and K. Skarstad, *Growth rate dependent numbers of SeqA structures organize the multiple replication forks in rapidly growing Escherichia coli.* Genes to cells : devoted to molecular & cellular mechanisms **14**, 643 (2009).

[47] M. C. Moolman, S. T. Krishnan, J. W. J. Kerssemakers, A. van den Berg, P. Tulinski, M. Depken, R. Reyes-Lamothe, D. J. Sherratt, and N. H. Dekker, *Slow unloading leads to DNA-bound β2-sliding clamp accumulation in live Escherichia coli cells.* Nature communications **5**, 5820 (2014).

[48] B. Roecklein, A. Pelletier, and P. Kuempel, *The tus gene of Escherichia coli: autoregulation, analysis of flanking sequences and identification of a complementary system in Salmonella typhimurium.* Research in microbiology **142**, 169 (1991).

[49] X. Wang, R. Reyes-Lamothe, and D. J. Sherratt, *Modulation of Escherichia coli sister*

chromosome cohesion by topoisomerase IV, Genes & Development **22**, 2426 (2008).

[50] M. C. Joshi, A. Bourniquel, J. Fisher, B. T. Ho, D. Magnan, N. Kleckner, and D. Bates, *Escherichia coli sister chromosome separation includes an abrupt global transition with concomitant release of late-splitting intersister snaps.* Proceedings Of The National Academy Of Sciences Of The United States Of America **108**, 2765 (2011).

[51] H. J. Nielsen, B. Youngren, F. G. Hansen, and S. Austin, *Dynamics of Escherichia coli chromosome segregation during multifork replication.* Journal of Bacteriology **189**, 8660 (2007).

[52] X. Wang, P. Montero Llopis, and D. Z. Rudner, *Organization and segregation of bacterial chromosomes.* Nature Reviews Genetics **14**, 191 (2013).

[53] C. J. Rudolph, A. L. Upton, A. Stockum, C. A. Nieduszynski, and R. G. Lloyd, *Avoiding chromosome pathology when replication forks collide.* Nature **500**, 608 (2013).

[54] H. Hendrickson and J. G. Lawrence, *Mutational bias suggests that replication termination occurs near the dif site, not at Ter sites,* Molecular Microbiology **64**, 42 (2007).

[55] C. Lesterlin, F.-X. Barre, and F. Cornet, *Genetic recombination and the cell cycle: what we have learned from chromosome dimers.* Molecular Microbiology **54**, 1151 (2004).

[56] R. E. Georgescu, Yao, N. Y, and M. O'Donnell, *Single-molecule analysis of the escherichia coli replisome and use of clamps to bypass replication barriers.* FEBS letters **584**, 2596 (2010).

[57] R. D. Shereda, A. G. Kozlov, and T. M. Lohman, *SSB as an organizer/mobilizer of genome maintenance complexes,* Critical Reviews in Biochemistry and Molecular Biology (2008).

[58] H. Boubakri, A. L. de Septenville, E. Viguera, and B. Michel, *The helicases DinG, Rep and UvrD cooperate to promote replication across transcription units in vivo.* The EMBO Journal **29**, 145 (2010).

[59] H. Hiasa and K. J. Marians, *Differential inhibition of the DNA translocation and DNA unwinding activities of DNA helicases by the Escherichia coli Tus protein.* The Journal of biological chemistry **267**, 11379 (1992).

[60] D. J. Sherratt, L. K. Arciszewska, and E. Crozat, *The Escherichia coli DNA translocase FtsK,* Biochemical Society Transactions **38**, 395 (2010).

[61] I. Grainge, *Simple topology: FtsK-directed recombination at the dif site.* Biochemical Society Transactions **41**, 595 (2013).

[62] J. Y. Lee, I. J. Finkelstein, L. K. Arciszewska, D. J. Sherratt, and E. C. Greene, *Single-molecule imaging of FtsK translocation reveals mechanistic features of protein-protein collisions on DNA.* Molecular Cell **54**, 832 (2014).

SUPPLEMENTARY INFORMATION

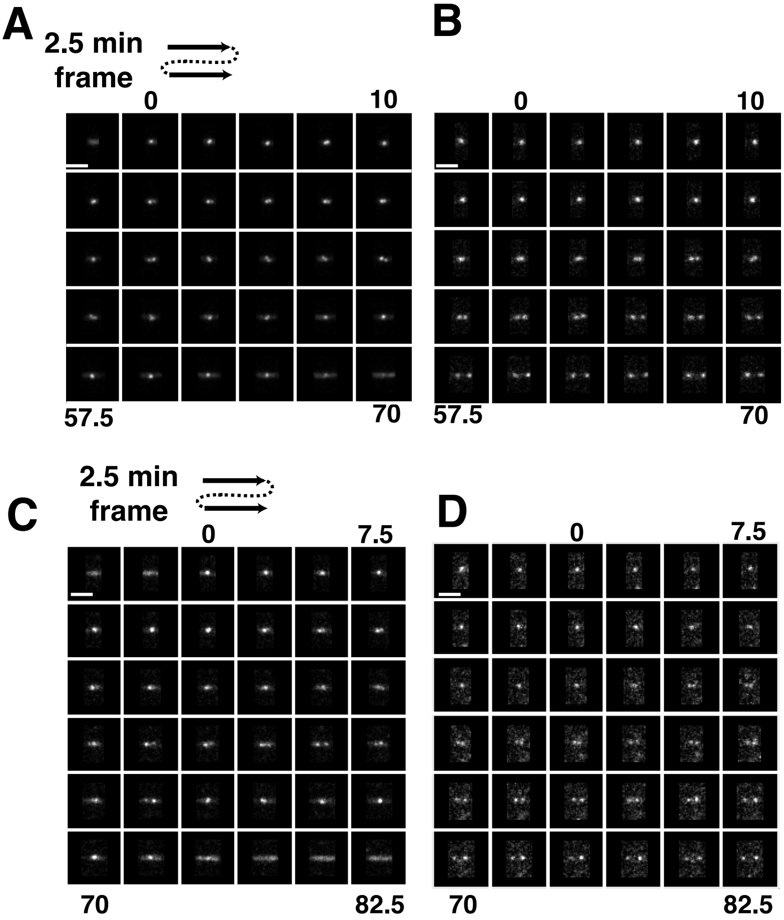

Supplementary Figure 6.1: Representative temporal montages of the YPet-DnaN and *ori1*-mCherry signals for a complete replication cycle. (A-B) Montages for *oriZ* cells. (A) YPet-DnaN montage and (B) *ori1*-mCherry montage. (C-D) Montages for *oriZ*:Δ*Tus* cells. (C) YPet-DnaN montage and (D) *ori1*-mCherry montage. Scale bars, 3 μm.

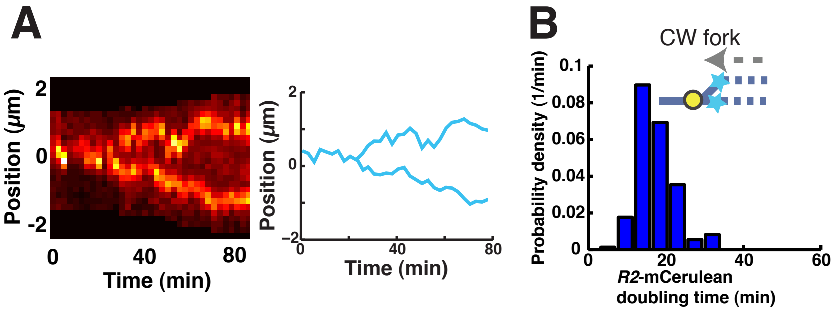

Supplementary Figure 6.2: Doubling time of the *R2*-mCerulean locus. (A) A representative *R2*-mCerulean fluorescent signal. (left) The kymograph of the *R2*-mCerulean locus for one complete replication cycle constructed by summation of the pixel intensities perpendicular to the long axis of the cell. (right) The *R2*-mCherry trace shown (left) determined from the Gaussian fitted positions from individual images for each time point. Images were acquired every 2.5 min during a time-lapse experiment. (B) The distribution of the time point during replication when the *R2*-mCerulean focus doubles. The mean doubling time of *R2*-mCerulean is $t_{\text{doubling}} = 17 \pm 5\,\text{min}$. (Error is ± SD, n = 167). (Inset) Schematical illustration indicating that the *R2*-mCerulean region has been replicated.

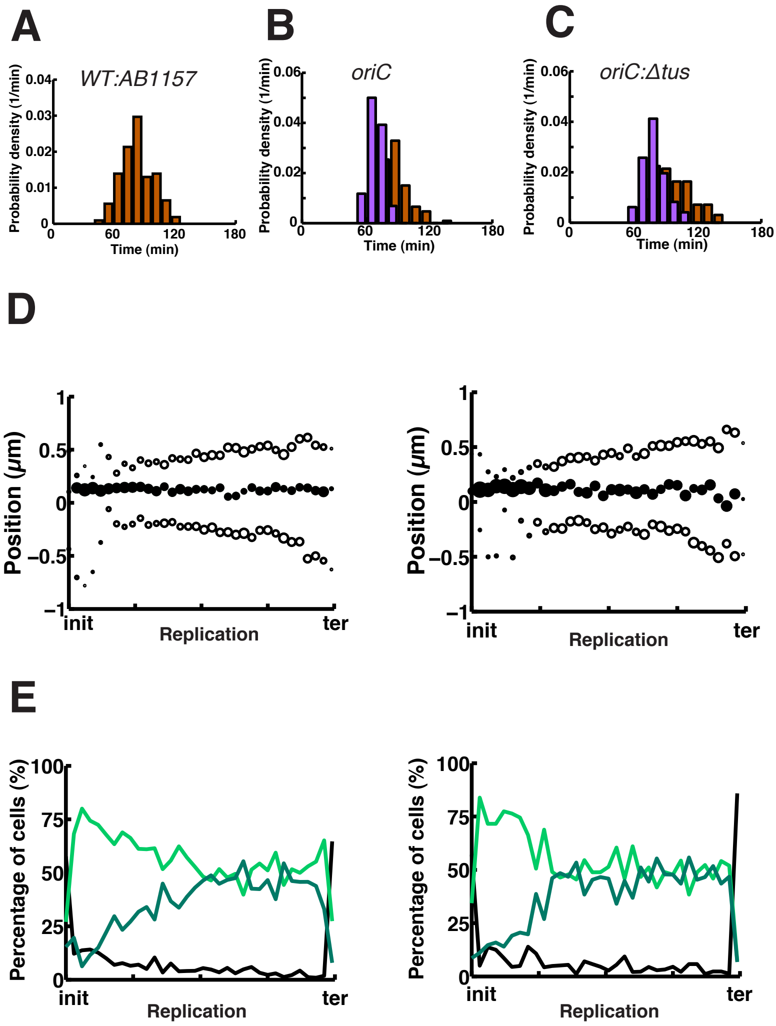

Supplementary Figure 6.3: Replication in *oriC* and *oriC*:Δ*Tus* characteristics. (A) Distribution of the division time for WT AB1157 cells. The average division time is $t_{\mathrm{div,AB1157}} = 83 \pm 16\,\mathrm{min}$ (Error is ± SD, n = 125). (B) Distribution of the division time (brown) and replication time (purple) for *oriC* cells. The average replication time $t_{\mathrm{rep,oriC}} = 70 \pm 7\,\mathrm{min}$, and the average division time $t_{\mathrm{div,oriC}} = 85 \pm 15\,\mathrm{min}$ (Error is ± SD, n = 110). (C) Distribution of the division time (brown) and replication time (purple) for *oriC*:Δ*Tus* cells. The average replication time $t_{\mathrm{rep,oriC:\Delta Tus}} = 80 \pm 11\,\mathrm{min}$, and the average division time $t_{\mathrm{div,oriC:\Delta Tus}} = 96 \pm 19\,\mathrm{min}$ (Error is ± SD). (D) Replisome dynamics for *oriC* and *oriC*:Δ*Tus* cells. Time-resolved traces of (left) *oriC*, and (right) *oriC*:Δ*Tus* cells. Here we plot a single DnaN-YPet focus (filled circles) and double DnaN-YPet foci (empty circles). The size of an individual circle at each time point is representative of the percentage of cells having that particular distribution of foci. The traces have been aligned with respect to initiation and termination of replication and binned. (E) The percentage of cells having a single focus (light green line), double foci (dark green line), and no foci (black line) as function of replication time. It is evident that the percentage of cells having a single focus or double foci is roughy equal for (left) *oriC* and (right) *oriC*:Δ*Tus* cells.

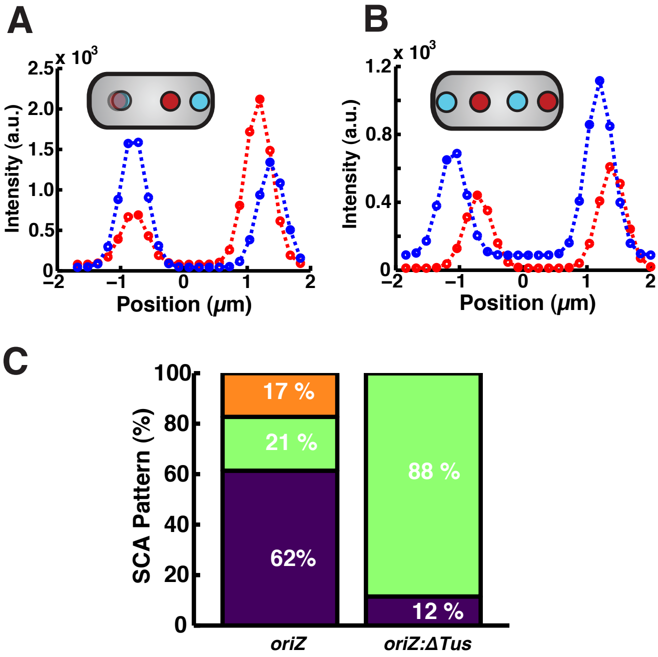

Supplementary Figure 6.4: SCA patterns. (A-B) In a minority of cells the fitted spatial intensity distributions. (A) *ori1*-mCherry and *R2*-mCerulean foci were overlapping. (B) RLRL configuration, which is symmetric and taken to be equal to LRLR. The insets in (A) and (B) are schematic depictions of the different chromosomal loci patterns. (C) The observed SCA pattern determined at the time point when replication was half way.

Plasmids	**Relevant genotype**	Construction
pKD46	Plasmid with λ-Red recombinase genes expressed under arabinose promoter	Created by standard cloning [2]
pCP20	Temperature sensitive plasmid with constitutively expressing flippase (FLP) enzyme.	Created by standard cloning [2]
pKD13	Template plasmid containing the FRT flanked kanamycin resistance gene (kanR) sequence.	Created by standard cloning [2]

Supplementary Table 6.2: Summary of different plasmids used in this study.

Strains	**Relevant genotype**	Construction
BN1110	AB1157 strain containing pKD46 plasmid	*E. coli* K-12 derivative [4]
BN1219	*YPet-dnaN* and *tetR-mCerulean*	P1-phage transduction [47]
BN1516	*kanR* gene recombined out	FLP/*FRT* recombination.
BN1598	Δ*Tus*	λ-red recombination: *FRT-kanR-FRT* from pKD13→BN1110
BN1868	*oriC:*Δ*Tus*	P1-phage transduction: BN1598→BN1516
BN1861	*Ypet-DnaN*, Δ*oriC*, and Δ*oriZ*	P1-phage transduction [34]
BN1869	*oriZ* with the *kanR* gene out recombined	FLP/*FRT* recombination
BN2111	*oriZ:*Δ*Tus*	P1-phage transduction: BN1598 → BN1869

Supplementary Table 6.3: Summary of different strains used in this study.

S6.1. CONSTRUCTION AND CHARACTERIZATION OF FLUORESCENT FUSION STRAINS

All strains are derived from the *E. coli* K12 AB1157 [1]. The strains used for this study were constructed by λ-red recombination [2] or P1-transduction [3]. A summary of the plasmids and strains used in this study are provided in Supplementary Tables 1 and 2.

Δ*Tus* IN WT AB1157

Utilizing λ-red recombination we created a ΔTus mutant in WT AB1157 by knocking out the open reading frame of the *tus* gene. The plasmid pKD13 (GenBank: AY048744.1) was used as a template plasmid for amplifying the FRT flanked kanamycin resistance gene (*kanR*) sequence used during λ-red recombination. The primer sequences used were: Forward 5' – CCA CGA CTG TGC TAT AAA ATA AGT ATG TTG TAA CTA AAG TGG TTA ATA TTT GTA GGC TGG AGC TGC TTC G – 3'; Reverse 5' – GAC AGC TGG GTA CGG CCA GAA CAG ATG GTC GGC AGT ATG AAA GCC GGG CGA TTC CGG GGA TCC GTC GAC C – 3'. The DNA fragment was gel purified, and ~ 700 ng of the linear DNA was used during electroporation of AB1157 cells over expressing the λ-red proteins from pKD46 [2]. The correct insertion of the fragment into the chromosome of the resulting strain was assayed by PCR. The oligonucleotides used were 5' – GCG CAC GAT GGT CAA GTC AC – 3' and 5' – TAC GGC CAG AAC AGA TGG TC – 3'. The sequence of the deleted region in this strain was verified and confirmed by DNA sequencing.

YPet-dnaN:tetR-mCerulean (*oriC*)

The *YPet-dnaN:tetR-mCerulean* (*oriC*) strain was constructed previously as described in *Moolman et al* [47].

YPet-dnaN:tetR-mCerulean:Δ*Tus* (*oriC:*Δ*Tus*)

The *oriC:*Δ*Tus* was constructed using P1 transduction. Firstly, the FRT flanked *kanR* gene in the *oriC* strain, used during previous recombineering, was recombined out using the temperature the sensitive Flippase (FLP) enzyme expressed from the pCP20 plasmid as described elsewhere [2]. Subsequently, the FRT flanked *kanR* gene from the Δ*Tus* strain was transduced into the *oriC* strain. The presence of the Δ*tus* knock-out was verified using the oligonucleotides: 5' – GCG CAC GAT GGT CAA GTC AC – 3' and 5' – TAC GGC CAG AAC AGA TGG TC – 3'. The sequence of the deleted region was confirmed by DNA sequencing.

oriZ

The *oriZ* strain was constructed previously as described in [34].

oriZ:Δ*Tus*

The *oriZ:*Δ*Tus* was constructed using P1 transduction. Firstly, the FRT flanked *kanR* gene in the *oriZ* strain, used during previous recombineering, was recombined out using the temperature the sensitive Flippase (FLP) enzyme expressed from the pCP20 plasmid as described elsewhere [2]. Subsequently, the FRT flanked *kanR* gene from the Δ*Tus* strain was transduced by P1 transduction into the out-recombined *oriZ* strain. The presence of the Δ*tus* knock-out was verified using the oligonucleotides: 5'– GCG CAC GAT GGT CAA GTC AC – 3' and 5' – TAC GGC CAG AAC AGA TGG TC – 3'. The correct deletion of the *tus* gene at the desired region was confirmed by DNA sequencing.

S6.2. DATA ANALYSIS

LOCALIZATION OF FOCI DURING REPLICATION

The acquired images were analyzed with custom-written MATLAB software (MathWorks) in combination with imageJ [6] as reported previously [47]. Briefly, we correct for uneven background and illumination heterogeneity per image. Subsequently, we detect foci in each bacterium that have an intensity above the cytoplasmic fluorescence intensity as defined by the median of the total cytoplasmic signal. The detected foci are localized in each individual image by perform a maximum-likelihood estimation (MLE) of a two-foci Gaussian fit [7–9]. The resulting fits are evaluated by rejecting the secondary fit if it is off-range, too weak compared to the brightest focus or to the total fluorescence intensity.

TIME-RESOLVED REPRESENTATION OF FOCI POSITIONS

To study the temporal behavior of the replisome and chromosomal loci, it is crucial to be able to evaluate the process of focus separation during replication. Obtaining average values of focus separation is somewhat impeded by i) the wide spread for individual cells in the appearance of 'one focus and two foci' observations and ii) the limited optical resolution to be able to discriminate one focus, from two closely adjacent ones. To minimize the influence of these factors, we proceed as follows when constructing averaged time-resolved position traces as in Figure 3A, 4B of the main text. First, for each individual cell, we normalize the time axis such that $t = 0$ corresponds to the moment of initiation, as determined from the first emergence of foci after the diffusive state, and that $t = 1$ amounts to the last time point that one or two foci are observed prior to the subsequent diffusive state. Secondly, we plot the average position for the cases of one or two foci respectively per normalized time. The size of the marker represents the percentage of cells found in this state.

S6.3. CALCULATING THE AVERAGE REPLISOME VELOCITY DURING REPLICATION

We calculate the average replisome velocity in our experimental conditions by making use of the average replication time $t_{\mathrm{rep,oriC}} \sim 70\,\mathrm{min}$ (Supplementary Information Figure 6.3B) in combination with the size of the *E. coli* genome (4.6 Mbp). This results in a velocity of $v_{\mathrm{rep}} \sim 550\,\mathrm{bp/s}$ for an individual replisome under our experimental conditions.

S6.4. M9 GROWTH MEDIUM USED IN EXPERIMENTS

1 L of M9 growth medium used in the experiments contains 10.5 g/L of autoclaved M9 broth (Sigma-Aldrich); 0.1 mM of autoclaved $CaCl_2$ (Sigma-Aldrich); 0.1 mM of autoclaved $MgSO_4$ (J.T.Baker); 0.3 % of filter-sterilized glycerol (Sigma-Aldrich) as carbon source; 0.1 g/L of filter-sterilized 5 amino acids, namely L-threonine, L-leucine, L-proline, L-histidine and L-arginine (all from Sigma-Aldrich) and $10\,\mu$L of 0.5 % filter-sterilized Thiamine (Sigma-Aldrich).

S6.5. PREPARATION OF CELLS FOR MICROSCOPY

Cells were streaked onto Luria-Bertani (LB)-plates containing the appropriate antibiotics. Single colonies from these plates were grown in M9 supplemented with 0.3 %

glycerol (Gly), essential nutrients (Supplementary Section S6.4), and with the appropriate antibiotics overnight at 37 °C with shaking. The following day, the cells were subcultured into the same medium and grown at 37 °C with shaking until an OD_{600} ~ 0.2 was reached. Cells were concentrated by centrifugation for 2 min at 16 100 g. The supernatant of the concentrated cells was decanted, and the pellet was resuspended in 50 μL M9-Gly with essential nutrients and injected into the microfluidic device. After injection into the device, the device was centrifuged for 10 min at 2500 g (Eppendorf 5810R). This centrifugation step assists the loading of the cells into the growth channels. Following centrifugation the device was mounted on the microscope with tubing attached to the inlet and outlet and incubated for ~ 45 min at 37 °C. After incubation, fresh M9-Gly with essential nutrients (Supplementary Section S6.4) and the appropriate antibiotics are flushed through the device. The syringe containing the medium is subsequently attached to an automated syringe pump that continuous injects fresh M9-Gly, essential nutrients and 0.2 mg/mL bovine serum albumin (BSA) into the device at a rate of 0.5 mL/hr.

S6.6. MICROFLUIDIC DEVICE FABRICATION

Cells are immobilized for imaging utilizing our version [39] of a previously reported microfluidic device [4]. A detailed description of the fabrication procedure can be found in [39]. In brief, electron-beam lithography in combination with dry etching techniques is used to fabricate the structures into a silicon wafer. This wafer is subsequently used to realize a negative mold of the structures with polydimethylsiloxane (PDMS). The resulting PDMS mold is then employed to successfully fabricate the positive structures with PDMS. Subsequently a cover glass is attached, and the device is used for time-lapse experiments.

S6.7. MICROSCOPE SETUP

Microscopy data were acquired on a commercial Nikon Ti microscope equipped with a custom-built laser excitation scheme similar to that reported previously [47]. In brief, a Nikon CFI Apo TIRF 100x, 1.49 NA oil immersion objective is used for excitation and detection. A standard Nikon brightfield halogen lamp and condenser components are used for imaging cell outlines. Excitation is performed using a Cobolt Fandango 515 nm continuous wave (CW) diode-pumped solid-state (DPSS) laser for YPet, Cobolt Jive 561 nm CW DPSS laser for mCherry, and a Cobolt Twist 457 nm CW DPSS laser for mCerulean. The laser beams are combined using dichroic mirrors (Chroma 575dcspxr, zt457dcrb) and subsequently coupled into a single-mode optical fiber (KineFLEX). The output of the fiber is expanded and focused onto the back focal plane of the objective mounted on the microscope. Notch filters (Semrock NF03-514E, NF03-561E) were used to eliminate any laser light leaking onto the camera. The emission of the different fluorescent proteins are projected onto the central part of an Andor iXon 897 Electron Multiplying Charge Coupled Device (EMCCD) camera using custom filter sets: Chroma z561, ET605/52m, zt561rdc (mCherry), Chroma z514, ET540/30m, zt514rd (YPet), Chroma z457/10x, ET490/40m, zt457rdc (mCerulean). A custom design commercial temperature control housing (Okolabs) is enclosing the microscope body is regulate the temperature at 37 °C. Sample position was controlled with a Nikon stage (TI-S-ER Motorized Stage Encoded, MEC56100) together with the Nikon Perfect Focus System (PFS) to eliminate

Z-drift during image acquisition. A personal computer (PC) running Nikon NIS elements software is used for controlling the acquisition.

S6.8. TIME-LAPSE DATA ACQUISITION

All data acquisition was performed on the previously described microscope in combination with a standard PC running Nikon NIS-elements (Supplementary Information Section S6.7). The order and type of fluorescence excitation was dependent on the strain being imaged.

For *oriC* and *oriC:*Δ*tus* cells, the cell outlines were imaged using standard brightfield illumination, and the YPet proteins were subsequently excited with the 515 nm laser line (80 ms exposure time). Time-lapse images were acquired every 2.5 min with the EMCCD gain set to 100.

For *oriZ* and *oriZ:*Δ*tus* cells, the cell outlines were again imaged using standard brightfield illumination, but different laser lines were used successively to excite the different fluorescent proteins. The sample was first excited with 515 nm (YPet), then 561 nm (mCherry) and lastly with 457 nm (mCerulean) with an exposure time of 80 ms in all the cases. The intensity for all the different measurement were kept constant. The intensity of the 515 nm and 561 nm lasers was $\sim 5\,\mathrm{W \cdot cm^{-2}}$, and the 457 nm laser was set to $\sim 2.5\,\mathrm{W \cdot cm^{-2}}$. Intensity calibration was performed according to [5]. Time-lapse acquisitions typically ran overnight, and spanning ~ 10 hrs of measurement.

SUPPLEMENTARY REFERENCES

[1] B. J. Bachmann, *Pedigrees of some mutant strains of Escherichia coli K-12.* Bacteriological Reviews **36**, 525 (1972).

[2] K. A. Datsenko and B. L. Wanner, *One-step inactivation of chromosomal genes in escherichia coli k-12 using pcr products.* Proceedings Of The National Academy Of Sciences Of The United States Of America **97**, 6640 (2000).

[3] L. C. Thomason, N. Costantino, and D. L. Court, *E. coli genome manipulation by p1 transduction.* Current protocols in molecular biology **Chapter 1**, Unit 1.17 (2007).

[4] P. Wang, L. Robert, J. Pelletier, W. L. Dang, F. Taddei, A. Wright, and S. Jun, *Robust growth of escherichia coli,* Current biology **20**, 1099 (2010).

[5] D. Grünwald, S. M. Shenoy, S. Burke, and R. H. Singer, *Calibrating excitation light fluxes for quantitative light microscopy in cell biology,* Nature protocols **3**, 1809 (2008).

[6] C. A. Schneider, W. S. Rasband, and K. W. Eliceiri, *NIH Image to ImageJ: 25 years of image analysis.* Nature Methods **9**, 671 (2012).

[7] R. E. Thompson, D. R. Larson, and W. W. Webb, *Precise nanometer localization analysis for individual fluorescent probes.* Biophysical Journal **82**, 2775 (2002).

[8] C. S. Smith, N. Joseph, B. Rieger, and K. A. Lidke, *Fast, single-molecule localization that achieves theoretically minimum uncertainty.* Nature Methods **7**, 373 (2010).

[9] K. I. Mortensen, L. S. Churchman, J. A. Spudich, and H. Flyvbjerg, *Optimized localization analysis for single-molecule tracking and super-resolution microscopy,* Nature Methods **7**, 377 (2010).

SUMMARY

DNA is the molecule of life. A living cell requires the genes that are encoded in its chromosomal DNA in order to survive. The accurate duplication of the chromosome prior to cell division is thus absolutely crucial to sustain life throughout generations. Although most of the players that safeguard the reliable replication of the chromosome prior to cell division are known, their detailed molecular actions and interactions remain an active area of research. A range of different methodologies has been developed over the years to gain insight into the dynamics of different proteins and protein complexes, both in bulk and at the single-molecule level. Single-molecule techniques provide one with added detailed insight into the process under invitation that might otherwise be obscured by ensemble-averaging methods. The dominant single-molecule methodologies that can access the dynamics of biological molecules in aqueous solutions are force spectroscopy and optical microscopy. These techniques, as well as specific highlighted studies, are reviewed in **Chapter 2**. The techniques described have for a large part mainly been used in experiments outside of the cell (*in vitro*). Relatively recent technological advances have made these techniques applicable to living cells. The environment of the cell (*in vivo*) is highly variable, crowded and can be significantly different from an *in vitro* situation. Additionally, individual cells (of the same species) display heterogeneity, and their behaviour depends on environmental conditions. Thus, studying proteins and protein complexes *in vivo* (with single-molecule sensitivity) provides one with detailed insight into their actions that might have been obscured when studied in an artificial environment outside of the cell.

This dissertation describes methods and experiments aimed at furthering our quantitative understanding of chromosomal replication on the single-cell level with single-molecule sensitivity. Quantitative fluorescence microscopy in combination with microfluidics provides an ‘ideal’ tool for studying proteins and protein complexes in live cells: ensuring exact protein labeling, high spatial control over individual cells and precise regulation of the environmental conditions. These factors are all necessary to reach quantitative conclusions. The exact fluorescent labeling of the protein of interest is essential for the accurate interpretation of the detected fluorescent signal. Having precise control over the environmental conditions and individual cells allows for accurate and reproducible results. In this dissertation, these techniques are employed to explore details of active chromosomal replication in living *E. coli* cells.

Spatial control of cells and the regulation of nutrients supplied are extremely important when conducting extended time-lapse microscopy. In **Chapter 3** a detailed fabrication protocol is presented of a microfluidic device designed to investigate single cells during steady-state growth when imaged using extended time-lapse microscopy. We utilize electron beam lithography for patterning, dry etching for realizing the structures into silicon, and PDMS for the final device used in experiments. We validate that a range of different size growth channels can be fabricated in silicon and reliably replicated to PDMS. We finally demonstrate the successfully utilization of the device for two different types of bacteria, namely *L. lactis* and *E. coli*.

In **Chapter 4** a quantitative look is taken at the analysis of a diffraction-limited focus inside the fluctuating and inhomogeneous background of a bacterial cell. Numerous algorithms are commonly employed to analyze fluorescent foci inside cells, but they have for a large part only been rigorously evaluated for conditions outside of the cell. The dynamic setting of a growing cell is essentially different than an artificial *in vitro* solution. We use a novel approach to evaluate the analysis of a focus in the environment of the cell by combining experimental data for the background fluorescence with simulation for the focus signal. This methodology enables us to assess the different focus analysis algorithms on 'data' that more accurately represent real experimental measurements than do pure simulation or *in vitro* conditions. Our results indicate that there is a clear background dependency on the accuracy with which the different algorithms evaluate the signal content and position of a focus. Utilizing our findings, we provide a number of quantitative guidelines for analyzing a focus in the noisy environment of the cell.

In the subsequent chapters we turn our attention from evaluating and developing techniques, to utilizing them in studying replication in live *E. coli* cells. We start by investigating the β_2 sliding clamp (β_2 clamp). The β_2 clamp is an essential protein complex involved in replication and repair. It is part of the replisome complex that is responsible for the accurate replication of the chromosome, and it ensures the sufficiently high processivity of the replicative polymerase for timely replication. Insight into its behaviour adds to our detailed understanding of replication and repair in general. In **Chapter 5** we quantitatively investigate the β_2 clamp dynamics in live, actively replicating *E. coli* cells. We employ microfluidics, wide-field fluorescence microscopy and photoactivatible fluorescence microscopy to determine the number of DNA-bound β_2 clamps during replication, as well as the effective loading and unloading rates. Our results indicate that β_2 clamps accumulate on DNA after initiation, and reaches a steady- state plateau that is maintained throughout the majority of the replication process. This build-up of DNA-bound β_2 clamps results from the relatively slow unloading of β_2 clamps from DNA. Using *in vivo* single-molecule imaging, we determine that a β_2 clamp remains DNA-bound on the order of minutes. Since β_2 clamps are involved in numerous different processes, ranging from controlling over initiation to DNA repair, our findings provide further insight in the details how clamps provide a platform to recruit different proteins to act on DNA.

A progressing replication fork encounters numerous obstacles, mainly in the form of DNA-bound proteins, which have to be surpassed to successfully complete replication. In **Chapter 6** we investigate the fate of an individual replisome *in vivo* when encountering the natural Tus-*ter* protein complex from the non-permissive direction in a strain with an ectopic origin. This position of the ectopic origin results in the clockwise (CW) replisome encountering the barrier significantly earlier on during replication than the counterclockwise replisome. Our data suggests that the CW replisome (as assessed by studying the β_2 clamp) remains stably bound to DNA after reaching the barrier. Furthermore, by evaluating the replication time, we conclude that the replication fork is slowed down at these barriers, but not halted indefinitely. We demonstrate that the presence or absence of the Tus-*ter* barriers effects the sister chromosome alignment (SCA) patterns. Interestingly, the resulting SCA pattern in the absence of the Tus-*ter* barriers is associated with fork stalling. This is most likely due to the CW replisome encountering other proteins actively working on the DNA in the terminus region. Our results illustrate that the replication fork is only slowed down by natural DNA-protein complexes and not halted indefinitely.

The work presented in this thesis describes a range of different methods developed and numerous experiments conducted to further our understanding of chromosomal replication in live *E. coli* cells. Chromosomal replication is a highly complex and dynamic process that requires approaches from different disciplines to allow us to unravel its molecular details further. Microfluidic devices are becoming increasingly popular in cellular biology in order to manipulate and study single living cells in a controlled manner. The combination of microfluidic devices with microscopes that have single-molecule sensitivity and accurate genetic manipulation of cells forms a platform with which scientists can investigate *in vivo* single proteins, protein-protein interactions, chromosome dynamics and cell heterogeneity to name but a few. We have demonstrated that by utilizing the above methods, we were able to obtain novel detailed insight into both the robustness of the replication process and the dynamic nature of the replisome. As with many answers (results), this process brings up many new questions that will most likely require even more of us as scientists in order to solve them.

SAMENVATTING

DNA is het molecuul van het leven. De genen, die worden gecodeerd in het chromosomale DNA, zijn noodzakelijk voor de cel om te overleven. De nauwkeurige verdubbeling van het chromosoom voorafgaand aan celdeling, is daarom van cruciaal belang voor het voortzetten van het leven door de generaties heen. Hoewel de meeste spelers die zorgen voor betrouwbare replicatie van het chromosoom voorafgaand aan de celdeling bekend zijn, blijven hun gedetailleerde moleculaire acties en interacties een actief onderzoeksonderwerp. Diverse methodes zijn door de jaren heen ontwikkeld om inzicht te krijgen in de dynamiek van verschillende eiwitten en eiwit-complexen, zowel in bulk als op enkel-molecuul niveau. Enkel-molecuul technieken bieden gedetailleerd inzicht in het onderzochte proces dat door het gebruik van *ensemble-average* methodes wellicht verborgen was gebleven. De gangbare enkel-molecuul methodologieën die inzicht verschaffen in de dynamica van biologische moleculen in een waterige oplossing, zijn kracht spectroscopie en optische microscopie. Deze technieken, evenals specifieke studies, worden beschreven in **Hoofdstuk 2**. Dergelijke technieken worden voor een groot deel gebruikt in proeven buiten de cel (*in vitro*). Relatief recente technologische ontwikkelingen hebben deze technieken echter ook toegankelijk gemaakt voor gebruik in levende cellen. Dit is belangrijk omdat de omgeving in de cel (*in vivo*) zeer variabel en druk is, en aanzienlijk kan afwijken van een *in vitro* situatie. Daarnaast vertonen afzonderlijke cellen (van dezelfde soort) heterogeniteit, en is hun gedrag afhankelijk van omgevingsomstandigheden. Het bestuderen van eiwitten en eiwitcomplexen *in vivo* (in enkele cellen met enkel-molecuul gevoeligheid) geeft daarom gedetailleerd inzicht in cellulaire activiteiten die niet waarneembaar zijn in een kunstmatige omgeving buiten de cel.

Dit proefschrift beschrijft methodes en experimenten die gericht zijn op het bevorderen van ons kwantitatieve begrip van chromosomale replicatie op het niveau van een individuele cel met enkele molecuul gevoeligheid. Kwantitatieve fluorescentie microscopie in combinatie met microfluïdica biedt een 'deale' manier om eiwitten en eiwitcomplexen in levende cellen te bestuderen: het zorgt voor exacte eiwitmarkering, hoge ruimtelijke controle over afzonderlijke cellen en een precieze regeling van de omgevingsomstandigheden. Deze factoren zijn allemaal noodzakelijk om tot kwantitatieve conclusies te kunnen komen. De exacte markering van het eiwit met een fluorescent eiwit is essentieel voor de correcte interpretatie van het gedetecteerde fluorescente signaal. De accurate controle over de experimentele omstandigheden en individuele cellen zorgt voor nauwkeurige, reproduceerbare resultaten. Deze technieken worden in dit proefschrift gebruikt om actieve chromosomale replicatie in levende *E. coli* cellen te onderzoeken.

Ruimtelijke controle van cellen en de regulatie van voedingsstoffen zijn van groot belang bij het uitvoeren van langedurige *time-lapse* microscopie experimenten. In **Hoofdstuk**

3 wordt een gedetailleerd fabricage protocol gepresenteerd van een microfluïdisch device ontworpen voor onderzoek aan enkele cellen tijdens *steady-state* groei tijdens een microscopie experiment over lange tijdschalen. In dit protocol maken we gebruik van elektronen- bundellithografie (*electron beam lithography*) voor patroonvorming, droogets technieken voor de fabricage van de structuren in silicium, en PDMS voor hun realisatie in het uiteindelijke device. We controleren of een reeks kanalen van verschillende groottes kunnen worden vervaardigd in silicium en betrouwbaar gerepliceerd kunnen worden in PDMS. Wij tonen het succesvol gebruik van het microfluïdische device voor twee verschillende soorten bacteriën, namelijk *L. lactis* en *E. coli*.

In **Hoofdstuk 4** nemen we een kwantitatieve kijk in de analyse van een door diffractie gelimiteerd focus (‘spot’) binnen de fluctuerende en inhomogene achtergrond van een bacteriële cel. Er zijn talrijke algoritmes die vaak worden gebruikt om fluorescerende spots in cellen te analyseren. Deze algoritmes zijn slechts beperkt geëvalueerd voor omstandigheden binnen de cel, terwijl de dynamische omgeving van een groeiende cel wezenlijk anders is dan een kunstmatige *in vitro* oplossing. We gebruiken een nieuwe benadering om de analyse van een spot in een cel te evalueren door het gebruik van de experimentele beelden voor de achtergrond fluorescentie met simulaties van een focus te combineren. Deze methode stelt ons in staat om de verschillende analyse algoritmes te evalueren op ‘data’ die echte experimentele metingen nauwkeuriger vertegenwoordigen dan pure simulatie of *in vitro* omstandigheden. Onze resultaten geven aan dat er een duidelijke achtergrond afhankelijkheid is van de nauwkeurigheid waarmee de verschillende algoritmen de sterkte van het signaal en de positie van de focus bepalen. Gebruikmakend van onze bevindingen, bieden we een aantal kwantitatieve richtlijnen voor het analyseren van een focus in de drukke omgeving van de cel.

In de hierop volgende hoofdstukken richten we onze aandacht op het toepassen van de verschillende technieken om replicatie in levende *E. coli* cellen te bestuderen. We beginnen met het bestuderen van de β_2 *sliding clamp* (β_2 *clamp*)). De β_2 *clamp* is een essentieel eiwitcomplex dat betrokken is bij de replicatie en het herstel van DNA. Het vormt deel van het replisoom complex dat verantwoordelijk is voor de nauwkeurige replicatie van het chromosoom en verzekert een voldoende hoge processiviteit van de replicatieve polymerase tijdens replicatie. Inzicht in het gedrag van de β_2 *clamp* draagt bij tot gedetailleerde kennis van DNA replicatie en herstelprocessen. In **Hoofdstuk 5** bestuderen wij de kwantitatieve dynamiek van de β_2 *clamp* in levende, actief replicerende *E. coli* cellen. We gebruiken microfluïdica, *wide-field* fluorescentiemicroscopie en *photoactivatible* fluorescentiemicroscopie om het aantal β_2 *clamp*, die DNA gebonden zijn tijdens replicatie, evenals het effectieve tempo van laden en lossen van *clamps* in kaart te brengen. Onze resultaten laten zien dat β_2 *clamps* ophopen op het DNA na initiatie, en een steady-state plateau vormen dat gedurende het grootste gedeelte van het replicatieproces gehandhaafd blijft. Deze ophoping van β_2 *clamps* op het DNA is het gevolg van het relatief trage tempo waarin de *clamps* van het DNA gelost worden. Met behulp van *in vivo* enkel-molecuul microscopie constateren we dat een β_2 *clamp* enkele minuten aan het DNA gebonden blijft. Aangezien de β_2 *clamps* betrokken zijn bij talloze processen, variërend van het beheersen van overinitiatie tot DNA-reparatie, bieden onze bevindingen inzicht in de details betreffende hoe *clamps* een platform vormen voor verschillende eiwitten om te binden en zodoende hun taken op het DNA kunnen verrichten.

Een bewegende replicatievork komt talrijke obstakels tegen, voornamelijk in de vorm van DNA-gebonden eiwitten, die verwijderd of omzeild moeten worden om succesvolle replicatie mogelijk te maken. In **Hoofdstuk 6** onderzoeken we het lot van een individueel replisoom *in vivo* als het een Tus-*ter* eiwitcomplex tegenkomt vanuit de niet doorlaatbare richting in een *E.coli* stam die een onnatuurlijke replicatieoorsprong heeft. De positie van de on-natuurlijke replicatieoorsprong zorgt ervoor dat het replisoom dat met de klok mee (KM) beweegt de barriére eerder tegenkomt dan het replisoom de tegen de klok in beweegt. Onze gegevens suggereren dat het KM replisoom stabiel gebonden blijft op het DNA na het bereiken van de barriére. Door het evalueren van de replicatie tijd, kunnen we vervolgens concluderen dat de replicatievork enkel vertraagd wordt door deze barriéres, en niet voor onbepaalde tijd wordt stopgezet. We tonen aan dat de aanwezigheid of afwezigheid van de Tus-ter barriéres zuster chromosoom uitlijning (ZCU) patronen beïnvloeden. Interessant is dat het resulterende ZCU patroon in de afwezigheid van de Tus-*ter* barriéres geassocieerd wordt met het stop zetten van een vork. Dit komt waarschijnlijk door dat de KM replisoom andere eiwitten tegenkomt die actief op het DNA in de regio van de terminus bezig zijn.

Dit proefschrift beschrijft verschillende methodes en experimenten die ontwikkeld en uitgevoerd zijn om ons begrip van chromosomale replicatie in levende *E. coli* cellen te bevorderen. Chromosomale replicatie is een zeer complex en dynamisch proces dat benaderingen vanuit verschillende disciplines nodig heeft om ons in staat te stellen om de moleculaire details verder te ontrafelen. Microfluïdica wordt steeds populairder in de celbiologie om enkele levende cellen te manipuleren en te bestuderen. De combinatie van microfluïdica met enkel molecuul microscopie en nauwkeurige genetische manipulatie van cellen vormt een platform waarmee wetenschappers enkele eiwitten, en eiwit-eiwit interacties, chromosoom dynamiek en cel heterogeniteit, om maar een aantal voorbeelden te noemen, *in vivo* kunnen bestuderen. We hebben aangetoond dat we door gebruik van de bovenstaande methodes nieuw inzicht hebben verkregen in zowel de robuustheid van het replicatieproces als de replisoom. Zoals wel vaker in wetenschappelijk onderzoek leidt dit proces tot veel nieuwe vragen die waarschijnlijk nog meer van ons als wetenschappers zullen vereisen om ze op te kunnen lossen.

ACKNOWLEDGEMENTS

Starting a PhD is like stepping into a time machine: in a blink of an eye you have reached your 'destination' - even if it does not always feel that way during the journey. This 'destination' is different for each and every one. That said, I believe all PhDs have a few things in common: working very hard (a.k.a. figuring out what the heck to do and doing it), meeting interesting and clever people, and more importantly receiving enormous support from colleagues, family members and friends that enable you to actually complete the journey. In the following paragraphs I would like to reflect back by acknowledging and thanking the numerous people that have made this journey possible for me.

Firstly I would like to thank my *promoter* and supervisor Nynke Dekker. Nynke, thank you for having had the trust in me to make the transition from physics to biology successfully. It has been an exhilarating journey (in a good way). I am extremely grateful for all the support I have received from you over the years. You gave me the freedom to explore and find my own research path. You have provided me with the privileged opportunity to expand as a scientist by attending excellent international courses and (inter)national conferences. On the social (team-building) side, you ensured we had fun group trips annually at many 'cool' places. I have also learned a tremendous amount from you directly. From your excellent writing skills, to your goal orientated working style to keep focused, whilst having an open mind to push the scientific boundaries. Given my slight perfectionistic character, you have also taught me that "perfect can be the enemy of good enough" - a valuable and time-saving lesson for the future. If I look back on how I was as a scientist when I started my PhD and who I am now: I have definably grown orders of magnitude. I am extremely grateful for your vast contribution to my development as a scientist. Hartelijk bedankt!

I am very fortunate to have a group of excellent scientists on my committee: Cees Dekker, Mark Leake, Peter Graumann, Christophe Danelon, Suliana Manley, Rodrigo Reyes-Lamothe, and Marileen Dogterom. I would like to thank each one of you for your time and interest in assessing this dissertation.

Now to the great people I have met and worked with within Bionanoscience. Firstly Sriram, my first partner in crime. You came not too long after my arrival. Together with you (and the help of others listed further down) we have set up the live-cell imaging branch of the Nynke Dekker Lab. Awesome, don't you think? I wish to thank you for the collaboration, and your always friendly and calm demeanor. It has been a pleasure working with you. I truly wish you the best with wrapping things up during the last stretch of your PhD. Good luck to Sumit and Roy with their PhDs and for taking over the live-cell rains - wishing you both success with the challenging and interesting work! Then there is Jacob, my second partner in crime. Jacob, ik heb veel van je geleerd. Niet allen Matlab en data analysen, maar ook over het bedrijven van onderzoek in het algemeen, en hoe om niet knetter gek te worden als dingen voor de 1000ste keer niet lukken. Hartelijk dank voor al je technische hulp en morele ondersteuning deze afgelopen jaren. Ik heb met veel genoegen met jou samengewerkt. Zhuangxoing, it was fun (and a lot of times funny) working with you. We have totally different styles, but somehow it clicked. Thank you for always being willing to help me out when something was unclear or did not work in the cleanroom. Mariana and Richard, it was great sharing an office with you - thanks for all the encouraging conversations. Francesco, thank you for all the time you took to contribute to my optics knowledge. I truly wish you (and your family) all the best in Montpellier. David, thank you for your technical advise and help over the years, but more importantly for your outrages jokes that can come at any time about anything, which gave a comic relief to get one through the tough days. Bojk, great that we met and got to know each other, and I wish you success with the last year of your PhD. Felix(io), it was a funny and cool experience sharing an office with you - thanks for all the laughs. Thanks also for always being willing to listen to my random cleanroom questions and double checking the *samenvatting* of this thesis. Bedankt man! Jan, I am very glad to have met you, and to have shared an office these last years. Thank you for always taking the time (does not matter how busy you are) to listen and provide support and advice on personal matters as well as any scientific topic. Good luck in Munich, you are (going to be) a great group leader. Thank you guys for your friendship. Fabai, thanks for your kind nature and willingness to always help out - good luck wrapping things up. Iwijn, thanks for all the good times at the fussball table - good luck at Cornell. Maarten, good luck with the last stretch of the PhD. Yaron, thanks for always being willing to help and being a walking encyclopedia of random facts - always a pleasure having a chat with you. Pawel, you're a fun person and it has been a pleasure working with you - thanks for the awesome karaoke performances in Belgium, they were great. Michiel, thanks for your support in the form of advise - I appreciated it very much. Aafke, het was super om met je samen te werken, veel success met het afronden van je PhD. I would like to thank the students that I supervised for all their hard work: Rick, Kars, Roy, Jasper, and Kasper. Dank jullie wel! Thanks to Theo, Susan, Serge and Bronwen for your help and patients with me in the biolab. Ilja, altijd geweldig om met je te praten over wetenschap of ditjes en datjes. Jelle en Dimitri, jullie zijn top! Men komt met een super vaag idee en niet lang daarna, boem!, het perfecte onderdeel is al af. Geweldig! Jaap, Sacha and Roland dank jullie wel voor al de technische ondersteuning. Magreet bedankt voor je hulp met de microscopen, en veel plezier met je nieuwe kleine. A great thanks to all the cleanroom people: Anja, Marco, Marc, Roel, Frank, Arnold, Hozanna. Liset, Amanda, Emmylou, Leonie, Jolijn en Dijana, super bedankt voor de morele en meer administratieve ondersteuning - altijd prettig om even met jullie te babellen.

Thanks to the different PIs for the stimulating discussions over the years: Juan, Anne, Marileen, Elio, Bertus, Marie-Eve, Chirlmin, Timon, Cees, Sander, David Grünwald.
Christophe, I can still remember when you, David Grünwald and me where the only people on the first floor - now there is almost too little space. I am very grateful that your door was always open to talk about topics ranging from fluorescence to babies - thank you very much. Greg Bokinsky, it has been a real pleasure meeting you. Thanks for all the

chats about science and non-science. Martin, I am very fortunate that our paths crossed. I have learned a lot from you in terms of science, but also about mindfulness and other 'random' topics - thank you for your personal support over the years. With such a growing department I have had the fortune of crossing paths with many wonderful people: Zhongbo, Erwin, Carsten, Bert, Thierry, Xander, Mina, Rutger, Gautam, Yera, Gary, Artur, Jelmer, Calin, Greg Scheider, Stephanie, Laura, Marek, Huong, Fabrizio, Peter, Helena, Daniel, Adi, Liliane, Andrew, Hugo, Marijn, Pauline, Regis, Zohreh, Kuba, Mahipal, Michela, Seungkyu, Orkide, Jorine, Rifka, Tessa, Stanley, Tim and Meghan, Alicia, Eugen, Ruben, Jetty, Jaco, Allard, Anna, Sophie, Gesa, Maurits, Victor, Vanessa, Dominik, Simon, Ruben, Luuk, Mohamed, Malwina, Jacqueline, Siddarth, Rifka, Nuria. Thanks to all of you for contributing to the great time I have had at BN.

A great thanks goes out to David Sherratt and Rodrigo Reyes-Lamothe for the fruitful and very inspiring collaboration: I learned so much from you both. Vincent Lorent, it was an exciting challenge having a cold atom tenured professor do his sabbatical on replication in live *E. coli*. I am glad to have met you - it was fun having you around!

Believe it or not, there is also a life before and after BN. I would like to thank my previous colleagues whom have contributed to my technical and scientific development: Angelique Botha, Ed de Leer, Eric van der Ham, Emile van Veldhoven, Paul Dekker, Dirk Voigt, Gerard Kotte, Jan Nieuwenkamp, Henk Nieuwenkamp, Richard Koops, Marc Pieksma, Rob Bergmans, Steven van den Berg, Marijn van Veghel, Paul van Kan, Johan van Seggelen, and Albert Dalhuijsen. Lydia de Koning en Daniël Bos, hartelijk dank voor jullie vriendschap over de jaren heen. Paul Urbach, hartelijk dank voor de optica kennis die je me hebt geleerd tijdens mij masters tijd - het kwam zeer van pas bij het opbouwen van een microscoop. Thanks to all my friends outside of BN for their enormous support throughout the years. I could not have done it without you all. Thanks to Barend and Marinda who every now and then sent an encouraging message - it was much appreciated! A special thanks goes to Jack, Charl and Handré who had to always listen to me complain about experiments not working, and my ideas of what to try next or just life in general. Thank you guys for being there for me.

Then there are my parents: Ma, Oom Klaas , Pa, en Ilse. Ek is verewig dankbaar vir julle ondersteuning, hulp, advies, geduld en liefde oor al die jare. Die geleenthede wat julle vir my gegee het, het dit moontlik gemaak vir my om vandag hier te kan wees - baie dankie. Meine Schwiegereltern, Helmut und Sigrid, ich danke Ihnen für die Unterstützung im Laufe der Jahre, aber noch wichtiger für meine liebe Frau Melanie. Meletjie, it is not possible for me to express how lucky and fortunate I am to have you as my wife. I am proud to be able to say that I can share my life with you, and together with Liam you make it full, interesting and awesome. Thank you so much for your unconditional love and support - I love you.

CURRICULUM VITÆ

Martinus Charl MOOLMAN

24-07-1981	Born in Pretoria, South Africa
2000-2003	B.Eng. University of Pretoria
2004-2009	Internship and successively as All-round Metrologist Van Swinden Laboratorium (VSL) - Length and Optics Groups
2006-2009	M.Sc. Department of Imaging Science & Technology, Delft University of Technology Masters research supervisors: prof. dr. H.P. Urbach (DUT) and dr. W.D. Koek (VSL)
2010-2014	Ph.D. Department of Bionanoscience, Delft University of Technology Supervisor: prof. dr. Nynke H. Dekker

LIST OF PUBLICATIONS

M. C. Moolman[‡], J. W. J. Kerssemakers[‡] and N. H. Dekker (2014) Quantitative analysis of sub-cellular fluorescent foci in live bacteria, *Submitted*.

M. C. Moolman[‡], S. T. Krishnan[‡], J. W. J. Kerssemakers, V. Lorent, D. J. Sherratt and N. H. Dekker (2014) The progression of replication forks at natural replication barriers in live bacteria., *Submitted*.

S. T. Krishnan, M. C. Moolman T. van Laar, A. S. Meyer and N. H. Dekker (2014) Essential validation methods for *E. coli* strains created by chromosomal engineering, *Submitted*.

M. C. Moolman, S. T. Krishnan, J. W. J. Kerssemakers, A. van Den Berg, P. Tulinski, M. Depken, R. Reyes-Lamothe, D. J. Sherratt and N. H. Dekker (2014) Slow unloading leads to DNA-bound β_2 sliding clamp accumulation in live *Escherichia coli* cells, *Nature Comm.* **5**, 5820.

M. C. Moolman[‡], Z. Huang[‡], S. T. Krishnan, J. W. J. Kerssemakers and N. H. Dekker (2013) Electron beam fabrication of a microfluidic device for studying submicron-scale bacteria, *J. Nanobiotechnology* **11**, 1-10.

D. Dulin, J. Lipfert, M. C. Moolman and N. H. Dekker (2013)
Studying genomic processes studied at the single molecule level: introducing the tools and applications, *Nat. Rev. Gen.* **14**, 2-9.

M. C. Moolman, W. D. Koek and H. P. Urbach (2009) A method towards simulating the total luminous flux of a monochromatic high power LED operated in a pulsed manner, *Optics Express* **17**, 17457-17470.

K. R. Koops, and M. G. A V̇eghel, G. J. W. L. and M. C. Moolman (2007) Calibration strategies for scanning probe metrology, *Meas. Sci. Technol.* **18**, 390-394.

[‡] Authors contributed equally to this work